MINISTÈRE DE L'ENSEIGNEMENT SUPÉRIEUR
ET DE LA RECHERCHE SCIENTIFIQUE
UNIVERSITÉ FERHAT ABBAS SÉTIF 1 (ALGÉRIE)

THÈSE

Présenté à la Faculté des Sciences
Département de Physique

Pour l'Obtention du Diplôme de

DOCTORAT

DOMAINE : Science de la Matière
FILIÈRE : Physique fondamentale
SPÉCIALITÉ : Physique du globe

Évolution spatio-temporelle de la sismicité de la partie Nord-Est de l'Algérie

SOFIANE TAKI-EDDINE RAHMANI

Présentée et soutenue publiquement le : 22/06/2024
Devant la commission d'examen:

Salim HOUAMER	Président	Prof, Université Ferhat Abbas Sétif
Issam ABACHA	Directeur de thèse	DR, CRAAG Sétif
Oualid BOULAHIA	Co-directeur de thèse	MRB, CRAAG Sétif
Hamoud BELDJOUDI	Examinateur	DR, CRAAG Alger
Abdelhak TALBI	Examinateur	DR, CRAAG Alger
Moulley Charaf CHABOU	Examinateur	Prof, Université Ferhat Abbas Sétif
Abdelaziz KHERROUBI	Invité	DR, CRAAG Alger
AbdelKarim YELLES-CHAOUCHE	Invité	DR, CRAAG Alger

Abstract

The seismic activity in Northeastern Algeria is characterized by the occurrence of swarms, often without a mainshock, or classic sequences comprising a mainshock followed by aftershocks. These seismic events exhibit strong temporal and spatial concentrations in both cases, lasting from days to months and spanning distances ranging from a few to tens of kilometers. Occasionally, these activities demonstrate a migration pattern over several kilometers across several weeks. While the advent of various seismological methodologies at CRAAG has enhanced seismic studies in Algeria, there remains a notable absence of detailed statistical analysis to characterize and categorize seismic sequences according to their spatio-temporal patterns and physical processes. This thesis aims to address this gap by employing robust statistical models to characterize earthquake sequences, focusing on quantifying their spatio-temporal patterns. It embarks on a comprehensive exploration of spatio-temporal pattern modeling, elucidating both mathematical and physical characteristics. Key aspects covered include determining magnitude completeness (m_c), understanding magnitude distribution using the Gutenberg-Richter model, and examining spatio-temporal models like the Omori-Utsu law and the ETAS (Epidemic Type Aftershock Sequence) model. Additionally, it highlights physical models such as Rate-and-state friction, Coulomb failure, and time dependent stress rate. The thesis also scrutinizes various statistical analysis approaches, exploring the effects of declustering on parameter estimation and the influence of misestimating completeness magnitude on ETAS parameters. It further investigates techniques for achieving unbiased parameter estimation and explores the impact of disregarding aseismic forcing transients. Moreover, it compares the isotropic and anisotropic spatial distribution of aftershocks, shedding light on the complexities of seismic activity. Another significant aspect of the study is the detection and characterization of earthquake swarms, utilizing spatio-temporal ETAS models and moment release time series analysis. Employing two methodologies to identify swarm-like behavior, the research considers the tectonic and geological characteristics of the area, offering valuable insights into the nature of seismic swarms. Special emphasis is placed on the Beni-Ilmane earthquake sequence, one of the most important seismic events in Northeastern Algeria, in terms of the number of earthquakes produced and studies conducted. Through the application of statistical tests, the research endeavors to understand the underlying mechanisms driving the heightened seismicity observed in this sequence, drawing comparisons with previous physical and geological studies. In conclusion, this thesis significantly contributes to the understanding of seismicity in Northeastern Algeria. The analyses conducted provide insights into the spatio-temporal characteristics of earthquakes, crucial for predicting and managing seismic risks in the region. The comprehensive categorization of seismic sequences enhances targeted mitigation strategies, making a valuable contribution to the field of seismic research and facilitating informed decision-making for earthquake-prone regions.

Keywords: Northeast Algeria, Spatio-temporal evolution, Statistical analysis, Swarm sequences, Seismic sequences, Fluid driven, Mainshock-aftershock sequences.

Résumé

L'activité sismique dans le nord-est de l'Algérie se caractérise par la survenue d'essaims, souvent dépourvus de choc principal, ou de séquences classiques comprenant un choc principal suivi de répliques. Ces événements sismiques présentent des concentrations temporelles et spatiales marquées dans les deux cas, d'une durée de quelques jours à plusieurs mois et couvrant des distances allant de quelques kilomètres à plusieurs dizaines de kilomètres. De temps à autre, ces activités montrent un schéma de migration sur plusieurs kilomètres sur plusieurs semaines. Bien que l'avènement de diverses méthodologies sismologiques au CRAAG ait amélioré les études sismiques en Algérie, on constate une absence notable d'analyses statistiques détaillées pour caractériser et catégoriser les séquences sismiques selon leurs schémas spatiotemporels et leur processus physique. Cette thèse vise à combler cette lacune en utilisant des modèles statistiques robustes pour caractériser les séquences sismiques, en mettant l'accent sur la quantification de leurs schémas spatiotemporels. Elle entreprend une exploration approfondie de la modélisation des schémas spatiotemporels, élucidant à la fois les caractéristiques mathématiques et physiques. Les aspects clés abordés comprennent la détermination de la magnitude de complétude, la compréhension de la distribution en magnitude en utilisant le modèle Gutenberg-Richter, et l'examen de modèles spatiotemporels tels que la loi d'Omori-Utsu et le modèle ETAS (Epidemic Type Aftershock Sequence). De plus, elle donne un bref apperçu des modèles physiques tels que le frottement entre états, la chute de contrainte de coulomb et le taux de contrainte dépendant du temps. La thèse examine également diverses approches d'analyse statistique, explorant les effets du dégroupement sur l'estimation des paramètres et l'influence de la mauvaise estimation de la magnitude de complétude (m_c) sur les paramètres ETAS. Elle enquête en outre sur les techniques permettant d'obtenir une estimation impartiale des paramètres et explore l'impact de l'ignorance du processus asismique transitoire. De plus, elle compare la distribution spatiale isotrope et anisotrope des répliques, mettant en lumière les complexités de l'activité sismique. Un autre aspect significatif de l'étude est la détection et la caractérisation des essaims sismiques, utilisant des modèles ETAS spatiotemporels et une analyse des séries temporelles de libération d'énergie. En employant deux méthodologies pour identifier un comportement semblable à un essaim, la recherche prend en compte les caractéristiques tectoniques et géologiques de la région, offrant des informations précieuses sur la nature des essaims sismiques. Une emphase particulière est mise sur la séquence sismique de Beni-Illman, l'un des événements sismiques les plus importants dans le nord-est de l'Algérie, en termes de nombre d'événements générés et d'études conduites. À travers l'application de tests statistiques, la recherche s'efforce de comprendre les mécanismes sous-jacents à l'augmentation de la sismicité observée dans cette séquence, en établissant des comparaisons avec des études physiques et géologiques antérieures. En conclusion, cette thèse contribue de manière significative à la compréhension de la sismicité dans le nord-est de l'Algérie. Les analyses réalisées fournissent des informations sur les caractéristiques spatiotemporelles des séismes, cruciales pour la prédiction et la gestion des risques sismiques dans la région. La catégorisation complète des séquences sismiques renforce les stratégies ciblées d'atténuation, apportant une contribution précieuse au domaine de la recherche sismique et facilitant la prise de décisions éclairées pour les régions sujettes aux tremblements de terre.

Mots clés: Nord-Est Algérien, Évolution spatio-temporel, Analyse statistique, Séquence en swarm, Séquence sismique, Déclenchement par les fluids, Séquences de séisme principal et de répliques.

نبذة مختصرة

تتميز النشاطات الزلزالية في شمال شرق الجزائر بظهور حشود زلزالية، تخلو في كثير من الأحيان من هزة رئيسية، أو تتكون من سلسلة كلاسيكية تتألف من هزة رئيسية تليها الاهتزازات الارتدادية. تتميز هذه الأحداث الزلزالية بتركيز زماني ومكاني قوي، يمتد من أيام إلى أشهر ويمتد لمسافات بين بضعة إلى عشرات الكيلومترات. في بعض الأحيان، تظهر هذه الأنشطة نمطًا للترحيل عبر عدة كيلومترات على مدى عدة أسابيع. في حين أن ظهور الأساليب الزلزالية المختلفة في مركز البحث في الفيزياء الفلكية والجيوفيزيائية التطبيقية قد عزز الدراسات الزلزالية في الجزائر، يظل هناك غياب ملحوظ للتحليل الإحصائي المفصل في هذا المجال. هذه الرسالة تهدف إلى معالجة هذه الفجوة من خلال استخدام نماذج إحصائية قوية لتوصيف التتابعات الزلزالية، مع التركيز على قياس خصائصها المكانية والزمانية. تبدأ الرسالة استكشاف شامل لنمذجة الأنماط المكانية والزمانية، موضحة كل من الخصائص الرياضية والفيزيائية. تشمل الجوانب الرئيسية المغطاة تحديد اكتمال القوة، وفهم توزيع القوة باستخدام نموذج غوتنبرغ-ريختر، وفحص النماذج الزمانية مثل قانون أوموري-أوتسو ونموذج ETAS. بالإضافة إلى ذلك، تلقي الضوء على النماذج الفيزيائية مثل إحتكاك المعدل والحالة، فشل كولومب، ومعدل التوترالمتعلق بالزمن. الرسالة العلمية أيضًا تدرس مختلف النهج التحليلية الإحصائية، وتستكشف تأثير إزالة التجميع على تقدير القياسات وتأثير تقدير مقدار الاكتمال بشكل غير صحيح على قياسات ETAS. وتحقق أيضًا في تقنيات تحقيق تقدير القياسات غير المتحيزة وتستكشف تأثير تجاهل العوامل الدافعة الزلزالية الغير لحظية. بالإضافة إلى ذلك، فإنها تقارن التوزيع المكاني للهزات الارتدادية المتساوية الاتجاهات وغير المتساوية الاتجاهات، مسلطة الضوء على تعقيدات النشاط الزلزالي. جانب آخر مهم في الدراسة هو كشف وتوصيف الحشود الزلزالية، باستخدام النماذج الزمانية والمكانية (ETAS) وتحليل سلاسل زمن إطلاق الزلزال. توظيف طريقتين لتحديد السلوك المشابه للحشود الزلزالية، ينظر البحث إلى الخصائص التكتونية والجيولوجية للمنطقة، مما يقدم رؤى قيمة حول طبيعة وسلوك الحشود الزلزالية. تُولي التركيز الخاص على تتابعات زلازل بني إلمان، واحدة من أهم الأحداث الزلزالية في شمال شرق الجزائر. من خلال تطبيق الاختبارات الإحصائية، يسعى البحث إلى فهم الآليات الأساسية التي تدفع بزيادة النشاط الزلزالي الملاحظ في هذه المنطقة، مع إجراء مقارنات مع الدراسات الفيزيائية والجيولوجية السابقة. في الختام، تساهم هذه الرسالة بشكل كبير في فهم النشاط الزلزالي في شمال شرق الجزائر. التحليلات التي أُجري

كلمات مفتاحية: شمال شرق الجزائر، تطور مكاني-زماني، تحليل إحصائي، حشود زلزالية، تتابعات زلزالية

Aknowledgment

As I stand at the pinnacle of completing my doctoral thesis in science, my heart overflows with gratitude for the incredible support and assistance I have received from numerous individuals who have played pivotal roles in shaping this significant phase of my life and career. I am immensely thankful to each one of you, and may God bless you abundantly.

First and foremost, my sincere thanks go to the esteemed members of the jury – Mr. HAMOUD BELDJOUDI, Mr. MOULLEY CHARAF CHABOU, Mr. TALBI ABDELHAK, Mr. YELLES-CHAOUCHE ABDELKARIM, and Mr. KHERROUBI ABDELAZIZ. Your willingness to evaluate and act as rapporteurs for this work, as well as allowing me the opportunity to defend it, is deeply appreciated. I extend my gratitude to Mr. HOUAMER SALIM for presiding over the thesis committee.

I am deeply thankful to my esteemed thesis supervisor, Mr. ABACHA ISSAM, who has been the guiding force behind this significant achievement. His decision to lead this research work has not only rejuvenated my academic journey but has also been instrumental in shaping a new trajectory for my career. His unwavering belief in my abilities and consistent encouragement to persist in my research endeavors have been invaluable. In essence, your mentorship has been the cornerstone of this achievement, and I am profoundly grateful for the positive impact it has had on both my academic and professional journey.

I want to extend my heartfelt appreciation to my co-supervisor, Mr. BOULAHIA OUALID, whose support has been instrumental in the success of my research. His guidance, advice, and encouragement have been constant sources of motivation throughout this journey. Mr. BOULAHIA OUALID not only provided valuable insights but also cheered me on during challenging moments

Gratitude extends to my colleagues, especially ROUBECHE KHALED, who has been a steadfast companion since university. Special thanks to TKHAMARINE EL-MAHDI for the meaningful time we spent together.

I want to express my thanks to my colleagues from CRAAG Setif – MEZIANE MOHANED, RADI ZOHIR, LAYADI KHALISSA, KHARCHOUCHE RADIA, CHABOU AMEL.

I also want to express my gratitude to BENDJAMA HICHEM, a colleague who has been a valu-

able support. Your collaboration and efforts have truly made a difference. Thank you.

I would like to extend my gratitude to all my colleagues at CRAAG Algiers, with a special mention to FETHI SEMMANE. Your consistent provision of opportunities and valuable advice has been instrumental in our collective success. I appreciate the collaborative spirit and the supportive environment you foster within our team.

I also want to express my thanks to DILMI TAKIEDDINE. Your camaraderie added a delightful touch to our professional journey, making it all the more memorable. Thank you for the joy and laughter we shared during those times.

A heartfelt thank you to CRISTINA CRESPO-MARTIN. Even though we worked together only through Zoom, our collaboration was more than just work. Our one-hour working sessions often turned into two hours of chatting and laughter, and I enjoyed every moment of it. Thank you so much.

I want to extend my deepest gratitude to all the wonderful friends I had the pleasure of making at GFZ in Germany – GHAZALL, DANI, DELL, EDA, ARUN, ANDRES, SOL, FRANCESCO, LOUISE, and FATIMA. Your company made the month we spent together incredibly enjoyable, and I hold every moment close to my heart. Each one of you contributed to creating a vibrant and supportive environment that enhanced both our personal and professional experiences. I would like to extend special thanks to Professor HAINZL SEBASTIAN for graciously agreeing to collaborate with me on my unconventional idea. Your openness to innovation and your willingness to explore new avenues have been truly inspiring. I am grateful for the opportunity to work alongside you.

I want to convey my heartfelt appreciation to BOGDAN ENESCU from Kyoto University for his unwavering support during my stay in Japan. His meticulous attention to every detail and dedicated efforts to ensure my days were both fruitful and joyful are gestures I will forever cherish. Thank you, BOGDAN, for everything, and I look forward to the prospect of future collaborations that are equally enriching.

I would also like to express my gratitude to LIKE, a wonderful companion during my time in Japan. Our shared experiences brought immense joy, and it is unfortunate that current circumstances make it challenging for us to meet. I have full confidence in your potential to become a remarkable scientist, and I wish you all the success in your endeavors.

To my parents, my eternal gratitude for the unwavering support and care throughout my journey. Mom, your dedication to raising us is unparalleled, and Dad, I wish you were here to witness the person I've become. Your love and guidance have been my pillars of strength.

To my dear brother and sister, thank you for everything. Despite the miles that separate us in

different countries and cities, our hearts remain close, and your support means the world. We may be apart in distance, but we are always together in spirit.

To my second family – ABDELNOUR BOUAOUD, BENTALEB LAMRI, LAMOURI ABDELRAOUF, REZZAZGUI ABDELAZIZ, MEHNAOUI YOUCEF, ROUEBEH FOUED, SARAOUI YAHIA, AOUN MALIK, MOUSLY ACHREF, and KEROUANI YOUNES – your companionship since high school is a treasure. Despite our playful banter, the bond we share is enduring. I love you all dearly!

To my fiancée, thank you for standing by my side through it all, even when I am a bit overdramatic at times. Your unwavering support adds a touch of beauty to our journey together.

Rahmani Sofiane Taki-Eddine

Seismology is the poetry of the earth, written in waves and vibrations.

Charles F. Richter

FORWORD

The intricate dance of the Earth's crust, expressed through seismic events, has been a source of fascination for scientists throughout the ages. As I introduce this thesis on the statistical analysis of seismicity in the Northeastern region of Algeria, I am reminded of the numerous hours dedicated to unraveling the concealed mysteries within the intricate patterns of seismic data.

The fascination with earthquakes and their enigmatic behavior has been a constant companion since my early days as a student. The seismic events that shape the Earth's crust are not merely geological occurrences; they are windows into the very essence of our planet's evolution.

The impetus to explore the statistical analysis of Algerian seismicity originated from my supervisors, who presented this intriguing subject to me. While the initial foray was challenging, grappling with the ambiguous link between statistical analysis and the physical processes governing earthquakes, I discovered an unexpected enjoyment in every moment of the journey. The path was rugged, marked by more valleys than peaks, yet the summit experiences were profoundly uplifting, unveiling dreams I never deemed attainable.

This thesis has not only enriched my academic journey but has also fostered lasting connections with individuals who have now become close friends. In this collaborative endeavor, I had the privilege of learning from the best, starting with my dedicated supervisors who provided a solid foundation for my understanding. And led me to be part of their respective projects that gave papers that I co-authored. Additionally, my institute (CRAAG), which provided the data, serves as a pivotal source of information essential for conducting my studies.

I owe a debt of gratitude to a diverse group of individuals from around the globe who generously welcomed me into their projects. It all began with Cristian Ghita from Romania, whom I had the pleasure of meeting at the IUGG conference, facilitated by the introduction from Professor Bogdan Enescu, a dear friend I met during my time at Kyoto University. Professor Enescu proposed that I join the research on seismicity in Romania, a collaboration that culminated in my role as the third co-author on a forthcoming paper slated for submission to Seismological Research Letters (SRL). I got also to meet and exchange ideas with Professor David Marsan who, by his papers, influenced my way of working.

My association with Kyoto University also led me to connect with a PhD student named Like An and professor Franscesco Grigoli, who quickly became a cherished friend and collaborator. Together, we are embarking on a joint venture to explore the fusion of innovative location techniques and their impact on statistical parameters.

Reflecting on these experiences, I am transported back to the transformative journey at the GFZ

Institute in Potsdam. During this period, I had the invaluable opportunity to meet Sebastian Hainzl, and our collaboration has evolved into a joint exploration of a novel approach to the ETAS model, aimed at determining the variable background rate. Sebastian Hainzl's influence on my knowledge has been profound; his papers have not only shaped my approach to work but also ignited a deeper understanding of seismic dynamics. Working alongside him is truly an honor and a testament to the collaborative spirit that defines seismic research.

Moreover, my time at GFZ extended beyond individual collaborations. I had the pleasure of meeting other Ph. D. students with whom I am now engaged in exchanging ideas and working on various projects. These interactions have further enriched my academic journey, fostering a collaborative environment where diverse perspectives converge to push the boundaries of seismic research Lastly, my paper "Time-dependent and spatio-temporal statistical analysis of seismicity: application to the complete dataset of the 2010 Beni-Illman seismic sequence," published in Geophysical Journal International (GJI), has led a fellow friend from Cameroon to invite me to join him in utilizing similar techniques for seismicity induced by fluids and magma intrusion. Seeing the impact of your work make you feel greatful for the journey.

After all these experiences, what I can say is that the most valuable lesson I have learned from this journey is humility. It underscores the realization that, despite acquiring knowledge, there is always a vast expanse yet to be explored. Additionally, understanding that each researcher has their own unique perspective, which should be respected, has taught me the importance of agreeing to disagree in the pursuit of collaborative and constructive dialogue.

As I conclude this journey, I am grateful for the invaluable experiences, the friendships forged, and the opportunities to contribute to the ever-evolving field of seismic research.

Contents

List of Figures

List of Tables

List of abbreviations

ADSN: Algerian Digital Seismic Network

G-R: Gunterberg-Richter

FMD: Frequency Magnitude Distribution

$\mathbf{m_c}$: Magnitude of Completeness

MAXC: Maximum Curvature

GFT: Goodness Of Fit

MBS: Magnitude of completeness $byb - value$ Stability

EMR: Entire Magnitude Range

MBASS: Median-Based Analysis of the Segment Slope

RS:Rate-and-State

CF: Coulomb Failure

TDSR: Time Dependent Stress Rate

STAI: Short-Term Incompleteness

ETAS: Epidemic Type Afterhock sequence

NND: Nearest Neighbour Declustering

PSHA: Probabilistic Seismic Hazard

ETASI: Epidemic Type Aftershock Sequence Incomplete

Mw: Moment Magnitude

ML: Local Magnitude

BI-MS: Beni-Ilmane MainShock

General Introduction

An earthquake, a natural occurrence resulting from the fracturing of rocks in the Earth's crust and lithospheric mantle, unfolds abruptly, releasing a substantial amount of energy in the form of seismic waves. These waves propagate in all directions, inducing ground shaking upon reaching the Earth's surface, occasionally leading to ground failure and causing adverse effects on human lives and activities.

The social and economic repercussions of earthquakes are profound, transcending geological impacts. Disruption of infrastructure, loss of property, potential loss of life, and the displacement of communities are among the social challenges. Economically, earthquakes can incur significant costs through the destruction of buildings, critical infrastructure, and disruptions to business activities. Understanding and mitigating seismic risks on a global scale are imperative for safeguarding communities and sustaining economic resilience in the face of these natural events.

Earthquakes are not isolated incidents but rather components of a sequence, often starting with a dominant event, known as mainshock, or in some cases, a subtle escalation in seismic activity termed foreshock activity. Subsequently, a series of smaller and less frequent earthquakes, termed aftershocks, occur in close spatio-temporal proximity to the mainshock. Some earthquake sequences may lack a dominant shock but can still elicit significant concern in society, referred to as swarms (Utsu, 2002).

Over the past two decades, research has focused on characterizing diverse earthquake sequences, exploring the interaction between earthquakes, their triggering effects, and their applications in earthquake forecasting and prediction. Various methods, such as statistical clustering theories and physics-based approaches, are employed to comprehend the spatio-temporal patterns

of earthquake clustering. While pinpointing earthquake prediction in terms of exact occurrence time, size, and location remains elusive, alternative approaches focus on estimating activity rates for different spatio-temporal frames for seismic hazard analyses (Utsu et al., 1995; Zhuang et al., 2002).

Physics-based and statistic-based models describing seismic occurrences are considered two sides of the same coin. Statistical models are seen as complementary or extensions of physical-based models, with the main difference lying in the required information. Statistical approaches treat earthquakes as entities with attributes like origin time, hypocentral coordinates, and magnitude, considered as random variables with associated probability distributions, typically sourced from earthquake catalogs. In contrast, the physics-based approach demands additional seismological attributes, such as seismic phases, and geophysical parameters like slip distribution over ruptured areas and regional stresses, for a more comprehensive understanding.

The statistical assessment of earthquake occurrence rates, aftershock sequences, and their temporal decay patterns aids in deciphering the underlying physics of earthquake nucleation. Additionally, the strength of faults and their response to dynamic stresses induced by seismic waves can be investigated through statistical analyses. This analytical framework allows researchers to draw comparisons to laboratory experiments and physical models, providing a deeper understanding of fault behavior under different loading conditions. The use of statistical seismology is pivotal for characterizing earthquake triggering effects, shedding light on the factors influencing seismicity and contributing to advancements in earthquake forecasting and prediction (Helmstetter and Sornette, 2002).

However, it's essential to acknowledge certain limitations associated with statistical seismology. One significant challenge lies in the inherent uncertainties and variability within seismic data, as cataloged earthquake information may be subject to biases and incomplete recordings. The accuracy of statistical models heavily relies on the quality and completeness of earthquake catalogs, and the presence of undetected seismic events can introduce biases in the analysis. Moreover, while statistical approaches provide valuable insights into seismic patterns and triggering effects, they may not capture the full complexity of the underlying physical processes governing earthquake interactions. The reliance on historical earthquake data also poses limitations in predicting future seismic

events accurately. Despite these challenges, statistical seismology remains a powerful tool for unraveling seismic complexities and enhancing our understanding of earthquake behavior. Although these techniques can be delicate to use, as explained, they are highly data-driven. Employing the correct approaches and comprehending the data being utilized may help mitigate any biases that could arise from these techniques. Furthermore, combining physical models with a deep understanding of the tectonic state of the region can create the perfect combination to unveil the complex features of the underlying mechanisms responsible for seismic activity (Reverso et al., 2018).

The Northern Algerian region is known for experiencing numerous seismic events throughout its history, some of which have been major. Examples include the earthquakes in Algiers in 1365 and 1716, Oran in 1790, Djidjelli in 1856, Gouraya in 1891, Aumale in 1910, Orleansville in 1954 (M6.7), El-Asnam (Chlef now) in 1980 (M7.1), Constantine in 1985 (M6.0), Tipasa in 1989 (M6.0), Mascara-Beni Choughrane in 1994 (M5.7), Ain Temouchent in 1999 (M5.9), Boumerdes-Zemmouri in 2003 (M6.8) and most recently, the Bejaia earthquake in 2021 (M6.0). This seismic activity, resulting from the convergence of the two major tectonic plates, African and Eurasian, has been historically studied primarily through the analysis of historical events. It was only after the El Asnam earthquake on October 10, 1980, that the beginnings of modern seismology emerged with the use of seismological instrumentation.

Following the Boumerdes earthquake on May 21, 2003, the CRAAG (Research Center in Astronomy, Astrophysics, and Geophysics) decided to establish the initial digital seismological network. This network, now recognized as the ADSN (Algerian Digital Seismic Network), began deployment in 2007, gradually expanding to include a total of 69 stations, comprising 17 broadbands, 01 very-broadband, and 51 short-periods (Yelles-Chaouche et al. (2022)).

The initial contribution to understanding seismic hazard in the entire Northeastern region was presented in Abacha, 2015. This work combined geological, tectonic, and seismological data to identify nine seismogenic zones, delving into two seismic sequences: the first, induced in Mila in 2007, and the second, tectonic in nature, occurring in Beni-Ilmane in 2010. However, caution is advised in interpreting seismic behavior in each zone due to the presence of several unknown faults. The spatial patterns of seismicity are complex and diffuse, often occurring away from the main active fault zones' transition areas.

More recently, advancements in understanding active deformation in the Eastern Algerian region have been made through Bougrine, 2019. The author reveals the deformation partitioned by the right-lateral strike-slip fault, "Gharimadou Nord Constantinois (GNC)," extending from Tunisia, cutting across the entire Northeast Algeria. Also known as "the North Constantinois Fault (NC) and Mcid Aïsha-Debbagh (MAD)," this fault plays a significant role, contributing to 44% of the oblique convergence between the African and Eurasian plates in Eastern Algeria. While the GNC fault accommodates right-lateral shearing between the two plates, the convergence component is distributed among offshore faults to the North ($\sim$1.5 mm/year) and the Gafsa fault system to the south ($\sim$1.5 mm/year).

Lastly, the study by Boulahia, 2022 significantly advanced our comprehension of recent seismic activity in Northeastern Algeria through spectral analysis and waveform modeling of significant events. This analysis provided crucial insights into rupture processes, fault geometries, and source parameters, essential for understanding earthquake interactions. Additionally, the use of precise earthquake relocation techniques revealed previously unmapped faults and transverse structures, enriching our understanding of regional seismicity.

Despite numerous studies, there has been no comprehensive statistical analysis of the Northeastern part of Algeria to characterize and categorize seismic sequences according to their physical processes, by understanding the statistical parameters to describe the ongoing process. Although studies on forecasting seismicity rate and mitigating the maximum magnitude in the Northern part of Algeria have already been conducted (Hamdache et al., 2019a; Hamdache et al., 2019b; Bellalem et al., 2023, Merdasse et al., 2023). This region has witnessed several seismic sequences in recent decades, exhibiting distinct patterns, including the occurrence of two or more strong shocks within a confined space and a short timeframe, accompanied by temporal and spatial migration. Considering the increasing global interest in this field, this thesis aims to characterize earthquake sequences in the Northeastern part of Algeria. It employs well-established and robust statistical models to quantify spatio-temporal and magnitude patterns of seismicity.

The thesis is structured into four chapters.

The first chapter delves into the spatio-temporal patterns models of seismicity, explaining the mathematical and physical characteristics of these models. It begins with determining the mag-

nitude of completeness (m_c), a crucial parameter before conducting any statistical analysis. The methods for determining this parameter are explored, considering their advantages and disadvantages. The chapter then addresses magnitude distribution, describing the Gutenberg-Richter (G-R) model with its two parameters, $b-value$ and $a-value$, which represent the stress state and rate of seismicity, respectively (Gutenberg and Richter, 1956). Temporal models are also discussed, including the Omori-Utsu law, which describes the temporal decay of aftershocks after the mainshock (Omori, 1894; Utsu, 1961), the analysis of the inter-event time for succecive events, and the temporal ETAS model (epidemic type aftershock sequence), known for its robustness (Ogata, 1988). The non-stationary ETAS model is introduced to describe seismicity triggered by aseismic transient forcing rate (Marsan et al., 2013). The chapter also covers spatio-temporal models, including the ETAS model with parameters variable in time and space (Ogata, 1998), and the Nearest Neighbor Declustering (NND) (Zaliapin et al., 2008), both helpful in understanding events generated by external and internal forcing. Finally, a brief insight into physical models like the Coulomb failure and the rate-and-state friction model (King et al., 1994; Dieterich, 1994), particularly the time-dependent stress rate model (Dahm and Hainzl, 2022), is provided, proving to be more effective than previously described models.

The second chapter will delve into various approaches that must be considered when conducting any statistical analysis. Firstly, it will assess the impact of declustering on the estimation of the $b-value$ and, consequently, the predicted maximum magnitude in a region. Following that, it will examine the advantages and disadvantages of all the techniques used to estimate the magnitude of completeness. Additionally, it will scrutinize the influence of misestimating the magnitude of completeness on the ETAS parameters, particularly the productivity factor $\alpha-value$. The chapter will also explore various techniques involved in both estimating the ETAS parameters to facilitate unbiased parameter estimation without sacrificing information. Furthermore, it will investigate the influence of neglecting aseismic forcing transients on the ETAS parameters. Finally, it will explore the disparities between the isotropic spatial distribution of aftershocks and the anisotropic one.

The third chapter focuses on the detection and characterization of earthquake swarms in the Northeastern part of Algeria, employing two methodologies. Firstly, the spatio-temporal ETAS model parameters were determined for the entire region using a bootstrap approach to assess un-

certainties. Subsequently, the region was divided into grid cells of dimensions 0.2°x 0.2°, and the transformed time was calculated in each grid cell. The '1σ criterion' (Nishikawa and Ide, 2017) was then applied to identify events exhibiting swarm-like behavior. For the second method, skewness and kurtosis of the moment release time series were computed for each cluster after identification using CURATE (Jacobs et al., 2013; Mesimeri et al., 2019). Two swarm catalogs were independently found and merged, applying additional criteria such as ensuring the difference between the largest and second-largest event in each cluster is less than one magnitude unit. Interpretations were based on the tectonic setting and geological area to understand the factors responsible for these earthquake swarms. This research, in which i served as the lead author, has been submitted for publication in **Natural Hazard (NH)**. The paper identifies a total of 32 seismic swarms and a few sub-swarms. Some of these swarms are associated with seismic sequences previously documented during my Ph.D. thesis, where i was a co-author.

The first sequence relates to the 2019 Jijel earthquake, which was published in the **African Journal of Science in 2021** (Yelles-Chaouche et al., 2021). The second sequence pertains to the earthquake activity along the E-W trending Mcid Aïcha-Debbagh fault in March 2017, published in the **Geosciences Journal in 2021** (Bendjama et al., 2021). The third sequence pertains to the Mw 5.0 El Aouana earthquake on January 24, 2020, and was reported in the **Pure and Applied Geophysics (PAGEOF) Journal in 2023** (Abacha et al., 2023b). Additionally, a tomography of the Bejaia-Babors region was conducted and submitted to **PEPI (Physics of the Earth and Planetary Interiors)**, which helped in the interpretation of the origin mechanisms of the identified swarms in the region.

The final chapter will delve into one of the most crucial seismic events in the Northeastern part of Algeria, the Beni-Ilmane earthquake sequence. To comprehend the heightened seismicity observed in this sequence, which surpassed the earthquake frequency of other sequences in the same region, various statistical tests were applied. The obtained results were meticulously compared to insights derived from preceding physical and geological studies conducted in the region. Three main studies were conducted to unravel the intricacies of this phenomenon. The first study focused on the migration of fluids across different faults, identified as a significant factor in the formation of seismic swarms. This phenomenon was unequivocally confirmed in the case of the 2010 Beni-

Ilmane sequence through a comprehensive 4D seismic tomography study, with a specific emphasis on the Vp/Vs ratio. The conclusive findings from this study were reported in 2023 in **the Journal of Seismology (JOSY)** (Abacha et al., 2023a). Furthermore, the assertion regarding fluid migration's role was substantiated by a statistical analysis, serving as the primary publication of this thesis, presented in the **Geophysical Journal International (GJI)** (Rahmani et al., 2023). Another study on the Beni-Ilmane sequence has been submitted to **GJI**, by Tikhamarine et al., promising a more intricate and comprehensive analysis of the seismic phenomenon.

In conclusion, all the tests and analyses conducted will contribute to a deeper understanding of the spatio-temporal characteristics of earthquakes in the Northeastern part of Algeria. This knowledge can be valuable for seismic hazard mitigation. The categorization of each seismic sequence into swarms or mainshock-aftershock sequences is particularly important. This classification can significantly enhance seismic hazard assessment efforts.

Categorizing seismic sequences is essential for seismic hazard assessment as it allows for a more refined analysis of earthquake patterns. Swarms, characterized by clusters of seismic activity, may indicate the presence of fluid migration along fault lines, potentially influencing seismic hazard (Atkinson and Adams, 2013). On the other hand, distinguishing mainshocks and aftershocks within a sequence is crucial for assessing the potential for secondary seismic events. This comprehensive categorization aids in the development of targeted mitigation strategies and improves our ability to predict and manage seismic risks in the Northeastern part of Algeria.

Chapter 1

Spatio-temporal earthquake patterns models

1.1 Introduction

Statistical methods play a pivotal role in seismology due to the incomplete understanding of earthquake processes. Statistical seismology involves analyzing the distributions of earthquake-related data and applying statistical techniques to address specific challenges. A primary goal is to distill the available data into a more manageable format for interpreting the underlying physical phenomena, primarily achieved through parameter estimation for the variables under study.

Within the realm of seismology, researchers frequently concentrate on examining the distributions of key earthquake parameters, such as magnitude, occurrence time, and location, to gain insights into the underlying physical mechanisms. Recently, there has been a growing interest in understanding the spatial and temporal complexities of earthquake occurrences and interactions, leading to an increased emphasis on investigating distributions of derived quantities. This chapter explores earthquake distributions in terms of magnitude, temporal aspects, and spatial characteristics. It is important to note that all figures presented in this chapter were generated using codes that we developed, with Matlab and Python languages, through synthetic tests, except for Figure 1.19, 1.20, and 1.21 in section 1.6.

1.2 Magnitude of completeness (m_c)

Evaluating the magnitude of completeness (m_c) in instrumental earthquake catalogs is a fundamental and necessary process for seismicity analysis. m_c is characterized as the minimum magnitude at which 100% of earthquakes within a specific space-time volume are reliably detected and recorded by a particular seismic network or instrument setup. The existence of m_c is generally due to:

- The signal is so small that it cannot be separated from the background noise.
- The earthquake is so small, that is not detected by a sufficient number of seismic stations to be recorded.
- Network operators decided that events below a certain threshold are not of interest.
- Some events are too small to be detected within the coda of larger events (increased noise).

Ensuring an accurate estimation of m_c is crucial because an excessively high value may result in under-sampling, which will lead to a loss of information, while an excessively low value can lead to inaccurate seismicity parameter values, introducing bias into the analysis through the use of incomplete data. This section will outline various methods for estimating m_c.

1.2.1 The maximum curvature (MAXC)

The maximum curvature (MAXC) technique, initially proposed by Wyss et al., 1999 and subsequently refined by Wiemer and Wyss, 2000, provides a swift and straightforward approach for estimating m_c. This method involves identifying the point of maximum curvature by pinpointing the peak value of the first derivative within the frequency-magnitude curve (Figure 1.1). Essentially, this corresponds to the magnitude bin with the highest frequency of events in non-cumulative frequency-magnitude distributions (FMD). Although this approach is easily applicable, it tends to underestimate m_c when dealing with gradually curved FMDs. However, Mignan, 2011 demonstrated that, within a localized dataset where variations in m_c are minimized, the MAXC technique

does not lead to m_c underestimation. Another advantage of the MAXC technique is its ability to provide a stable result with a smaller number of events compared to alternative methods (Mignan, 2011).

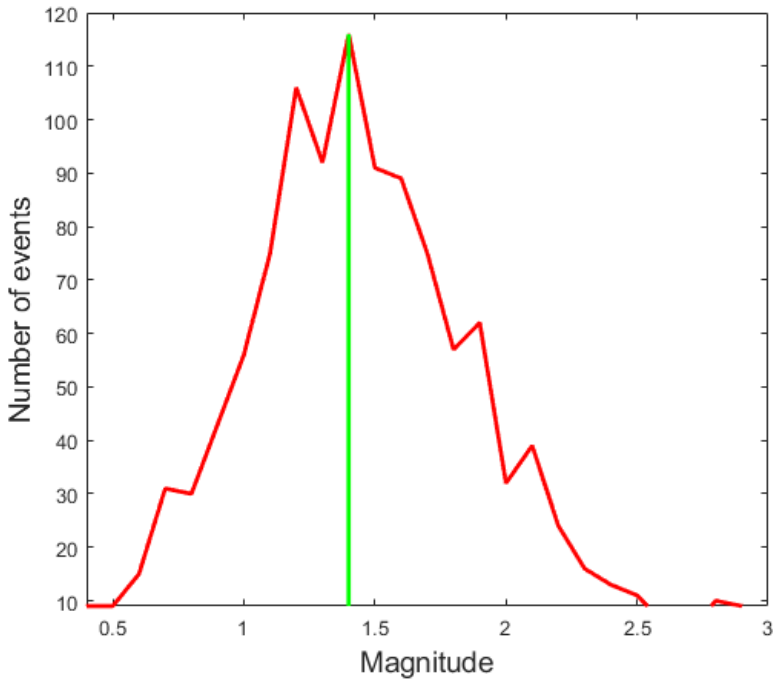

Figure 1.1: Illustration showcasing the identification of the highest point on the non-cumulative distribution of magnitudes. The red solid line represents the non-cumulative distribution of magnitudes, while the green line represents m_c, set at 1.4 for this test, in the synthetic catalog.

1.2.2 The goodness of fit (GFT)

The Goodness-of-fit test (GFT), introduced by Wiemer and Wyss, 2000, determines m_c by assessing the agreement between the observed FMD and synthetic distributions. The measure of GFT is quantified by the parameter R, representing the absolute difference in the number of events within each magnitude bin between the observed and synthetic Gutenberg-Richter (G-R) distributions (Gutenberg and Richter, 1956) (refer to section 1.3). Synthetic distributions are generated based on the estimated values of a and b (discussed in section 1.3) for magnitudes greater than or

equal to the cutoff magnitude m_{cut}.

$$R(a, b, m_{c0}) = 100 - (\frac{\sum_{m_{cut}}^{m_{max}} |B_i - S_i|}{\sum_i B_i}.100), \tag{1.1}$$

in the Equation 1.1, B_i and S_i represent the observed and predicted cumulative number of events in each magnitude bin. m_c is determined at the initial m_{cut} where the observed data for $m \geq m_{cut}$ is fitted by a straight line (in a log-lin plot) at a fixed confidence level, e.g., $R = 90\%$ or 95% (Figure 1.2). Woessner and Wiemer, 2005a demonstrated that the GFT-90% approach tends to provide m_c estimates at the lower end of the m_c distribution compared to other techniques, with results closely aligned with those obtained using the MAXC method.

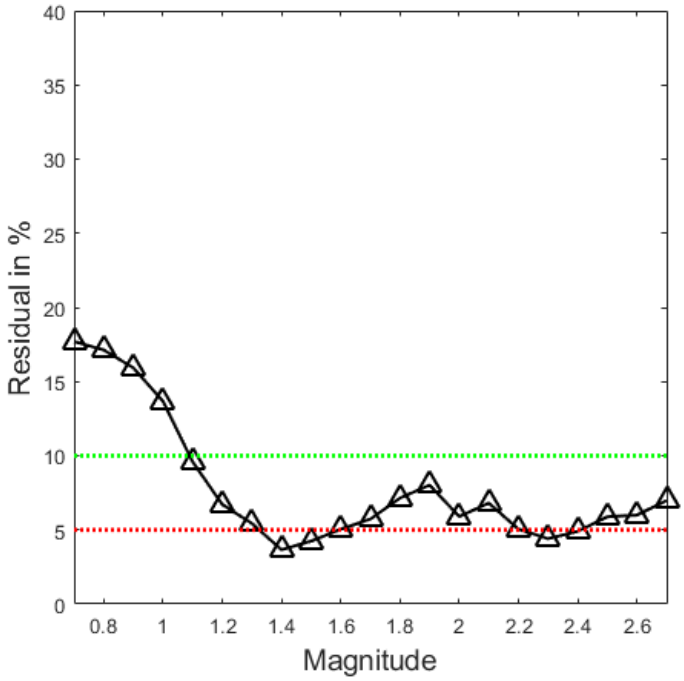

Figure 1.2: Determination of m_c using GFT Ttchnique. The black triangles represent the residuals in % for each magnitude. The dashed green line represents 90% of residuals, with $m_c = 1.1$, and the dashed red line represents 95% of residuals, with $m_c = 1.4$.

1.2.3 Magnitude of completeness by b-value stability (MBS)

Cao and Gao, 2002 utilized the stability of the $b - value$ (refer to section 1.3) with respect to m_{cut}, referred to as MBS by Woessner and Wiemer, 2005a, to estimate m_c. This approach operates

under the assumption that $b-value$ estimates increase when $m_{cut} > m_c$ and remain constant when $m_{cut} \geq m_c$. If $m_{cut} < m_c$, the resulting $b-value$ is inaccurate. As m_{cut} approaches m_c, the b-value approaches its true value, maintaining constancy for $m_{cut} > m_c$, forming a plateau (Figure 1.3). The authors arbitrarily defined m_c as the magnitude where the change in $b-value$ (Δb) between two consecutive magnitude bins is smaller than 0.03. However, Woessner and Wiemer, 2005a identified this criterion as unstable due to potential strong variations in the frequency of events within individual magnitude bins. To introduce an objective measure and enhance numerical stability, Woessner and Wiemer, 2005a employed the $b-value$ uncertainty (δb) according to Shi and Bolt, 1982 as the criterion:

$$\delta b = 2.3b^2\sqrt{\frac{\sum_{i=1}^{N} m_i - \langle m \rangle^2}{N(N-1)}}, \tag{1.2}$$

with $\langle m \rangle$ being the mean magnitude and N the number of events. m_c is then defined as the first magnitude increment at which $\Delta b = |b_{ave} - b| \leq \delta b$.

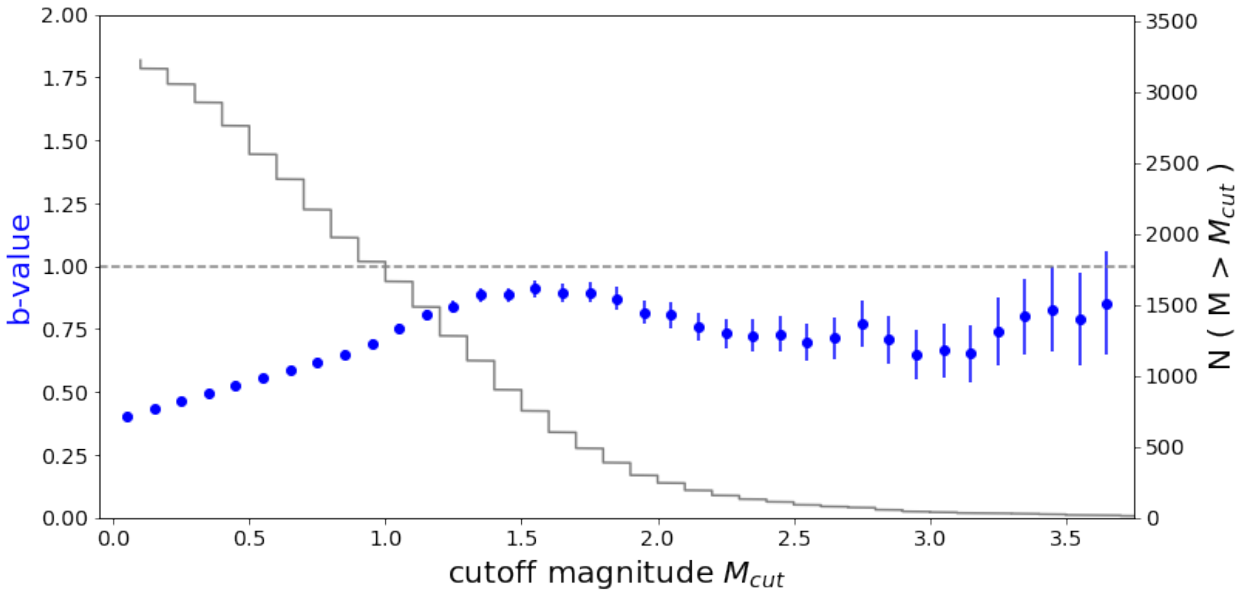

Figure 1.3: m_c determination via MBS, testing with $m_c = 1.4$. The gray solid line illustrates the cumulative number of events above each m_{cut}, the blue circles indicate the associated $b-values$ with their uncertainty, and the gray dashed line represents the true $b-value$.

1.2.4 The entire magnitude range (EMR)

Woessner and Wiemer, 2005a introduced a method for estimating m_c by considering the entire magnitude range (EMR), encompassing events below m_c. This model comprises two components: the G-R law for the complete segment and the cumulative normal distribution for the incomplete segment of the non-cumulative FMD. The aim of the model is to reproduce the entire FMD, accommodating the incompletely observed portion. However, this approach has faced criticism, as noted by Kagan, 2002. The EMR method shares similarities with the one proposed by Ogata and Katsura, 1993. The non-cumulative FMD can be characterized by the intensity λ (normalized number of events) at magnitude m, expressed as:

$$\lambda(m) = \lambda_0 q(m), \tag{1.3}$$

with

$$\lambda(m|\beta) = exp(-\beta m), \tag{1.4}$$

where $\beta = b.log(10)$, with b representing the $b - value$ of the G-R law (refer to section 1.3), and $q(m)$ a detection function with $0 \leq q \leq 1$. q is commonly defined as the cumulative normal distribution of mean μ and standard deviation σ (e.g., Ogata and Katsura, 1993 ; Iwata, 2008), expressed as:

$$q(m|\mu,\sigma) = \int_{-\infty}^{m} \frac{1}{\sqrt{2\pi}\sigma} exp(\frac{-(x-\mu)^2}{2\sigma^2})dx, \tag{1.5}$$

with

$$m_c = \mu + n\sigma, \tag{1.6}$$

where n indicates the confidence level. $n = 0$ means that 50% of the events are detected above m_c. $n = (1, 2, 3)$ means that 68%, 95% and 99% of the events are detected (Figure 1.4).

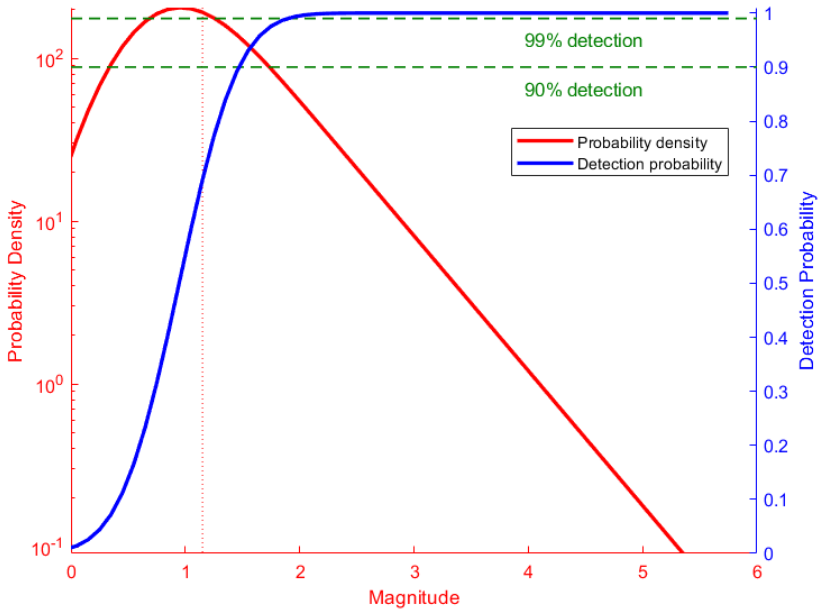

Figure 1.4: A synthetic example illustrating the determination of m_c using the EMR technique. m_c is defined as the first magnitude above a 90% detection probability. The red solid line represents the probability density function, the blue solid line represents the detection probability, and the two dashed green lines correspond to 90% and 99% detection probability, with $m_c = 1.7$ and 1.9, respectively. The red dashed line represents m_c determined by MAXC, with $m_c = 1.1$.

1.2.5 Median-Based Analysis of the Segment Slope (MBASS)

The Median-Based Analysis of the Segment Slope (MBASS), introduced by Amorese, 2007, is a non-parametric approach for estimating m_c. It employs an iterative process to detect multiple change points in the non-cumulative FMD. The Wilcoxon rank sum test is utilized to determine the acceptance or rejection of the null hypothesis. The MBASS technique can identify various discontinuities in the FMD, with the primary one corresponding to m_c. Additional discontinuities may align with breakpoints at higher magnitudes (e.g., Wesnousky, 1994).

1.2.6 Short-term incompleteness (STAI)

Intense earthquakes commonly result in incomplete aftershock records immediately following their occurrence, primarily due to coda wave overlap (Hainzl, 2016a; de Arcangelis et al., 2018).

The abbreviated event records in the short term can significantly obscure both the "true" decay following the Omori Law (Omori, 1894; Utsu et al., 1995) (refer to section 1.4), and the "true" aftershock productivity of the triggering event (refer to section 1.4), leading to an overestimation of the Omori parameter c and an underestimation of the productivity parameter. Helmstetter et al., 2006 developed an empirical relationship between the mainshock magnitude and m_c to determine the duration of data incompleteness after a powerful mainshock. The relationship is described as $m_c(m,t) = m_{main} - 4.5 - 0.75\log(t)$, where m_{main} is the magnitude of the mainshock, and t is the relative time to the mainshock. Figure 1.5 showcases an example of a synthetic catalog generated, including incompleteness right after the occurrence of the mainshock.

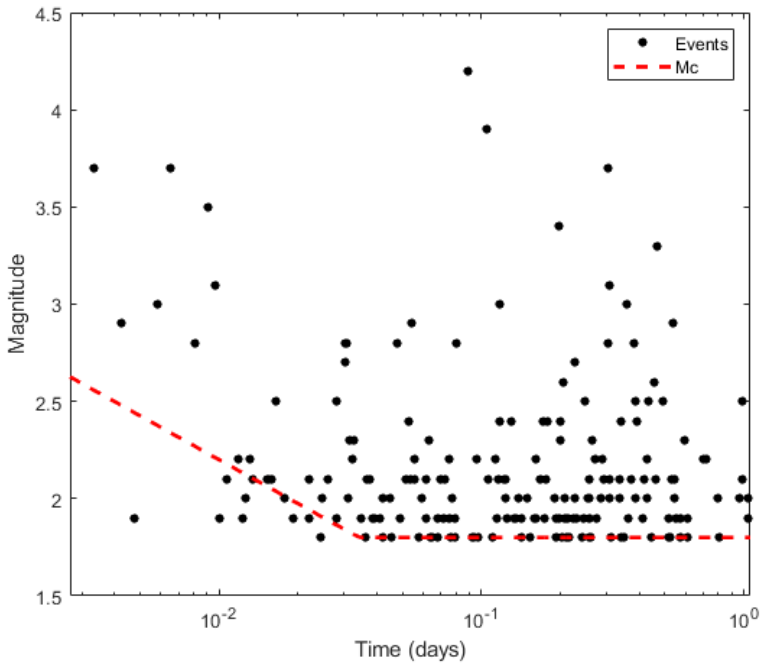

Figure 1.5: illustration of STAI. The black dots represent the synthetic earthquakes, and the dashed red line represent $m_c(t)$.

1.2.7 Rate dependent magnitude of completeness

Hainzl, 2016b illustrated the variability in determining m_c relative to seismicity rates. Initially, the author employed a maximum likelihood method to compute the $b-values$, treating the seismic data as a function of the estimated local earthquake rate. Assuming a constant FMD, incomplete

recordings is expected to result in an apparent decrease in the estimated $b - value$. The observed rate of $b-value$ decrease was then used to estimate the time-varying m_c. The essential assumptions of this approach are as follows:

1. The seismic network's minimum completeness magnitude (m_{c0}) is tied to the sensitivity of the recording system during low seismicity periods, a value traditionally established through conventional methods like MAXC, GFT, MBS, EMR, and MBASS.

2. Within short time frames, earthquake occurrences can be approximated using a stationary Poisson process. This approximation resonates with the idea that seismicity is often well-explained by a blend of stationary and non-stationary Poisson models, which encompass factors like tectonic background activity, Omori-type aftershocks, and transient aseismic forcing.

3. The earthquakes are consistently recorded by the same stations.

4. The rate of earthquakes with magnitudes $m \geq m_{c0}$ is denoted by r.

5. An earthquake cannot be adequately distinguished through seismogram analysis if it occurs less than Δt after the last event of equal or larger magnitude.

6. An earthquake catalog is considered complete for $m \geq m_{c0}$ if earthquakes with magnitude m_{c0} are recorded with a probability P_c.

Given these assumptions, the probability that an event of magnitude m_{c0} has no predecessor of magnitude $m \geq m_{c0}$ within the precursory time interval Δt (and therefore can be recorded) is:

$$P_{\Delta t} = exp(-\Delta t), \tag{1.7}$$

according to the Poisson model. This directly yields the maximum rate (r_{max}), which is linked to the probability (P_c) used for completeness definition, to b expressed as:

$$r_{max} = \frac{-ln(P_c)}{\Delta t}. \tag{1.8}$$

Thus, any period exhibiting a seismicity rate $r \geq r_{\max}$ is automatically classified as incomplete (Figure 1.6). Typically, Δt (and hence r_{max}) may vary with the magnitude level (m_{c0}) due to longer coda duration associated with stronger earthquakes. It's essential to note that no explicit spatial component is introduced, consistent with assumption (3). Short-term earthquake clustering is typically driven by spatially confined seismic events, satisfying this assumption. However, extending this approach to larger spatial scales might overestimate $m_c(t)$ in remote regions where independent seismic networks record simultaneous earthquakes.

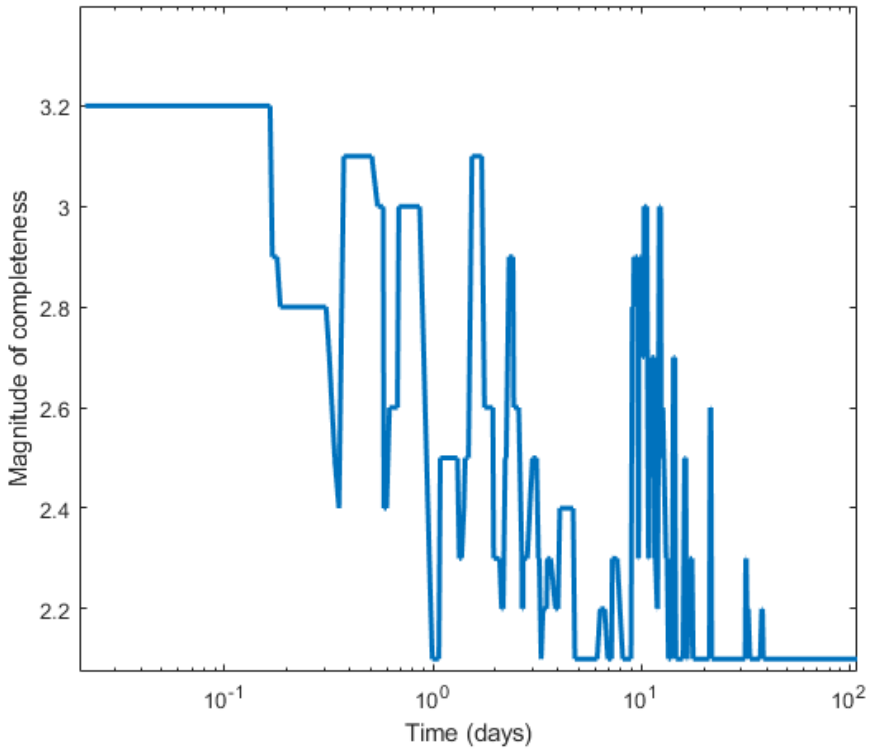

Figure 1.6: m_c dependence on rate. Illustrated through a synthetic example.

1.2.8 Summary

All these methods have their advantages and disadvantages, depending on the data used, whether it's a small sample of earthquakes or a large one, local earthquake analysis or regional/global assessments, earthquake sequences, or general seismicity. Instead of relying on a single specific method, the recommended approach is to try all of them, test their effectiveness, and select the one yield-

ing the highest result to avoid complications. The selection of m_c and strategies for overcoming encountered problems are further elaborated in chapter 2, section 2.4.

1.3 Magnitudes distribution

A common finding in seismology is that smaller earthquakes tend to happen more frequently than larger ones (Figure 1.7). The G-R law, established by Gutenberg and Richter, 1956, is a firmly established empirical principle in the field. Within a specific region, the G-R law characterizes the distribution of earthquake frequencies in relation to their magnitudes above a certain threshold as follows:

$$log10(N_{\geq m}) = a - bm, \tag{1.9}$$

where N is the number of events equal to or greater to m, m being the magnitude and a, b are constant to be determined. The most important parameter is the $b-value$ which, mathematically, express the proportion of small and large earthquakes, physically, it's negativaly proportional to the stress stat and act somehow as a stress-meter. This interpretation of the $b-value$ is observed in different fault types where high $b-values$ are found for normal faults (low stress), intermediate values for strike-slip faults (intermediate stress) and low values for reverse faults (high stress) (Schorlemmer and Wiemer, 2005). The $b-value$ is also used for earthquake forcasting by analysing its temporal and spatial distribution to map the stress state of a region in time and space. One exemple, Gulia and Wiemer, 2010 found a decrese of the $b-value$ just before the parkfield Mw=6.0 indicating an increase of the stress state in the region.

Generally the two constant of the G-R law, a and b values, are either determined using a least squares regression by fitting the straight line of the G-R distribution, or by using the maximum likelihood method (Utsu, 1961).

Given an earthquake dataset with magnitudes m, a maximum likelihood estimate of the $b-value$ is (Aki, 1965; Utsu, 1961):

$$b = \frac{1}{log10(\overline{\mathrm{m}} - m_{min})}, \tag{1.10}$$

where $\overline{\mathrm{m}}$ represents the mean-value of the magnitudes in the dataset and m_{min} represents the binning correction which is expressed by $m_{min} = m_c - \Delta m/2$, where m_c is the magnitude of completeness and Δm is the binning of the magnitude distribution. The maximum-likelihood estimation of the $a - value$ is as follow :

$$a = log10(N_{\geq m_c}) + bm_c, \tag{1.11}$$

where N is the number of earthquake equale or greater to m_c.

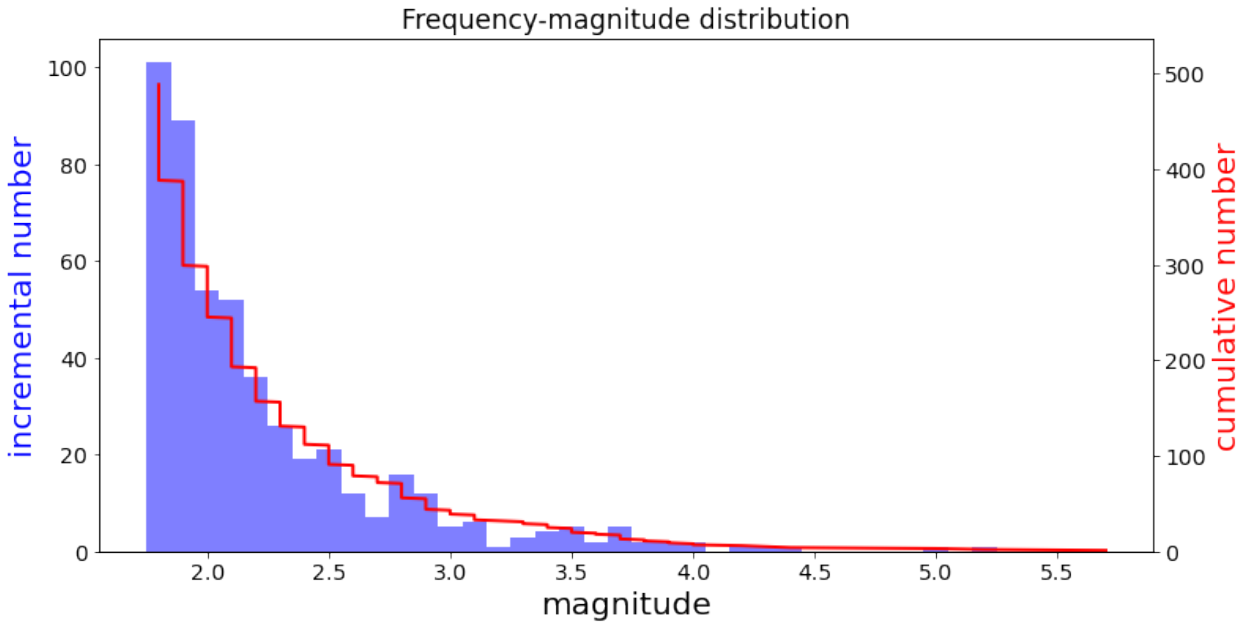

Figure 1.7: Illustration of FMD with a synthetic example. The solid red line represents the cumulative number of earthquakes, while the histograms depict the incremental number of earthquakes.

1.4 Temporal distribution

The first law describing the temporal distribution of aftershocks was the Omori-Utsu law which express the temporal decay of aftershocks in time following a mainshock (Omori, 1894; Utsu, 1961; Utsu et al., 1995), expressed as:

$$\frac{dn}{dt} = \frac{k}{(t+c)^p}, \tag{1.12}$$

where n is the number of aftershocks, t is the time relative to the mainshock and k, c, p are constant to be determined. The $k-value$ expresses the productivity of aftershocks, the $c-value$ is the time in which the rate of aftershocks is roughly constant, and the $p-value$ is the constant that control how fast is the temporal decay. To calculate the number of aftershocks in a time period after the mainshock we simply integrate Equation 1.12 from 0, occurence time of the mainshock, to t_{max}, end time of the studied period, which will give:

$$n = k[\frac{1}{(p-1)(c+t_{max})^{p-1}} - \frac{1}{(p-1)c^{p-1}}]. \tag{1.13}$$

Since Omori's law was first formulated in 1894, researchers have extensively examined aftershock sequences stemming from both shallow and deep mainshocks in various tectonic settings. These investigations have spanned oceanic spreading centers and transform faults (Bohnenstiehl et al., 2002), continental transform fault zones (Kisslinger and Jones, 1991), continental collision zones (Pavlis and Hamburger, 1991; Nyffenegger and Frohlich, 2000), subduction zone environments (Wiens and McGuire, 2000), and even aftershock sequences related to nuclear explosions (Gross, 1996). A comprehensive review of the statistical aspects of Omori's law and a summary of numerous studies on aftershock sequences can be found in Utsu et al., 1995. Kisslinger and Jones, 1991 delves into the connection between fault zone properties and Omori's law, while Davis and Frohlich, 1991 investigate regional variations in the decay laws of aftershock sequences. One notable outcome of these investigations is the recognition that both the productivity of aftershocks, quantified by the number of aftershocks, and the Omori law decay parameter $p-value$ exhibit significant variations across different tectonic environments. A high $p-value$ indicates a faster decay rate of aftershocks over time compared to a lower $p-value$. For instance, Davis and Frohlich, 1991 noted that earthquakes occurring at depths exceeding 70 km tend to produce fewer and smaller aftershock sequences. In contrast, shallow subduction zone earthquakes tend to generate more aftershocks than their counterparts in shallow ridge-transform zones. Additionally, intermediate-depth earthquakes, though infrequent, have been found capable of producing aftershock sequences in collisional plate boundary settings like the Pamir-Hindu Kush region. Investigations of aftershock sequences in subduction zones have revealed that earthquakes occurring as deep as approximately 650 km can be highly productive in terms of the number of aftershocks (Wiens and Gilbert, 1996).

Notably, deep earthquakes in regions such as Japan and Indonesia often exhibit low or no aftershock productivity (Wiens and Gilbert, 1996). Omori's law decay parameter $p - value$ has been a focal point in the study of aftershock sequences. Utsu et al., 1995 reported a range of published $p - values$ from 0.6 to 2.5, with a median of 1.1. In California, for shallow aftershock sequences, Kisslinger and Jones, 1991 observed $p - values$ ranging from 0.7 to 1.8, with a mean of 1.1. Bohnenstiehl et al., 2002 presented $p - values$ of 1.74 and 2.37 for two aftershock sequences associated with the mid-Atlantic ridge spreading, and $p - values$ in the range of 0.94 to 1.29 for three aftershock sequences related to transform faults offsetting the ridge. In the Pamir-Hindu Kush region, Pavlis and Hamburger, 1991 indicated a $p - value$ close to 1 for three sequences with mainshocks occurring at approximately 200 km depth. However, Nyffenegger and Frohlich, 2000 found $p - values$ of 0.53 and 0.83 for the two most significant aftershock sequences studied by Pavlis and Hamburger, 1991. In the case of aftershock sequences following the deep 1994 Tonga and Bolivia earthquakes, $p - values$ similar to those for shallow sequences were observed, with a $p - value$ of 1.19 for the Bolivia event (Nyffenegger and Frohlich, 2000) and 1.006 for the Tonga event (Wiens and McGuire, 2000). Interestingly, it has been observed that the value of p does not correlate with either the magnitude of the mainshock or m_c (Utsu, 1961; Kisslinger and Jones, 1991; Utsu et al., 1995). This suggests that $p - value$ may reflect characteristics of the fault system and the surrounding rock material. Additionally, some authors have noted a correlation between high $p - values$ and high surface heat flow (Kisslinger and Jones, 1991; Kisslinger and Jones, 1991). In contrast to the behavior of the decay parameter $p - value$, the remaining parameters of Omori's law, $k - value$ and $c - value$, display significant variability based on the chosen m_c. Utsu et al., 1995 demonstrated that increasing m_c leads to lower values of both $k - value$ and $c - value$, implying a potential interdependence between these parameters, possibly reflecting the same underlying physical process. The parameter $c - value$ in Omori's law, often considered as a time offset to account for incomplete aftershock detection in the immediate aftermath of the mainshock, has raised debates. While it is commonly interpreted this way (Utsu et al., 1995; Kisslinger and Jones, 1991), it's worth noting that positive $c - values$ have been observed in adequately recorded aftershock sequences. However, interpreting $c - value$ remains a topic of controversy, with some arguing that it primarily reflects incomplete detection of aftershocks based on statistical analyses of earthquake catalogs (Kagan, 2004; Kagan and Houston, 2005; Lolli and Gasperini, 2006). Fig-

ure 1.8 illustrates an exemple of the Omori-Utsu rate decay for a $c - value$ of 0 days (dashed black line) and a $c - value$ of 0.7 days (solid black line).

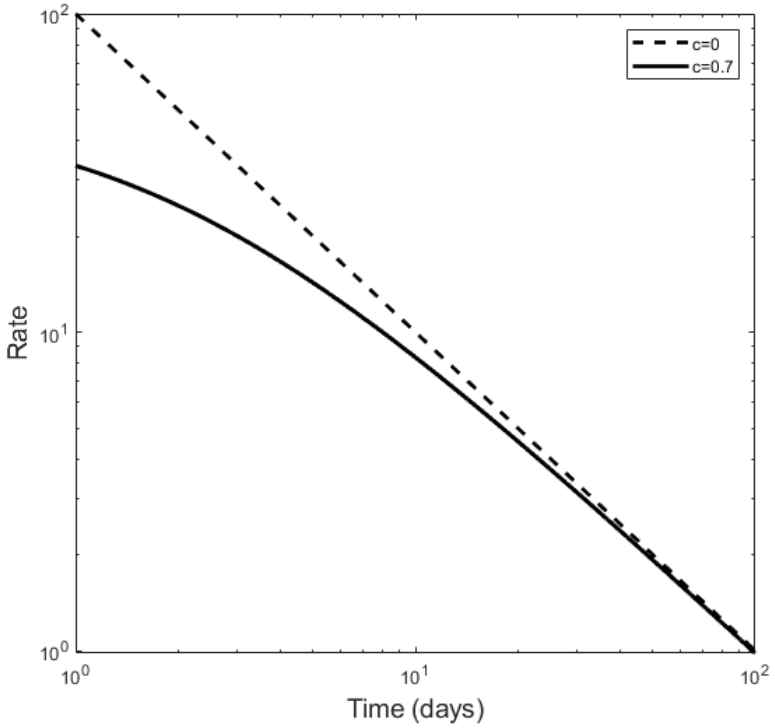

Figure 1.8: Representation of the Omori-Utsu law decay of aftershocks for k=90, and $p = 1.0$, with c=0.7 (solid black line) and c=0 (dashed black line).

The Omori-Utsu parameters are generally optimized by using the maximum likelihood function described as follow:

$$L(\theta) = \sum_{i=1}^{N} ln(\lambda_{t_i}) - \int_S^T \lambda_{t_i} = Nln(k) - p\sum_{i=1}^{N}(t_i + c) - KA(c,p), \tag{1.14}$$

where

$$A(c,p) = \begin{cases} ln(T+c) - ln(S+c), & \text{if } p = 1. \\ [(T+c)^{1-p} - (S+c)^{1-p}]/(1-p), & \text{if } p \neq 1. \end{cases}, \tag{1.15}$$

λ_{t_i} represents the Omori-Utsu function. S is the start time of the target period for optimization, and T is the end time of the target period for optimization. The maximum likelihood estimates of the parameters k, c, and p are those that maximize the likelihood function.

Another way to explain the temporal distribution of earthquakes is analyzing the inter-event time distribution. Previous studies have demonstrated that the probability density function of inter-event time between consecutive earthquakes can be approximated by a gamma function (Corral, 2003), expressed as:

$$p(\delta t) = Ce^{-\mu\delta t}\delta t^{-n}, \tag{1.16}$$

with $p(\delta t)$ is the probability density function of the inter-event time distribution, δt is the inter-event time between consecutive earthquakes, n a model parameter expressing the branching ratio (Helmstetter and Sornette, 2003), which is the fraction of aftershocks among all the events, μ the forcing rate or background rate, and C a normalization constant. Hainzl et al., 2006 showed that the forcing rate and the branching ratio can be estimated according to:

$$\mu = \frac{E(\delta t)}{var(\delta t)}, \tag{1.17}$$

$$n = 1 - \mu E(\delta t), \tag{1.18}$$

where $E(.)$ and $var(.)$ are respectively the mean and variance of the inter-event time. For short inter-event times, the distribution diminishes in accordance with δt^{-1} (Figure 1.9, dashed black line). This phenomenon can be attributed to Omori-like aftershock activity, with a $p - value$ approaching 1. Howerver, for larger inter-event times the distribution follow a more poissonian model according to $exp(-\delta t)$ (Figure 1.9, solid black line).

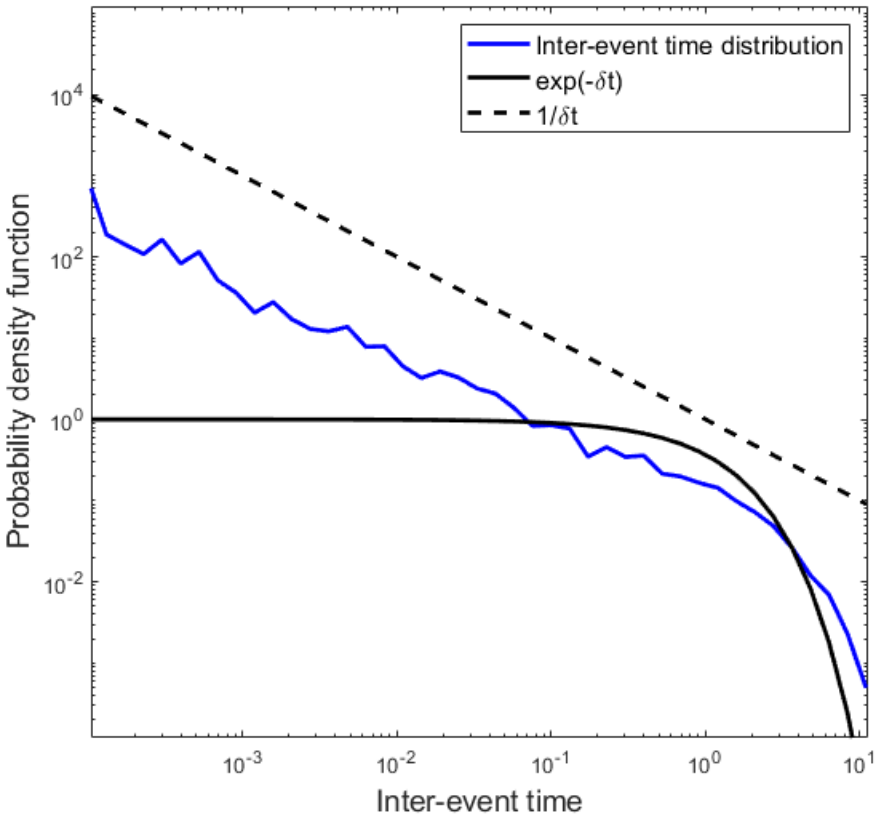

Figure 1.9: Log-log representation of inter-event time probability density function. The blue solid line illustrates the probability density function of inter-event times of the synthetic catalog. The solid black line represents an exponential ($\exp(-\delta t)$) distribution, while the black dashed line represents a power-law (δt^{-1}) distribution.

The most common known model to use for analyzing temporal patterns of earthquakes is the ETAS model (Epidemic Type Aftershocks Sequence) (Ogata, 1988), described as:

$$\lambda(t) = \mu + \sum_{i:t_i<t} k e^{\alpha(m_i - m_c)}(t - t_i + c)^{-p}, \tag{1.19}$$

where m_c is the completeness magnitude of the catalog, t_i and m_i represent the time occurrence and magnitude of the i^{th} event , α denotes the efficiency in generating aftershock by an event of a specific magnitude, and k, c, p are the Omori-Utsu parameters. The productivity factor α is highly sensitive to the changes of m_c and is generally in the range from 1.2-2.3 for aftershock sequences and below 1 for seismic swarm activity (Ogata, 1992). It has also been interpreted that lower

$\alpha - value$ leads to a high probability of a small events to generate a much larger event (Kumazawa and Ogata, 2014). Figure 1.10 illustrates an example of the number of aftershocks triggered for magnitudes ranging from 0 to 5 with an $\alpha - value$ of 2.

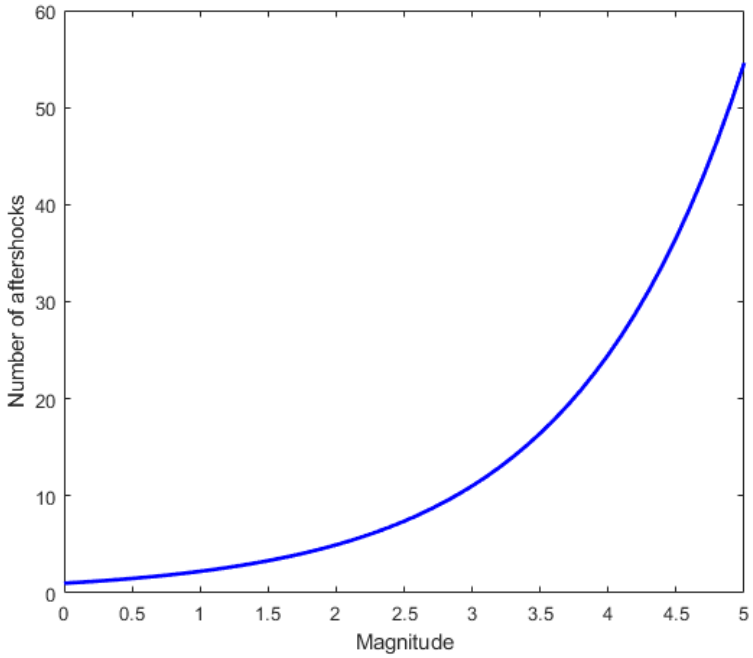

Figure 1.10: ETAS productivity evolution with each magnitude according to a synthetic catalog for α=2.

In accordance with the ETAS model, we categorize earthquakes into two groups: independent events, referred to as mainshocks, and dependent events, known as aftershocks. Earthquakes are considered mainshocks when they result from factors such as tectonic loading and fluid intrusions, independent of the occurrence of other seismic events. On the other hand, aftershocks are induced by static or dynamic stress alterations and/or seismically-triggered fluid movements, and they are, to some extent, linked to preceding earthquakes. Figure 1.11 showcase an exemple of the ETAS rate for a synthetic catalog generated with the parameters μ=1, k=0.01, c=0.01 days, α=2, and p=1.1.

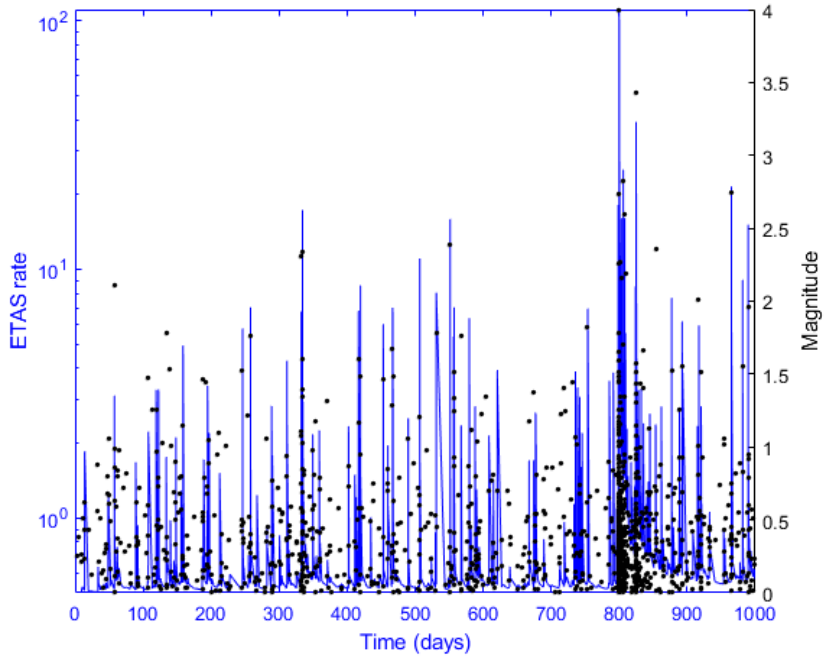

Figure 1.11: ETAS rate based on a synthetic catalog. The blue solid line represents the modeled ETAS rate, and the black dots represent the synthetic catalog.

The ETAS parameters are determined by maximizing the maximum likelihood function defined as:

$$L(\theta) = \sum_{i=1}^{N} ln(\lambda(t_i)) - \int_S^T \lambda(t_i), \tag{1.20}$$

where $\lambda(t_i)$ is the ETAS function (Equation 1.19), S is the the starting time of the studied period, and T is the end time of the studied period. We visually assess the goodness-of-fit of the estimated ETAS model by comparing the cumulative number of observed earthquakes, with magnitudes m greater than or equal to m_c, to the cumulative number calculated from the estimated ETAS model. To achieve this, we compute the theoretical cumulative function $\Lambda(t)$ of the underlying earthquakes at time t and $\Lambda_N(t)$ of the detected earthquakes. These functions are respectively calculated following Equation 1.21. We define the transformed time $\tau \equiv \Lambda(t)$:

$$\Lambda(t) = \int_S^T \lambda(t)dt. \tag{1.21}$$

If the estimated model is correct, the observed earthquakes in the transformed time should

exhibit characteristics of a stationary Poisson process. Consequently, the observed cumulative number in the transformed time will be represented by a nearly straight line when plotted. This crucial analysis serves as an indicator of the goodness-of-fit for the estimated model (Ogata, 1988).

Marsan et al., 2013 developed a new approach for a variable forcing rate in time (Hainzl, 2016a, Crespo-Martín et al., 2021). This method is based on the estimation of both the time-dependent background rate and ETAS parameters by using the maximum likelihood estimation (MLE) with n-nearest-neighbor smoothing of the background rate. The overall steps to follorw are:

- Estimate the ETAS parameters with a constant background rate in time $\mu(t) = \mu_0$ by maximizing the log-likelihood.
- Calculate the probability that each event belongs to the background. This probability is defined as (Zhuang et al., 2002).

$$\phi_i = \frac{\mu(t_i)}{\mu(t_i) + \vartheta(t_i)}. \tag{1.22}$$

- Smooth the background rate by using the n-nearest-neighbors (n_e). The best n_e will be chosen according to the Akaike criteria (Akaike, 1974).

$$AIC(n_e) = -L + \frac{N}{n_e}, \tag{1.23}$$

  where L is the maximum-likelihood value of the model fit and N is the number of earthquakes.

The procedure will be repeated until the convergence to the best model. To show how the AIC criteria is used to choose a proper smoothing window for the variable background rate, we generated two synthetic catalogs with one having a constant background rate in time, and one with a variable background rate. The results found are depicted in Figure 1.12 and Figure 1.13. The results show that in each case the method can recover the true background rate with the AIC showing the best window.

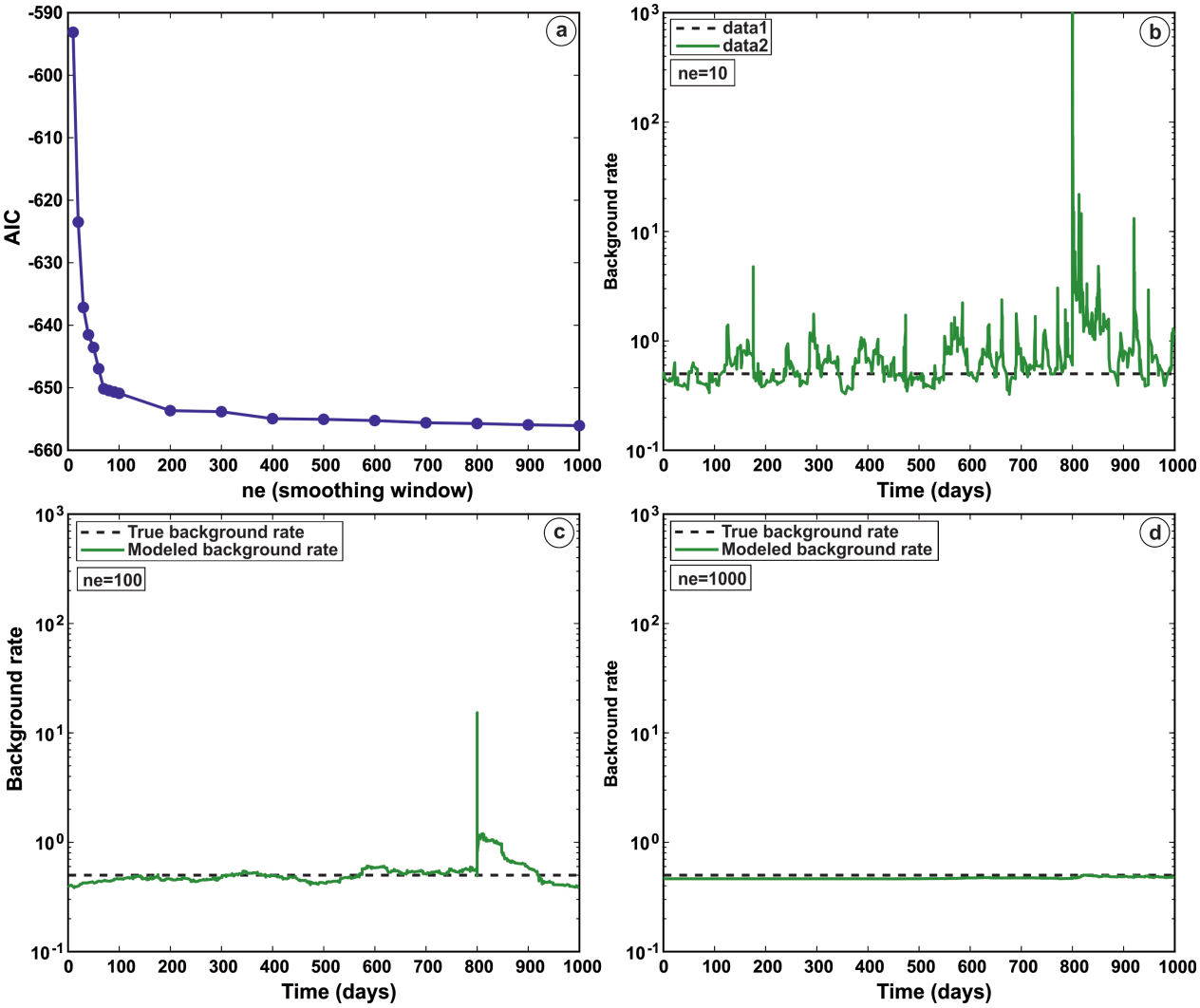

Figure 1.12: (a) AIC against smoothing window. (b) Background rate for a smoothing window of 10 events (solid green line) compared to the true background rate (dashed black line). (c) Background rate for a smoothing window of 100 events (solid green line) compared to the true background rate (dashed black line). (d) Background rate for a smoothing window of 1000 events (solid green line) compared to the true background rate (dashed black line).

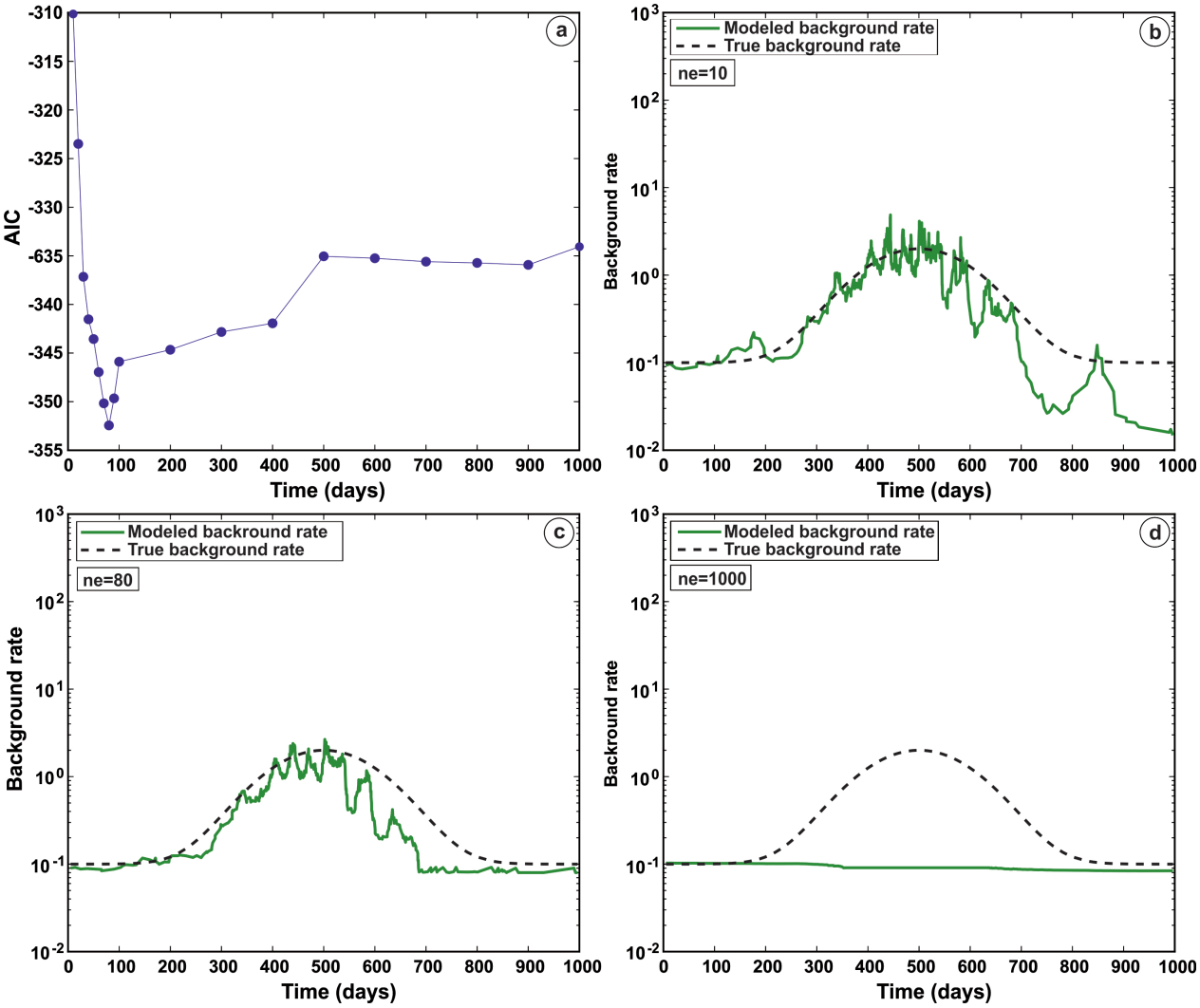

Figure 1.13: (a) AIC against smoothing window. (b) Background rate for a smoothing window of 10 events (solid green line) compared to the true background rate (dashed black line). (c) Background rate for a smoothing window of 80 events (solid green line) compared to the true background rate (dashed black line). (d) Background rate for a smoothing window of 1000 events (solid green line) compared to the true background rate (dashed black line).

This specific formulation of the ETAS model is particularly well-suited for scenarios where a fault undergoes external forcing. Three primary cases exemplify this applicability. Firstly, a constant forcing rate is represented by a consistent background rate over time, reflecting the straightforward situation of a fault system enduring continuous tectonic loading (Figure 1.14a). The second case is characterized by earthquake swarms featuring a swift transition from low to high seismic activity. This can occur, for instance, due to external factors like fluid or magma intrusion. The abrupt surge in seismic activity is typically attributed to aseismic processes such as the migration

of fluids or the gradual onset of slow earthquakes. Notably, the absence of a large earthquake at the onset of activity makes it challenging to attribute the sudden increase in seismic activity to seismic events (Figure 1.14b). Lastly, the third case pertains to seismic swarms originating from slow, transient deformations (Figure 1.14c).

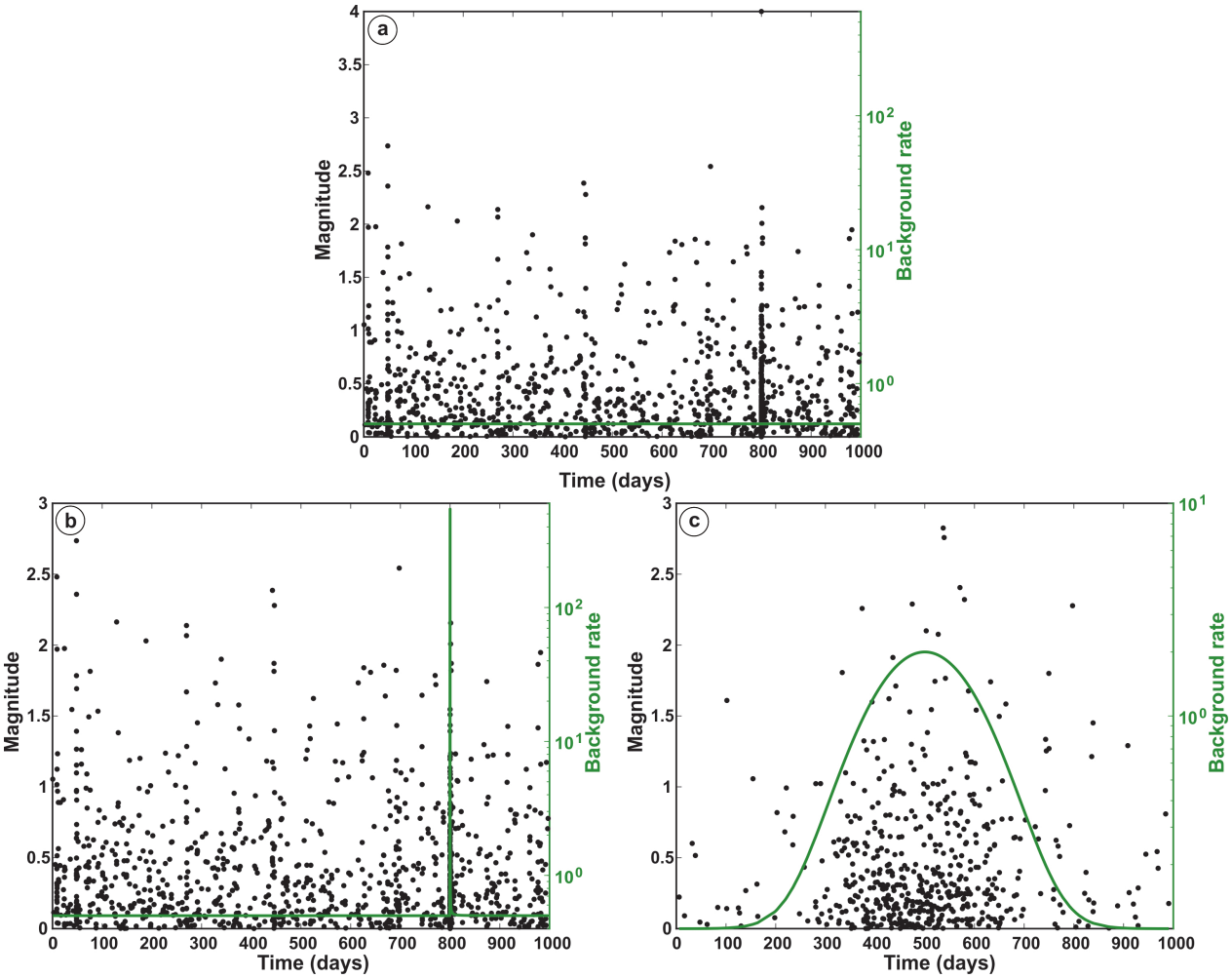

Figure 1.14: (a) Synthetic exemple for a constant background rate (solid green line). (b) Synthetic exemple for a rapid onset of the background rate (solid green line). (c) Synthetic exemple for a smooth variation of the background rate (solid green line).

1.5 Spatio-temporal characteristics

Ogata, 1998 extended the ETAS model to a space time component with the assumption that :

$$\lambda(t,x,y,m) = \mu(x,y) + \sum_{i:t_i<t} k(m_i)g(t-t_i)f(r_i(x,y),m_i), \tag{1.24}$$

where

$$k(m_i) = Ke^{\alpha(m_i-m_c)}, \tag{1.25}$$

and

$$g(t-t_i) = (t-t_i+c)^{-p}, \tag{1.26}$$

the spatial $f(r_i(x,y),m_i)$ kernel models the 2D-distribution of aftershocks locations. In conventional ETAS model approaches, the triggering event is assumed to be a point source, distributing its offsprings isotropically around its epicenter (Figure 1.15). A classical definition of an isotropic kernel (Ogata, 1998; Grimm et al., 2021) is:

$$f(r_i(x,y),m_i) = \frac{q-1}{D.exp(\gamma(m_i-m))}(1+\frac{\pi r_i(x,y)^2}{D.exp(\gamma(m_i-m_c))})^{-q}, \tag{1.27}$$

where $r_i(x,y)$ denotes the point-to-point distance between a potential aftershock location (x,y) and the coordinates (x_i,y_i) of the triggering event i, and m_i is the magnitude of the event i. The kernel is constrained by the parameters D and γ that control the magnitude-dependent width of the kernel, and parameter q that describes the exponential decay of the function with growing spatial distance. A high value for the q parameter indicates that the triggering effect is mainly confined in a relatively small area, whereas small q value indicates a gradual spatial decay of aftershock productivity.

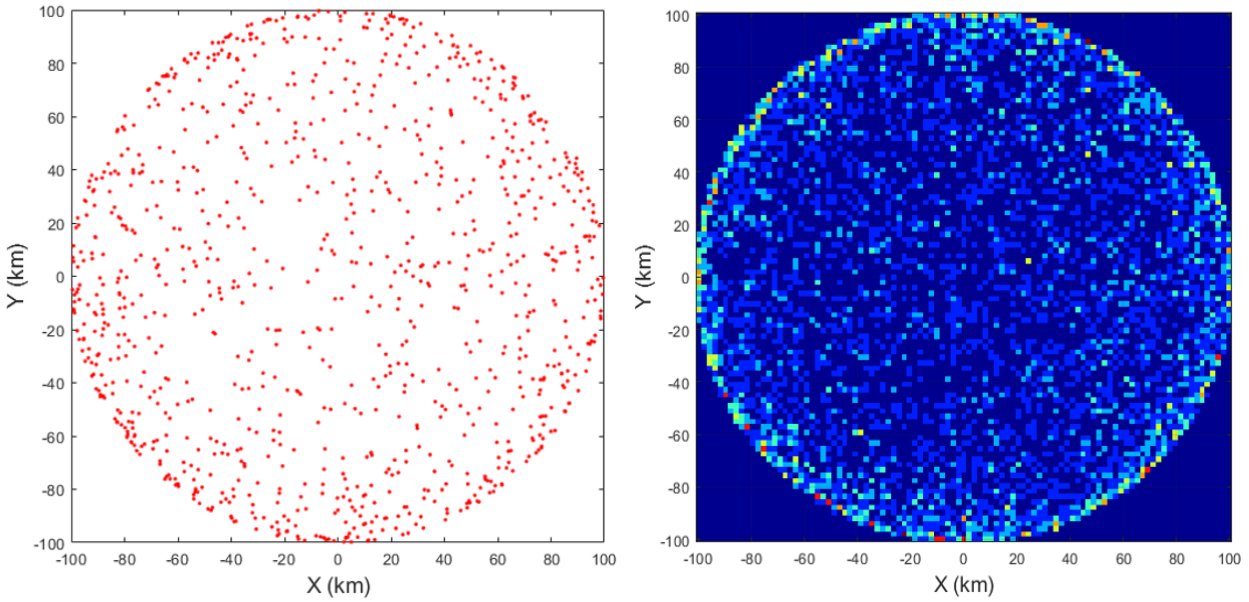

(a) (b)

Figure 1.15: (a) Isotropic spatial distribution of events. (b) Isotropic spatial density of events.

Since, the distribution of aftershocks in space shows a more anisotropic distribution (Figure 1.16), the formulation of Equation 1.27 was changed by Grimm et al., 2021 to:

$$f(r_i(x,y),m_i) = \frac{q-1}{D.exp(\gamma(m_i-m))}(1+\frac{2l_i r_i(x,y)+\pi r_i(x,y)^2}{D.exp(\gamma(m_i-m_c))})^{-q}. \tag{1.28}$$

In this spatial model, the distance term $r_i(x,y)$ denotes the point-to-line distance between the potential aftershock location (x,y) and the estimated rupture segment of triggering event i with length l_i. That is, the kernel assigns constant density along the rupture line segment, with a power-law decay to the sides. Note that the anisotropic kernel is a generalization and collapses to the isotropic model if the triggering location is assumed to be a point source with rupture extension $l_i = 0$.

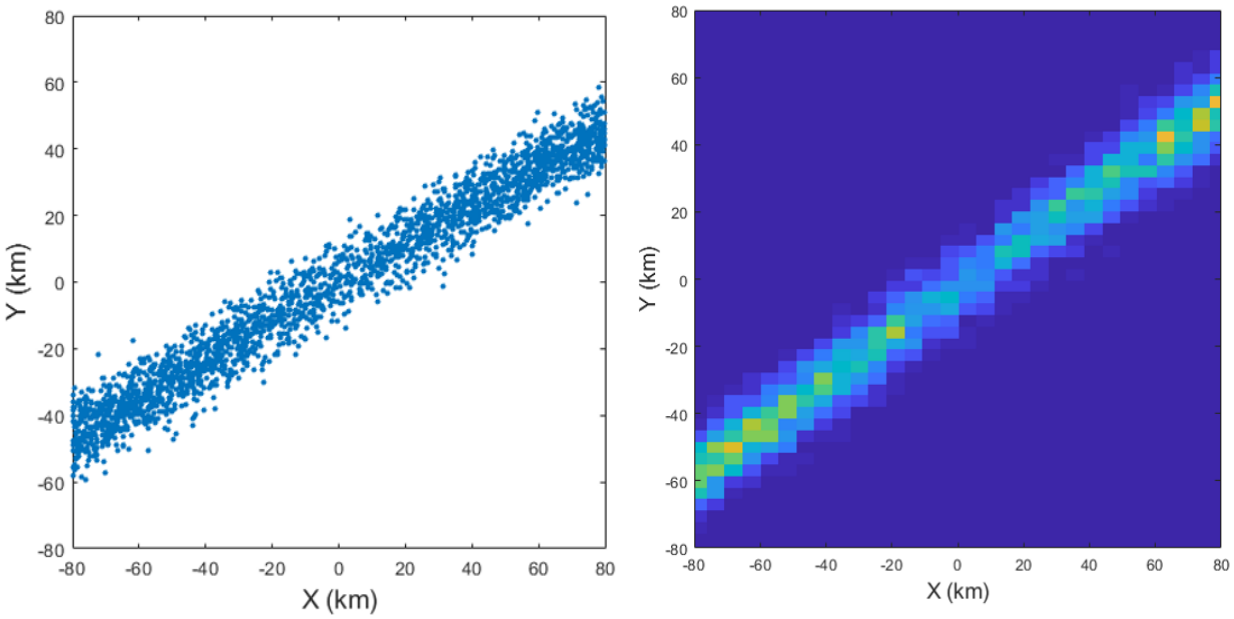

(a) (b)

Figure 1.16: (a) Anisotropic spatial distribution of events. (b) Anisotropic spatial density of events

The background rate ($\mu(x, y)$) is dependent of space and independent of time, we generally use a 2D gaussian kernel to smooth the background rate in space according to :

$$\mu(x, y) = \sum_{i=1}^{N} \phi_i \frac{1}{2\pi h_{si}} e^{-\frac{r^2}{2h_{si}^2}}, \tag{1.29}$$

with ϕ_i being the background probability of the i^{th} event, and h_{si} the spatial bandwidth to smooth the 2D gaussian kernel. To estimate the parameters of the spatio-temporal ETAS model we usually use a semi-parametric optimization following the steps below:

1. Set the probability ϕ_i that an earthquake is a background event to 0.5 for all events.
2. Calculate the background rate according to Equation 1.29.
3. Estimate the parameters μ, K, α, c, p, D, γ, and q by maximizing the $L - value$ in the equation below and store the corresponding $L - value$.

$$L(\theta) = \sum_{i=1}^{N} ln(\lambda(t, x, y, m)) - \int_0^t \int_{x_1}^{x_2} \int_{y_1}^{y_2} \lambda(t, x, y, m). \tag{1.30}$$

4. For all events, calculate the background probability $\phi_i = \frac{\mu(x,y)}{\lambda(x,y,t)}$.

5. Repeat steps (1) to (4) until L is converged.

The ETAS model serves as a crucial method for distinguishing mainshocks (background events) from aftershocks, and identifying seismic activity clusters. Other techniques for catalog declustering also exist, such as the Nearest-Neighbor Declustering (NND). In this method, the fundamental element is the proximity between earthquakes in the space-time-magnitude domain, emphasizing the nearest-neighbor relationship (Zaliapin and Ben-Zion, 2013).

Take into account an earthquake catalog in which each event i is defined by its occurrence time t_i, hypocenter r= (x_i, y_i, z_i), and magnitude m_i. The measure of earthquake $j's$ proximity to the preceding earthquake i is asymmetric in time and is explicitly defined as:

$$n_{ij} = \begin{cases} t_{ij}(r_{ij})^d 10^{-bm_i}, & \text{for } t_{ij} > 0. \\ \infty, & \text{for } t_{ij} \leq 0. \end{cases}, \tag{1.31}$$

in this context, $t_{ij} = t_j - t_i$ represents the intercurrence time between events, taking a positive value if event j occurred after event i; $r_{ij} \geq 0$ denotes the spatial distance between earthquake hypocenters (or epicenters); d stands for the fractal dimension of the hypocenters (or epicenters); and b is the $b - value$ of the G-R law. For every event j, we determine its distinct nearest neighbor (parent) i by assessing the proximity outlined in Equation 1.31. The corresponding nearest-neighbor proximity is denoted as n_{ij}:

$$n_{ij} = min(n_{ij}, i < j), \tag{1.32}$$

the event j is consequently labeled as an offspring of i. As per this definition, every event (excluding the initial one in the catalog) possesses a singular parent and has the potential for multiple offspring. The spatial and temporal distances between event j and its parent i, normalized by the magnitude m_i of the parent event, are described, by (Zaliapin et al., 2008), as:

$$T_{ij} = t_{ij} 10^{-bm_i}, \tag{1.33}$$

$$R_{ij} = r_{ij}^d 10^{-pbm_i}, \tag{1.34}$$

$$q + p = 1, \tag{1.35}$$

hence, $log10(n_{ij}) = log10(T_{ij}) + log10(R_{ij})$. Zaliapin et al., 2008 and Zaliapin and Ben-Zion, 2013 demonstrated that a Poisson marked field with a stationary time component, a uniform or inhomogeneous random space component, and a G-R magnitude distribution results in a unimodal distribution of $(log10(R), log10(T))$ concentrated along a line defined by $(log10(R), log10(T)) = const$. Conversely, observed seismicity exhibits a bimodal distribution of $(log10(R), log10(T))$. One mode closely resembles that in a Poisson field, representing background events. The other mode is situated significantly closer in time and space to the origin, signifying clustered events. This bimodality has been observed across multiple regions and scales. The bimodal nature of observed seismicity aids in the detection and declustering of clusters. Figure 1.17 showcases an example of a synthetic catalog generated by the ETAS model (using the same parameters as in section 1.4) and declustered with the NND technique.

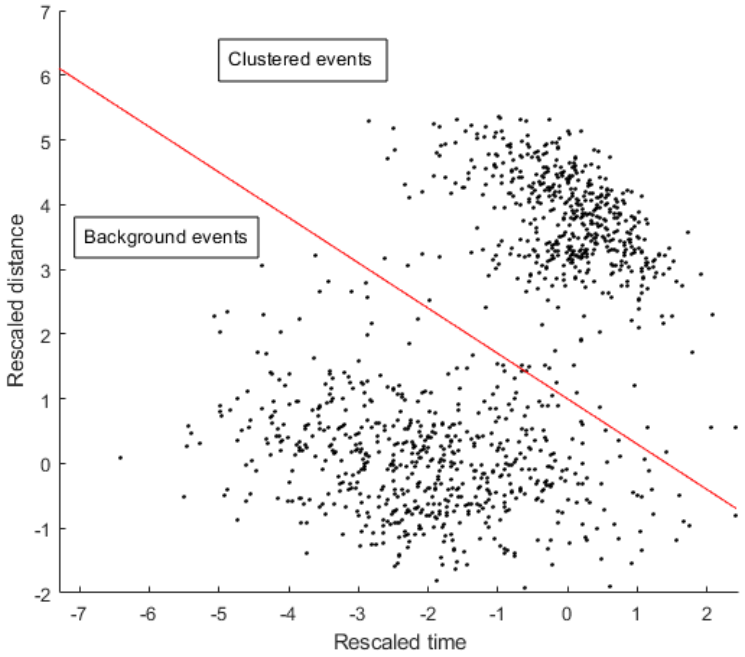

Figure 1.17: Representation of the NND echnique for a synthetic catalog.

Other techniques, so called window based declustering, are straightforward. For each earthquake in the catalog with magnitude m, subsequent shocks are classified as aftershocks if they occur within a designated time interval $T(m)$ and a specified distance interval $L(m)$ (van Stiphout

et al., 2011). Examples of windowing techniques include the algorithm developed by Gardner and Knopoff, 1974. Reasenberg, 1985 method is the most widely recognized approach to declustering, known for its cluster identification methodology.

1.6 Physical models

From a statistical standpoint, earthquakes can be conceptualized as points in both space and time. However, when considering the physical mechanisms involved, the generation of earthquakes is intricately tied to the accumulation of stress within the brittle crust. This stress buildup ultimately leads to the rupture of pre-existing faults in the crust. While measuring absolute stress magnitudes in the crust is challenging, the stress changes induced by earthquakes can be calculated. Different physical phenomena exist to explain the role of earthquakes in inducing stress changes, giving rise to two main types.

Static stresses represent the permanent stress state of a given area. Alterations in static stresses constitute a lasting modification dependent solely on the co-seismic displacement of the fault. During an earthquake, stresses are liberated along the fault plane and extend beyond the rupture zone, primarily concentrating at the fracture ends (Chinnery, 1963; Das and Scholz, 1981). The spatial variations of static stresses diminish rapidly with the epicentral distance Δ, following a Δ^{-3} decay pattern (Hill and Prejean, 2015). As a result, the potential for static triggering is concentrated in the near field, typically within a few fault lengths, encompassing the radius where aftershocks are localized.

Dynamic triggering, the second type, occurs when there is a causal link between the local response to seismic waves generated by a distant event (Hill and Prejean, 2015). While this response should be immediate due to the non-permanent nature of deformation, activation delays, ranging from seconds to hours, have been observed (e.g., Brodsky et al., 2000; Gomberg, 2001). The challenge lies in demonstrating that local activities are indeed triggered by a distant earthquake rather than occurring coincidentally.

Beyond tectonic loading, other external forces, such as fluid migration induced by volcanic

activity or human fluid injection, significantly influence earthquake occurrences. The circulation of fluids in the crust induces stress variations. By increasing pore pressure, fluids reduce effective normal stresses along pre-existing structures, preventing brittle rupture (Nur and Booker, 1972). Conversely, a decrease in pore pressure can stabilize the fault, leading to periods of seismic quiescence. Fluids play a pivotal role in promoting fault weakening, either facilitating seismic slipping or inducing aseismic rupture, depending on the circumstances (King Hubbert and Rubey, 1959).

The Rate-and-State (RS) and Coulomb Failure (CF) models represent two extensively applied physics-based seismicity models. Both models operate under the assumption of pre-existing fault populations responding to Coulomb stress changes. In the CF model, the focus lies on the absolute Coulomb stress, triggering instantaneous events when stress surpasses a threshold. On the other hand, the RS model relies solely on stress changes. Both models demonstrate the capability to predict background earthquake rates and time-dependent stress effects. However, the RS model, distinguished by its three independent parameters, offers an added dimension by accounting for delayed aftershock triggering.

1.6.1 Rate-state friction model (RS)

Dieterich, 1994 bridged the gap between statistical and physical seismicity model by proposing a relationship between the rate of seismicity and the stress state history, one formulation is

$$R = \frac{r_0}{\dot{\tau}_r.\gamma}, \tag{1.36}$$

where r the background rate of seismicity, which is assumed constant in time, $\dot{\tau}_r$ is the background shear stressing rate and γ is a state variable that depends on the shear and normal stressing history acting on the population of potential seismic sources. Dieterich, 1994 derived the following ordinary differential equation for γ

$$\dot{\gamma} = \frac{1}{A.\sigma}[1 - \gamma.\dot{\tau} + \gamma(\frac{\tau}{\sigma} - \alpha)\dot{\sigma}], \tag{1.37}$$

where A is a constitutive parameter relating changes in instantaneous slip rate to friction, σ and τ

are the effective normal stress and shear stress (respectively) acting on the population of sources, and α is a constitutive parameter that relates change in normal stress to friction.

Dieterich, 1994 applies the RS dependent friction model to analyze the occurrence of aftershocks. This model establishes a connection between steps in shear and normal stresses on faults and the failure times of a fault population. The seismicity rate remains constant if the rate of tectonic loading is steady. In the RS friction model, static stress changes associated with a mainshock lead to a stepwise increase in sliding speed and a reduction in the time to failure of pre-existing faults in the surrounding region.

Dieterich, 1994 demonstrates, assuming a constant normal stress, that the RS friction model aligns with Omori's law (refer to section 1.4) for the rate of aftershocks, providing a possible explanation for the observed decay in aftershock rates. The model also predicts an initially constant aftershock rate before transitioning to a power-law decay over time. A fault population governed by RS friction becomes a physical model predicting a non-zero value of c in the Omori law (Equation 1.38).

$$R(t) = \frac{r}{exp(\frac{-\Delta\tau}{A.\sigma}) + t.\dot{\tau}_r/A.\sigma} \approx \frac{k}{c+t}, \tag{1.38}$$

where $\Delta\tau$ is the difference in shear stress, and t, is the time since the mainshock. Under the assumption of a constant stressing rate before and after the mainshock, the parameter c is inversely related to the stress change. Larger stress changes result in smaller values of c, indicating a faster approach to the power-law decay of seismicity rates. This is explained by the fact that larger stress changes bring more earthquakes closer to failure sooner, causing the seismicity rate to begin its decay earlier than in the case of smaller stress changes. Notably, RS friction suggests an inverse relationship between the Omori law parameter c and the magnitude of the mainshock, where a larger mainshock corresponds to a smaller value of c in the resulting aftershock sequence. Figure 1.18 illustrates a the decay of aftershocks for diffrent stress changes.

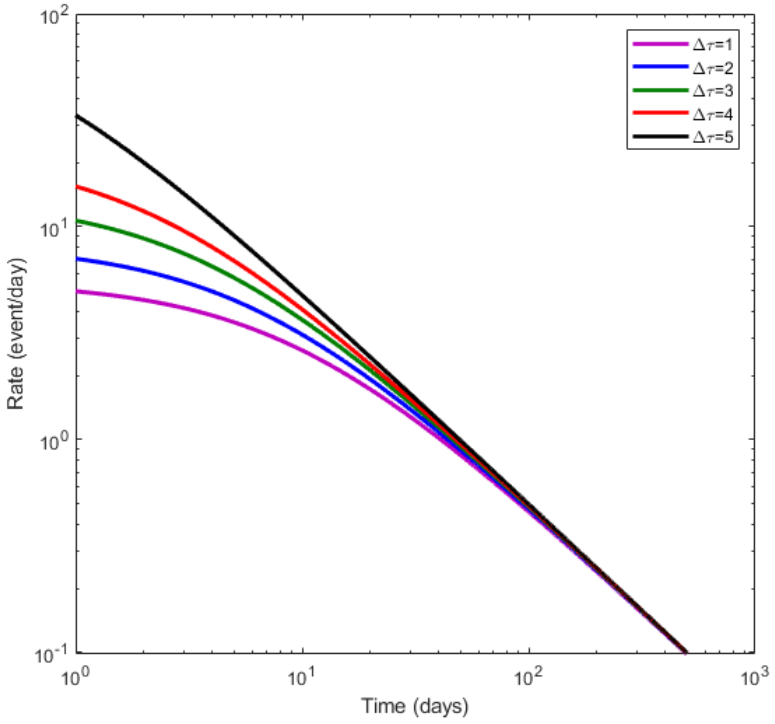

Figure 1.18: Log-log illustration of the temporal decay of aftershocks rate for diffrent stress changes.

1.6.2 The Coulomb failure (CF)

Coulomb failure stress, also known as Coulomb failure criterion or Coulomb yield criterion, is a concept in geology and mechanics that describes the conditions under which a material will fail (i.e., fracture or undergo irreversible deformation) when subjected to shear stress. According to the Coulomb failure criterion, failure occurs when the shear stress on a plane reaches a critical value defined by the formula:

$$CFS = \tau + \mu(\sigma_n + P) - S, \tag{1.39}$$

where τ is the shear stress, σ_n is normal stress, and P is the pore pressure. The coefficient of friction μ and the cohesion S are both assumed to be constant. Positive changes in the stresses and/or pore pressure move a fault closer to the failure stress by an amount:

$$\Delta CFS = \Delta\tau + \mu(\Delta\sigma_n + \Delta P) = \zeta. \tag{1.40}$$

In the CF model, the occurrence of an earthquake is immediately triggered when the Coulomb stress (τ_c) at the source surpasses the inherent cohesive strength (τ_0), which ζ is the difference between them (Figure 1.19).

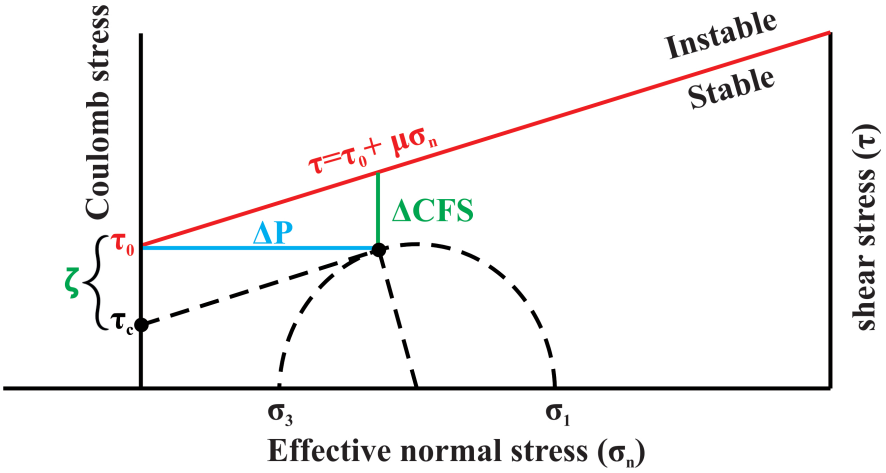

Figure 1.19: Schematic illustration of Coulomb failure stress changes ΔCFS and critical fluid pressure changes ΔP plotted in a Mohr stress diagram required to cause the slip of an individual fault or asperity (the black circle). The Coulomb Failure line is plotted in red. The symbol ζ represents the difference between the strength threshold, τ_0, and the actual Coulomb stress, τ_c, at the source.

For a consistently applied and uniformly distributed stressing rate τ_c the time-to-failure (t_f) for a source is straightforwardly determined by:

$$t_f = \frac{\tau_0 - \tau_c}{d\tau_c/dt} = \frac{\zeta}{\dot{\tau}_c}, \tag{1.41}$$

consequently, the density distribution of sources for a constant rate r_0 is:

$$\chi = (\frac{r_0}{\tau_c})H(\zeta), \tag{1.42}$$

where H is the Heaviside function ($H(\zeta)$=1 for $\zeta \geq 0$ and 0 else). Figure 1.20 depicts a schematic representation of the CF theory.

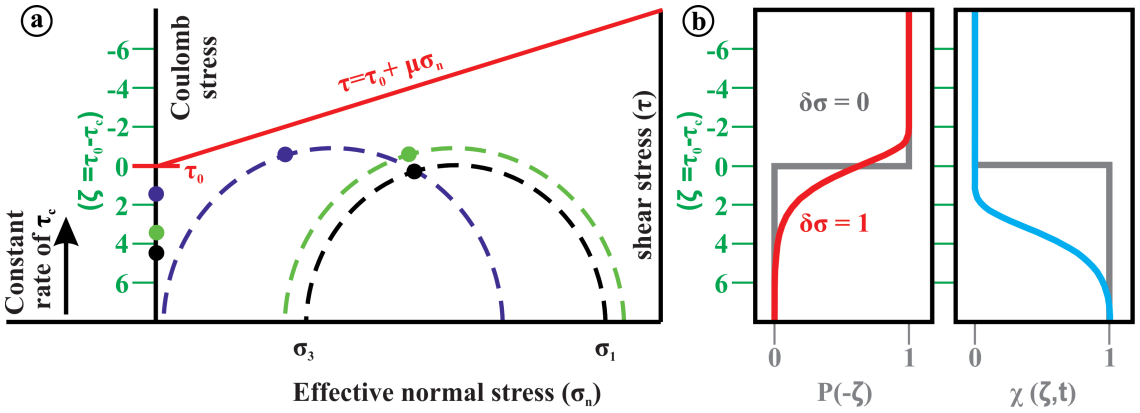

Figure 1.20: (a) The Coulomb Failure within the Mohr stress diagram, where the three colored circles indicate the state of stress on individual faults or asperity. (b, left-penal) Trigger probability function $p(-\zeta)$ (gray line, associated with $\delta\sigma$ = 0) and the CF model for a uniform pre-stress density distribution$\chi(\zeta)$. In the TDSR model, the probability is a smooth function, as indicated by the non-zero skin parameter $\Delta\sigma$ (red line). (b, right-penal) Normalized distribution of source stresses are defined by an initial susceptibility function $\chi(\zeta, t)$ (modified from Dahm and Hainzl, 2022).

1.6.3 Time-Dependent Stress Response Model (TDSR)

The CF model oversimplifies the process by assuming a fixed threshold that instantaneously triggers events. However, instabilities are realistically expected to manifest at various stress levels. To address this, Dahm and Hainzl, 2022 introduced the TDSR model as a modification of the CF model. The TDSR model incorporates the delayed nucleation of both tensile and shear cracks by introducing a stress-dependent mean time-to-failure ($\overline{t_f}$) following an exponential function:

$$\overline{t_f} = t_0 e^{\frac{\zeta}{\delta\sigma}}, \tag{1.43}$$

the constant t_0 represents the average delay time for a critically stressed source (ζ = 0). The parameter $\delta\sigma$ governs the escalation of ($\overline{t_f}$) with ζ and is referred to as the skin parameter (Figure 1.20).

In the scenario where $\delta\sigma \longrightarrow 0$,

$$\begin{cases} \overline{t_f} \longrightarrow \infty & \text{for } \zeta > 0 \text{ (stable)} \\ \overline{t_f} \longrightarrow 0 & \text{for } \zeta < 0 \text{ (instantaneous failure)} \end{cases}, \tag{1.44}$$

this scenario aligns with the principles of the CF model. The total event rate of the volume at time t is given by:

$$R(t) = \int_{-\infty}^{+\infty} \frac{\chi(\zeta, t)}{\overline{\mathrm{t_f}}(\zeta)} d\zeta \tag{1.45}$$

$\chi(\zeta, t)$ is the time-dependent density distribution of sources at the different stress levels. Noting that the mean failure rate for N sources is given by $N/\overline{\mathrm{t_f}}$, where $\overline{\mathrm{t_f}}$ is independent of time. To utilize this relationship for rate forecasts, it is essential to track the evolution of $\chi(\zeta, t)$. Dahm and Hainzl, 2022 addressed this by employing various assumptions and simplifications in their analytical and numerical solutions. Analytical predictions for the model can be derived for certain simplified stress scenarios, as detailed in Table 1.1.

Uniform Initial Distribution With Constant Loading	$\chi_0 \dot{\sigma_c} \frac{1-e^{(-\frac{\delta\sigma}{\dot{\tau_c} t.})(1-e^{-\frac{\dot{\tau_c} t}{\delta\sigma}})e^{-\frac{\zeta_{min}-\dot{\tau_c} t}{\delta\sigma}}}}{1-e^{-\frac{\dot{\tau_c} t}{\delta\sigma}}}$
Stationary seismicity	$\frac{r_0}{\dot{\tau_c}} e^{-\frac{\delta\sigma}{t_0 \dot{\tau_c} e^{-\frac{\zeta}{\delta\sigma}}}}$
Stress step	$\frac{r_0}{e^{-\frac{\Delta\tau_c}{\delta\sigma} - \frac{\dot{\tau_c}}{\delta\sigma} t}}$
Changing Stressing Rates	$\frac{r_0}{(1-\frac{\dot{\tau_c}}{\dot{\tau_{c,a}}})e^{-\frac{\tau_{c,a}}{\delta\sigma}} + \frac{\dot{\sigma_c}}{\dot{\tau_{c,a}}}}$

Table 1.1: TDSR functions for diffrent case of seismicity rate.

Figure 1.21 exemplifies the use of TDSR in studying induced seismicity at the Groningen field, Netherlands, known for being one of the world's largest gas reservoirs. The figure compares the results of the TDSR model with other models, with Dahm and Hainzl, 2022 adjusting the remaining free parameters to match the observed annual rates of earthquakes above magnitude 1.45, considered the estimated completeness magnitude since 1993. Their findings suggest that:

- The CF model with uniform pre-stress conditions cannot fit the observations, neither for critical nor for subcritical conditions.
- TDSR and RS assuming an initially constant background seismicity rate lead to identical fits.

- RSsubcrit leads to almost the same result as RS but with a significantly larger background stressing rate.

- The rate of seismic activity decline is significantly affected by the assumed pre-stress distribution, as shown in Figure 1.21. Models like RS and TDSR, with various pre-stress assumptions, display similar decay patterns. However, a Gaussian distribution leads to a much sharper decline, indicating faster depletion of seismic sources. This finding has important implications for seismic hazard studies.

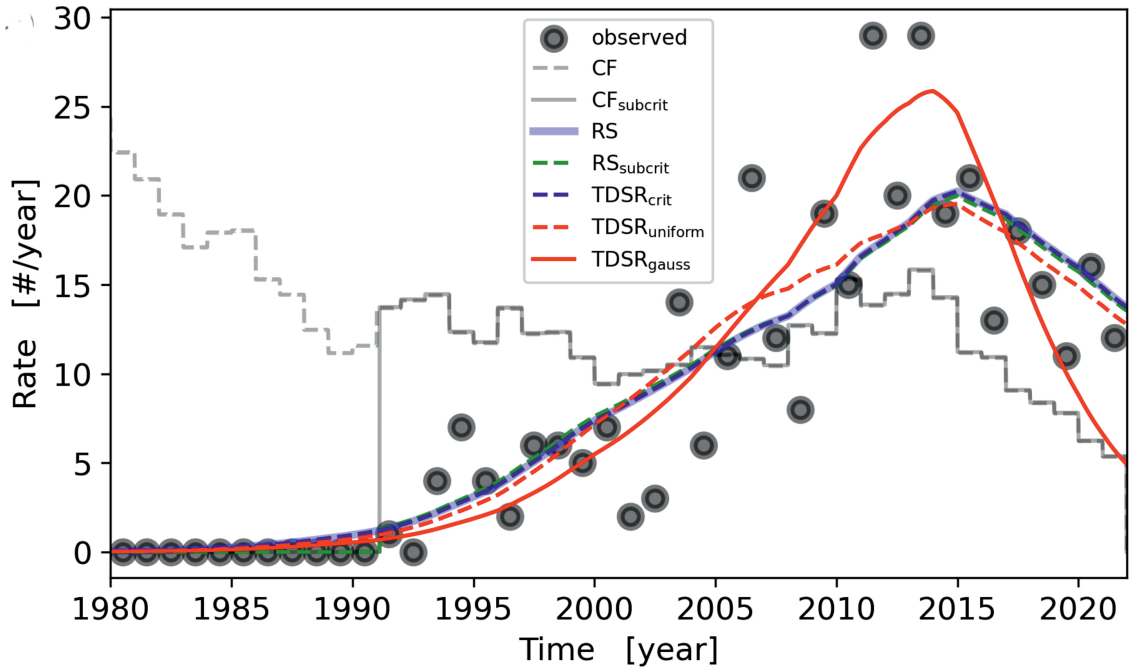

Figure 1.21: Applying the time-dependent stress response (TDSR) model to the Groningen gas field (from Dahm and Hainzl, 2022. The seismic response of the TDSR model to average pressure variations in the Groningen gas field is illustrated here. Data points represent the yearly rate of earthquakes with magnitudes exceeding 1.45. For comparison, the subcritical Coulomb Failure (CF) model (CFsubcrit) and the subcritical rate-and-state (RS) model (RSsubcrit) are also depicted. In both CFsubcrit and RSsubcrit, an initial stress gap of 8.5 MPa was assumed, occurring just prior to the initial recorded earthquakes in 1991. Notably, the RS model yields an identical forecast to the TDSR model.

1.7 Conclusion

This chapter provides an overview of magnitude, temporal and spatio-temporal models in seismicity. Additionally, it includes presentations of other physical models that can explain earthquake triggering mechanisms and spatio-temporal patterns of seismic activity. These models can be subject to biases stemming from partial data.

In conclusion, statistical methodologies emerge as indispensable tools in seismology, crucial for navigating the inherent uncertainties surrounding earthquake processes. The scrutiny of earthquake-related data distributions and the strategic application of statistical techniques are paramount for effectively addressing the multifaceted challenges within the field. While researchers have traditionally concentrated on dissecting fundamental earthquake parameters, such as magnitude, occurrence time, and location, this chapter endeavors to extend the analytical scope.

However, these methods can be subject to biases resulting from the incorrect estimation of m_c and catalog errors that can impact statistical parameters. Thus, understanding the seismicity catalog and each piece of information along with its associated errors is crucial and primordial. The next chapter will focus on the different biases that can be encountered when using statistical analyses and the corrections that need to be applied to avoid them.

Chapter 2

A deep dive in understanding earthquakes catalog

2.1 Introduction

Understanding the flaws in earthquake catalogs is one of the most crucial steps before conducting any statistical analysis. Statistical models heavily depend on the data, and the inversion of statistical parameters yields results based on the processed data. Therefore, a thorough analysis of the catalog is essential, involving high-resolution location, homogeneous magnitude estimation, temporal constraints, and the selection of appropriate statistical models.

In this chapter, we will address biases encountered in statistical analysis by:

Firstly, we will define what constitutes an earthquake catalog, identify the necessary parameters, and highlight potential errors. Next, we will explore the decision of whether to decluster a catalog and determine the most suitable technique for doing so. Subsequently, we will compare different techniques for determining m_c, discussing their respective advantages and disadvantages. We will also delve into the impact of temporal incompleteness on estimating ETAS parameters and propose solutions to mitigate these issues. Furthermore, we will examine the influence of non-stationarity in the background rate on the estimation of ETAS parameters, by highlighting the usefulness of a time-dependent background rate to address and prevent biases resulting from its non-stationarity.

Finally, we will discuss spatial errors and recommend models that should be incorporated into the ETAS model to mitigate these spatial issues. All the synthetic tests were conducted using Python and MATLAB codes

2.2 Earthquake catalog

Seismic networks provide earthquake catalog data, serving as the primary source of information for earthquake studies. A typical earthquake catalog includes details such as the location, time, magnitude, depth, and focal mechanism of recorded seismic events. Since earthquake catalog data serve as the sole representation of reality, ensuring the quality of the data is exceptionally crucial, especially during statistical analysis. Biases can be introduced from various sources, with the most crucial ones being errors in earthquake locations and magnitude estimations.

2.2.1 Earthquake location

The determination of earthquake locations relies on two crucial procedures: accurately picking the arrival times of the P-wave (longitudinal wave) and the S-wave (shear wave), and establishing a specific velocity model for both seismic waves in the studied region. Therefore, the precision of earthquake location data hinges on the accuracy of the velocity model. Lateral variations in velocity can introduce potential systematic errors, especially since seismic networks typically employ 1D velocity models, with 3D models less frequently utilized. Calibration efforts aim to improve existing velocity models by locating events with known parameters, such as mine blasts or quarry blasts, or by dividing the network area into smaller regions with distinct 1D models.

Once a velocity model is established, the earthquake location algorithm predicts the arrival times of P and S waves, which are then compared to observed arrival times. The hypocenter location is determined by minimizing the differences between predicted and observed times. Arrival time errors may also be introduced, contingent on the timing of recorded waveforms, with older recordings often affected, especially in cases where GPS receivers were not available.

Methods for earthquake location include both linear and non-linear approaches. Linear meth-

ods, employing partial derivatives and matrix inversion, are computationally faster than non-linear methods, but their efficacy relies on the quality of the initial guess. In contrast, non-linear models do not depend on an initial guess and provide solutions that account for uncertainties (Husen and Hardebeck, 2010).

Earthquake location errors can be categorized based on the following criteria:

- Measurement errors in seismic arrival times.
- Modeling errors in calculated travel times.
- Non-linearity of the earthquake location problem

2.2.2 Magnitude errors

In the context of magnitude errors, we are addressing alterations in the magnitude type (e.g., Local magnitude, Moment magnitude) provided or changes in the algorithms utilized for magnitude estimation. Such inconsistencies have the potential to introduce heterogeneity to an earthquake catalog. Werner and Sornette, 2008 demonstrate how uncertainties in magnitudes can influence seismic rate estimates and forecasts. Moreover, magnitude uncertainties may result in deviations from the G-R law, impacting estimates of m_c, as highlighted by Mignan, 2011.

Finally, the incorrect estimation of m_c can introduce biases in the estimation of statistical parameters. As discussed in chapter 1, section 1.2, STAI and temporal fluctuations in m_c can severely underestimate the $b-value$ and the productivity factor α. Therefore, incorporating a time-variable $m_c(t)$ or choosing an appropriate one is a crucial step in any analysis of the earthquake catalog. In section 2.4, we will discuss how to properly choose m_c.

2.2.3 summary

Statistical models heavily rely on data, making it imperative to conduct a thorough analysis of the catalog before initiating any seismicity analyses. This involves assessing the accuracy of the location, ensuring the precise estimation of magnitudes, and validating the m_c estimations. Various

sources of bias can influence the seismicity catalog, including natural factors such as the impact of aseismic transients on statistical parameter estimates and STAI (refer to chapter 1, section 1.2). Additionally, man-made biases, such as network densification over time or declustering, can also play a role. Subsequent sections will delve deeper into these biases.

2.3 To decluster or not to decluster ?

Declustering serves the purpose of classifying earthquake catalogs into independent events (mainshocks) and dependent events (afterrshocks) (refer to chapter 1, section 1.5). In this section, we will assess various declustering techniques on synthetic data to examine their impact on the FMD. First, we generate a synthetic catalog based on the ETAS model with the following parameters: μ=1, p=1.20, c=0.001, k=0.0059, α=2, D=0.5, q=1.5, γ=1, and with a $b-value$ set to 1. Figure 2.1 displays the synthetic catalog generated, containing 1800 events with three mainshock-aftershock sequences occurring around 580, 650, and 700 days, and the entire catalog having a maximum magnitude of 3.5.

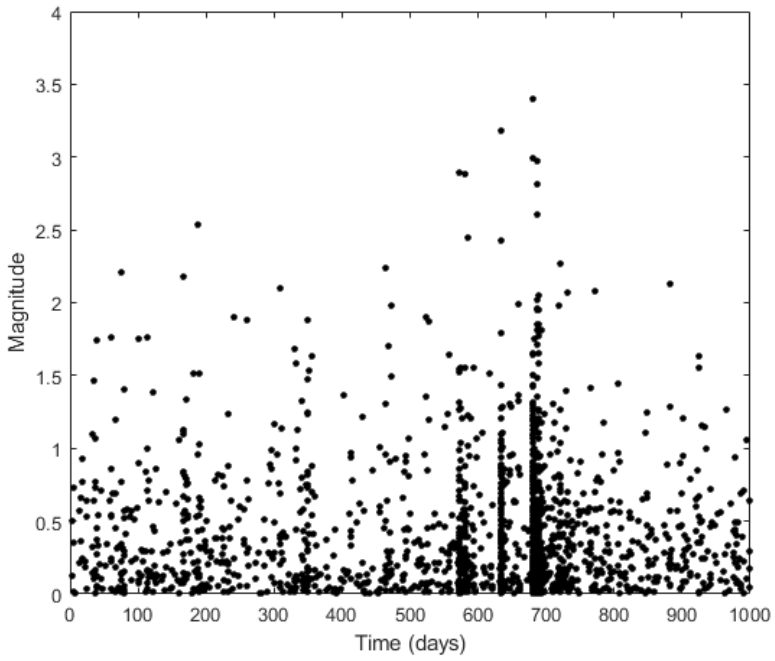

Figure 2.1: Synthetic catalog according to the ETAS model.

The choice of a low $k - value$ aims to diminish the ability of smaller events to generate larger events and increase the overall earthquake count (Kumazawa and Ogata, 2014), the $\alpha - value$ selected corresponds to that commonly found in normal tectonic regimes where mainshock-aftershock sequences are more prevalent (Ogata, 1992), and the chosen $b - value$ is representative of typical values found in various regions worldwide (Wyss et al., 2004).

The four techniques to be tested in this section are those explained in chapter 1, section 1.5, namely the spatio-temporal ETAS model, the NND technique, and the window-based methods (Reasenberg's algorithm and Gardner and Knopoff technique). The cumulative number of mainshocks, according to these declustering techniques, is represented in Figure 2.2. Upon observing the results, it is evident that the number of events in the declustered catalogs decreases by more than 50% compared to the full catalog, ranging from approximately 500 to 800 events, depending on the declustering technique. Additionally, it can be observed that the increase in the number of events related to the aftershocks (Figure 2.2, black solid line) disappears, confirming the effectiveness of the declustering procedure.

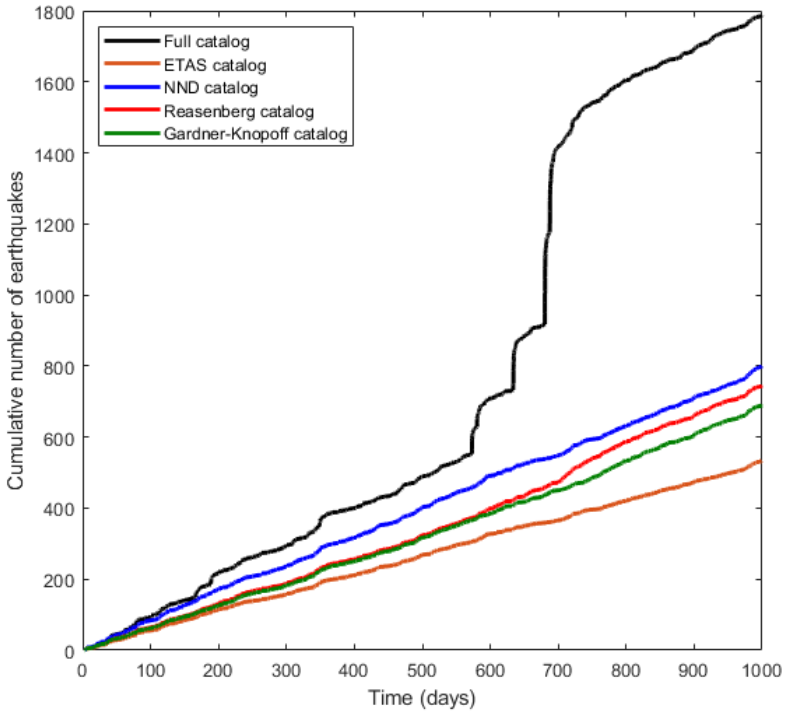

Figure 2.2: Cumulative number of mainshocks declustered compared to the full catalog.

We proceede with estimating the b and a values for each catalog using the maximum likelihood technique (refer to chapter 1, section 1.3). Figure 2.3 and Figure 2.4 illustrate the FMD of events, with the event rate ($a-value$) plotted against magnitude on a log10 scale. The event rate is notably lower for each declustered catalog compared to the full catalog, primarily due to the exclusion of aftershocks. Table 2.1 presents the results for each catalog, showing a decrease in the $b-value$ for each declustering technique. Only the ETAS model was able to recover the true $b-value$, while the Gardner-Knopoff method exhibited a notable decrease in the $b-value$, mainly attributable to the relative increase of larger events. A lower $b-value$ estimation can lead to an unrealistic estimate of the number of events with larger magnitudes.

In summary, three main trends are visible: "aggressive" declustering, as implemented by the Gardner-Knopoff technique, tends to exclude a higher number of small events, resulting in a decrease in the $b-value$. In contrast, the ETAS model does not impact the $b-value$ estimation. Finally, the NND technique and Reasenberg's method exhibit a slightly smaller decrease in the $b-value$, but they still cannot fully recover the true $b-value$.

Declustering method	$-value$	$b-value$
Full catalog	3.25	1
ETAS catalog	2.76	0.99
Gardner-Knopoff catalog	2.91	0.88
Reasenberg catalog	2.84	0.96
NND catalog	2.76	0.95

Table 2.1: G-R law parameters for the full catalog and the declustered ones

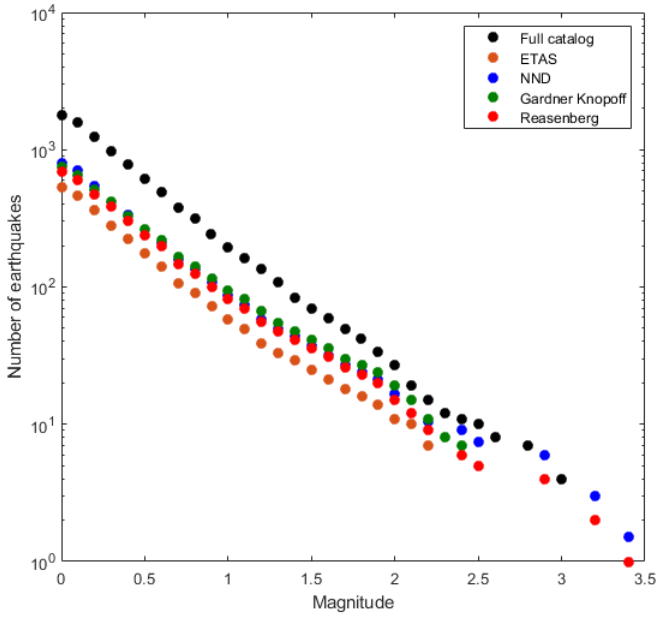

Figure 2.3: FMD of mainshocks declustered compared to the full catalog.

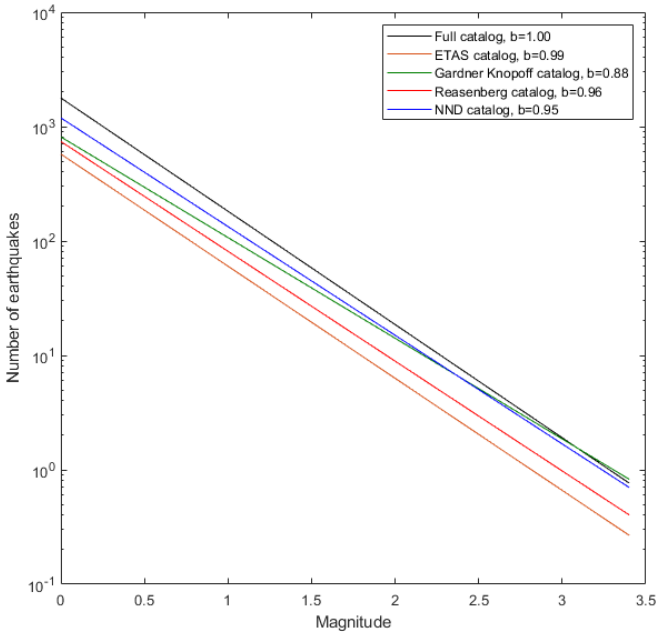

Figure 2.4: G-R law fit for declustered catalogs compared to the full catalog.

We conduct a simulation to predict the largest magnitude of a catalog using the different $b-values$ determined for each declustered catalog. To achieve this, we generate 10,000 earthquake catalogs by employing the parameters of the ETAS model used to create the synthetic earthquake catalog, with the sole modification being the replacement of the $b-value$ found for each declustered catalog. Subsequently, we creat a probability density function (PDF) from our results to observe the variations across each declustered catalog. The results found from this simulation are depicted in Figure 2.5. This analysis provides insights into the potential range of maximum magnitudes that could occur based on the specific $b-values$ obtained through different declustering techniques.

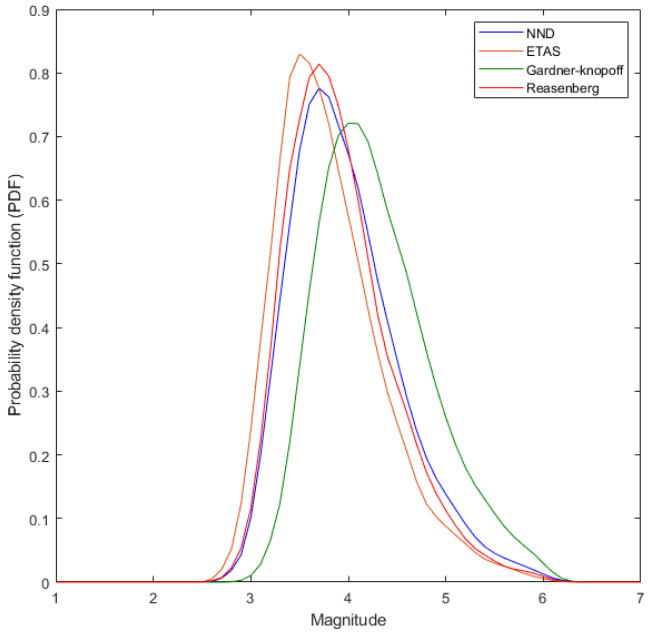

Figure 2.5: Probability density function of the largest magnitude predicted for the full catalog and the declustered ones

It is evident that as the $b-value$ decreases, the magnitude of the largest event increases. This implies that an underestimation of the $b-value$ may lead to an overestimation of the maximum magnitude in a given region. While one might instinctively believe that overestimating the maximum magnitude is preferable to underestimating it, it is crucial to take into account the economic conditions of each country. Striking the right balance between the observed reality and the economic aspects of the region becomes vital, especially for those engaged in determining seismic hazards. Alternatively, understanding the fundamental physical mechanisms responsible for gener-

ating earthquakes may also be influenced when utilizing declustering to interpret the $b-value$. As mentioned in chapter 1, section 1.3, the $b-value$ acts somewhat like a stress meter, and underestimating it may result in a biased interpretation of the stress state in the region.

These results are consistent with the findings of Mizrahi et al., 2021b. In their study, where they determined the $b-values$ for the entire Californian earthquake catalog, including the declustered events, they observed that the ETAS model maintained an unchanged $b-value$. However, the Gardner-Knopoff declustering method, heavily underestimate the $b-value$. They also highlighted that all declustering techniques underestimated the true event rate. On the other hand, Eroglu Azak et al., 2018 propose that the effectiveness of each declustering technique depends on considering each tectonic region separately. They suggest a careful examination of catalogs and the tectonic setting before applying any declustering technique. Furthermore, they advocate that if the declustered catalog and the full catalog share the same $b-value$, it is acceptable to decluster. Finally they interpret differences in $b-values$ as possibly indicating that clustered events and mainshocks do not follow the same tectonic regime. This observation, although potentially evident, raises the possibility that the reduction in the number of earthquakes post-declustering could contribute to smaller $b-values$.

Probabilistic seismic hazard assessment (PSHA) relies on a Poisson distribution for earthquake occurrence, an assumption intended to be maintained through the process of declustering. However, the absence of a standardized method for declustering, coupled with the lack of an objective criterion to distinguish mainshocks, aftershocks, and foreshocks, significantly impacts the results. Additionally, the potential threat posed by aftershocks was highlighted in a study by Marzocchi and Taroni, 2014, revealing that declustering can lead to an underestimation of PSHA. In response, Iervolino et al., 2018 and Iervolino, 2019 proposed a generalization of the hazard integral to reintroduce aftershock hazard in PSHA. Contrastingly, Nandan et al., 2019 proposed employing the ETAS model for seismicity rate assessment. In their study conducted in California for pseudo perspective forecasting, the ETAS model outperformed all other techniques.

Revisiting the initial question: To decluster or not? The answer is both yes and no. While PSHA require a Poissonian distribution of earthquakes, recent advancements in the field propose models that incorporate aftershocks to characterize the complete seismicity rate. However, scien-

tists continue to use conventional methods for determining PSHA without fully considering these recent findings. Despite this, it remains crucial to address the issue and search for a proper solution.

2.4 How to properly choose the magnitude of completeness?

The selection of m_c stands out as a critical preliminary step before embarking on any statistical analysis (refer to chapter 1, section 1.2). Hence, it is imperative to accurately estimate m_c, considering that even minor temporal variations can introduce bias into the statistical analysis. In this section, we will systematically examine each factor that influences m_c and its impact on our statistical parameters, particularly the ETAS model. Initially, we assess m_c estimation for varying sample sizes (number of events) by generating synthetic catalogs with m_c=2 and a $b-value$ of 1. Introducing incompleteness to the catalogs is achieved using the EMR technique with parameters μ=1 and σ=0.25. Catalogs are then generated with sample sizes ranging from 25 to 1500. m_c is subsequently determined using four techniques outlined in chapter 1, section 1.2. To gauge the uncertainties in the m_c estimates, a bootstrap approach is employed. Bootstrap sample earthquake catalogs are formed by randomly selecting, with replacement, an equivalent number of events from the original catalog. For each bootstrap sample earthquake catalog, m_c and δm_c are calculated . The results obtained are depicted in Figure 2.6, the red line represent the mean m_c from the bootstrap estimation, and the gray solid line represente the uncrtanties δm_c.

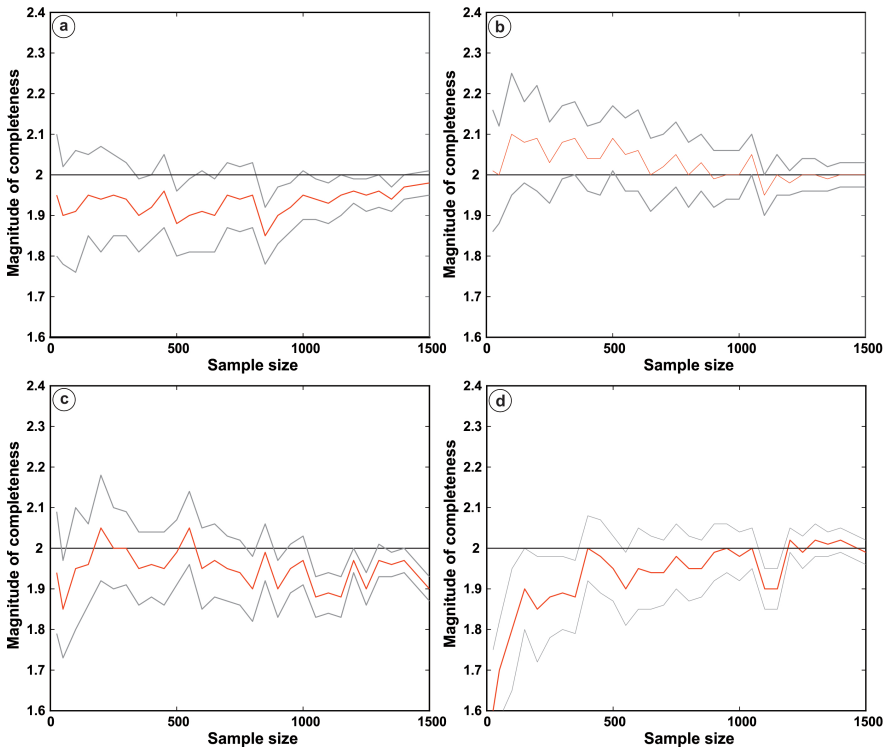

Figure 2.6: (a) MAXC method estimation of m_c for different sample size. (b) EMR method estimation for different sample size. (c) GFT method estimation of m_c for different sample size. (d) MBS method estimation for different sample size

Both the MAXC and GFT-95% approaches consistently exhibit an underestimation of m_c by $\sim$ 0.1, with MAXC consistently yielding the smallest values (Figure 2.6a, and c). The EMR method effectively recovers $m_c \approx 2.0$ for larger sample sizes but tends to overestimate it for sample sizes $\sim<$ 600 (Figure 2.6b). In contrast, the MBS approach significantly underestimates m_c, particularly for small sample sizes ($\sim<$ 500), displaying a notable dependence on the number of data points (Figure 2.6d). The trend of δm_c (ranging between $\sim$ 0.2 and 0.04) decreasing with an increase in sample size aligns with expectations, as smaller sample sizes lead to higher parameter variability (Figure 2.6, gray lines). This pattern of decreasing uncertainty with an increase in the number of data points is consistent with the statistical principle that a larger sample size generally results in more precise parameter estimates. Smaller sample sizes inherently lead to greater variability in the calculated parameters, contributing to larger uncertainties. This observation underscores the importance of considering the sample size when interpreting the uncertainties associated with seismic parameters. From these tests, the EMR method proved to be the most effective in recovering

the true m_c.

To explore the impact of temporal variations in m_c on the ETAS parameters, we conducted three distinct synthetic tests. Initially, we generated a synthetic catalog using the ETAS model with the following parameters: k=0.015, α=2.1, c=0.01, p=1.2, and μ=1. Subsequently, we replicated three different tests based on the methodology outlined by Hainzl et al., 2013, each with varying parameters. These tests focus solely on the conventional temporal ETAS model. Following this, we applied different solutions and compared them to the true synthetic parameters. The series of synthetic tests is as follows:

- The first synthetic catalog exhibits time-dependent incompleteness for lower magnitudes ranging from 0 to 0.5. We incorporate incompleteness using the EMR technique during magnitude generation, ensuring that events with magnitudes in the range of 0-0.5 are partially excluded. This scenario, referred to as case-1, represents a typical catalog found in current practice, where detection depends on the level of noise in the region, leading to variations in the temporal evolution of m_c (Figure 2.7).

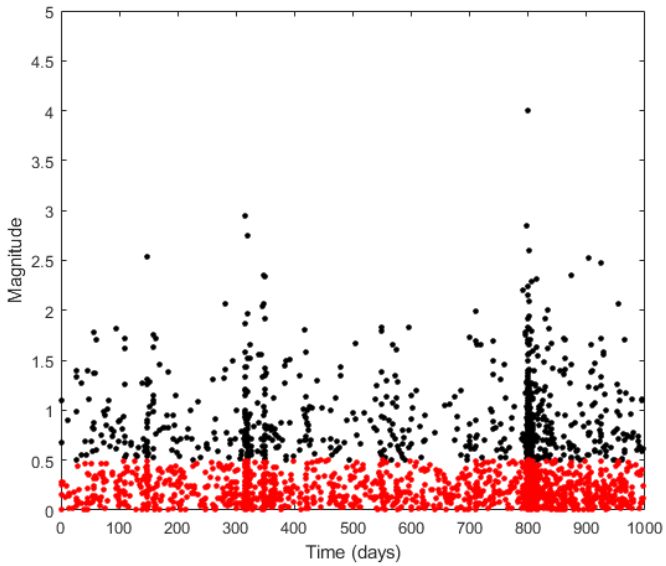

Figure 2.7: Synthetic catalog with incompleteness below 0.5. The black circles represent synthetic earthquakes in the complete range ($\geq$0.5), and the red circles represent the incomplete part (m<0.5)

- The second synthetic catalog has all earthquakes occurring between 500 and 700 days with

magnitudes ranging from 0 to 0.5 removed, creating partial incompleteness and inducing a time-dependent m_c. This scenario simulates a situation where some stations in the network configuration are non-operational for a period of time. We will refer to this case as case-2 (Figure 2.8).

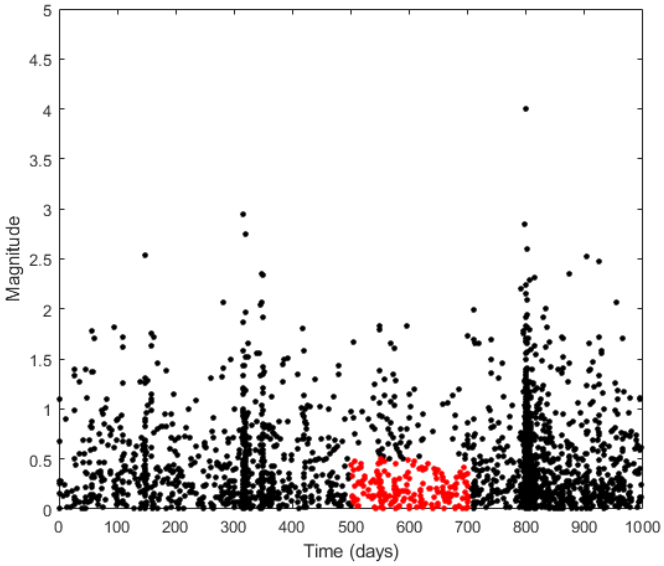

Figure 2.8: Synthetic catalog with partial incompleteness < 0.5, from 500 to 700 days (red circles).

- The third synthetic catalog will incorporate STAI following major mainshocks. STAI will be implemented by removing events based on the empirical relationship discussed in chapter 1, subsection 1.2.6, as outlined in Helmstetter et al., 2006. All earthquakes that do not satisfy the conditions of the empirical relationship will be removed from the synthetic catalog. This scenario will be denoted as case-3 (Figure 2.9).

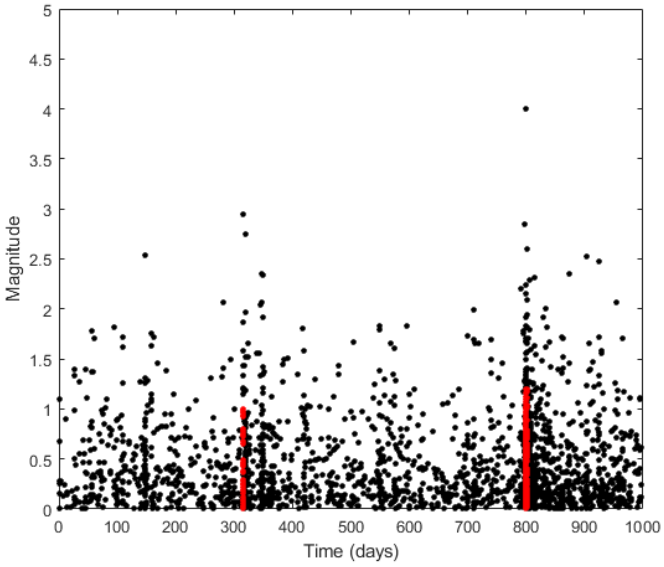

Figure 2.9: Synthetic catalog with STAI for periods after two mainshocks for magnitude 3 and 4 (red circles).

The estimated parameters of the ETAS model are outlined in Table 2.2.

Case	μ	p	c	k	α
True parameters	1.00	1.20	0.010	0.015	2.10
Case-1	0.98	1.19	0.015	0.006	2.06
Case-2	0.92	1.22	0.034	0.028	1.94
Case-3	0.96	1.18	0.021	0.020	1.98
Case-2, with m $\geq m_c$+0.5	0.99	1.21	0.012	0.013	2.08
Case-3, with excluding the events from the incomplete part	1.02	1.19	0.009	0.016	2.12

Table 2.2: ETAS parameters determined for each case.

Specifically, it was observed that partialy excluding events ranging from magnitude 0 to 0.5 from the catalog in case-1 results in a reduction of the parameter k and a slight increase in the $c-value$, without introducing any bias in the other parameters (Table 2.2). However, the other two cases lead to a significant underestimation of the $\alpha-value$, and an over estimation of both the $c-value$ and $k-value$. This discrepancy can be explained by the fact that in case-2, the absence of events, with magnitude ranging from 0 to 0.5, in the 200-day time period reduces the productivity of larger shocks and increases it for smaller events. In case-3, scaling the incompleteness time period

with the mainshock magnitude diminishes the apparent productivity of larger events compared to lower magnitudes, which results also in an increase of the $k-value$. In the latter case, the bias in α is relatively small if the catalog is taken for a long period but for a short period (seismic sequence) the bias can become larger.

This analysis highlights that catalog errors in both case-2 and case-3 introduce significant biases in the estimation of α. However, two solutions can be implemented: firstly, optimizing only for events with magnitudes above the highest m_c in the catalog, which in this case is $m \geq 0.5$ (applied to case-2), and secondly, excluding events occurring during incompletely recorded time periods immediately following large earthquakes (applied to case-3). These solutions have proven effective in mitigating bias in parameter estimation (refer to Table 2.2).

Other solutions, proposed by Hainzl, 2016a and Mizrahi et al., 2021a, exist to account for time-varying m_c on a short or long-term scale.

Firstly, Hainzl, 2016a included information on STAI in the ETAS model by incorporating the rate dependent m_c (refer to chapter 1. section 1.2). The methodology is grounded in the straightforward assumption that an earthquake of magnitude m becomes indistinguishable and undetectable by seismogram analysis if it occurs within a blind time T_b after an event of equal or larger magnitude (Hainzl, 2016a; Lippiello et al., 2016). Building on this premise, Hainzl, 2016a derived the functional form of the apparent seismicity rate R, and magnitude distribution F based on recorded, incomplete catalog data. Notably, R and F are contingent on the true underlying rate R_0 at time t and the time-invariant, true magnitude distribution F_0. The probability of observing an earthquake with a specific magnitude $m \geq m_c$ at time t is determined by the likelihood that no earthquake occurred between $t - T_b$ and t with a magnitude larger than m. Assuming an (inhomogeneous) Poisson process with the true rate R_0, which represent the temporal ETAS function (refer to chapter 1, section 1.4, Equation 1.19), the detection probability P_d is given by:

$$P_d(m,t) = e^{(-N_0(t)F_0(m))}, \tag{2.1}$$

where $F_0(m)$ is the true cumulative distribution function of earthquake magnitudes, and N_0 is the true number of expected $m \geq m_c$ events, i.e., the integral of R_0 over the time interval $[t - T_b, t]$.

The product $N_0(t).F_0(m)$ represents the expected number of events with a magnitude larger than m occurring in the interval T_b. With this detection probability, both the apparent rate and magnitude distribution can be analytically determined. Hainzl, 2016a demonstrated that the apparent rate is specifically given by:

$$\begin{aligned} R(t) &= \int_{m_c}^{m_{max}} R_0(t).P_d(t,m) \\ &= \int_{m_c}^{m_{max}} R_0(t).e(-N_0(t)F_0(m)) \\ &= \frac{1}{T_b}(1 - e^{-T_b R_0(t)}), \end{aligned} \tag{2.2}$$

and the apparent magnitude distribution becomes:

$$\begin{aligned} F(m,t) &= \int_{m_c}^{m_{max}} F_0(m).P_d(t,m) \\ &= \int_{m_c}^{m_{max}} F_0(m).e^{(-N_0(t)F_0(m))} \\ &= \frac{1 - e^{-T_b R_0(t)F_0(m)}}{1 - e^{-T_b R_0(t)}}, \end{aligned} \tag{2.3}$$

in both equations, the approximation is considered valid because seismicity rates typically do not vary significantly over the time scale of T_b which is in the order of seconds to minutes; thus, $N_0(t) = R_0(t).T_b$.

Figure 2.10 illustrates the relation between the true rate and, the apparant rate for diffrent T_b values. It becomes evident that the impact of incompleteness strongly increases with increasing T_b, but with a T_b=0, the relation between the apparant rate and the true rate becomes linear.

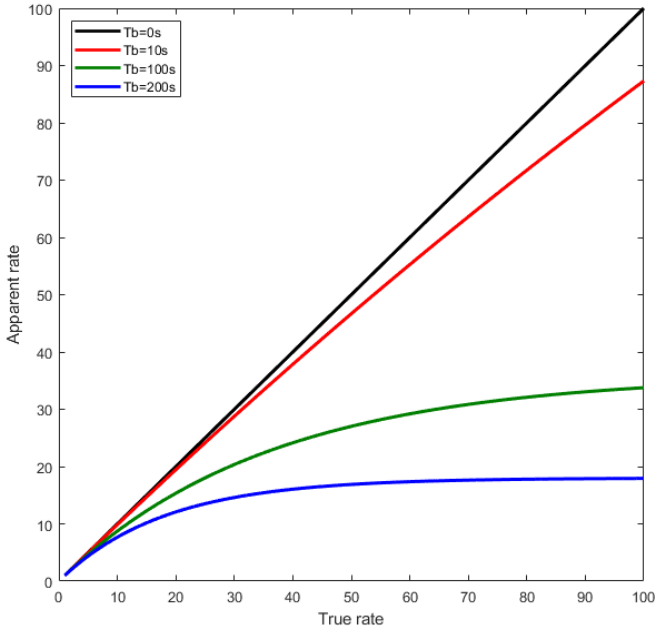

Figure 2.10: Aftershocks rate decay for different blind time.

To estimates to ETAS parameters with the new information for STAI, we optimize the maximum likelihood of the apparant rate $R(t_i)$ with the magnitude distribution accounting for incomplete part of the catalog $f(t_i, m_i)$, as defined in the equation below:

$$L(\theta) = \sum_{i=1}^{N} ln(f(t_i, m_i)R(t_i)) - \int_S^T R(t_i)dt, \tag{2.4}$$

thus the probability density function of the magnitude distribution of the incomplete part of the catalog is given by:

$$f(t_i, m_i) = ln(10)bN_0(t)\frac{10^{-b(m-m_c)}e^{-N_0(t)10^{-b(m-m_c)}}}{1 - e^{-N_0(t)}}, \tag{2.5}$$

here, the optimization of both the ETAS parameters and the $b - value$ in the G-R model is carried out simultaneously. This is because the function describing the magnitude distribution depends not only on the $b - value$ but also $N_0(t)$, which contain the ETAS parameters. Therefore, in addition to the 5 parameters of the ETAS model, the $b - value$ and the blind time are also included as parameters to be fitted. This new model was named as ETASI (Epidemic Type Aftershock

Sequence Incomplete).

We replicated case-3 by generating only one seismic sequence containing STAI for a mainshock of magnitude 4, and for a time period of 5 days, using the same ETAS parameters. We then attempted to fit the synthetic data by both ETAS and ETASI. Table 2.3 depicts the comparison beween the true parameters, ETAS inversion and ETASI inversion. The obtained results indicate that by incorporating information to address STAI, we can avoid excluding events occurring just after a significant mainshock, leading to the identification of the true ETAS parameters with a still slight overestimation of the $c-value$ (Table 2.3). In fact, incorporating incompleteness (Figure 2.11b) results in an underestimation of the $\alpha - value$ when using the conventional ETAS model (Table 2.3). This underestimation, in turn, leads to a misrepresentation of the predicted model (Figure 2.11a). In the case of ETASI, the true observed model is accurately recovered (Figure 2.11a).

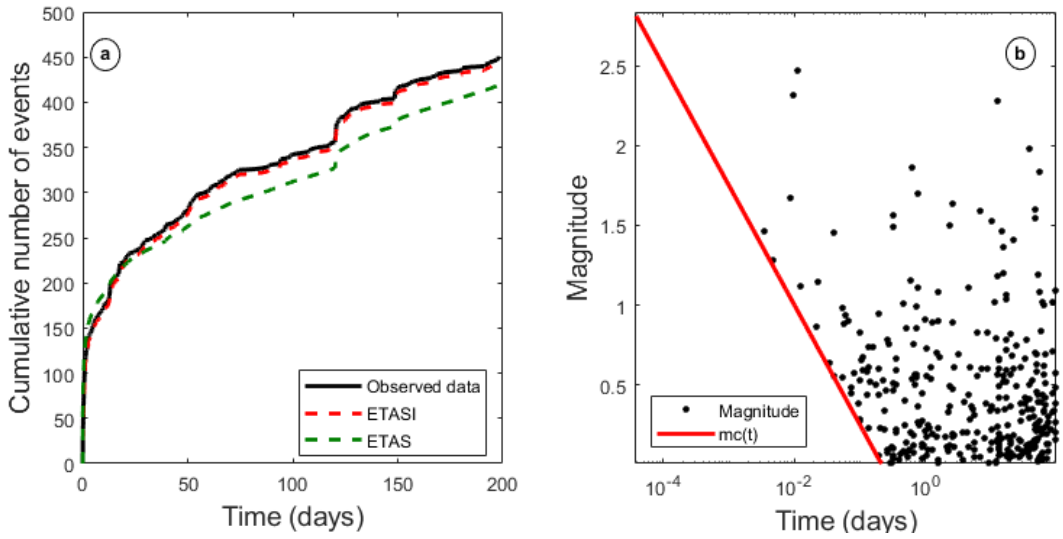

Figure 2.11: (a) Fitting of the cumulative number of earthquakes using both the ETAS model (green dashed line) and the ETASI model (red dashed line). (b) Short-term incompleteness of the fitted catalog.

Model	μ	p	c	k	α	T_b
True parameters	1.00	1.20	0.010	0.015	2.10	-
ETAS	0.94	1.18	0.026	0.024	1.88	-
ETASI	1.02	1.19	0.017	0.018	2.09	260

Table 2.3: Comparison between the true parameters of the synthetic catalog and the parameter inversion of ETAS and ETASI.

Secondly, the methodology proposed by Mizrahi et al., 2021a yields substantial improvements when applied to catalogs exhibiting changes of m_c in the long term. As time progresses and seismological science advances, additional stations are installed to enhance the detection capabilities for smaller events. Ignoring these changes in the network configuration can lead to biases in estimating m_c, introducing errors that may impact the accuracy of statistical parameter estimates.

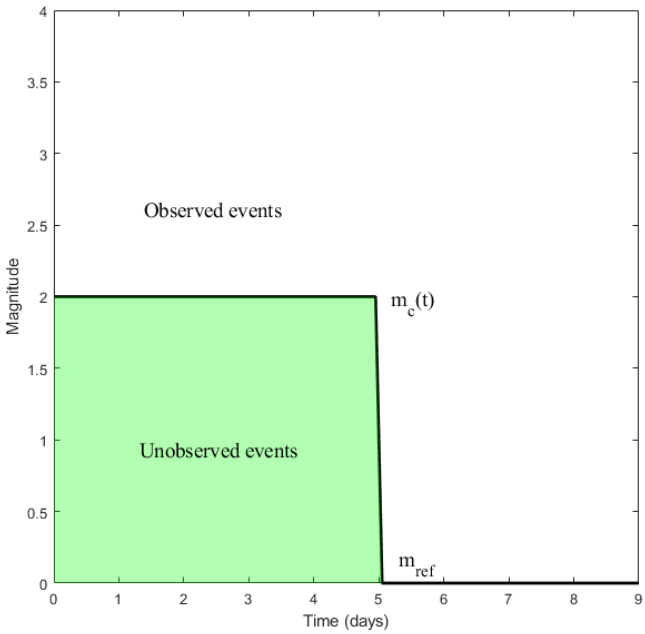

Figure 2.12: Schematic representation of $m_c(t)$ and m_{ref}. The green area represents the unobserved events, and the white area represents the observed events. m_{ref} is defined as the minimum of $m_c(t)$.

The concept of a long-term, time-dependent m_c acknowledges that requirement for complete recording of all potential triggers may be compromised. In the given context, we define m_{ref} as the minimum magnitude, denoted as $min[m_c(t_i)]$, where $m_c(t_i)$ represents the minimum magnitude for events in the complete catalog at times t_i. This definition implies that for times when $m_c(t) > m_{ref}$, the requirement of complete recording of all potential triggers may be violated. Events falling within the magnitude range of m_{ref} to $m_c(t)$ are not considered part of the complete catalog and are deemed unobserved, even if they might have been detected by the network. Consequently, the ETAS model requires adjustment to account for the possibility that event was triggered by an unobserved event (Figure 2.12).

Let's now consider the ratio $\xi(t)$, which represents the relationship between the expected number of events triggered by an unobserved event and the expected number triggered by an observed event at time t:

$$\xi(t) = \frac{\int_{m_{ref}}^{m_c(t)} f_{GR}(m)G(m)dm}{\int_{m_c(t)}^{\infty} f_{GR}(m)G(m)dm}, \tag{2.6}$$

$f_{GR}(m) = \beta.e^{-\beta.(m-m_{ref})}$ is the probability density function of magnitudes according to the G-R law, with $\beta = b.log(10)$, b being the $b-value$, and $G(m)$ is the total number of expected aftershocks larger than m_{ref} following an event of magnitude m, which is the integral of the aftershock contribution in the temporal ETAS model (chapter 1,section 1.5, in Equation 1.19). Analogously, the ratio between the expected fraction of unobserved events and the expected fraction of observed events at time t is given by:

$$\zeta(t) = \frac{\int_{m_{ref}}^{m_c(t)} f_{GR}(m)dm}{\int_{m_c(t)}^{\infty} f_{GR}(m)dm}, \tag{2.7}$$

if $\beta > \alpha$ (productivity factor of the ETAS model), both $\xi(t)$ and $\zeta(t)$ are well-defined, we have:

$$\begin{aligned}\xi(t) =& \frac{\int_{m_{ref}}^{m_c(t)} e^{-\beta.(m-m_{ref})}.e^{\alpha(m-m_{ref})}dm}{\int_{m_c(t)}^{\infty} e^{-\beta.(m-m_{ref})}.e^{\alpha(m-m_{ref})}dm} \\ &= -\frac{e^{(\alpha-\beta)\Delta m}-1}{e^{(\alpha-\beta)\Delta m}} \\ &= e^{(-(\alpha-\beta)\Delta m(t))}-1,\end{aligned} \tag{2.8}$$

and

$$\begin{aligned}\zeta(t) =& \frac{\int_{m_{ref}}^{m_c(t)} e^{-\beta.(m-m_{ref})}dm}{\int_{m_c(t)}^{\infty} e^{-\beta.(m-m_{ref})}dm} \\ &= -\frac{e^{-\beta\Delta m}-1}{e^{-\beta\Delta m}} \\ &= e^{(\beta\Delta m(t))}-1,\end{aligned} \tag{2.9}$$

where $\Delta m(t) = m_c(t) - m_{ref}$. The condition $\beta > \alpha$ is generally fulfilled in naturally observed catalogs (Helmstetter and Sornette, 2003). The ETAS model λ_j comprises the sum of the background rate and aftershock rates of all events. In the case of time-varying m_c, an event j can be triggered not

only by observed events i, but also by unobserved events k. Therefore, λ_j is generalized by adding the expected rate of aftershocks of unobserved triggering events at that time, $g_{kj}.\xi(t_k)$, where g_{kj} is the rate of aftershocks in the temporal ETAS model. This yields: $\lambda_j = \mu + \sum_j g_{kj}(1 + \xi(t_k))$. The generalized definitions of the probability that an event is a background event or triggered event ϕ_j^{ind} and ϕ_{ij}^{trigg} are given by:

$$\phi_{ij}^{trigg} = \frac{g_{ij}}{\mu + \sum_{k:t_k<t_j} g_{kj}(1 + \xi(t_k))}, \tag{2.10}$$

$$\phi_{ij}^{ind} = \frac{\mu}{\mu + \sum_{k:t_k<t_j} g_{kj}(1 + \xi(t_k))}, \tag{2.11}$$

note that the probability ϕ_{ij}^{trigg} that an event j was triggered by an unobserved event is given by $\phi_j^{ind} + \phi_{ij}^{trigg} + \sum \phi_{kj} = 1$. In the special case of $m_c(t) = m_{ref}$, where $\xi(t) = 0$, and $\zeta(t) = 0$, the estimated number of background events and triggered events, which are found by summing the probabilities, of the prior event above m_{ref} , including unobserved events. Similar to amplifying the triggering power, the observed event numbers are adjusted to account for unobserved events. Whene an event is observed at time t_j , we expect that $\zeta(t_j)$ events occurred under similar circumstances but were not observed. This yields:

$$N_{back} = \sum_j \phi_j^{ind}(1 + \zeta(t_j)), \tag{2.12}$$

$$N_{trigg} = \sum_j \phi_{ij}^{trigg}(1 + \zeta(t_j)), \tag{2.13}$$

With these refined definitions, the parameters of the ETAS model can be inverted using the methodology outlined by Veen and Schoenberg, 2008. This process involves the application of the Expected Maximization (EM) procedure, which accommodates missing data by assuming the existence of corresponding unobserved data points for each observed data point. It is noteworthy that this particular definition has been incorporated into the temporal ETAS model, as opposed to its utilization in the spatio-temporal ETAS model by Mizrahi et al., 2021a. Consequently, a key distinction arises where $\xi(t)$ in the spatio-temporal ETAS model is a function of α, β, γ, and q—parameters linked to magnitude (refer to chapter 1, section 1.5, in Equation 1.24, 1.25, and

1.27). In our context (temporal ETAS), however, $\xi(t)$ is solely dependent on α and β (Equation 2.8).

To test the efficiency of this procedure, we generated an earthquake catalog that contain high changes in m_c over long periods of time. The parameters used to create this synthetic catalog are k=0.010, α=1.80, c=0.01, p=1.2, and μ=1. Then, we introduced incompleteness so that from 0 to 1900 days , $m_c = 2$, from 1900 to 3800 days, m_c=1, and from 3800 to 5000 days, m_c=0.5 (Figure 2.13). In this particular case, m_{ref}=0.5 representing $min[m_c(t)]$.

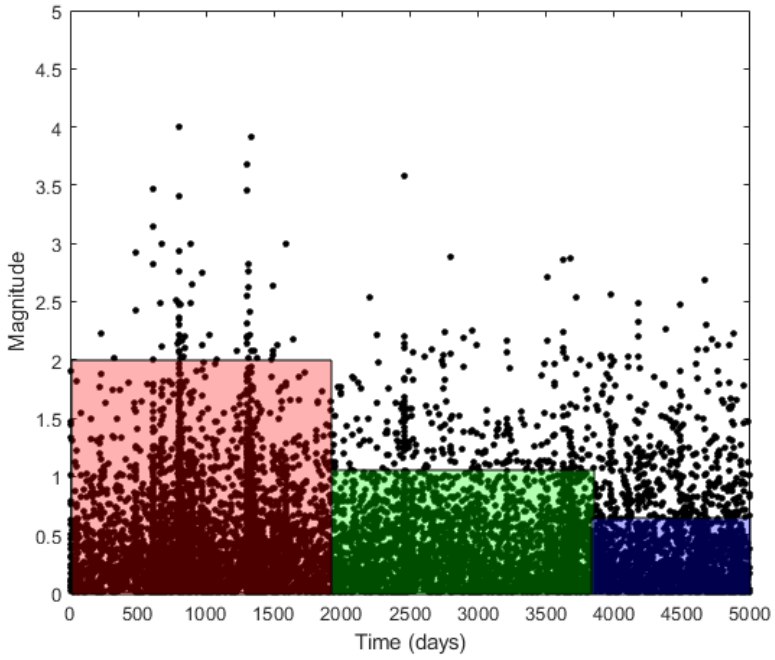

Figure 2.13: Synthetic catalog with a variable m_c, representing a scenario of network densification over time.

This synthetic catalog represents a scenario where network densification is ongoing over time, resulting in a reduction of m_c. It is crucial to consider such changes, as explained earlier, because alterations in the m_c can introduce biases in ETAS and G-R law parameters. Some solutions, such as adopting the highest value of m_c, have been proposed, but this approach systematically reduces the number of events, resulting in a loss of information. Conversely, selecting the smallest value of m_c can introduce biases in the parameters. This type of bias can be assimilated to case-1 in the first synthetic test with a larger time scale.

We applied the modified ETAS model, which accounts for changes in m_c over time, and com-

pared it with selecting the lowest value in the temporal distribution of m_c. The results indicate that opting for the minimum value of m_c results in an overestimation of the $k-value$ and $c-value$ and a significant underestimation of the $\alpha-value$ (Figure 2.14, blue circles). Conversely, when utilizing the ETAS model with a variable m_c over time, we obtained nearly the same true values as provided, resulting in more robust results (Figure 2.14, red circles). It is noteworthy that even in the previous synthetic tests, the $p-value$ remains unaffected. Therefore, we can conclude that the $p-value$ is the only parameter not influenced by changes in m_c (as explained in chapter 1, section 1.4).

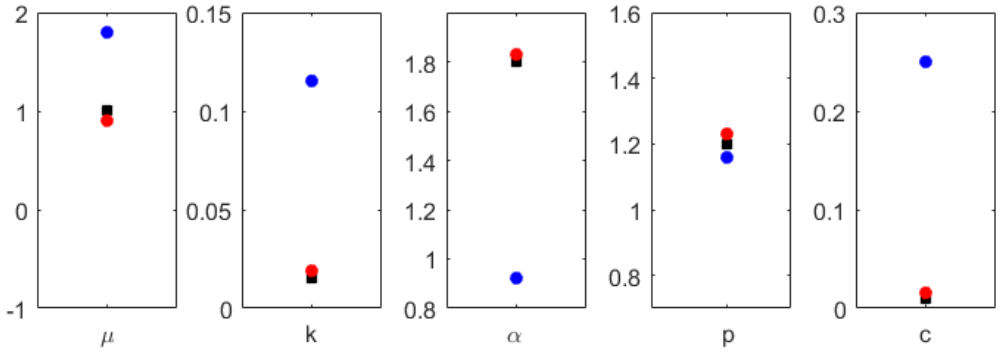

Figure 2.14: Inversion results of the ETAS parameters for the minimum magnitude (blue circles) and the ETAS model with variable magnitude of completeness (red circles) compared to the true values (black squares).

2.5 Influence of a time dependent background rate on the estimation of the ETAS parameters

We investigated the impact of three distinct forms of time-dependent aseismic forcing on parameter estimation. In the first case (case-1), the backgorund rate is ocnstant in time, which can be assimilated to a constant tectonic loading, $\mu(t) = \mu_0 = 1$ (Figure 2.15a). The second case (case-2) simulates the anticipated effects associated with an underlying aseismic stress step, such as those related to fluid intrusion. In this scenario, aseismic transient triggering is modeled using an Omori–Utsu-type decaying rate, $\mu(t) = \mu_0 + k(t-t_0)^{-p} = 1 + 0.0059(t-500)^{-1.2}$ (Figure 2.15b). The third case (case-3) simulate temporal changes in background forcing exhibit smooth variations, generally associated with slow transient deformation. The background rate is modeled using

a gaussian function, $\mu(t) = \mu_0 + (\mu_1 - \mu_0)e^{(t-t_0)^2/2\sigma^2} = 1 + (4-1)e^{(t-700)^2/100^2}$ (Figure 2.15c). The other four parameters (α, k, c, and p) chosen for each case are listed in Table 2.4.

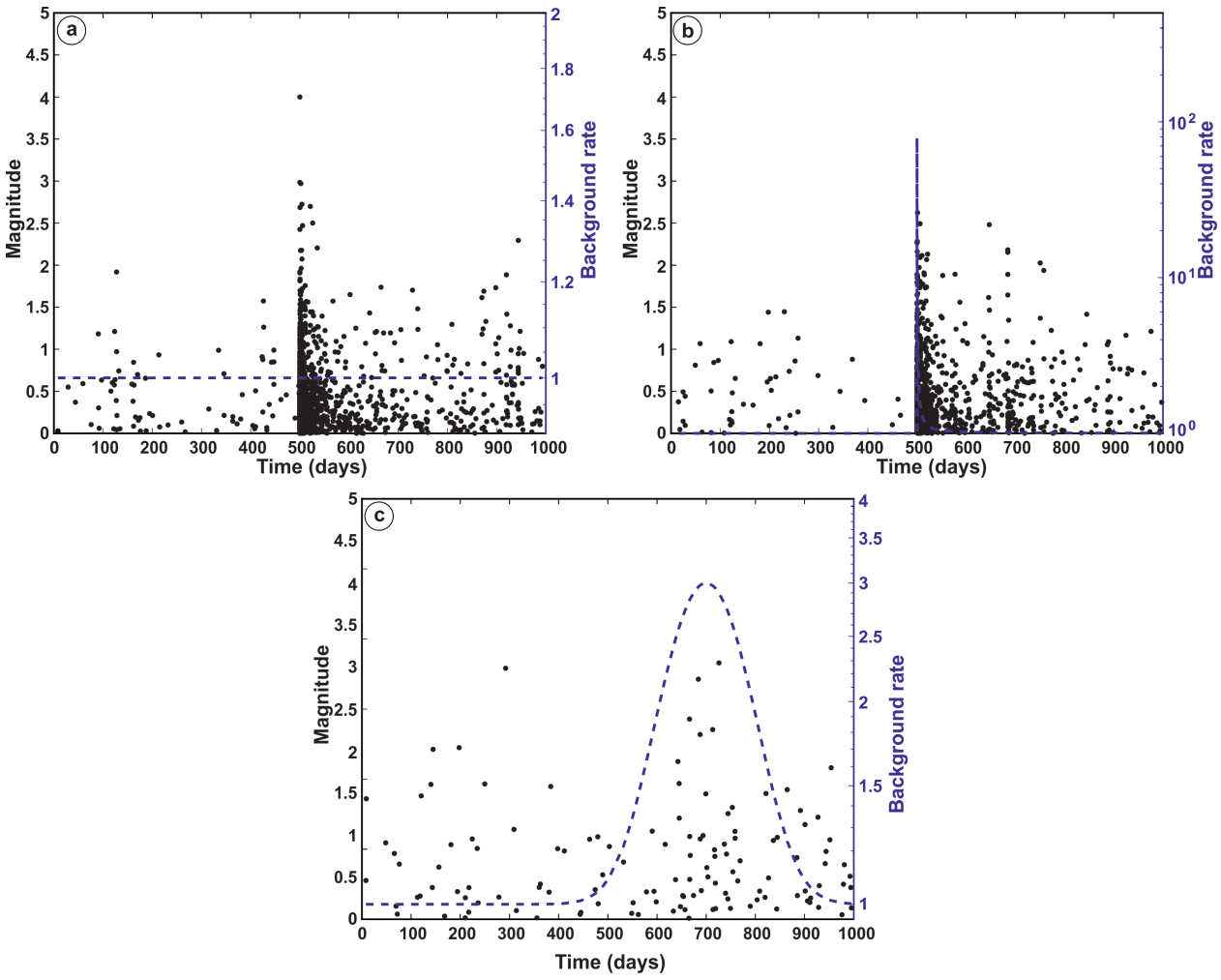

Figure 2.15: (a) Synthetic catalog with a constant background rate. (b) Synthetic catalog with transient background rate. (c) Synthetic catalog with a gaussian background rate

For each case, we conducted parameter estimation through two distinct methodologies. The first adheres to the conventional ETAS model which account for a constant background rate, while the second employs the time-dependent background rate ETAS model (Marsan et al., 2013).

In the context of case-1 featuring constant background rate, both methodologies produce comparable and unbiased estimates for the true underlying parameters (Table 2.4). Conversely, in simulations entailing time-dependent forcing (case-2 and case-3), the method proposed by Marsan et al., 2013 consistently identifies time-dependent forcing as the preferred solution, with parameter

estimation nearly unbiased (Table 2.4). On the other hand, estimating ETAS parameters under the assumption of constant background rate results in markedly biased aftershock productivity parameters when aseismic forcing is present. Notably, parameters k and α are highly impacted (Table 2.4). k is overestimated, and α is significantly underestimated (Table 2.4). This can be explained by the fact that assuming a constant background rate in a context of swarm-like activity increases the capacity of smaller earthquakes to generate aftershocks (overestimation of the $k-value$) and decreases the productivity of larger events (underestimation of the $\alpha-value$). Thus, the time-varying background rate proves to be highly efficient in modeling swarm-like seismicity. These results are comparable to those found by Hainzl et al., 2013, where in the case of synthetic testing, the time-dependent background rate ETAS was accepted as the best model for modeling seismic activity generated by external forcing.

Case	μ	p	c	k	α
Case-1 true parameters	1.00	1.20	0.010	0.0059	2.10
Case-1 inverted parameters (constant background rate)	1.01	1.18	0.009	0.0062	2.15
Case-1 inverted parameters (time-dependent background rate)	1.02	1.21	0.011	0.0058	2.12
Case-2 true parameters	-	1.20	0.010	0.0059	2.10
Case-2 inverted parameters (constant background rate)	2.14	1.24	0.013	0.0150	1.72
Case-2 inverted parameters (time-dependent background rate)	-	1.18	0.014	0.0055	2.09
Case-3 true parameters	-	1.20	0.010	0.0059	0.80
Case-3 inverted parameters (constant background rate)	3.54	1.18	0.012	0.0360	0.31
Case-3 inverted parameters (time-dependent background rate)	-	1.23	0.011	0.0057	0.82

Table 2.4: ETAS parameters determined for each case by comparing the true parameters with the inverted ones using both the constant background rate ETAS model and the time-dependent background rate model.

2.6 Spatial biases corrections

In the application of the ETAS model accurate earthquake location holds critical significance for various aspects of spatio-temporal analysis. The ETAS model, commonly used for describing seismic clustering, particularly aftershocks, relies on precise location information. Location errors can influence cluster identification, potentially leading to mischaracterization of clustering patterns. Moreover, these errors can introduce biases in estimating key parameters such as mainshock pro-

ductivity, aftershock triggering behavior, and background seismicity rates. Accurate locations are essential for capturing spatial variations in seismicity rates, and errors in location data may result in an incorrect assessment of the spatial distribution of earthquake activity. Additionally, location errors can violate model assumptions regarding stationarity and isotropy, impacting the testing and calibration of the ETAS model. Aditionnaly, two other source of biases must be took into concideration.

The first bias is to neglect the anisotropic distribution of aftershocks (chapter 1, section 1.5), which can lead to an underestimation of the productivity factor α (Grimm et al., 2021). The isotropic model is adequate for small rupture extensions (moderate earthquakes) but becomes problematic for larger events in which the aftershocks will be distributed along a longer fault plane (Figure 2.16)."

The second bias is linked to the infinit spatial extent of the spatial density of earthquakes. According to the conventional definition of an infinite spatial kernel, aftershock triggering tends to be biased towards the numerous smaller events. These smaller events possess greater flexibility in mimicking anisotropic event alignments compared to the fewer, more powerful mainshocks. Consequently, this bias can result in unrealistically distant trigger impacts for smaller magnitudes and a significant underestimation of the direct aftershock productivity stemming from strong events. This, in turn, leads to a smoothing effect on temporal event distributions (Grimm et al., 2021).

To address this issue, one idea is to integrate an anisotropic function for the aftershock distribution into the spatio-temporal ETAS model (refer to chapter 1, section 1.4, in Equation 1.28), and confine the distribution of events only to the rupture length by incorporating a distance threshold dependent on the magnitude of the event. Figure 2.16 represents a simulation for both isotropic and anisotropic kernel distributions, restricted to the rupture length.

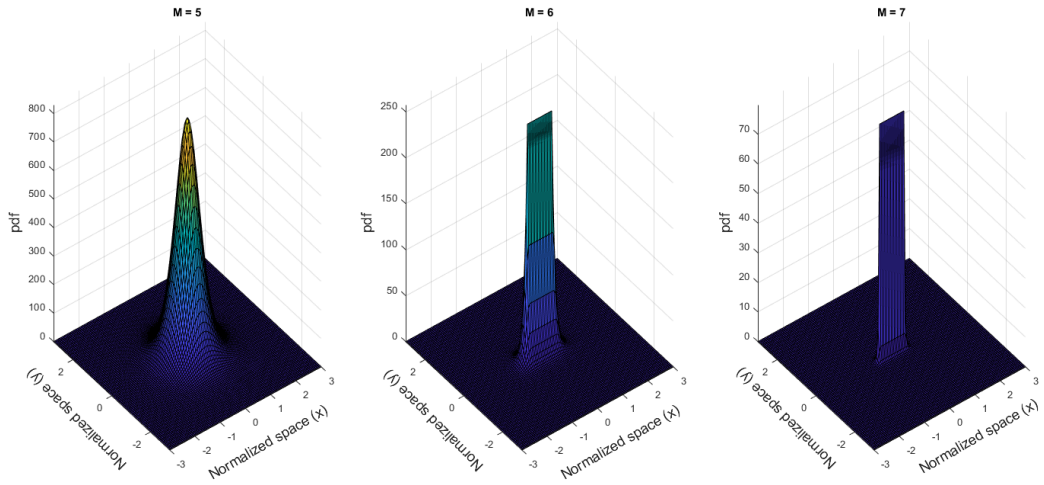

Figure 2.16: Visualization of the spatial kernels restricted, with an isotropic distribution for a shock of magnitude 5, and anisotropic for shocks of magnitude 6 and 7.

2.7 Conclusion

This chapter emphasizes the significance of carefully understanding the data, as numerous biases can be introduced to the earthquake catalog. Neglecting these biases may lead to false results and, consequently, a misinterpretation of the underlying physical processes. Firstly, the choice of the declustering technique is crucial to avoid biases in the $b - value$. Than, a meticulous estimation of m_c is essential. It is imperative to comprehend the advantages and disadvantages of each technique available. Additionally, studying the temporal variation of m_c is crucial, as temporal fluctuations can introduce biases to statistical parameters, even over short periods. For instance, STAI, to which the ETAS model is highly sensitive, can be addressed by either considering the largest m_c or incorporating parameters in the model that account for these changes, such as rate-dependent m_c or long-term methods for incompleteness. Another critical consideration is the influence of aseismic transient forces, such as fluids, which cannot be avoided. Neglecting these forces may result in biases in the estimation of ETAS parameters. Therefore, a non-stationary ETAS model is preferable, as it can capture both a constant background rate and a variable one. This flexibility is a powerful tool for understanding changes in seismic activity. Finally, before applying any statistical model, the spatial parameters of earthquakes (longitude, latitude, and depth) must be

well-constrained. A comprehensive understanding of the spatial distribution of events is necessary to choose an appropriate model between anisotropic and isotropic models and to restrict the spatial extent of aftershocks. By addressing these considerations, you can initiate the analysis of the catalog and gain insights into the underlying physical processes.

Chapter 3

Detection and Characterization of Earthquake Swarms in the Northeastern Part of Algeria

3.1 Introduction

In the realm of seismic phenomena in the Northeastern part of Algeria, two distinct types of seismic sequences emerge, rooted in the temporal and spatial attributes of events (Utsu, 2002). Firstly, (foreshocks-) mainshock-aftershocks activity is characterized by a major event of a defined magnitude followed by a decrease in subsequent event magnitudes over time (Figure 3.1a, b). Secondly, Swarm-type activity is defined by irregularities in temporality, lacking a mainshock or involving a succession of several mainshocks (Figure 3.1c, d).

Various physical mechanisms, including creeping, slow slip events, magmatic intrusion, and fluid migration, often contribute to earthquake swarms (Hill, 1977; Vidale and Shearer, 2006; Lohman and McGuire, 2007; Bourouis and Cornet, 2009, Hainzl and Ogata, 2005, Pacchiani and Lyon-Caen, 2010; Yoshida, 2019; Mesimeri et al., 2023). Regions with elevated heat flow and reduced viscosity are suggested to be more prone to producing swarms rather than mainshock-aftershock sequences (Ben-Zion and Lyakhovsky, 2006; Yang and Ben-Zion, 2009). Additionally,

earthquake-earthquake interactions, such as static stress transfer, can influence the temporal evolution and spatial migration observed in complex seismic sequences (Mesimeri et al., 2023).

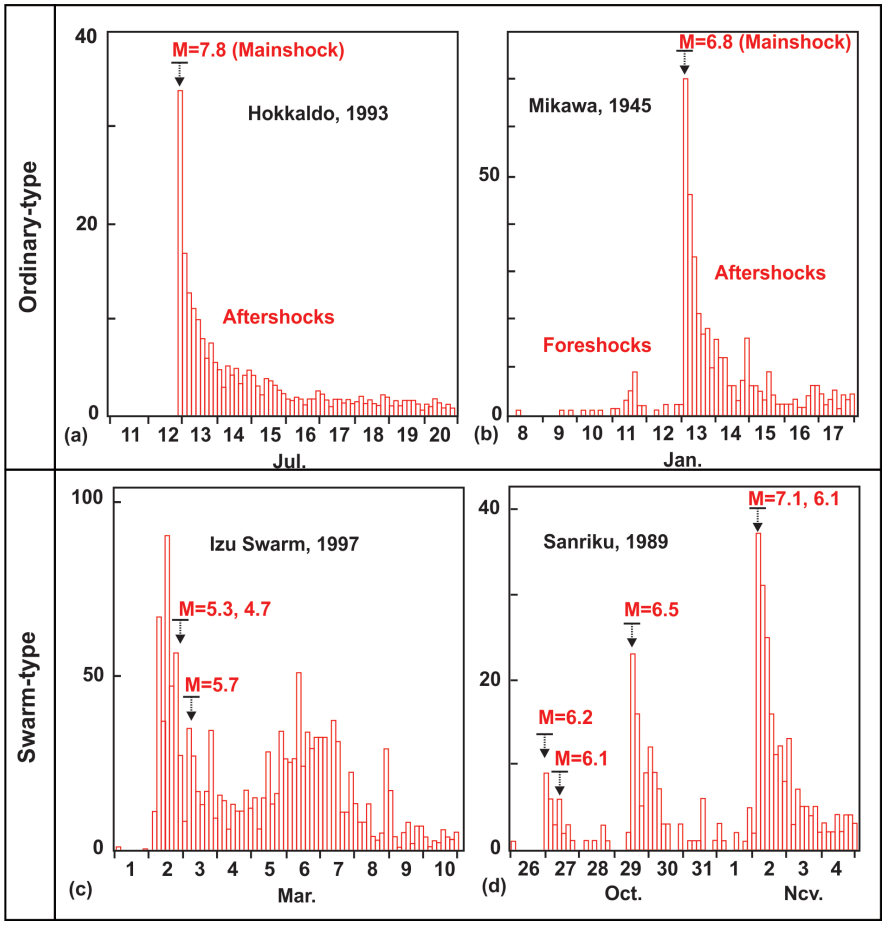

Figure 3.1: Example of seismic sequences with the temporal variation of the number of earthquakes. (a) Mainshock-aftershocks sequence; (b) Foreshocks-mainshock-afterchocks sequence; (c) Swarm-type sequence with no clear mainshock; (d) Succession of mainshock-aftershocks sequences (modified from Utsu et al., 1995). Ordinary-type sequences encompasse (a) and (b), while swarm-type include (c) and (d).

Seismic activity in Northern Algeria stands as a crucial subject of investigation, given its profound impact on the socio-economic development of the country. This seismicity is a consequence of the geographical position of Algeria at the boundary between the African and Eurasian plates within the Western Mediterranean region. The NW-SE convergence of these plates is linked to the counterclockwise rotation of Africa relative to Eurasia, with a pivotal Euler pole (EP) situated off the coast of Morocco, because of oceanic expansion at the Atlantic Ridge, occurring at a rate of 25 mm/year in the North and 40 mm/year in the south (Demets et al., 1994; Nocquet) (Figure 3.2a).

This convergence has led to the creation of relief features, including the mountain ranges found in the Tellian Atlas System (e.g., Hodna, Bibans, and Babors). Seismic activity is predominantly concentrated along the Algerian margin, including the Tellian Atlas in the North (Figure 3.2b), which is generally related to Neogene basins such as the Mitidja, and Mila-Constantine basins (MB, and M-CB in Figure 3.2c) (Abacha, 2015). Conversely, areas further south, such as the High Plateaus or the Saharan Atlas, experience comparatively less impact from current active deformation (Figure 3.2b).

A notable characteristic of Algerian seismicity is its pronounced concentration in the eastern part of the country, where nearly two-thirds of seismic events have occurred to date (Abacha, 2015; Yelles-Chaouche et al., 2022), (Figure 3.2b). In this region, a distributed deformation pattern is observed, primarily marked by low to moderate-magnitude seismic sequences associated with various strike-slip faulting mechanisms. These include NE–SW left-lateral, NW–SE right-lateral, and WNW–ESE right-lateral faults, with the M'cid Aïcha-Debbagh Fault (MADF) standing out as the most significant (Abacha and Yelles-Chaouche, 2019; Bendjama et al., 2021; Boulahia et al., 2021; Abacha et al., 2023b) (Figure 3.2c). To a lesser degree, there are also instances of E-W thrust faults, particularly observed in the offshore region (Yelles-Chaouche et al., 2021; 2023). A distinctive feature of these seismic sequences is their tendency to manifest with two or more mainshocks, comparable to exemples from Figure 3.1c, and d, coupled with a considerable number of seismic events, often exhibiting spatio-temporal migration (Khelif et al., 2018; Yelles-Chaouche et al., 2019; Abacha and Yelles-Chaouche, 2019; Bendjama et al., 2021; Boulahia et al., 2021; Boulahia, 2022; Abacha et al., 2022, 2023a). In contrast, western Algeria displays a more uniform and homogeneous deformation pattern compared to its eastern counterpart. Seismicity in this region predominantly occurs along a 200 to 300 km wide band, characterized by active thrust faulting, indicative of concentrated deformation within a compressive stress regime. Notably, this area is susceptible to high-magnitude earthquakes typically of the mainshock-aftershock type, exemplified by the 1980 El Asnam earthquake with a magnitude of 7.3 (Ouyed et al., 1981). This clarifies why we have focused our attention on the Northeastern region of Algeria.

Major progress has been made in seismic monitoring in Algeria since 2000, with the first reinstallation of the former seismic monitoring network (Réseau Algérien de Surveillance et d'Alerte

Sismique: REALSAS), partially destroyed in the 1990s, and the second in 2007, with the deployment of the more modern Algerian Digital Seismic Network (ADSN; Yelles-Chaouche et al., 2022), (Figure 3.2c). The latter allows a more realistic view of Algerian seismicity through the acquisition of a large amount of seismic data and also by the possibility of studying the more recent moderate events. Hence, our focus in this study is primarily on a 2007-2020 catalog.

This chapter focuses on seismic swarm detection from the 2007-2020 catalog, utilizing two methodologies - the spatio-temporal Epidemic-Type Aftershock Sequence (ETAS) model and skewness and kurtosis of the moment release time series analysis. The comprehensive examination contributes to seismic hazard assessment, providing insights into the dynamic behavior of seismic events. This research enhances our understanding of seismic risks, contributing to refining hazard models and formulating effective preparedness measures (Nishikawa and Ide, 2017; Mesimeri et al., 2019; Jacobs et al., 2013; Yelles-Chaouche et al., 2022).

3.2 Methodology description

The study utilized data from the Algerian Digital Seismic Network (ADSN) covering the Northeastern part of Algeria, spanning from 2007 to 2020. The decision to exclude data preceding 2007 was made due to the establishment of the permanent network by ADSN in that year, ensuring consistency. Including earlier data could introduce bias into the estimation of m_c (refer to chapter 2, section 2.4). The region was partitioned into grids measuring 0.2°x 0.2°, and for each grid cell, m_c was calculated. The highest value among these, 2.8, was selected to minimize biases in estimating statistical parameters. The study considered a total of 2354 events for analysis (Figure 3.2d).

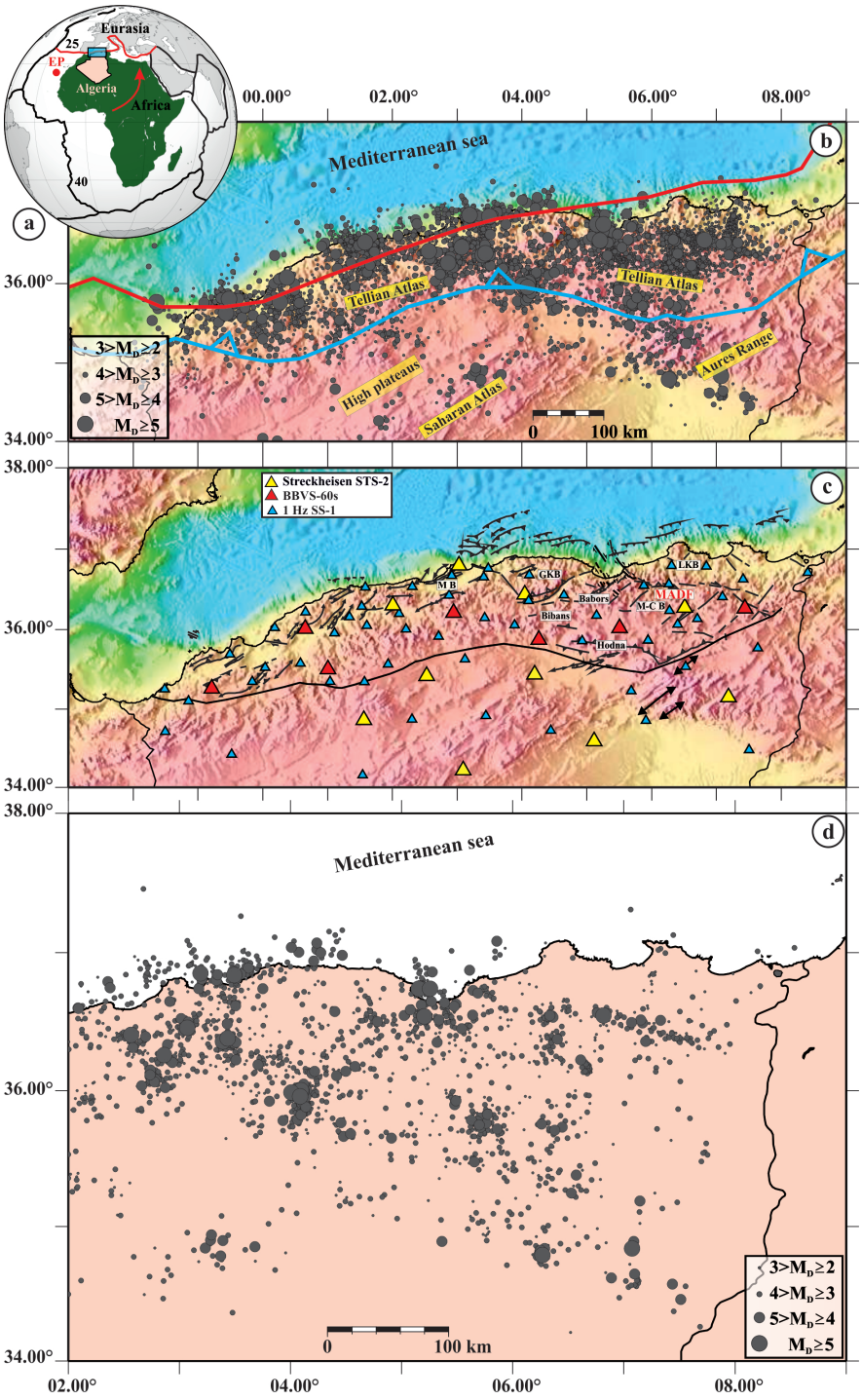

Figure 3.2: (a) Algeria's location in Africa, illustrating its border with the Eurasian Plate and the African Plate. The numbers represent the velocity expansion in mm/year. The studied area is highlighted by a blue box. (b) Spatial distribution of the Algerian earthquake catalog. The main Algerian geological units are named on a yellow background. The red line represents the Eurasia–Africa Plate boundary (simplified from Bird, 2003), and the blue line represents the deformation front of Tell. (c) Spatial distribution of the Algerian Digital Seismic Network (ADSN). The main tectonic structures are also represented by solid black lines. The main Tellian Atlas mountain ranges are named on a white background. (d) Spatial distribution of earthquakes above the magnitude of completeness.

Two methods were used to detect seismic swarms. In the first one, we calculated the spatio-temporal ETAS model parameters (refer to chapter 1, section 1.5) using a bootstrap approach to quantify the uncertainties. Than from each cell grid, we determine the transformed time according to:

$$\Lambda(t) = \int_{T_{start}}^{T_{end}} \iint_{S} \lambda(t_i, x_i, y_i), \tag{3.1}$$

where $\lambda(t_i, x_i, y_i)$ represents the spatio-temporal ETAS function (see chapter 1, section 1.4). from this we convert the occurence time (t_i) in a region S into transformed time $\tau(t) \equiv \Lambda(t)$ (refer to chapter 1, section 1.4). Nishikawa and Ide, 2017 introduced the '1σ criterion' suggesting that swarm sequences should follow the condition $\tau_{i+1} - \tau_i + \sigma < 1$ for five concecutive events. Here, $\tau_{i+1} - \tau_i$ represent the number of event expected between two succecive events, and σ is the standard deviation which is equal to $\sqrt{\tau_{i+1} - \tau_i}$. We rearranged this formulation for 5 succecive events and we have:

$$\tau_{i+1} - \tau_i < (\frac{\sqrt{5} - 1}{2})^2 \approx 0.382. \tag{3.2}$$

We applied this condition to each grid cell to determine the events that have swarm tendency. Figure 3.3 depicts two exemples of transformed time within a grid cell: one where no swarm is detected (Figure 3.3a), and another where a swarm is identified (Figure 3.3b).

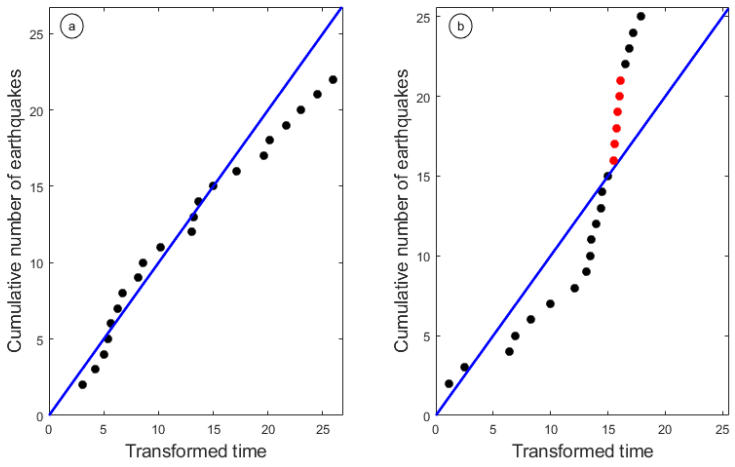

Figure 3.3: (a) Transformed time computed for seismicity without any swarm, and a line with a slope of unity is also depicted. (b) Transformed time calculated for seismicity containing swarm (red circles), and a line with a slope of unity is also included in the plot.

Once these events were identified, we organized them into clusters and implemented additional criteria to prevent false positive clusters. The initial criterion entails choosing clusters where the magnitude difference (Δm) between the largest event and the second-largest event is less than one unit. This criterion aligns with Bath's Law, which suggests that this difference is usually greater than or equal to one unit in a typical earthquake sequence. The second criterion involves considering only clusters where the first event has a background probability exceeding 0.5, thereby excluding abnormal high-rate earthquake sequences (Nishikawa and Ide, 2017).

The second method employed adopts a different approach by utilizing the seismic moment release. Previous research has indicated that mainshock-aftershock sequences often exhibit a pronounced surge in seismic moment release at the onset of the sequence. In contrast, earthquake swarms typically demonstrate a more uniformly distributed moment release over time. Quantifying the weighted skewness (S) of the moment release time series distribution has proven to be a valuable metric in distinguishing between mainshock-aftershock sequences and swarm-like sequences, as demonstrated in prior studies (Roland and McGuire, 2009; Chen and Shearer, 2011; Mesimeri et al., 2016; Zhang et al., 2016;Passarelli et al., 2018).

$$S = \frac{\sum_1^N (t_i - \bar{t})^3 m_0(i)}{\sigma^3}, \tag{3.3}$$

where t_i represents the occurrence time since the beginning of the sequence, $\bar{t}$ is the weighted mean time, $m_0(i)$ denotes the moment release for the i^{th} earthquake, and σ^3 is the cubed standard deviation. According to their findings, mainshock-aftershock sequences should exhibit a positive skewness (skewed to the left), while swarm sequences should have small positive to zero values of skewness. Building upon this method, Mesimeri et al., 2019 recommended calculating the kurtosis (K) of the moment release history for each earthquake sequence.

$$K = \frac{\sum_1^N (t_i - \bar{t})^4 m_0(i)}{\sigma^4}. \tag{3.4}$$

High values of K indicate a heavy-tailed distribution, similar to mainshock-aftershock sequences (Figure 3.4a), whereas earthquake swarms tend to exhibit more of a normal distribution (Figure 3.4b).

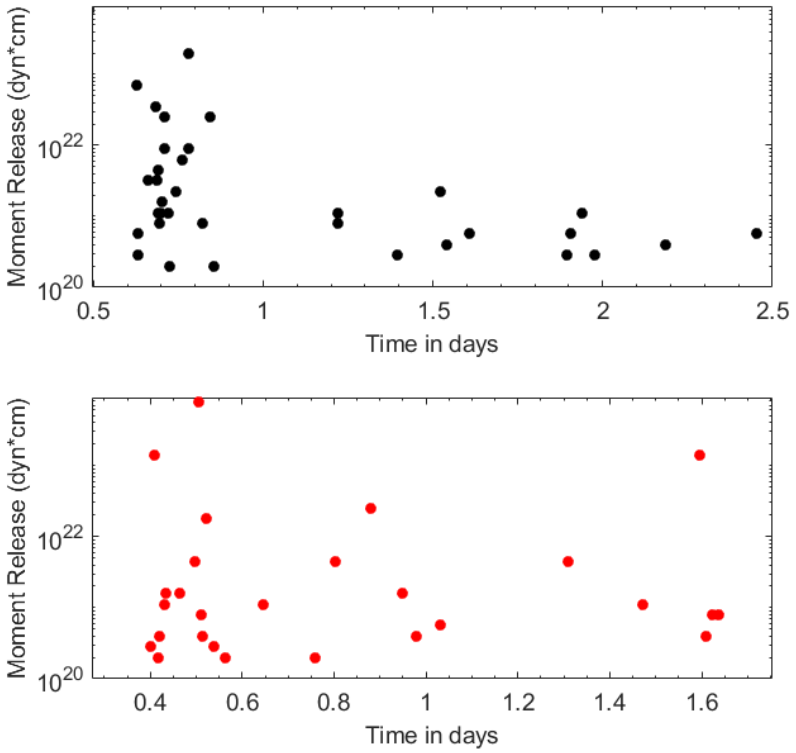

Figure 3.4: Temporal distribution of seismic moment release for a Mainshock-Aftershock sequence (depicted by black circles) and a swarm sequence (depicted by red circles).

When plotting K against S, a parabolic relationship between the two parameters becomes apparent (Cristelli, 2014; Sattin et al., 2009). Before calculating these parameters, we initially utilized CURATE (Jacobs et al., 2013) to extract clusters, which were subsequently employed to compute S and K for each cluster. These values were then used to categorize sequences into swarm-like sequences and mainshock-aftershock sequences. Following this categorization, we fitted the parabolic relationship between the two parameters.

3.3 Detected swarms

The model parameters fitted using the bootstrap approach for the ETAS model are as follows: $k = 0.37 \pm 0.03$ events, $c = 0.03 \pm 0.04$ days, $\alpha = 1.42 \pm 0.0095$, $p = 1.07 \pm 0.003$,$D = 0.000090 \pm 0.04\ deg^2$, $q = 1.61 \pm 0.006$, and $\gamma = 0.25 \pm 0.14$ (Figure 3.5). It's important to note that these

parameter values represent the mean triggering effect for the entire region. Therefore, earthquake sequences with higher productivity may be interpreted as swarms. However, the Δm criterion is designed to exclude such sequences from our analysis. 72% of the entire dataset is interpreted as background events, with parameters A and α indicating that an earthquake of magnitude 5 can trigger 8.41 aftershocks.

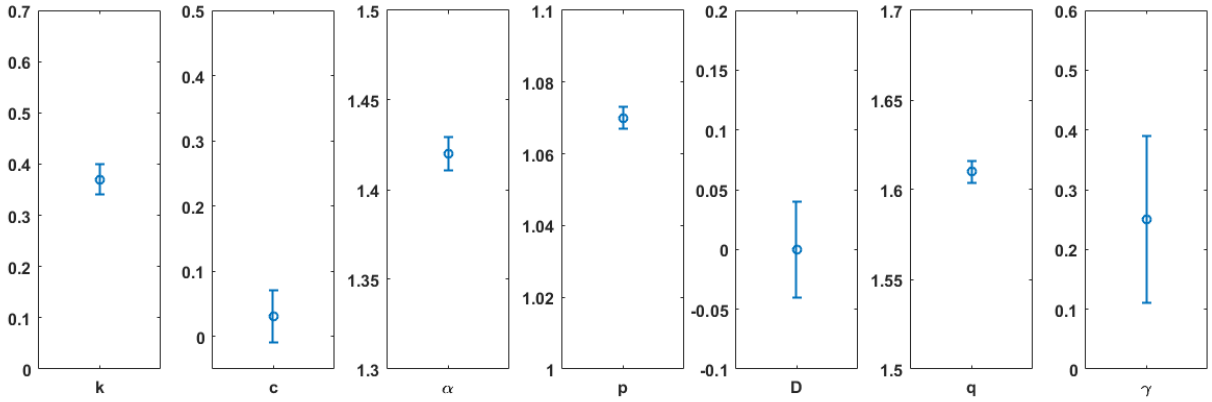

Figure 3.5: Error bars for the ETAS parameters computed using the bootstrap approach.

In total, 37 clusters were identified, comprising 313 events, which represent approximately 13% of the overall seismicity. The minimum and maximum number of events for all clusters are 5 and 30, respectively, with durations ranging from 0.17 day to 68 days. Figure 3.6 illustrates an example of the swarm event detected in 2011.

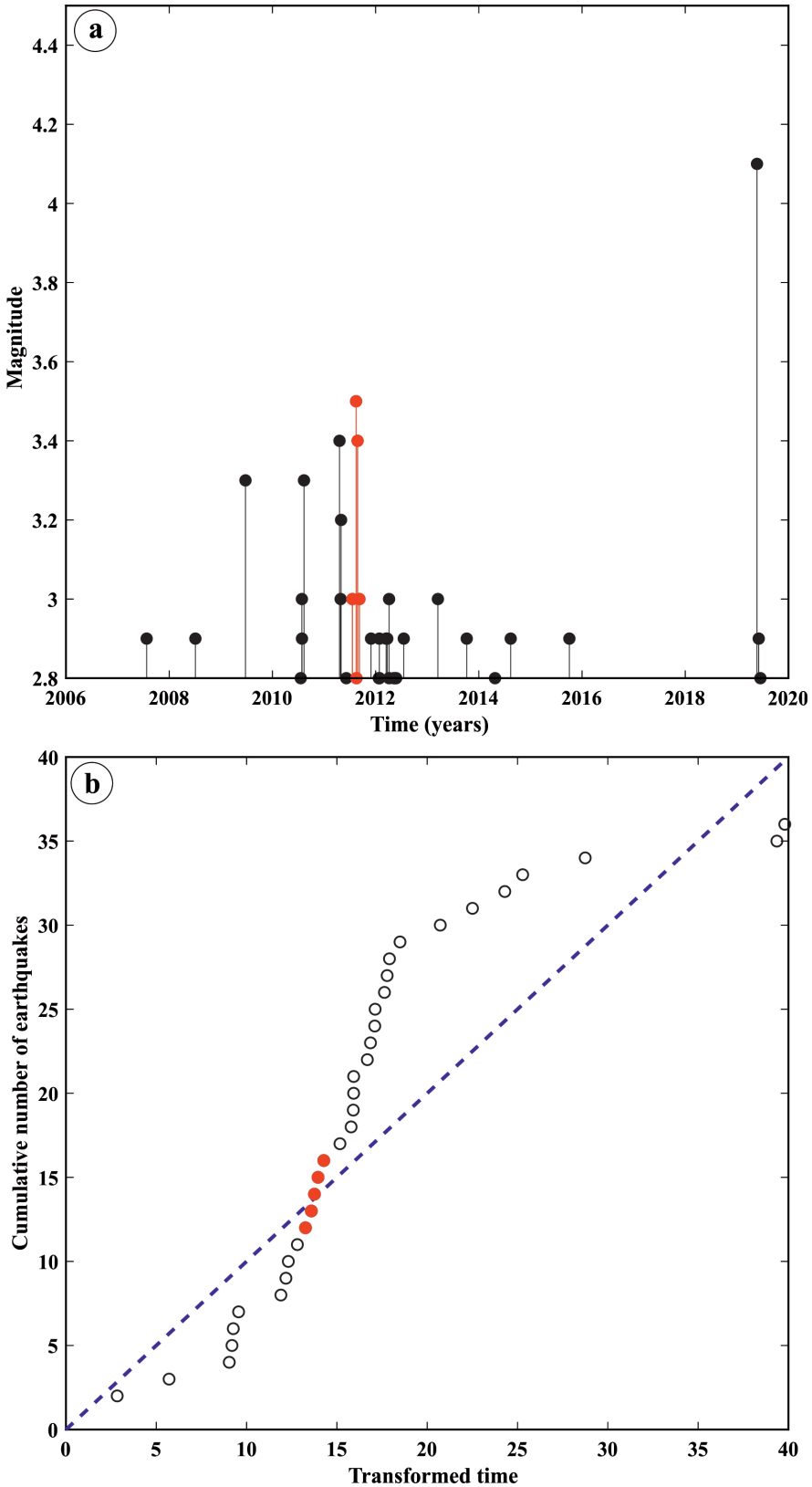

Figure 3.6: (a) Magnitude-time diagram depicting an earthquake swarm in 2011. Red circles highlight earthquake swarms identified through our analysis, while black circles represent non-swarm events. (b) Graph illustrating the transformed time calculation for seismic activity.

Conversely, the analysis of skewness and kurtosis, from the second method, yielded 32 clusters with 621 events, constituting 26% of the entire seismicity. Each cluster has a minimum of 5 events and a maximum of 191 events, with durations ranging from 1 day to 100 days. The parabolic fit between kurtosis and skewness (see Figure 3.7) produced the following results in the equation below:

$$K = 1.01S^2 + 1.41S + 2.01 \tag{3.5}$$

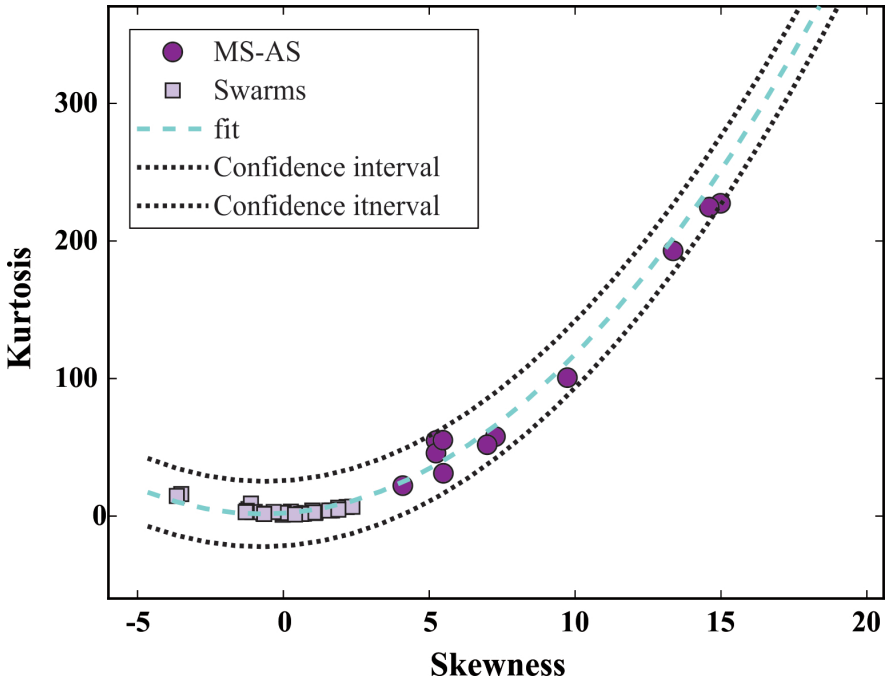

Figure 3.7: A parabolic relationship between skewness and kurtosis observed in the analyzed earthquake clusters.

The disparity in the numbers of swarm events and their durations arises from the distinct approaches of the two techniques. The first technique identifies swarm seismic events within each cluster, while the second method analyzes each cluster to determine if it exhibits swarm-like behavior. The spatial distribution of those clusters by both techniques is plotted on Figure 3.8a, and b, respectively. The combination of the two results led to 39 clusters. Some clusters, due to their proximity in both time and space, were merged into a single cluster. This consolidation process ultimately yielded a total of 32 final clusters (Figure 3.8c).

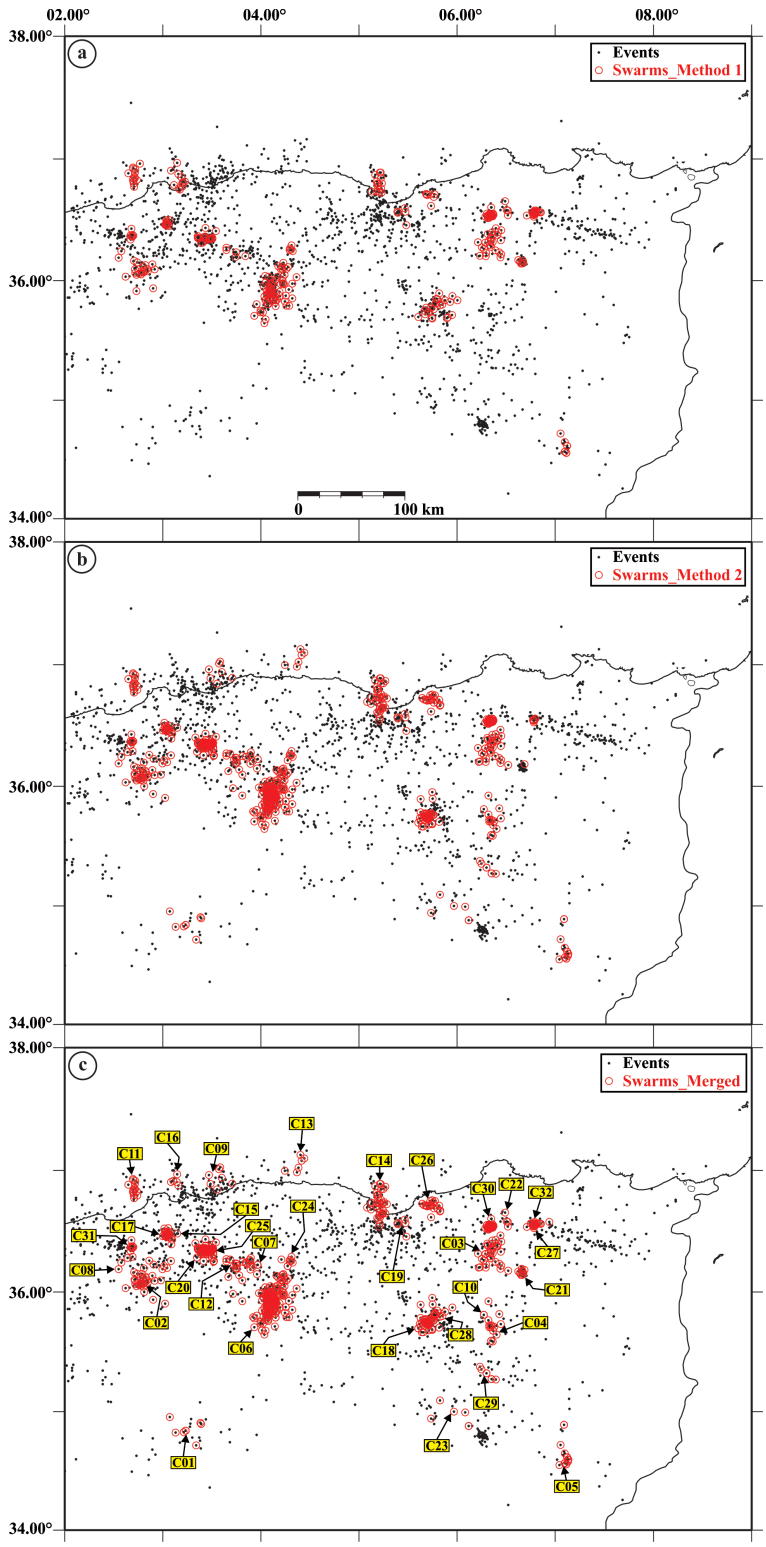

Figure 3.8: (a) Spatial distribution of earthquake swarms detected using the 1σ criterion. (b) Spatial distribution of earthquake swarms identified by analyzing the temporal distribution of seismic moment release. (c) Spatial distribution of earthquake swarms merged from the two methods. The distinct seismic swarms are labeled as C01-32.

Combining the results from both techniques, we integrated all the events to compile a comprehensive swarm catalog for the Northeastern part of Algeria. In total, 676 events were identified as swarms, constituting 29% of the entire seismicity in the region (Figure 3.9a). The magnitude against time of the detected swarm compared to the entire catalog, is also plotted in (Figure 3.9b)

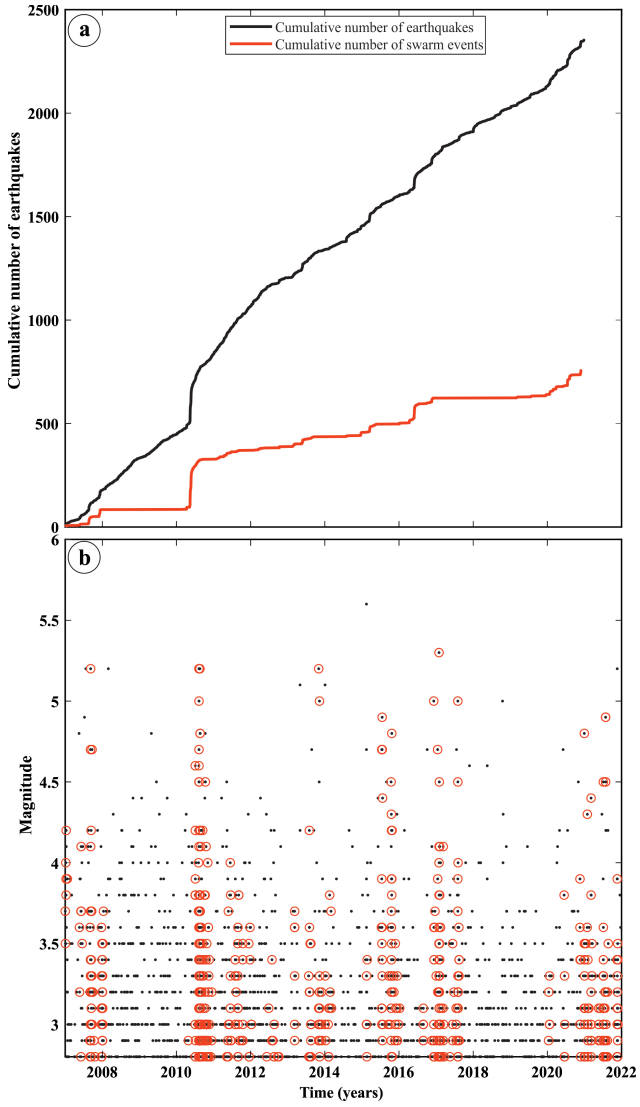

Figure 3.9: (a) Cumulative number of observed events (depicted by the black line) and cumulative number of swarm events (depicted by the red line). (b) Magnitude versus time chart, where black dots represent all earthquakes, and red circles specifically denote swarm events.

The number of events in each cluster ranges from 5 to 191, with a mean of 19.40 events and a standard deviation of 35.08 events (Figure 3.10c). The duration of each swarm ranges from 0.9 days to 118 days, with a mean of 25 days and a standard deviation of 29.21 days (Figure 3.10d).

The maximum magnitude ranges from 3.0 to 5.3, with a mean of 4.05 and a standard deviation of 0.68 (Figure 3.10b). The magnitude difference between the largest shock and the second-largest shock ranges from 0.1 to 0.7, with a mean of 0.26 and a standard deviation of 0.17. The low mean of the difference between the largest shock and the second-largest shock suggests that no clear mainshocks were detected in each swarm cluster, which is a typical feature of swarm sequences. The analysis of the G-R law parameters for all events in the seismic swarm catalog yielded a $b-value$ equal to 0.82±0.03 and an $a-value$ equal to 5.10±0.05 (Figure 3.10a). Interpreting the $b-value$ as a stress meter, the low value found suggests a region influenced by high stress. However, analyzing the entire region might not be meaningful, and consideration should be given to analyzing the $b-value$ for each zone. The small number of events in each zone introduces high uncertainties in the $b-value$ analysis, potentially leading to misleading interpretations.

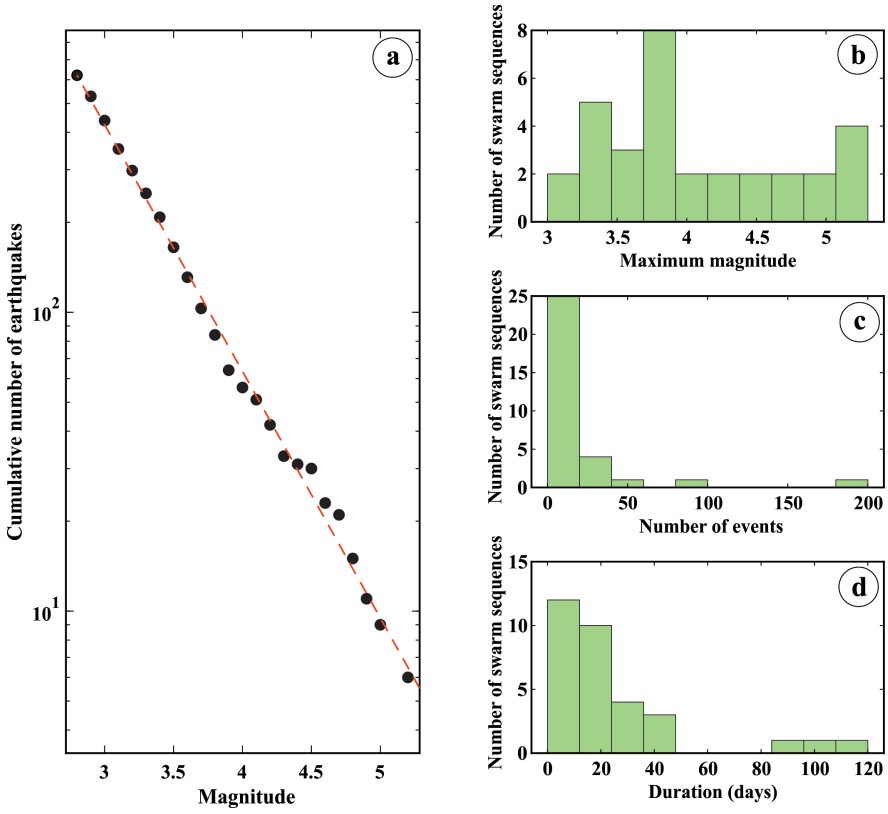

Figure 3.10: (a) Frequency-magnitude distribution of the swarm events. The dashed line refers to a Gutenberg-Richter relation with b = 0.87. (b) Histogram of the maximum magnitude. (c) Histogram of the number of events. (c) Histogram of the time duration.

3.4 Possible origin of earthquake swarms detected

Abacha, 2015 marked the initial endeavor to identify seismic swarms across the entire Northeastern region. This comprehensive study amalgamated geological, tectonic, and seismological data to delineate nine seismogenic zones. It delved into two significant seismic sequences: the first induced, occurring in Mila in 2007 (Semmane et al., 2012), and the second, unfolding in Beni-Ilmane in 2010, characterized by two triggering mechanisms: tectonic loading (Yelles-Chaouche et al., 2014) and fluid migration (Abacha et al., 2014). Furthermore, the research shed light on the phenomenon of typical swarms lacking clear mainshocks, often associated with factors such as reservoir water level fluctuations following heavy precipitation, as well as heightened interstitial pressure resulting from fluid injection or water circulation within hydrothermal systems. Building upon this foundation, employed three statistical approaches in an attempt to elucidate the nature of these swarms further.

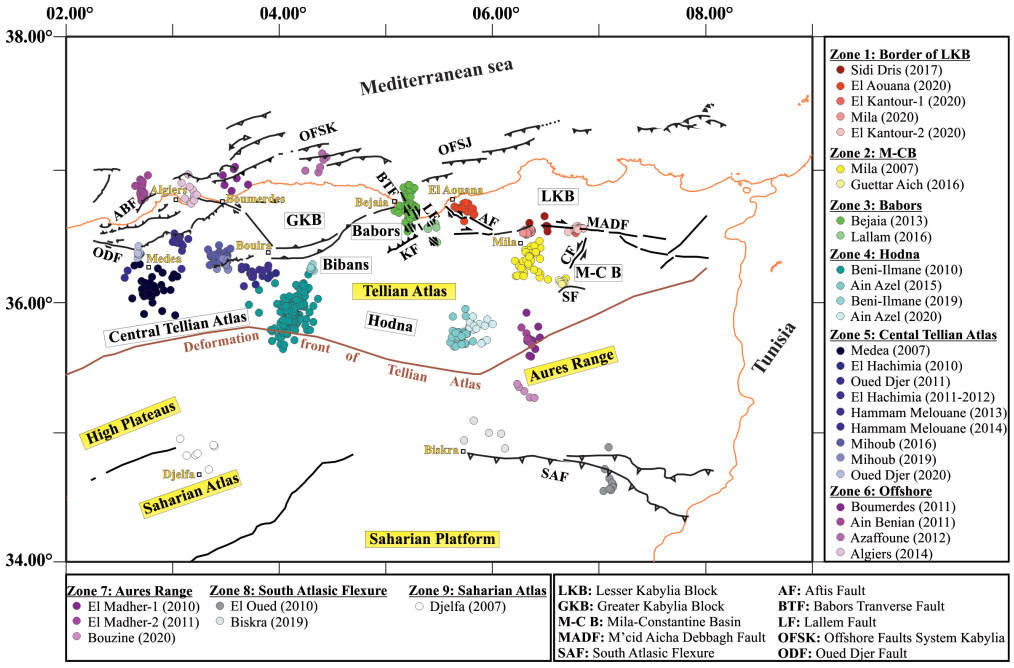

Figure 3.11: Spatial distribution of 32 swarm clusters color-coded based on the 9 identified zones, with a gradual scale corresponding to their occurrence time in each zone.

In Northeastern Algeria, our analysis revealed the presence of 32 swarms, some of which include sub-clusters, belonging to 13 sequences characterized by a succession of several mainshock patterns, alongside 19 distinct swarms lacking a clearly identifiable mainshock. To interpret the

results, we categorized the clusters into nine zones based on their geological and tectonic attributes (Figure 3.11).

3.4.1 Zone 1: Along the southern and western borders of the LKB

Seismic activity in this zone primarily clusters around the Lesser Kabylia Block (LKB), particularly along major tectonic faults such as the M'cid Aicha Debbagh Faults (MADF) to the south and the Aftis Fault (AF) to the west (see Figure 3.2b). Conversely, seismicity within the LKB seems to be less pronounced (refer to Figure 3.2b). Yelles-Chaouche et al., 2021 attribute this discrepancy to the block's inherent rigidity, attributed to its Paleozoic geological formations. In this first zone, five clusters were identified, starting with C22 (see Figure 3.8c), which corresponds to a portion of the seismic crisis recorded in the Sidi Dris region between March 4 and March 16, 2017 (Figure 3.11). A comprehensive study conducted by Bendjama et al., 2021 reveals an unusual spatial distribution, with events arranged linearly along two NNW-SSE parallel sinister faults, resembling two parallel channels (Figure 3.12). Such a configuration is often associated with seismicity induced by fluid injection (e.g., Calò et al., 2011). The Sidi Dris crisis warrants further investigation, particularly concerning a spatio-temporal analysis of the multiplets and repeaters very likely to exist, taking into account the short duration of the activity, which occurred during only two days, March 4 and 5. At this stage, we can categorize this seismic swarm as likely induced, possibly associated with fluid circulation.

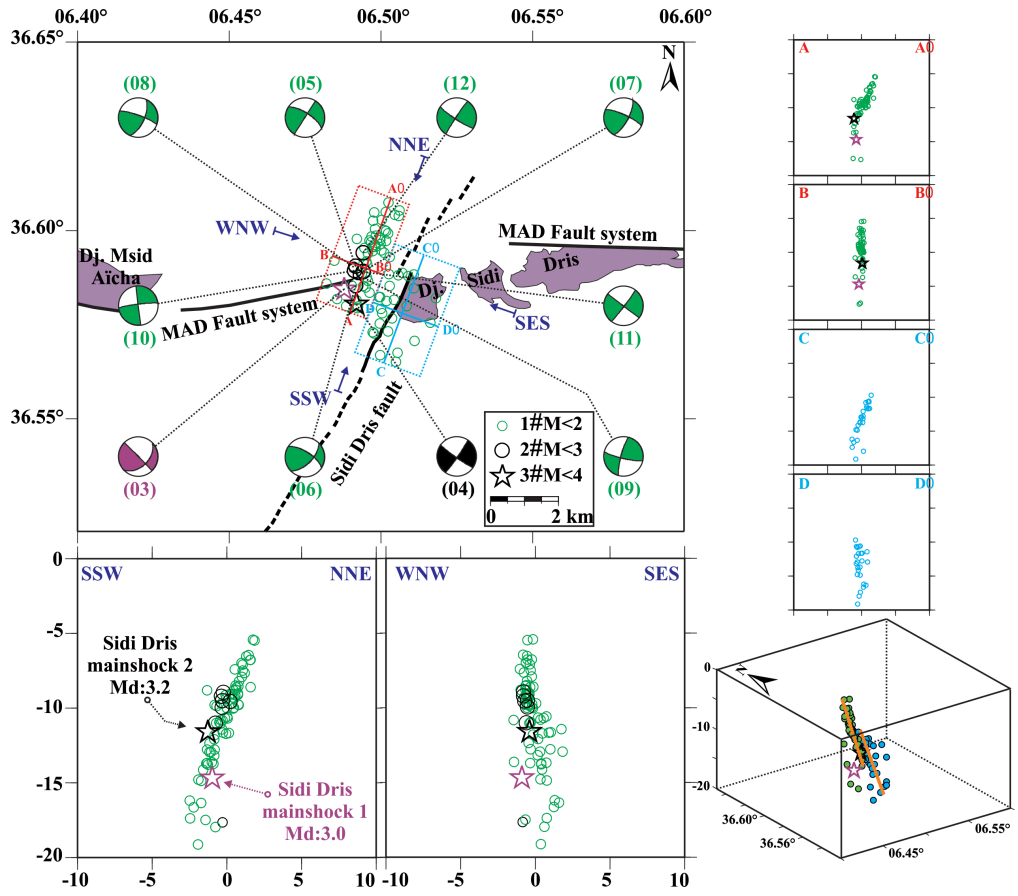

Figure 3.12: Map and cross sections of the Sidi Dris region highlighting the distribution of 83 well-located events and the focal mechanism solutions of several key events. The red rectangle (∼4 km long ∼1.5 km wide) surrounds the western seismicity cluster oriented N20°E, and the blue rectangle (∼3 km long and ∼4 km wide) surrounds the eastern cluster (Bendjama et al., 2021).

The second cluster, C26 (see Figure 3.8c), recorded in January-February 2020, encapsulates the seismic activity of the 2020 El Aouana sequence, characterized by two larger events with magnitudes of Mw 5.0 (LE-1) and Mw 4.4 (LE-2). This cluster was triggered by the NW-SE right-lateral strike-slip motion along the El Aouana fault, which is a segment of the Aftis fault (AF in Figure 3.11). Abacha et al., 2023b revealed a clear migration from the NW to the SE from the LE-1 towards the LE-2 then from the LE-2 to the SE end (Figure 3.13a). While the migration of seismicity typically serves as a reliable indicator of fluid involvement in the triggering process, the seismic tomography study conducted by Abacha et al. (under review at PEPI) reveals a low Vp/Vs value, suggesting the absence of fluid implication (Figure 3.13b). Consequently, the triggering mechanism for the El Aouana swarm remains ambiguous at this stage.

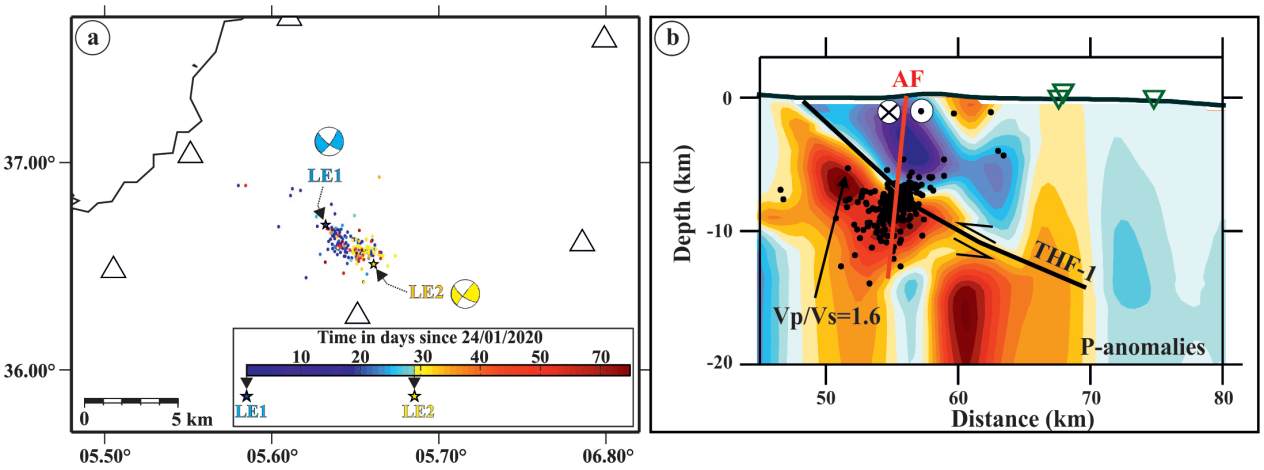

Figure 3.13: (a) Spatial distribution of El-Aouana sequence (Abacha et al., 2023b). (b) P-wave velocity 978 anomalies in the El Aouana region (Abacha et al. under review at EPEI).

In the El Kantour region, we identified two swarms, C27 and C32. The first occurred in January 2020 concurrently with the El Aouana sequence, while the second, the most significant, took place in November of the same year. It is worth mentioning that the area also experienced a Mw 4.7 earthquake on March 5, 2017, along with 25 aftershocks, coinciding with the Sidi Dris crisis (C22). The collective seismic activity observed in the El Kantour region provides insight into the static stress transfer between these events (Figure 3.14). In particular, the occurrence of the mainshock of the November sequence a few kilometers south of the main swarm (C32), indicates a likely stress transfer from the segment responsible for the Mw 5.3 mainshock to the segment generating the main swarm as documented in Bendjama, 2022. Such stress transfers are known to contribute to the occurrence of seismic swarms.

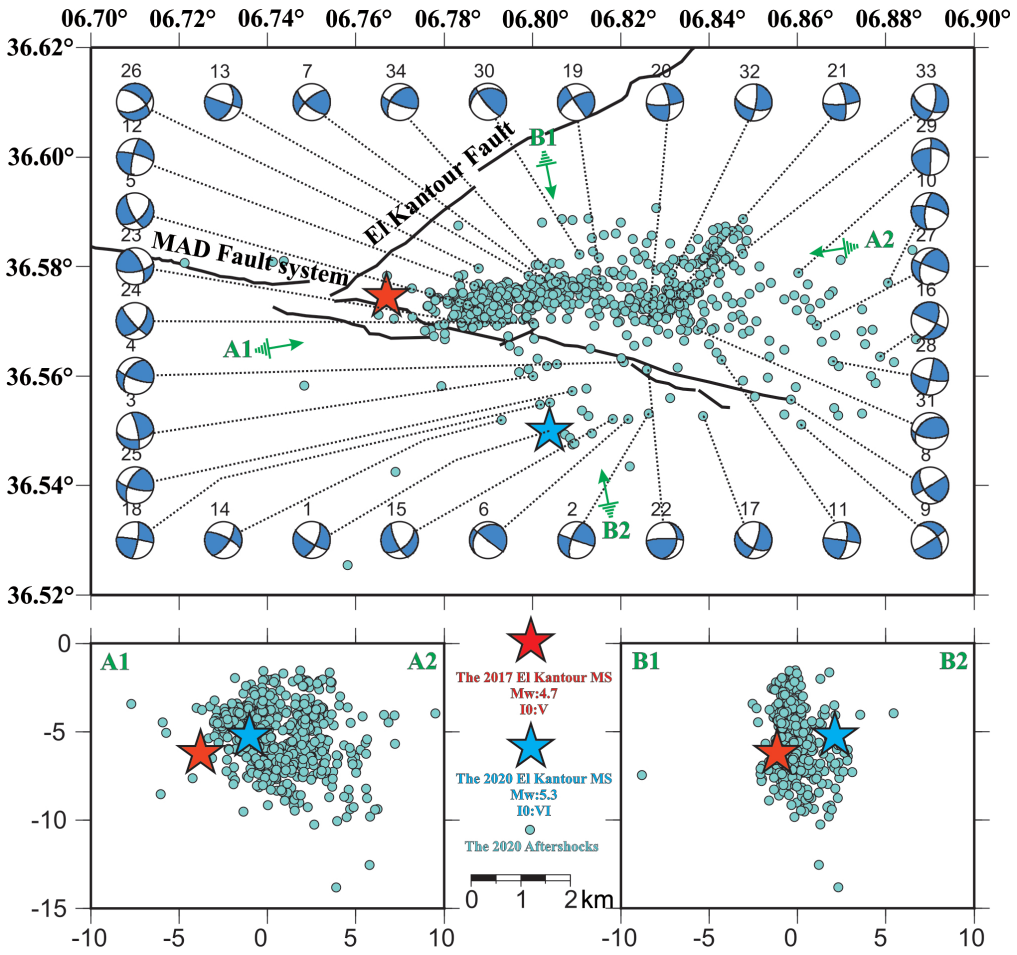

Figure 3.14: Distribution of aftershocks of the November 2020 El Kantour Earthquake sequence with the focal mechanisms of significant aftershocks: red star denotes the 2017 event (Mw 4.7), blue star represents the most recent event (Mw 5.3). A1-A2 is a deep-seated cross-section along the aftershock cloud E-W (swarm C32); B1-B2 is a perpendicular cross-section to the previous one. The black lines indicate the two significant faults in the MAD zone (E-W) and El Kantour (NE-SW) (Bendjama, 2022).

The latest seismic swarm (C30) occurred near the Beni-Haroun dam, situated at the western terminus of the MADF, positioned between the El Aouana and El Kantour sequences. This event corresponds to the Mila sequence observed in July-August 2020. The Mila sequence was characterized by a series of two mainshocks measuring Mw 4.8 and Mw 5.0, along with an E-W spatio-temporal migration pattern (Figure 3.15a, and b). Boulahia, 2022 confirmed that the sequence or C28 swarm was triggered by fluid infiltration and pore-pressure migration, supported by modeling the events using the equations proposed by Shapiro et al., 1997.

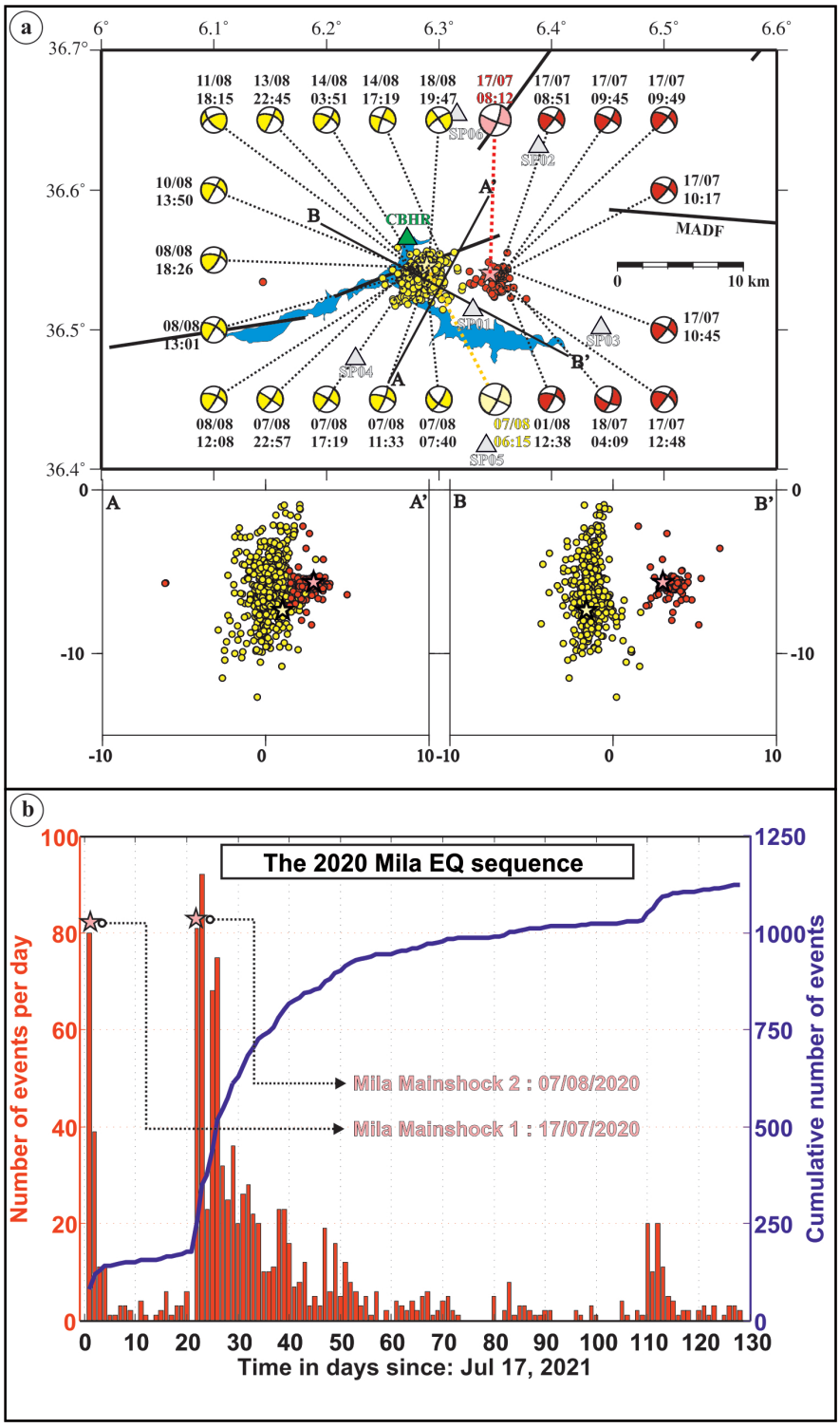

Figure 3.15: (a) Horizontal and vertical distributions of the 981 relocated events from the Mila seismic sequence spanning August to July 2020, also depicting some focal mechanisms. (b) Number of events per day (histograms) and the cumulative number of earthquakes (blue line) Boulahia, 2022.

The occurrence of four seismic swarms along the AF and MADF, which delineate LKB throughout 2020, likely suggests both static and dynamic stress transfers among these events. The static transfer primarily affected a localized area like the El Kantour region, while dynamic stresses were induced by seismic waves along the AF and MADF, as exemplified by the El Aouana and El Kantour swarms, which started on January 24, 2020, and January 29, 2020, respectively. Moreover, the presence of these seismic swarms along the extensive MADF, spanning over 80 km, suggests its division into small segments where seismic energy is dispersed. This mechanism potentially mitigates the risk of a single large, catastrophic earthquake. Nonetheless, we cannot dismiss the possibility of such an event if multiple segments were to rupture simultaneously.

3.4.2 Zone 2: Mila-Constantine basin

In contrast to other intramountain basins in the Tellian Atlas, the Mila-Constantine basin is situated at a higher altitude. Known for its predominantly low to moderate seismic activity (Abacha, 2015), this region has also experienced occasional strong earthquakes, such as the Constantine earthquake in 1985 with a magnitude of Ms 6.0 (Bounif et al., 1987). Within this context, two seismic swarms, C03 and C18, have been identified, corresponding to the Mila crisis of 2007 and the Guettar Aich crisis of 2016, respectively.

The Mila swarm (C03) is further characterized by two sub-clusters: one occurring in August 2007 and the other in November-December 2007. Semmane et al., 2012 attributed the November-December sub-cluster to induced seismicity resulting from water infiltration into the soil, facilitated by preexisting fractures, faults, and karsts, during water transfer between the Beni-Haroun dam and Oued Athemania reservoir. The study revealed that only 45% of the transferred water was recovered at the Oued Athmania reservoir, with a significant portion of slightly pressurized water leaking through defective joints in a tunnel passing through the Akhal mountain (Figure 3.16a). Additionally, the authors found a strong correlation between the number of events and the pumping rate (Figure 3.16b). Subsequent statistical analyses conducted by Abacha, 2015 and Abacha et al., 2022 supported this conclusion. On the other hand, previous studies have linked the August sub-cluster with a water pumping test (Figure 3.16c).

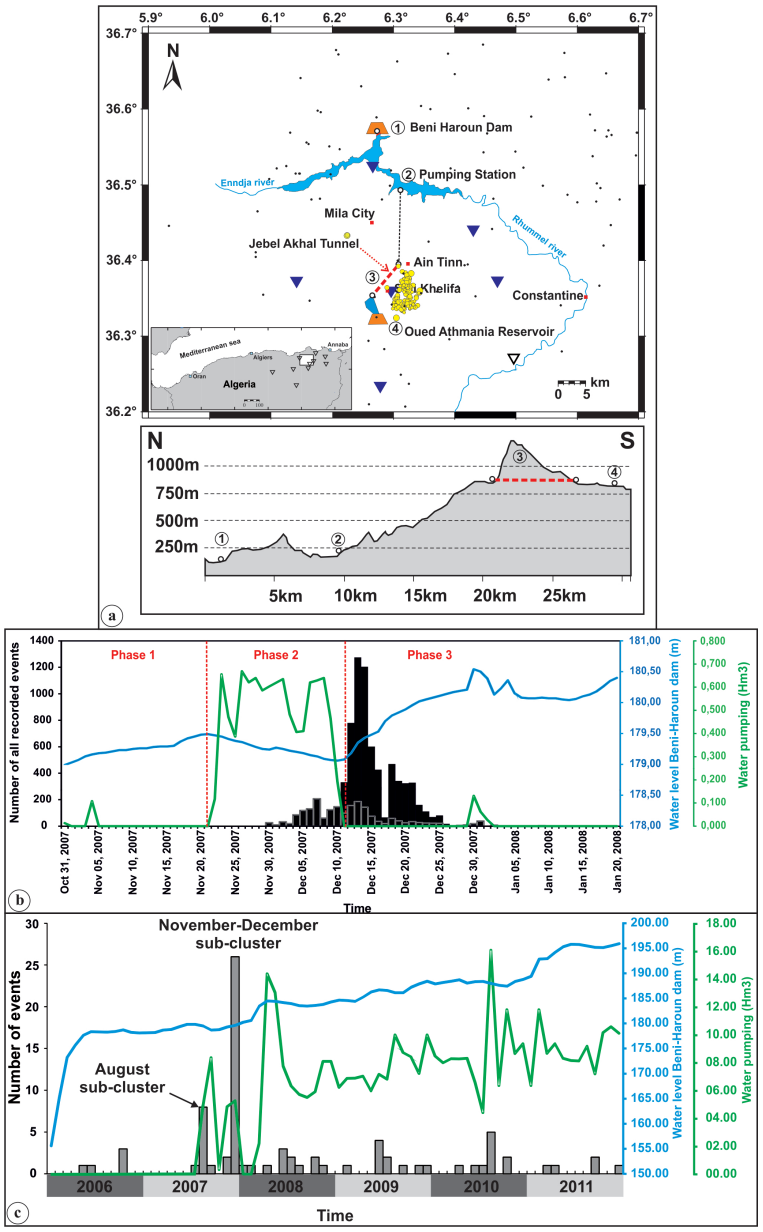

Figure 3.16: (a) Study area featuring the Beni Harroun dam and the swarm cluster location: The top section shows the water conveyance system (dashed lines), the tunnel through Jebel Akhal (red dashed line), seismic events over a two-year period (2006–2007) (Black dots), the locations of the temporary seismic network (reverse triangles), and the earthquake swarm detected (yellow circles). The bottom section provides a North-South topographic profile of the water conveyance system. (b) Daily recorded seismic events are plotted alongside the Beni Harroun (BH) filling rate (blue line) and the volume of water pumped (green line). (c) Context of long-term seismic activity. (modified from Semmane et al., 2012).

The Guettar Aich swarm (C21 in Figure 3.8c) was situated North of the E-W reverse Sigus fault (SF in Figure 3.11) and SW of the NE-SW left-lateral strike-slip Constantine fault (CF in

Figure 3.11), which was responsible for the 1985 Constantine earthquake. Both faults could potentially serve as the source of C21. However, the triggering mechanism remains uncertain. It could be attributed to a creeping phenomenon associated with the SF, especially if we know that microseismicity occurs almost constantly in the region, even observable in catalog records preceding 2007, or another underlying cause.

3.4.3 Zone 3: Bejaia-Babors

Numerous researchers (Harbi et al., 1999; Yelles-Chaouche et al., 2006; Beldjoudi et al., 2009) previously attributed the primary source of seismic activity in the Bejaia-Babors zone to the Kherrata reverse fault (KF). However, two recent studies by Boulahia et al., 2021 and Abacha et al., 2023b have revealed the existence of a newly discovered NW-SE dextral Bejaia-Babors shear zone (BBSZ), which has been identified as the main contributor to recent seismic activity in the region. The BBSZ is delineated from the east by the AF and from the west by the Babors Tranverse Fault (BTF), a right-lateral strike-slip fault divided into four segments (Figure 3.11). The identification of the BTF was made through analysis of the event distribution during the 2012-2013 Bejaia-Babors earthquake sequences, comprising four mainshocks and their corresponding aftershocks on 28 November 2012, 22 February, 19 May, and 26 May 2013, respectively (Boulahia et al., 2021) (Figure 3.17a, b, and c). This sequence is represented here by the C14 swarm, which is subdivided into three sub-clusters corresponding to the second, third, and fourth clusters identified in Boulahia's study. Additionally, Boulahia's study demonstrated a clear migration of seismicity from the NW to the SE (Figure 3.17d), indicating potential fluid involvement through the seismicity modeling by Shapero equation (Figure 3.17e). The recent study by Abacha et al. (under review at EPEI) has further revealed the presence of a fluid reservoir near the third segment of the BTF, characterized by a high Vp/Vs ratio (Figure 3.17f). Therefore, it is inferred that the C14 swarm was generated by fluid circulation. In addition to the influence of fluids, Boulahia et al., 2021 demonstrated the interaction between the four segments of BTF in terms of Coulomb stress transfer (Figure 3.17a, b, and c).

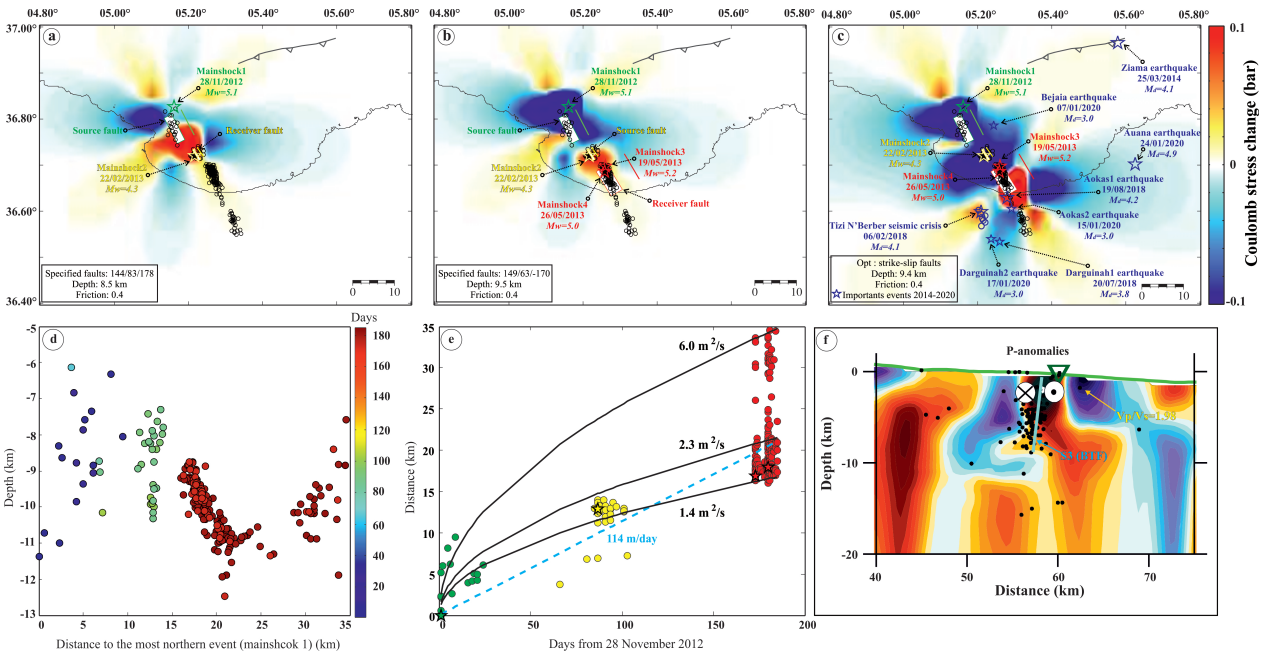

Figure 3.17: (a) Coulomb stress change caused by a the 2012 Bejaia earthquake (Event 1) in terms of triggering the February 2013 event (Event 2), (b) Events 1 and 2 in terms of triggering the 19 May 2013 sequence (Events 3 and 4), and (c) the cumulative effect of Events 1–4 on optimally oriented fault planes. The white rectangles represent the surface faults. (d) The map shows a migration pattern. Earthquakes that belong to different clusters are denoted with different colors. (e) Hypocentral separation of events with time since the first event for the entire sequence. Thick black curves show diffusion rates of 1.4 m^2/s, 2.3 m^2/s, and 6 m^2/s, respectively. The dashed blue line is a constant migration velocity of 144 m/day. Colored circles are earthquakes in identified clusters: C1 (green), C2 (yellow), and C3–C4 (red) (Boulahia et al., 2021). (f) P-wave velocity anomalies 988 in the region (Abacha et al. under review at EPEI).

Many other segments have been identified within the BBSZ, including the NW-SE right-lateral strike-slip Lallam fault (LF in Figure 3.11), responsible for the 2006 Lallam earthquake with a magnitude of Mw 5.2 (Beldjoudi et al., 2009). From Figure 3.11, it is evident that a small cluster (C19) was recorded in 2016, precisely situated on LF, likely indicating its source. However, the specific triggering process remains unknown.

3.4.4 Zone 4: Hodna range

The Hodna Massif stands as a prominent geological feature in the southern sector of the Tellian Atlas, extending in a WNW–ESE orientation from the Bibans range to the Aures massif. Over the past decade, the Hodna zone has experienced four seismic swarms, alternating between two

primary areas: (1) the Beni-Ilmane region at the Northwest end of the Hodna Massif, characterized by swarms C06 and C24, and (2) the Ain Azel region at the southeast end of the Hodna Massif, exhibiting swarms C18 and C28 (Figure 3.11).

Cluster C06, boasting the highest event count (191 events), encapsulates the seismic sequence of Beni-Ilmane in May 2010, which stands as one of the most comprehensively studied phenomena in the Northeastern region of Algeria. This prominence is attributed to the plethora of completed or ongoing publications on the subject (Yelles-Chaouche et al., 2014;Abacha et al., 2014; 2019; 2023a;Abacha and Yelles-Chaouche, 2019; Beldjoudi et al., 2016; Hamdache et al., 2017; Beldjoudi, 2020; Rahmani et al., 2023). Characterized by the occurrence of three significant seismic events with magnitudes exceeding 5 and an exceptionally high productivity rate (25,000 events). In addition to tectonic loading, other mechanisms contributed to the sequence triggering, including static stress transfer, fluid dynamics, and aseismic slip transients with spatio-temporal event migration. These factors imply a complex interplay of processes. More details about the sequence are provided in chapter 4.

Transitioning to the southeastern sector of the Hodna range, specifically to the Ain Azel region, which was notably marked by the 2015 seismic activity showcased by the C18 swarm. This area witnessed two main seismic events on March 15th and 21st, 2015, measuring magnitudes of Mw 4.6 and 4.9, respectively, alongside a notable frequency of activity with 1008 events attributed to two fault segments (Figure 3.18a, b, and c) (Abacha et al., 2022). Recent research has further unveiled the role of fluid involvement caused by the circulation of thermal waters in the triggering mechanism through an analysis using three statistical models (Figure 3.18d, e, and f). Further east, the C28 swarm was recorded exactly 5 years after the C18, suggesting an eastward migration of seismicity. However, the statistical study was conducted hastily, particularly in determining the magnitude of completeness. Therefore, it is necessary to repeat this study to account for biases stemming from errors in the catalog.

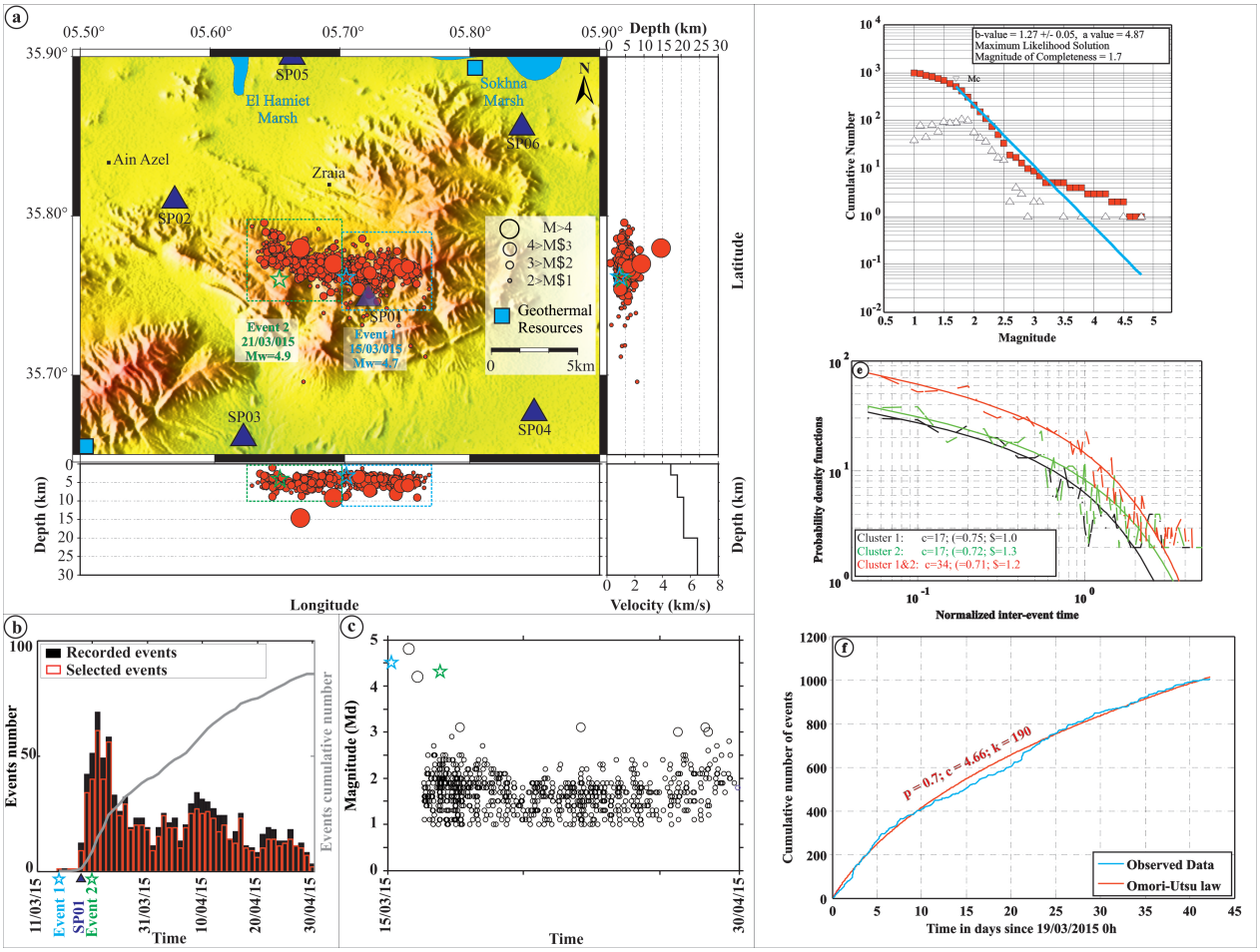

Figure 3.18: Ain Azel earthquake swarm. (a) Spatial distribution of 862 events with nearby thermal sources. (b) Events' number/cumulative number of events per time. (c) The magnitude evolution per time. (d) Gutenberg–Richter law. (e) Inter-event time analysis. (f) Omori law (Abacha et al., 2022).

In summary, the swarms identified in the Hodna range, specifically in the Beni-Ilmane (C06 and C24) and Ain Azal (C18 and C28) regions, have been validated to have an aseismic process in their triggered mechanism, as supported by subsequent studies. Additionally, the spatio-temporal migration of events within each swarm has been confirmed, with a short time interval estimated at several days. Furthermore, an inter-swarm migration spanning a larger time frame, estimated at years, has also been postulated.

3.4.5 Zone 5: Central Tellian Atlas

This zone encompasses several Tellien sub-domains, including the Bibans range, Blida Atlas, and Tablat Atlas. It hosts the highest number of seismic swarms (09 clusters), which comprise C02, associated with the 2007 Medea sequence; C07 and C12, linked to the El Hachimia seismicity between 2010 and 2012; C08 and C31, corresponding to the Oued Djer seismic activity recorded in 2011 and 2020; C15 and C17, related to the 2013-2014 Hammam Meloune sequences; and finally, the 2016 and 2019 Mihoub sequence with C20 and C25.

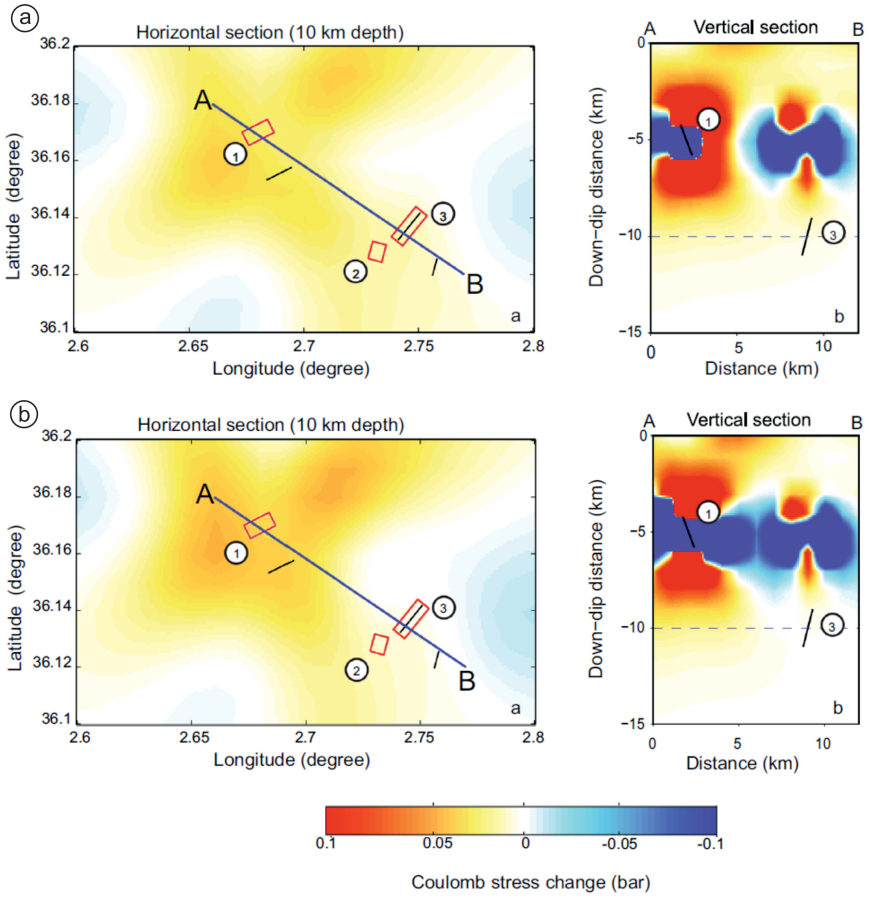

Figure 3.19: At the top, ΔCFF (Coulomb Failure Function change) due to source faults 1 and 2 (strike 15, dip 65, rake -18) on the receiving fault 3 (strike 219, dip 74, rake -5) for $\mu' = 0.4$. (a) Horizontal section (plan view) calculated for $\mu' = 0.4$ at a depth of 10 km. (b) A vertical section A-B showing variations in ΔCFF with depth. The source fault here encompasses the combined contributions of faults 1 and 2 (not shown in the figure). Fault 3 is the receiving fault. At the bottom, ΔCFF due to source faults 1 and 2 on the receiver fault 3 for $\mu' = 0.1$. The figure is structured similarly to the one at the top (Dabouz et al., 2021).

The 2007 Medea seismic sequence comprised three moderate events occurring between May and August 2007, with magnitudes of Mw 4.4, 4.1, and 4.6, respectively, and a notably low productivity rate (58 events relocated). Dabouz et al., 2021 conducted a study to calculate static stress changes, aiming to elucidate the interconnections among these events (Figure 3.19a, and b). The findings revealed interactions among the faults associated with these seismic occurrences throughout the sequence. Considering the low productivity rate and the outcomes of the static stress change analysis, we infer that this swarm (C02) likely occurred due to stress transfer, with no apparent aseismic process involved.

The El Hachimia swarms were situated in the Bouira sub-basin, bordered to the south by the Bibans range. Seismic activity in the area was consistently recorded from 2010 to 2011, where it can be encompassed into two main clusters. The initial cluster, C07, occurred within a relatively short period (July-August 2010), while the second cluster, C12, extended over a more extended period, with two sub-clusters observed in 2011 and 2012. It is worth noting that this region has experienced several historical earthquakes exceeding magnitude 5, with the most notable being the Aumale earthquake of 1910, which registered Ms = 6.6 (Benouar et al., 1994). The presence of swarms in an area characterized by significant historical seismic activity can be explained as a precursor of a large event (Michael and Toksöz, 1982; Evison and Rhoades, 2000; Shanker et al., 2010). The precise mechanism behind these seismic events remains unclear; however, Abacha, 2015; Abacha et al., 2022 suggest a connection to thermal water circulation based on certain statistical patterns.

The two Oued Djer swarms, C08 in 2011 and C31 in 2020, occurred in the vicinity of the January 2, 2018 ML 5.0 earthquake, situated southwest of the Mitidja basin (MB, in Fig. 1) (Mohammedi et al., 2019). It is noteworthy that this region was also the site of a notable historic earthquake in 1988, measuring magnitude 5.4. The triggering mechanism for both swarms remains unclear.

The Hammam Melouane region, situated in the Blida Atlas south of the Mitidja Basin, experienced two swarms, C15 in 2013 and C17 in 2014, which constitute the Hammam Meloune sequence from 2013 to 2014. This sequence included two significant earthquakes of magnitudes Mw 5.0 and 4.9, respectively (Yelles-Chaouche et al., 2017; Boulahia, 2022). Boulahia, 2022 iden-

tified two fault segments in the area. One segment, associated with the 2013 sequence, represents a dextral strike-slip fault-oriented NW-SE. The second segment, related to the 2014 sequence, also exhibits a dextral strike-slip fault orientation NW-SE but is slightly offset from the first segment, suggesting a possible curved fault (Figure 3.20). The spatio-temporal evolution of seismic events indicates a Northward migration, possibly attributed to fluid involvement. It is worth noting that a third subsequence occurred on February 10, 2016, with a magnitude of ML 4.8. However, this subsequence did not meet the criteria to be classified as a swarm in the study.

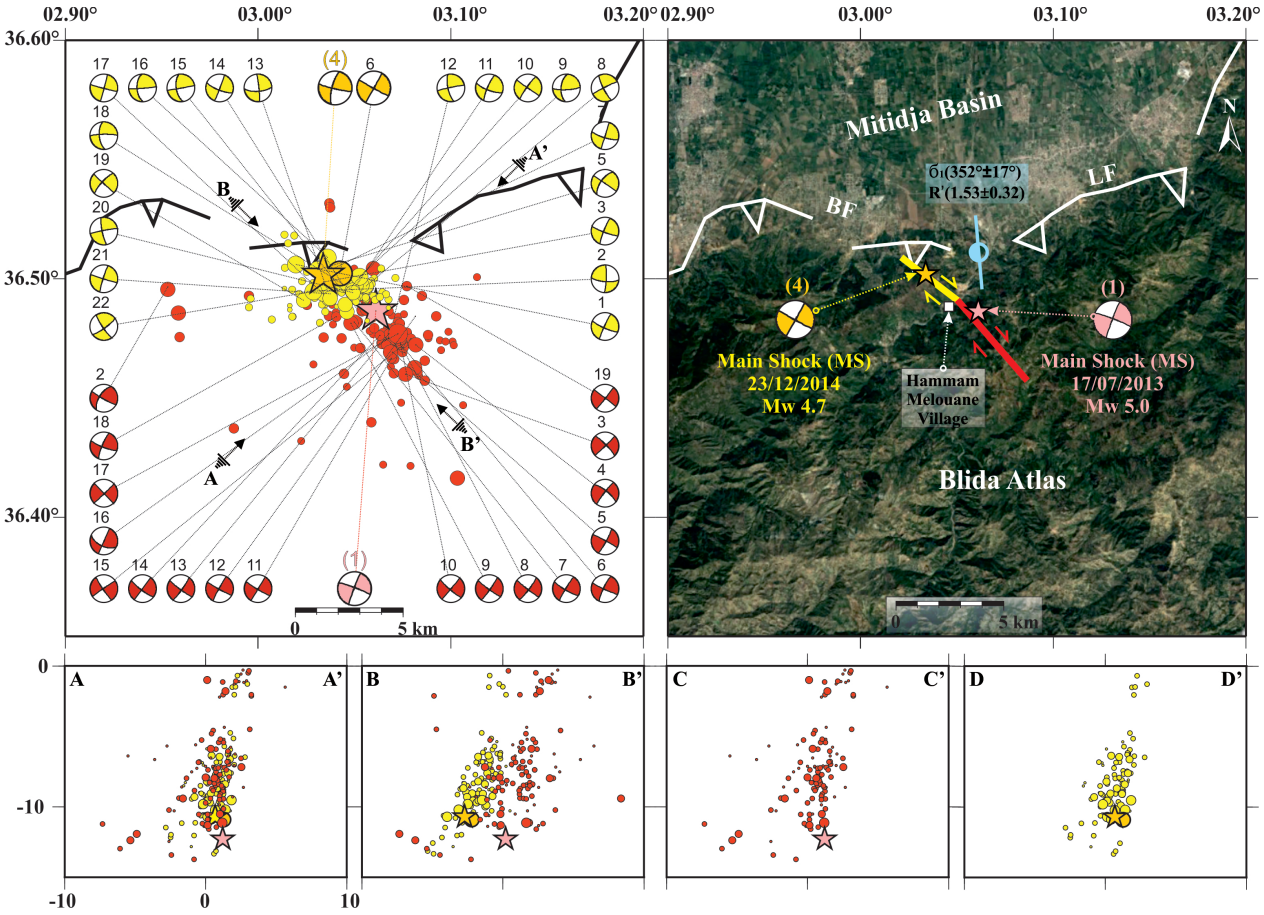

Figure 3.20: The spatial distribution (horizontal and vertical) of relocated events of the Hammam Melouane seismic sequences, along with their focal mechanisms, for the 2013 and 2014 sequences. A-A': Vertical section across both clusters, B-B': Parallel section across both clusters. C-C': Vertical section on the 2013 cluster, and D-D': Vertical section on the 2014 cluster Boulahia, 2022.

The most recent seismic sequence in this zone is the Mihoub sequence, which occurred in the Tablat Atlas in 2016 and is represented by the C20 cluster with 81 events (the second largest after the Beni-Ilmane sequence in 2010). This sequence included two mainshocks on April 10 and July

15, 2016, with magnitudes ML 4.9 and Mw 5.4, respectively. Two fault segments are responsible for this sequence: the first is an EW-directed segment with a strike-slip character, where the initial event of the sequence (ML 4.9 on April 10, 2016) was located. The second fault plane, where the most significant event of the sequence occurred on May 28, 2016 (Mw 5.4), is a reverse fault plunging towards the southeast (Khelif et al., 2018). This last study calculated the static stress change caused by the initial event (ML 4.9) of the sequence. The results indicate that the fault plane of the largest event in the sequence (Mw 5.4) and most of the aftershocks occurred within an area of increased Coulomb stress (Figure 3.21). Therefore, it is plausible to assume that this swarm was generated by stress transfer. Four years later, a small swarm (C25) was recorded in the same region southeast of C20, possibly indicating a migration of the rupture to the adjacent segment. Moreover, seismicity migration within and between swarms serves as a reliable indicator of fluid dynamics implying probably a complex interplay.

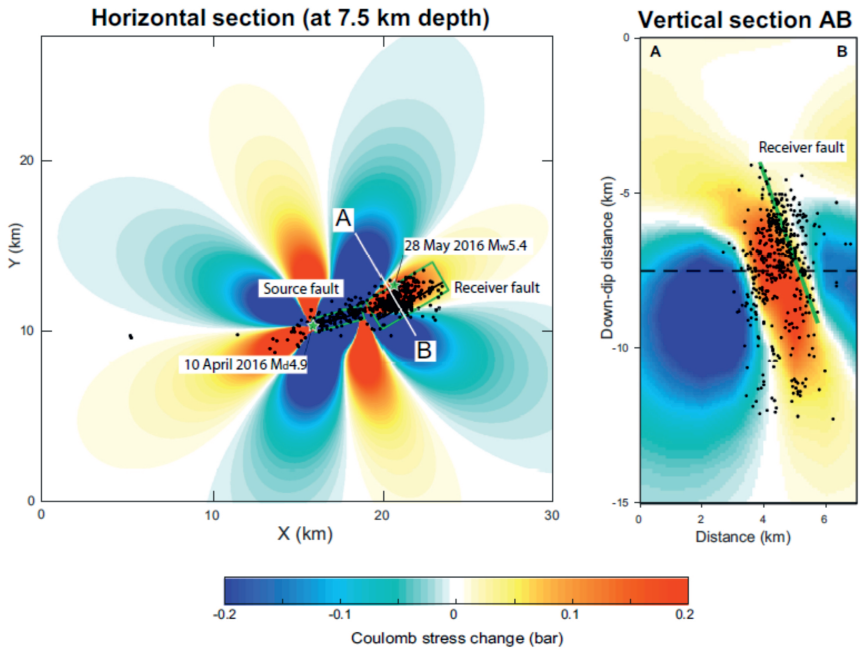

Figure 3.21: Change in Coulomb stress due to the E–W fault segment (strike N70°E, dip 77° to SSE) on the NE–SW specified fault segment (strike N60°E, dip 70°to SE, rake 130°). Blue colors indicate a decrease in stress; hot colors (red and yellow) indicate an increase. (left) Horizontal section on 7.5 km depth, green rectangles represent vertical projection of the two fault segments. (right) vertical section AB following depth, green line indicates the receiver fault (Khelif et al., 2018).

3.4.6 Zone 6: Offshore Algeria margin

For decades, the seismic activity along the Algerian margin has been poorly understood, largely due to the limited capabilities of the seismic network and a lack of marine investigations. The offshore region of Northern Algeria has been the site of several significant historic marine seismic events, including the 1365 Algiers Earthquake, the 1790 Oran Earthquake, and the 1856 Jijel earthquake sequence. In more recent times, the eastern-central margin has experienced three earthquakes with magnitudes greater than 6: the 1989 offshore Ms 6.0 Tipaza Earthquake, the 2003 Mw 6.8 Boumerdes Earthquake, and the 2021 Mw 6.0 Bejaia Earthquake (Yelles-Chaouche et al., 2021; 2022; 2023). Recognizing the critical need to enhance our understanding of the Algerian margin's geodynamics and to study its tectonic structures, several marine projects have been launched recently. These projects, including MARADJA1 and MARADJA2/SAMRA in 2003 and 2005, respectively, and SPIRAL in 2009, have employed high-resolution methods to achieve these goals (Yelles-Chaouche et al., 2022).

The present study identified four swarms along the Offshore Fault System Kabylia (OFSK). The first, C09 in 2011, coincides with the area of aftershocks from the 2003 Boumerdes earthquake and could be considered part of the aftershock sequence of this event. It is important to note that many major earthquakes produce aftershocks for extended periods (Chen and Shearer, 2011). The subsequent cluster, C11, was located off the coast of Ain Benian in 2011, coinciding with the location of the 1996 Ain Benian earthquake of ML 5.7. Yelles Chaouche et al., 2009 identified an asymmetrical submarine fold-fault oriented NE-SW (ABF in Fig. 7) in the region, with an estimated uplift rate of 2 mm/year in the Plio-Quaternary. These authors linked the Aïn Benian earthquake to this structure (ABF). It is possible that the swarm in question was associated with this structure; however, further investigation is required to fully understand its mechanical behavior.

The third cluster, C13, was detected in a particularly intriguing area off the coast of Azzafoune in 2012. This region presents a concerning gap between two areas already affected by significant earthquakes: the Mw 6.8 Boumerdes earthquake in 2003 to the west and the Mw 6.0 Bejaia earthquake in 2021 to the east. Despite this swarm, there have been no other notable seismic events in the region. It is important to note that the area contains significant structures (see Fig. 7) that accommodate an average deformation rate of 1.5 mm/year. It is highly probable that this swarm

could be a precursor to a major destructive earthquake, similar to the El Hachimia swarms.

The final cluster, C16, represents the seismic sequence of Algiers in 2014, featuring two main events of Mw 5.5 and ML 3.9. Yelles-Chaouche et al., 2019 demonstrated that this sequence was triggered by a curved NE–SW-striking reverse fault for the largest event, with a minor strike-slip fault roughly aligned N–S intersecting the eastern part of the reverse fault for the smaller event (Figure 3.22). The authors also calculated the Coulomb stress changes following the Mw 5.4 event. The results indicate that the rupture of the ML 3.9 event, along with nearly all aftershocks occurring within a day of the largest event, were located in an area of heightened Coulomb stress. Therefore, swarm C16 may have been triggered by static stress transfer within the sequence, in addition to the dynamic stress transfer among all these seismic swarms along the OFSK, which were recorded for only about one year. This scenario mirrors what was observed in the swarms detected along the MADF in Zone 1.

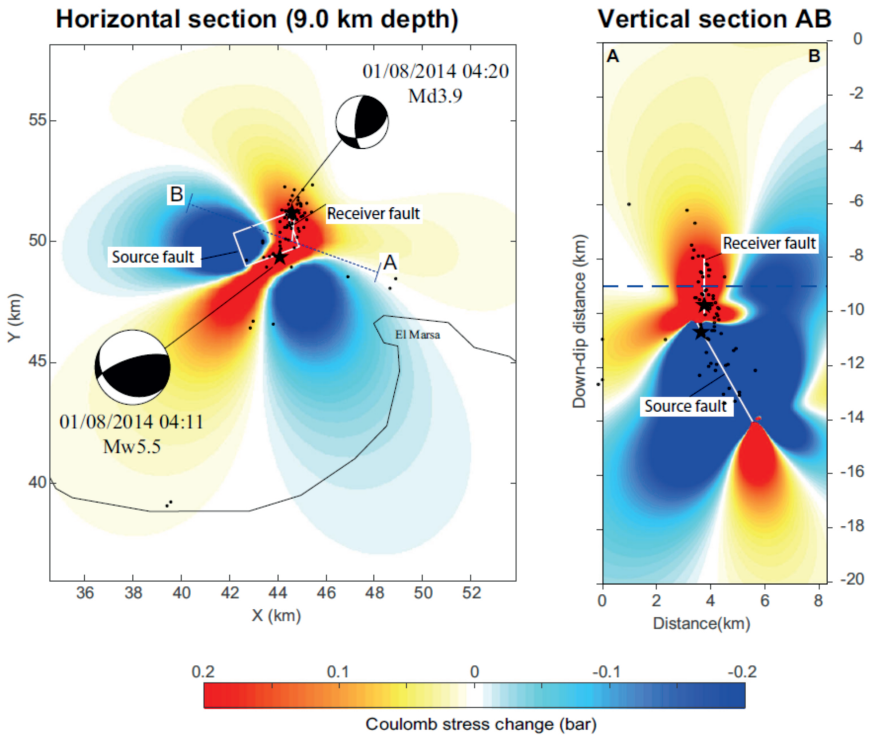

Figure 3.22: Change in Coulomb stress due to the mainshock on the N– S-aligned fault. Blue colors indicate a decrease in stress; hot colors (red and yellow) indicate an increase. White rectangles represent projections of the source and receiver faults. Black dots represent aftershocks in the first day after the mainshock. (Left) Horizontal section at 9.0 km depth. (Right) Vertical section A–B (Yelles-Chaouche et al., 2019).

3.4.7 Zone 7: Aures range

This zone is typically characterized by low seismic activity, punctuated by occasional moderate earthquakes. Of particular note are three significant earthquakes along the deformation front of the Tellian Atlas: the earthquake of the year 267, which serves as a reference earthquake in this area; the 1885 earthquake with a maximum intensity of Imax = VIII MSK; and the 1924 earthquake with a magnitude of Ms = 5.3.

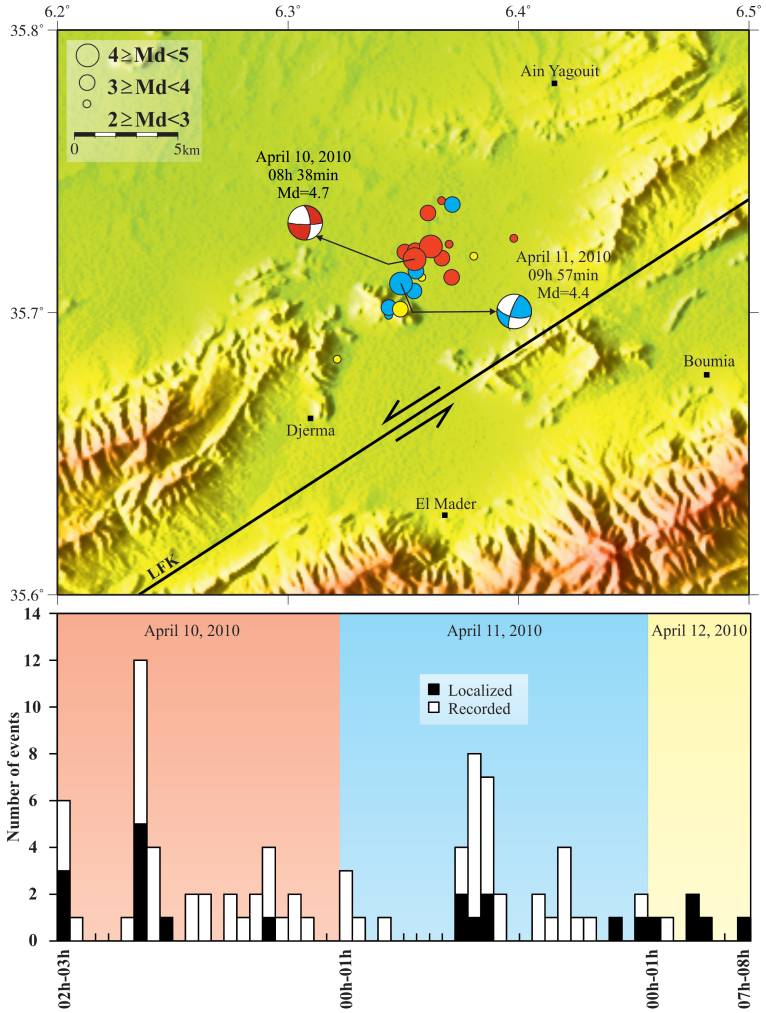

Figure 3.23: (Top) Spatial distribution of the 20 localized seismic events of El-Madhar crisis. The red, blue, and yellow events are those localized on April 10, 11, and 12, 2010, respectively. (Bottom) Histogram representing the number of recorded and localized events over time (Abacha, 2015).

Three small swarms were identified: C04 and C10 in the El Madhar region, and C29 in the

Bouzine region. The first cluster represents the El Madhar crisis that occurred in April 2010, with two main events on April 10 (ML=4.7) and April 11 (ML=4.4). Abacha, 2015 attributed this crisis to a NE-SW right-lateral strike-slip fault, based on the distribution of events and the focal mechanisms of the two main events (Figure 3.23). This fault showed a migration pattern towards the southwest. The occurrence of two seismic events with a migration pattern is often indicative of fluid movement. This was further supported by the occurrence of the second C10 cluster exactly one year later in the same region. Several kilometers south of the El Madher swarms, cluster C29 was located in 2019 in a seismically anonymous region if we exclude the three historic earthquakes mentioned above.

3.4.8 Zone 8: South Atlasic Flexure

The WNW–ESE South Atlasic Flexure (SAF) serves as a significant boundary between the Aures Range and the Saharan Platform. This fault system has been associated with several historical earthquakes, such as the 1869 Biskra earthquake (I0 = VIII–IX, Harbi, 2001), as well as more recent events like the 2007 ML 5.2 El Oued earthquake (Abacha, 2015), and the 2016 ML 5.1 Biskra earthquake (Yelles-Chaouche et al., 2017). The SAF accommodates a deformation rate of 1.5 mm/yr (Bougrine et al., 2019).

Two seismic swarms have been identified along the SAF. The C05 swarm was located 5 km south of the 2007 El Oued earthquake in May 2010, which has been termed the 2010 El Oued Crisis by Abacha and Yelles-Chaouche, 2019. This crisis began with an event of ML 4.0 and was followed by a series of micro-events. The cause of this swarm remains unknown. The C23 swarm was located around Biskra City in 2019, a few kilometers west of the 2016 earthquake. This raises questions about a potential relationship between them. Therefore, further investigation is needed to understand the tectonic characteristics of this zone.

3.4.9 Zone 9: Saharian Atlas

The Saharan Atlas is a geological unit and mountain range that experiences fewer earthquakes compared to the Tellian Atlas, primarily due to its distance from the collision zone between the

African and Eurasian plates. Despite this, some moderate and isolated earthquakes have been recorded sporadically. It is important to note that this mountain range extends towards the southwest, forming the High Atlas in Moroccan territory. The High Atlas experienced the Adssil earthquake in September 2023, with a magnitude of Mw 6.8. Studying seismic activity along this lineament is crucial for gaining a clearer understanding of tectonic patterns. A detailed study of the Djelfa swarm, C01, recorded in 2007 presents an excellent opportunity for this purpose. Since this study does not accurately determine its source, additional geological and geophysical investigations are necessary.

In summary, we have identified swarms linked to underground fluid circulation, others generated by stress transfer either static or dynamic, and yet others by aseismic sliding or long-duration aftershocks. Some cases are influenced by complex interactions, as seen in the seismic sequences of Beni-Ilmnae in 2010, Bejaia-Babors in 2012-2013, and Mihoub in 2016. However, there are also cases where the triggering mechanism remains unknown or ambiguous, warranting further in-depth study to understand the underlying tectonic patterns.

3.5 Conclusion

This study delved into the identification and characterization of earthquake swarms in the Northeastern part of Algeria as it is most susceptible to this type of seismic activity. Employing the '1σ criterion' and computing the kurtosis and skewness of the temporal release of seismic moment, we aimed to discern seismic patterns. Despite the disparate nature of the two methods, their outcomes demonstrated a high degree of comparability, revealing nearly identical clusters with variations in event numbers. To enhance the overall understanding, the two swarm catalogs were merged, resulting in a more comprehensive swarm catalog. This study focused on the period from 2007 to 2020, as it represents the Algerian catalog's most reliable period in terms of detection capacity and data accuracy. A total of 32 swarm clusters were identified, and subsequent categorization based on geological and tectonic contexts was conducted. The mechanisms accountable for swarm cluster generation varied across zones. In some instances, fluid involvement led to heightened seismicity, while others were associated with static or dynamic stress transfer. How-

ever, certain clusters remained enigmatic, requiring further studies for a more precise interpretation (refer to Table 3.1).

Understanding the mechanisms responsible for swarm cluster generation is vital for assessing seismic hazard accurately. It not only aids in identifying areas prone to increased seismic activity but also facilitates the development of more targeted and effective strategies for seismic risk mitigation. While this study sheds light on various aspects of seismic behavior, the enigmatic nature of certain clusters emphasizes the need for ongoing research to refine our understanding and improve the precision of seismic hazard assessments in the Northeastern part of Algeria.

Table 3.1: List of identified seismic swarm clusters along with their potential origins

Seismic Swarm	**Origin**
C30: The 2020 Mila Eq Sequence (Z1) C03: The 2007 Mila Crisis (Z2) C14: The 2012-2013 Bejaia-Babors Eq Sequence (Z3) C06: The 2010 Beni-Ilmane Eq Sequence including the C24 2019 swarm (Z4) C18: The 2015 Ain Azel Eq Sequence including the C28 2020 swarm (Z4)	Fluid involvement
C22: The 2017 Sidi Dris Crisis (Z1) C15-C17: The 2013-2014 Hammam Melouane Eq Sequence (Z5) C20: The 2016 Mihoub Eq Sequence including the C25 2019 swarm (Z5) C04-C10: The 2010-2011 El Madher Crisis (Z7)	Probable fluid involvement
C27-C32: The January-November 2020 El Kantour Swarms C14: The 2012-2013 Bejaia-Babors Eq Sequence (Z3) C06: The 2010 Beni-Ilmane Eq Sequence including the C24 2019 swarm (Z4) C20: The 2016 Mihoub Eq Sequence including the C25 2019 swarm (Z5) C02: The 2007 Medea Eq Sequence (Z5) C16: The 2014 Algiers Eq Sequence (Z6)	Stress transfer
C06: The 2010 Beni-Ilmane Eq Sequence including the C24 2019 swarm (Z4)	Aseismic slip
C09: The 2011 Boumerdes Swarm (Z6)	Long-Lived Aftershocks
C20: The 2016 Mihoub Eq Sequence including the C25 2019 swarm (Z5) C14: The 2012-2013 Bejaia-Babors Eq Sequence (Z3) C06: The 2010 Beni-Ilmane Eq Sequence including the C24 2019 swarm (Z4)	A complex interplay
C26: The 2020 El Aouana Eq Sequence (Z1) C21: The 2016 Guettar Aich Swarm (Z2) C19: The 2016 Lallam Swarm (Z3) C07-C12: The 2010-2011 El Hachimia Smarms (Z5) C08-C31: The 2011 and 2020 Oued Djer Swarms (Z5) C13: The 2012 Azzafoune Swarm (Z6) C29: The 2019 Bouzine Swarm (Z7) C04: The 2007 El Oued Swarm (Z8) C23: The 2019 Biskra Swarm (Z8) C01: The 2007 Djelfa Swarm (Z9)	Unidentified process

Chapter 4

Overview on the Beni-Ilmane seismic sequence

4.1 Introduction

The 2010 Beni-Ilmane earthquake sequence stands as the most important seismic crisis that happened in the last decade. It began on May 14, 2010, with the first strong shock having a magnitude of ML 5.4 (BI-MS1), followed by two others with magnitudes of ML 5.3 each (BI-MS2 and BI-MS3), occurring after two and nine days, respectively. Despite the moderate deformation rate of 1.5 mm/year, the 2010 Beni-Ilmane earthquake sequence, taking place on the southern deformation front of the Tellian Atlas, and ∼100 km south of the Eurasia–Africa Plate boundary (Figure 4.1a), generated approximately 25,000 events within the first two weeks, making it the most significant seismic sequence in Northern Algeria. Notably, seismic sequences in the region often involve two or more mainshocks accompanied by spatial migration (Figure 4.1b), as explained in chapter 3, with the Beni-Ilmane sequence standing out due to its exceptionally high event count.

Numerous studies have investigated the 2010 Beni-Ilmane earthquake sequence, leading to the development of seismotectonic models. (Yelles-Chaouche et al., 2014) proposed a model involving a reverse E-W fault and a strike-slip NNE-SSW fault, while (Beldjoudi et al., 2016) assigned each mainshock to different segments. Subsequently, Tikhamarine et al. (under review at GJI) proposed

the most representative tectonic model, incorporating all faults contributing to the sequence based on a detailed analysis of multiplets and repeaters. Additionally, seismic tomography models by Abacha et al., 2014 and Abacha et al., 2023a aimed to understand the depth distribution of seismic activity. Hamdache et al., 2017 performed statistical analyses using various methods. Finally, Beldjoudi, 2020 examined the static Coulomb stress transfer between the three main faults mentioned in Beldjoudi et al., 2016. However, the full understanding of earthquake activity in the region remains elusive.

This chapter offers fresh insights into seismic activity analysis in the region. Firstly, we determined m_c, considering potential biases stemming from alterations in the network configuration and catalog incompleteness. This approach enabled the application of the Omori-Utsu law, Gutenberg-Richter law, the analysis of inter-event times, and the ETAS model (both temporal and spatio-temporal). Secondly, a time-dependent background rate ETAS model was employed to discern the mechanisms driving seismic activity in the region. Lastly, we replicated the methodology of Abacha et al., 2023a, calculating the Vp/Vs ratio and juxtaposing the outcomes with our results. Collectively, these methodologies contribute to a more global comprehension of seismic activity in the region, aiding in the identification of potential seismic hazard risks.

4.2 Description of the seismic sequence

The 2010 Beni-Ilmane earthquake sequence occurred in the southern deformation front of the Atlas Tellian region, situated in a geologically intricate area between the Hodna and Bibans Mountain ranges, specifically in the southern part of the NE-SW Djebel Choukchot massif (Figure 4.1c). This massif has undergone significant deformation, resulting in the formation of a network of faults and fractures with diverse types and orientations (Yelles-Chaouche et al., 2014; Beldjoudi et al., 2016; Abacha et al., 2023a). Owing to two distinct tectonic phases, the geological formations in the region display specific characteristics. Firstly, two main domains exist: the Sub-Bibanic allochthonous and Djebel Choukchot Parautochtonnous. These domains are primarily composed of Jurassic, Upper Cretaceous, Eocene, and Miocene sedimentary cover, thrust onto the Pre-Atlasic autochthonous domain of the Hodna basin, which consists of Ouanougha Miocene sediments. Sec-

ondly, there is a strike-slip tectonic setting that intersects these geological formations and the surrounding thrust faults (refer to Figure 4.1d).

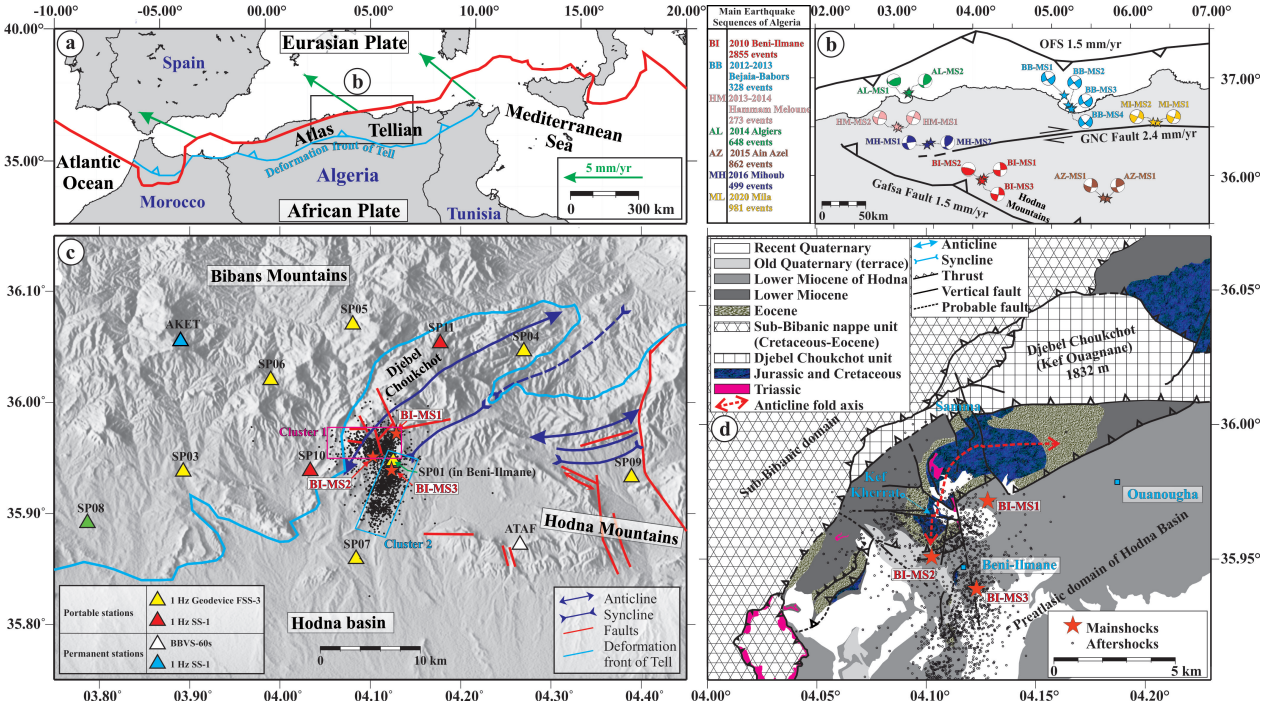

Figure 4.1: (a) Map of the southern part of the Western Mediterranean, delimiting the Tellian Atlas System Tell (one of the main geological units in Algeria). The red line represents the Eurasia-Africa Plate boundary (simplified from Bird, 2003), and the blue line represents the deformation front of Tell. Predicted velocities along the Eurasia–Africa Plate boundary (green arrows) are simplified from Nocquet et al., 2006. (b) Spatial partitioning of strain in Northeastern Algeria along the three major tectonic structures, which are schematized in black lines according to the study of Bougrine et al., 2019. The mainshocks and their focal mechanism of the main seismic sequences are also shown. (c) Tectonic map of the study area on a local scale, showing the seismic sources (black dots) with the three mainshocks (red stars) and the seismic stations (triangles). (d) Geology of the epicentral area (modified from Beldjoudi et al., 2016; Abacha et al., 2023a)), showing the 2876 events that represent the complete number of located events.

The relocated hypocenters (2876 events), which represent the total of number of earthquakes recorded during four months since the 14 May, were distributed into two main clusters, Cluster 1 oriented E-W and Cluster 2 oriented NNE-SSW (Figure 4.1c). The identification of these clusters was based on three criteria established in previous studies. Firstly, the seismotectonic criterion, as proposed by Yelles-Chaouche et al., 2014, used well-located aftershocks and focal mechanisms for earthquakes with a magnitude ≥ 4, revealing two clusters with different orientations (E-W for Cluster 1 and NNE-SSW for Cluster 2), attributed to high-angle reverse and near-vertical left-lateral

strike-slip faults, respectively (Figure 4.2).

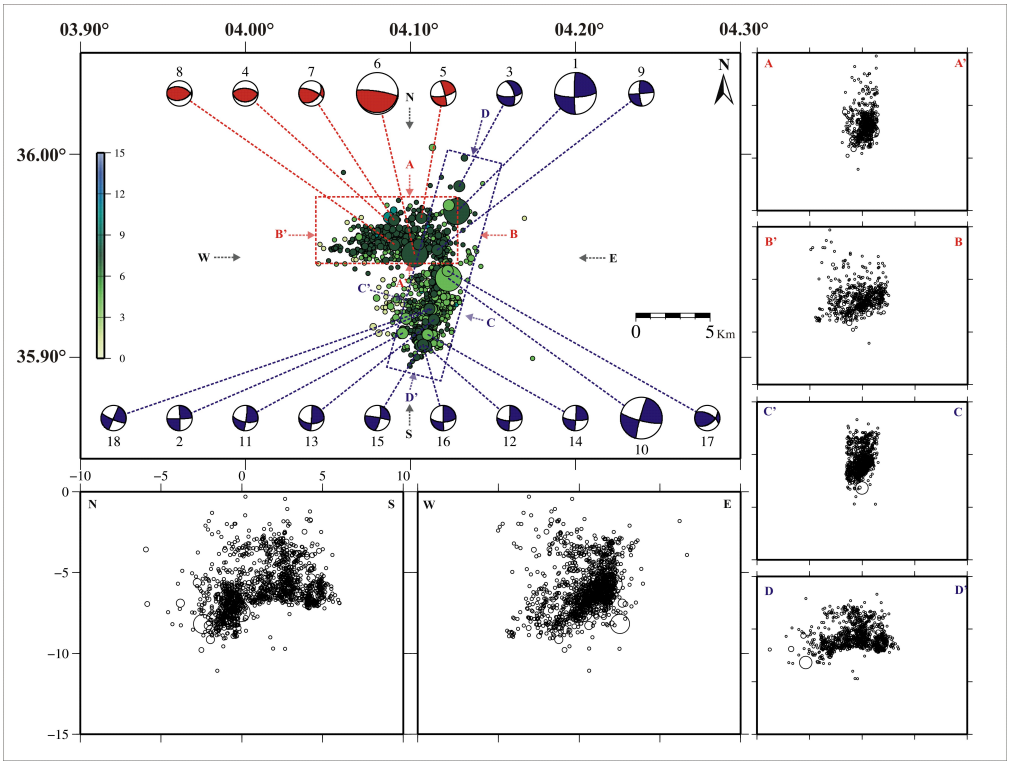

Figure 4.2: Horizontal and vertical distributions of the 1403 relocated events, showing focal mechanisms of events with M $\geq$ 4. The E-W rectangle represents the first cluster and the NNE-SSW rectangle represents the second cluster (Yelles-Chaouche et al., 2014).

Secondly, Abacha et al., 2023a divided the dataset into episodes, noting spatial separation between the clusters, particularly in Episodes A and B, where Cluster 2 displayed heightened activity along the strike-slip fault (Figure 4.3). Thirdly, the same study by Abacha et al., 2023a supported this choice, as it identified two distinct triggered processes for each cluster through seismicity migration analysis (Figure 4.3).

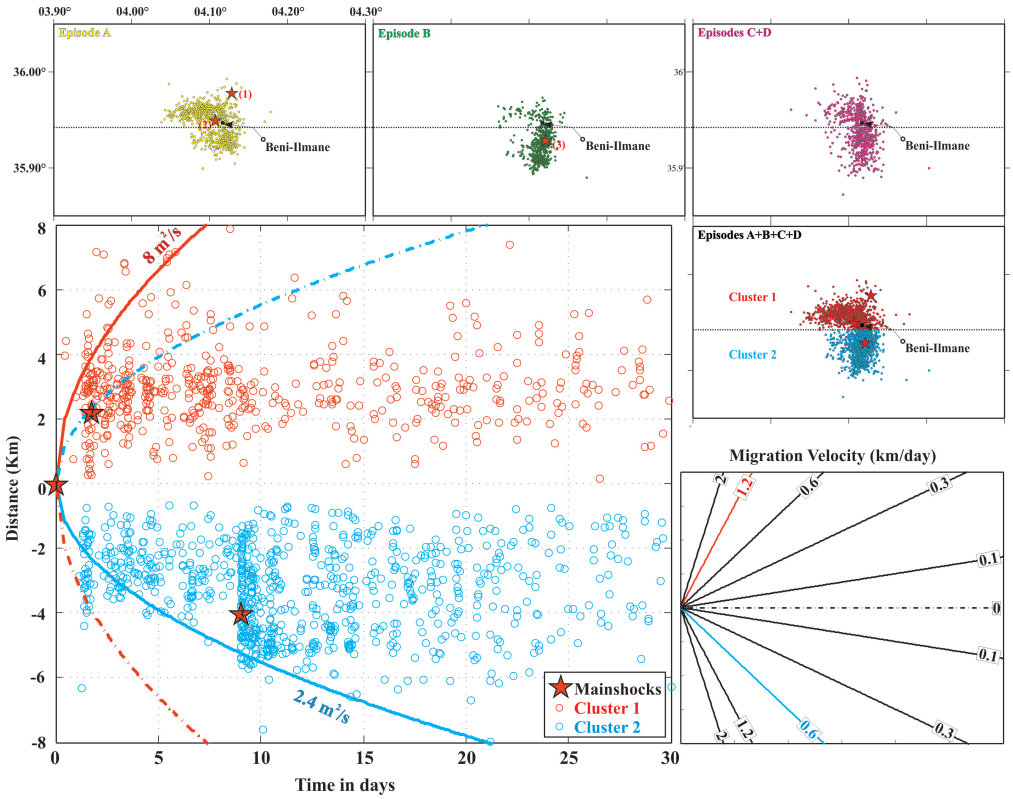

Figure 4.3: Spatio-temporal diagram for the evolution of the 2010 BI earthquake sequence over time since the first mainshocks on 2010 May 14. Parabolic theoretical curves of the probable triggering fronts considering hydraulic diffusivity values D = 8 m^2s^{-1} for Cluster 1 (upper curve) and D = 2.4 m^2s^{-1} for Cluster 2 (bottom curve). The migration velocity-indicating lines in the box in the bottom-right corner refer to horizontal migration (Abacha et al., 2023a).

4.3 Magnitude distribution analysis

Before delving into any statistical analysis, establishing m_c is crucial, as indicated in chapter 1, section 1.2 and 2, section 2.4. Various techniques were employed to determine a robust magnitude of completeness. It is noteworthy that within one day of the initial mainshock, a temporary network was deployed to enhance the network's detection capability. While beneficial for detecting smaller earthquakes, this installation introduced bias into the estimation of statistical parameters. Consequently, we conducted a re-evaluation of earthquake detection using only the permanent network. A total of 815 events were detected using this procedure.

Methods employed to determine m_c included MAXC, EMR, and GFT (refer to chapter 1,

section 1.2), utilizing a bootstrapping approach to quantify uncertainties. The bootstrap analysis encompassed a sample size of 300 events, consistent with Woessner and Wiemer, 2005b findings, demonstrating the stabilization of the m_c variance for a sample size equal to or exceeding 200 events.

The initial method, MAXC, yielded an m_c of 2.1 with an uncertainty of 0.05. Typically, this method does not exhibit a distinct magnitude peak, but in this case, a clear peak is observable (Figure 4.4).

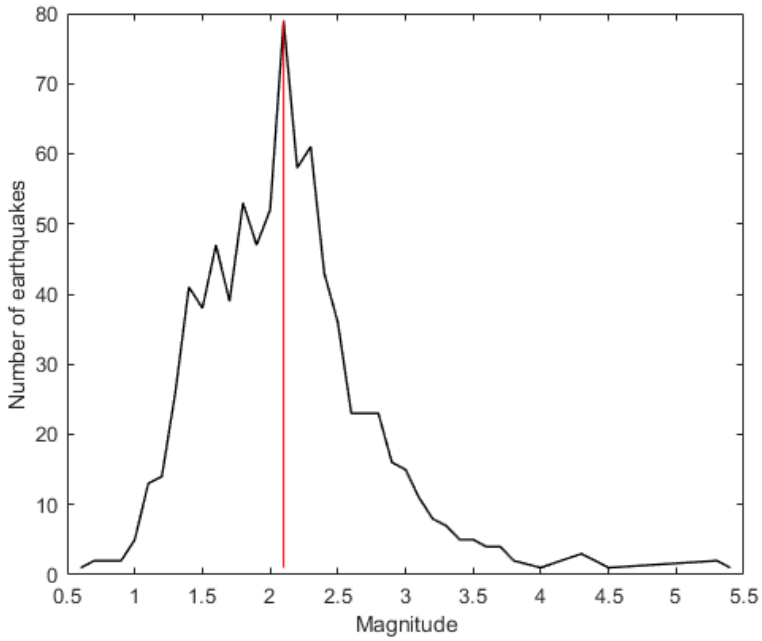

Figure 4.4: Non-cumulative distribution of earthquakes magnitude. The red line represent m_c of the catalog.

The second method used is the GFT, which, at a residual level of 95%, estimated m_c for the complete catalog to be 2.0 with a standard deviation of 0.08. This result implies that, at a 95% residual level, seismic events with magnitudes equal to or greater than 2.0 are reliably detected in our seismic catalog (Figure 4.5). Notably, a lower residual level of 90% yielded a slightly reduced m_c value of 1.9 (Figure 4.5). The standard deviation of 0.08 provides insights into the stability and consistency of the estimated m_c. A lower standard deviation suggests a more robust estimation, while a higher value may indicate greater variability in the data or potential sensitivity to certain

parameters. In comparison to the MAXC method, the uncertainty is much higher. Considering this uncertainty, the estimated m_c could potentially be higher, around 2.1.

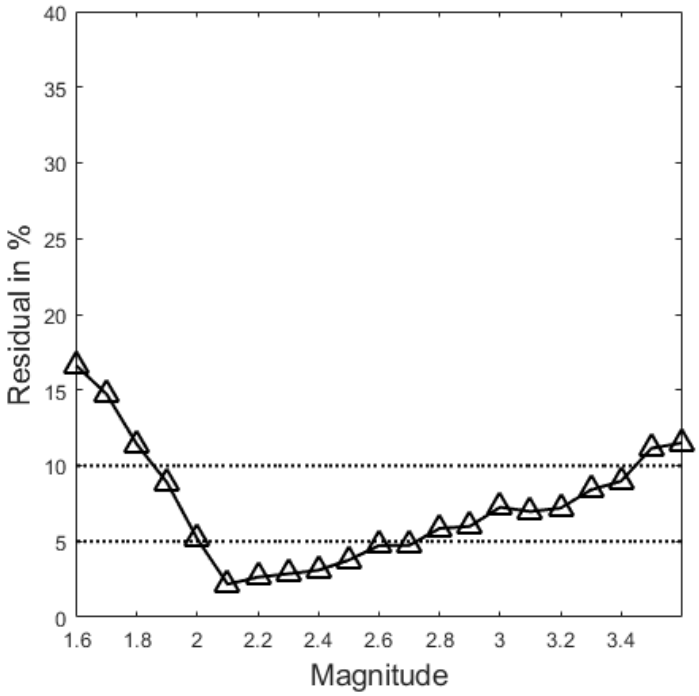

Figure 4.5: Residual against magnitude. the two black dashed lines represent the residual at 90% and 95%.

The final technique employed is EMR, considered the most reliable one. m_c determined, using this method, is 2.1 with a standard deviation equal to 0.04 (Figure 4.6). Along with m_c, two additional parameters are determined. The first parameter, μ, represents the magnitude at which 50% of the seismicity is detected, found to be 1.01 in our study. The second parameter, σ, corresponds to the standard deviation and is equal to 0.56 in our case.

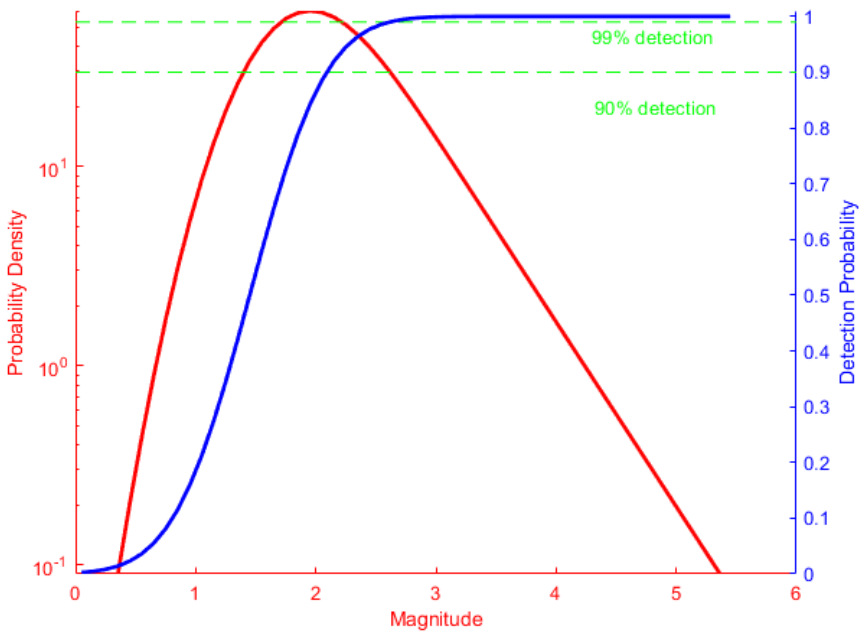

Figure 4.6: Probability density function of the magnitude distribution. The blue solid line represent the detection probability, the red solid line represent the probability density function of the magnitude distribution, and the two greed dashed lines represent the detection probability at 90 and 95%.

After conducting various tests utilizing different techniques, $m_c = 2.1$ was selected due to being the highest value, even when considering the associated uncertainty. Opting for the maximum value of m_c may result in some information loss, but it serves to mitigate biases in the estimation of statistical parameters.

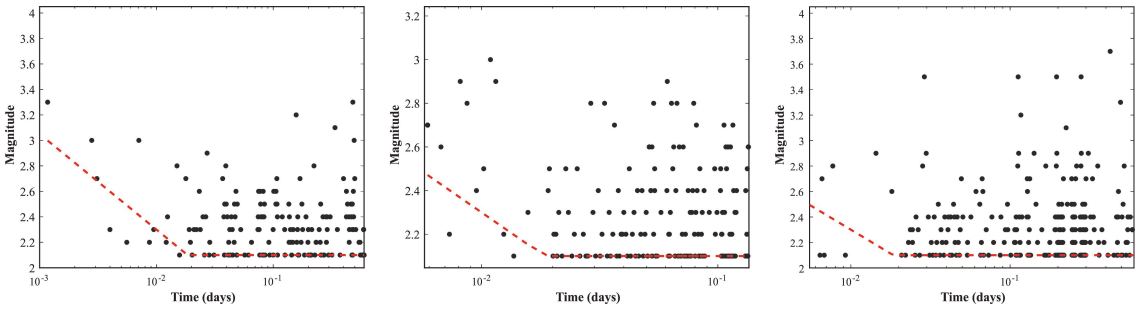

Figure 4.7: Magnitude versus time representing short-term incompleteness for BI-MS1, BI-MS2, and BI-MS3, from left to right.

Another issue addressed pertains to STAI, wherein we employed the empirical relationship between m_c and the magnitude of the mainshock (refer to chapter 2, section 1.2). All events

occurring during the period of incompleteness were excluded from the calculation and estimation of the parameters (Figure 4.7).

From the 815 events detected (Figure 4.8a), a total of 433 events were retained (Figure 4.8b), significantly fewer than those encompassed by the complete recording process, yet still unbiased for parameter estimation. The spatio-temporal evolution, depicted in Figure 4.8c, illustrates that both clusters initiated nearly simultaneously, with the bulk of events in the first cluster. However, following BI-MS3, activity shifted predominantly to the second cluster, with some events lingering in the Northern part, particularly in the last days of activity, indicating a sort of N-S migration. This pattern holds valid for all events in the sequence, as evidenced by both Abacha et al., 2023a and Tikhamarine et al. (under review at GJI). This suggests that the selected set of partial events in this study concerved the patterns of the global dataset. Furthermore, the seismic activity sources were concentrated in a roughly 10 km deep strip, aligning with the seismogenic layer of all Algerian seismicity (Yelles-Chaouche et al., 2022).

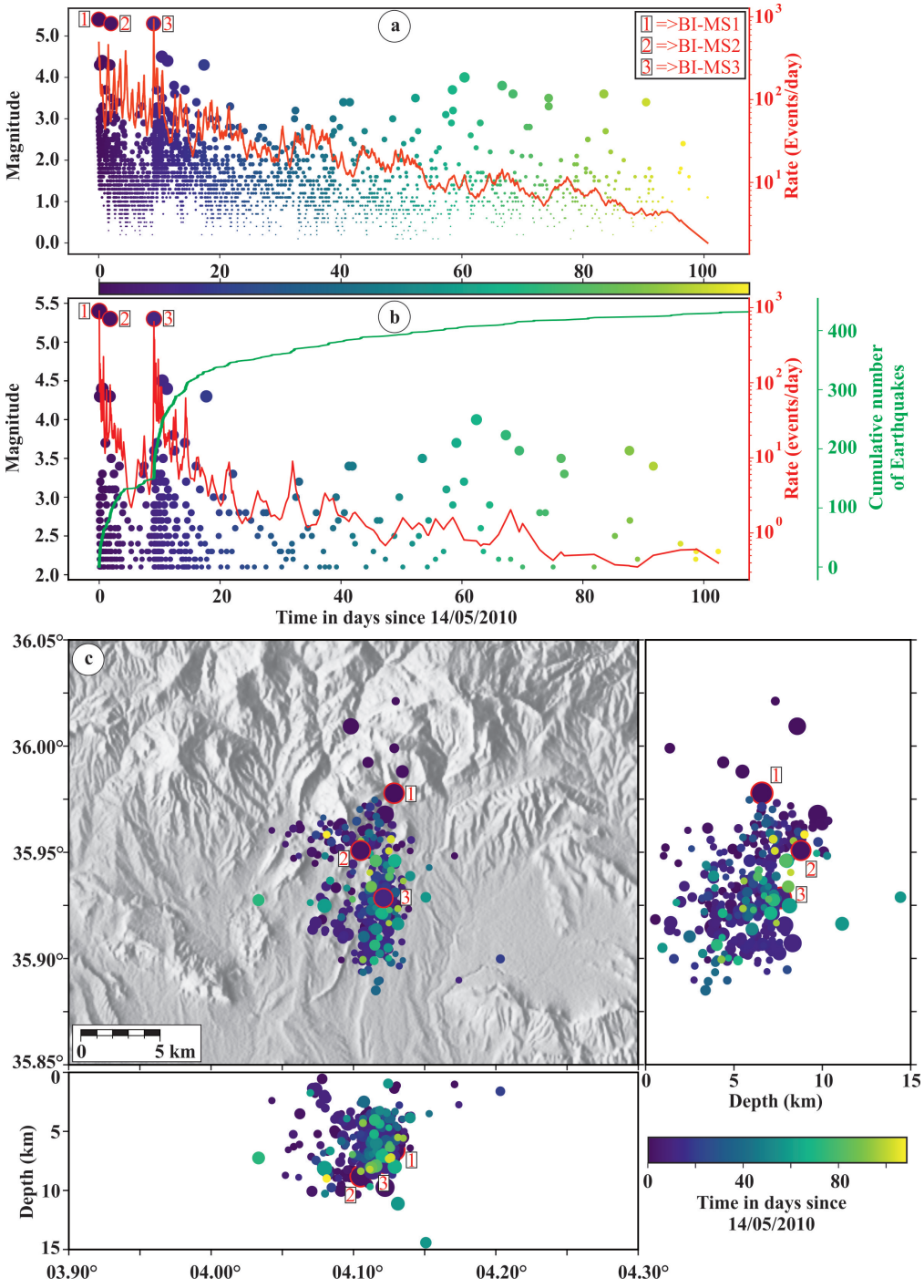

Figure 4.8: (a) Magnitude-time with the event rate (red line) of the events recorded by the permanent network. (b) Magnitude-time with the cumulative number of events plot (green line) and event rate (red line) of the Beni-Illmane seismic sequence above m_c. (c) the spatial distribution of the relocated earthquakes with two vertical sections oriented across and along the hypocenter trend, where symbol size is proportional to the magnitude. Events are color coded according to their occurrence times.

m_c determined, we can now process the estimation of the magnitude distribution parameters (see chapter 2, section 1.3). The estimation of the $b-value$ and $a-value$ were computed using the maximum likelihood technique with a bootstrap approach. The results illustrate the FMD of the seismic sequence, revealing a $b-value$ of 0.87±0.02 for $m_c > 2.1$ (Figure 4.9a), signifying the dominance of larger events in the sequence. The binning strategy adopted in this study is set to 0.1. Larger bin sizes were avoided as they can introduce biases in the final results, potentially leading to the underestimation of the $b-value$ (Marzocchi and Sandri, 2009;Marzocchi et al., 2019).

The observed plate or deviation for events with magnitudes < 2.1 may be attributed to partial incompleteness. To track changes in the G-R law parameters, the seismic sequence was divided into two periods based on the observed variations in the cumulative number of events (Figure 4.8b). The first period, spanning from BI-MS1 to the event before BI-MS3, is characterized by a $b-value$ of 0.82±0.06 and an $a-value$ of 3.87 for m_c equal to 2.1 (Figure 4.9b). In the second period, post BI-MS3, there is an increase in both the $b-value$ and $a-value$, each equal to 0.90±0.03 and 4.27, respectively, for m_c equal to 2.1 (Figure 4.9c). These changes are associated with the relative increase in smaller earthquakes during the second period compared to the first one. However, considering uncertainties, the b and $a-values$ found for each phase are quite similar.

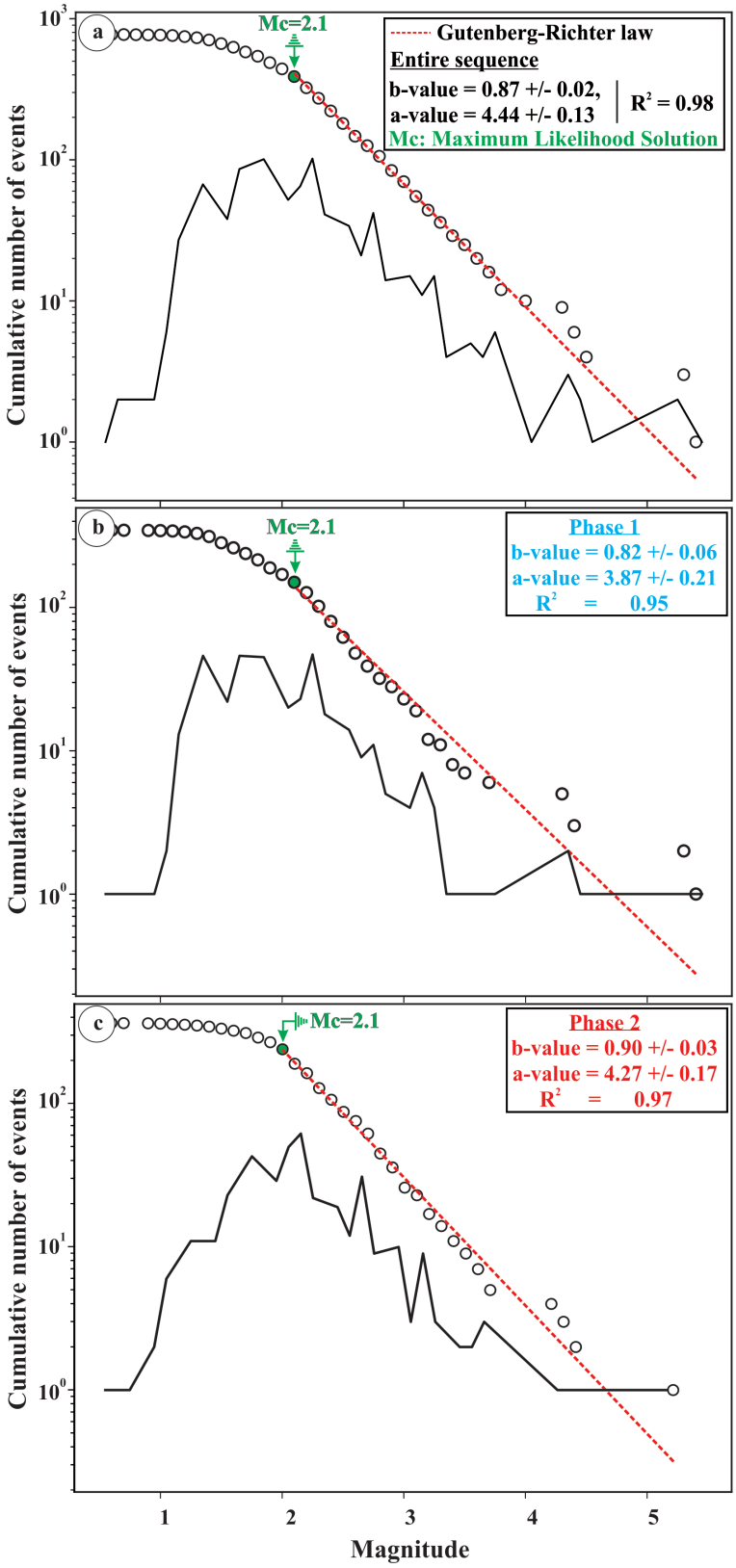

Figure 4.9: (a) Frequency-magnitude distribution of the entire sequence. The dashed line refers to a Gutenberg-Richter relation with b = 0.87. (b) Frequency-magnitude distribution of the first phase with a $b-value$ of 0.82. (c) Frequency-magnitude distribution of the second phase with a $b-value$ of 0.90.

4.4 Spatio-temporal Charecteristics

To examine the temporal characteristics of the Beni-Ilmane seismic sequence, we initially applied the Omori-Utsu model to the entire sequence following BI-MS1 of ML 5.4 (refer to chapter 1, section 1.4). The model parameters were obtained through maximum likelihood estimation, yielding p = 1.56, c = 5.03 days, and k = 723.45 (Figure 4.10a). The elevated $p - value$, compared to typical values ranging from 0.8 to 1.2 in different seismic sequences (Utsu et al., 1995; Hainzl and Marsan, 2008), and the high $c - value$ (typically ranging from 0.5 to 20 hours, Utsu et al., 1995) suggest a potential influence of secondary aftershock sequences triggered by aftershocks. This effect can impact the temporal decay, especially in our case where three strong shocks occurred in less than 10 days. This type of phenomenon can be tricky to interpret since it has not been established that the $c - value$ has a clear correlation with the physical state of the region. It may be a subject of research that can be analyzed in the future.

A noticeable increase in the number of events per day immediately after the occurrence of BI-MS3 is evident (Figure 4.10a). To examine changes in the Omori-Utsu parameters, we divided the seismic sequence into two periods, similar to the approach used for the G-R law. Both periods appear to conform to the Omori-Utsu law. In the first phase, a low $p - value$ of 0.7, within the mentioned typical range, was found (Figure 4.10b). The fit also revealed a low $c - value$ of 0.0045. However, the second phase displayed elevated p and $c - values$ (Figure 4.10c).

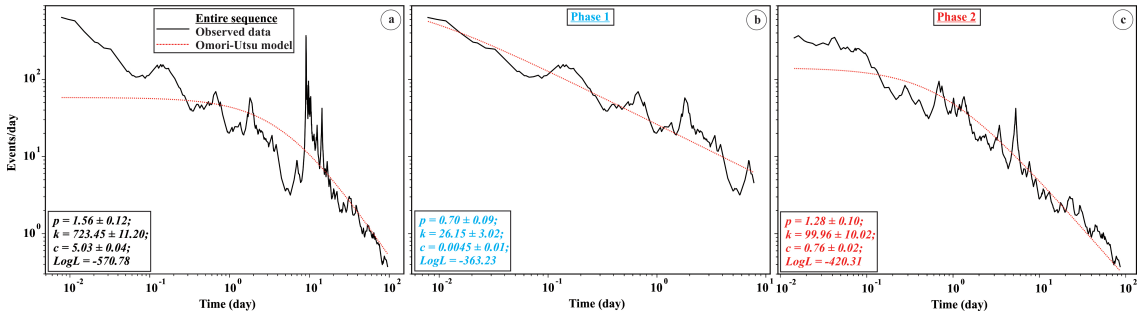

Figure 4.10: (a) Aftershock decay in comparison to the fit of the Omori-Utsu law of the entire sequence. (b) and (c) aftershock decay in comparison to the fit of the Omori-Utsu law for phases one and two respectively.

The examination of inter-event times through the modified gamma function (refer to chapter 1, section 1.4) unveiled a background rate (μ) of 1.36, signifying that 146 events (34%) were inde-

pendent, with a branching ratio (n) of 0.656 (Figure 4.11a). The distributions exhibit a strong correlation with the modified gamma function, while deviating significantly from an exponential distribution. The latter, expected in a Poissonian process where activity is uncorrelated in time.

To delve deeper into the evolution of the background rate, we employed a moving window approach, estimating it with windows of 100 events and a step size of 10 events (Figure 4.11b). The findings indicate an increase in the background rate following both BI-MS1 and BI-MS3, suggesting that the background contribution undergoes dynamic changes.

This dynamic evolution of the background rate provides valuable insights into the seismic activity's temporal behavior. The observed increase following significant mainshocks (BI-MS1 and BI-MS3) suggests a complex interplay between mainshock occurrences and subsequent changes in the background seismicity.

Additionally, the identification of 146 events (34%) operating independently underscores the heterogeneous nature of the seismic activity, with a substantial portion exhibiting a degree of autonomy from the mainshock-induced changes. This highlights the need for a nuanced understanding of the underlying processes governing seismicity, as it involves a combination of correlated and uncorrelated events.

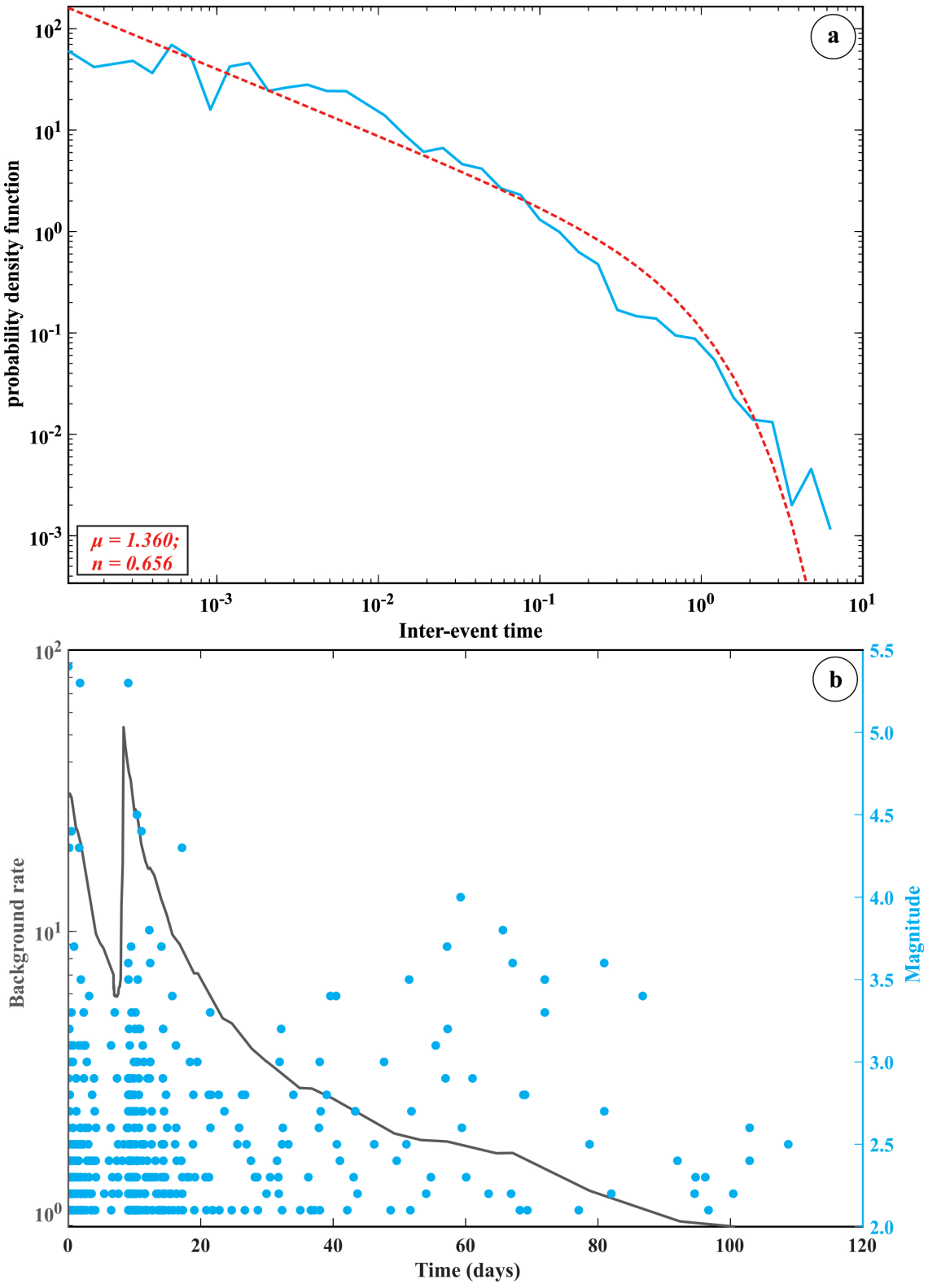

Figure 4.11: (a) Probability density function of inter-event time (balck line) with the gamma distribution fit (red dashed line). (b) Background event rate modeling with a moving window of 100 events using the inter-event time declustering.

We explored several probability distribution functions, such as the Weibull, Log-Normal, and Exponential functions, to model the inter-event time distribution (Figure 4.12). For each distribution, we conducted fitting for the scale parameter (α) and the shape parameter (β), except for the Exponential function, which only has a scale parameter, and the log-Normal, which comprises a log-scale and a log-shape, using the Akaike criterion. The results, along with each distribution function, are presented in Table 4.1.

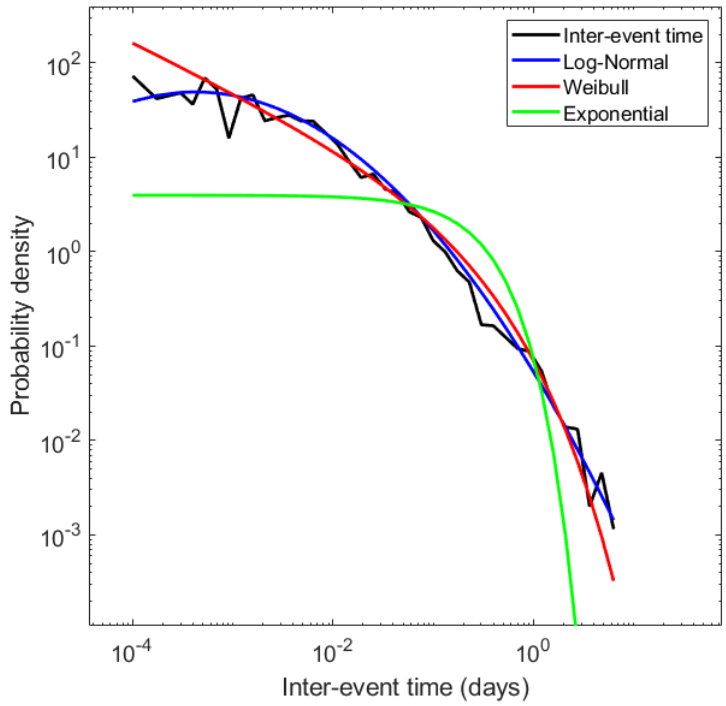

Figure 4.12: Probability density function of the inter-event times for the examined clusters along with the fit of different statistical distributions (Lognormal, Weibull, and Exponential).

It is commonly understood that the Exponential function is often used to characterize events assumed to be independent of each other in time. On the contrary, the Weibull and Log-Normal functions do not assume independence between events. As is known, the Exponential distribution is memoryless and does not take into account the preceding event, whereas the Log-Normal and Weibull distributions do consider the preceding event. Our findings reveal that the Log-Normal function provides the best fit for our model, having the lowest AIC (Table 4.1), capturing both short and long inter-event times. This suggests that earthquakes in our study are not independent but instead exhibit clustering behavior. The Log-Normal distribution, being more flexible, proves

to be a suitable model for capturing the complex temporal patterns observed in seismic events. However, it is important to note that no additional information about the temporal behavior can be inferred solely from these tests.

Distribution	Density function	α	β	AIC
Weibull	$\frac{\beta}{\alpha^{\beta}}\delta t^{\beta-1}e^{(\frac{\delta t}{\beta})^{\beta}}$	0.10	0.49	-1281.31
Log-Normal	$\frac{1}{\delta t\beta\sqrt{2\pi}}e^{-\frac{1}{2}(\frac{ln(\delta t-\alpha)}{\beta})^2}$	-3.34	2.10	-1513.02
Exponential	$\frac{1}{\alpha}e^{-\frac{\delta t}{\alpha}}$	0.25	-	-863.82

Table 4.1: Estimated parameters for the different distributions along with the AIC criteria.

We proceeded to estimate the parameters of the ETAS model (see chapter 1, section 1.4) (Figure 4.13a). The branching ratio was found to be less than 1 (0.48) with AIC = -1455.3, suggesting the assumption of a stable optimal model (Sornette and Werner, 2005). Plotting the cumulative number of events against transformed time revealed both negative and positive deviations (Figure 4.13b), indicating instances where the ETAS model overestimates and underestimates earthquake occurrences, respectively. The low $\mu - value$ of 0.17 implies a low forcing rate, signifying that only 4% of events are externally triggered. The obtained low $\alpha - value$ aligns with previous findings for swarm activities (0.35-0.85), distinguishing them from non-swarm activity characterized by higher $\alpha - values$ (1.2-3.1). Deviations in seismic activity, reflecting relative quiescence and activation in seismicity through downward and upward trends, are typically associated with changes in specific parameters (Kumazawa and Ogata, 2014).

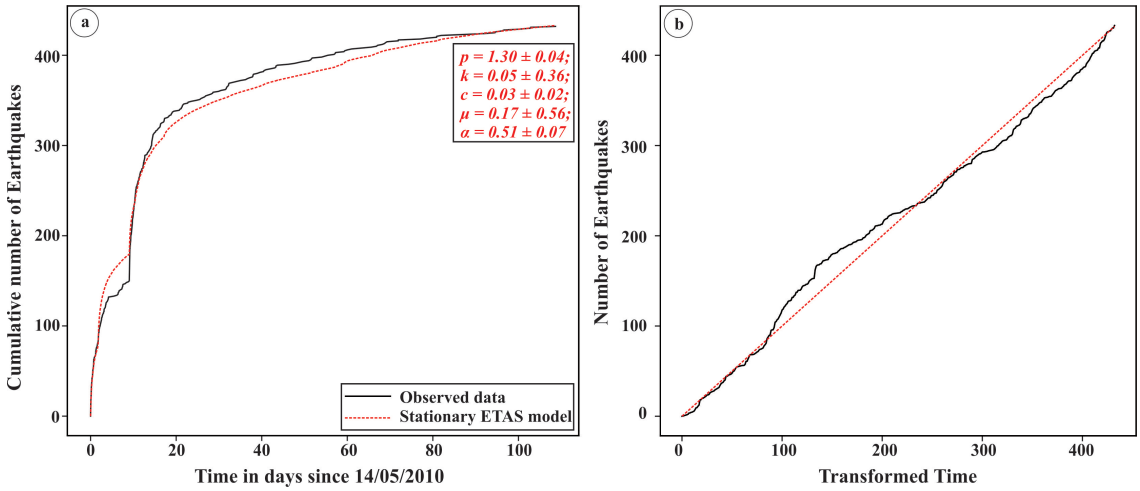

Figure 4.13: (a) Cumulative number of earthquakes observed and modeled. (b) Number of earthquakes versus transformed time according to the ETAS model.

To further examine the changes in the ETAS parameters, we implemented a moving window analysis with a window length of 100 events and a step size of 10 events. The four parameters, k, α, p, and c, were fixed based on our previously obtained results, and only the background rate (μ) was calculated for each window. This approach enables a detailed investigation into the temporal variations of the background seismicity rate while holding the other ETAS parameters constant. By fixing k, α, p, and c according to our findings, we isolate the changes in the background rate, allowing us to discern patterns and trends over successive windows of seismic events. The resulting figure (Figure 4.14) provides a visual representation of how the background rate evolves throughout the seismic sequence. Any discernible trends, spikes, or anomalies in the background rate within each window can offer valuable insights into the dynamic behavior of seismicity following specific triggering events.

This analysis complements our earlier examination of the inter-event time distribution and enhances our understanding of the temporal dynamics of seismic activity. It serves as a targeted exploration of how the background seismicity rate responds to variations in the seismic sequence, shedding light on potential correlations with mainshocks or other influencing factors. In addition, the temporal evolution of the background rate with the ETAS model reveals a similar trend to that observed for the background rate with inter-event time distribution using the same window length. Notably, the increase in the background rate just after BI-MS3 doesn't decrease sharply but instead

shows a more gradual, resembling an envelope-like pattern in the part where high seismic activity is observed (Figure 4.14).

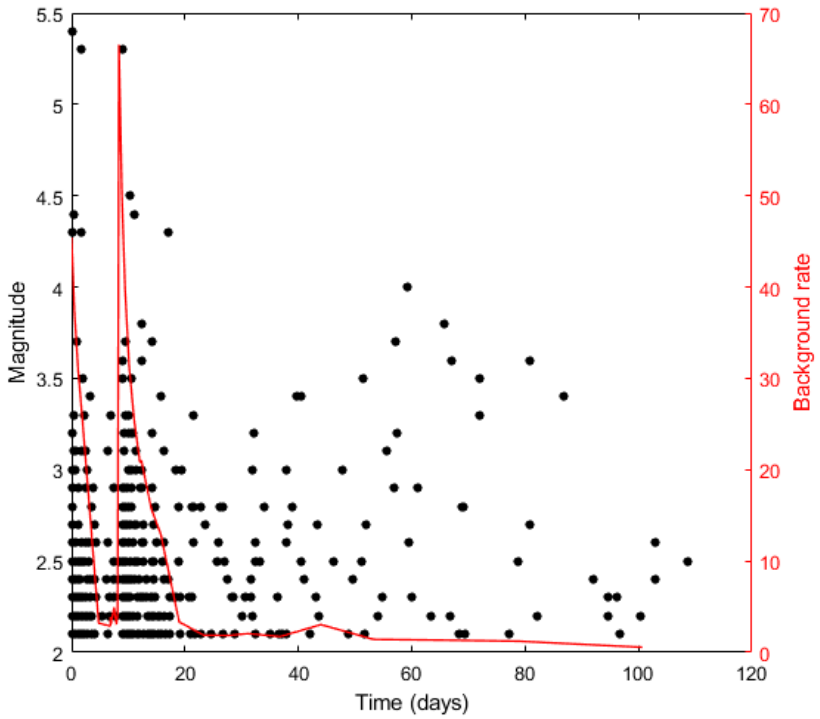

Figure 4.14: Background event rate modeling with a moving window of 100 events using the ETAS parameters.

Furthermore, we applied the spatio-temporal ETAS model (refer to chapter 1, section 1.5). The resultant parameters found are μ=1.00, k=0.027, c=0.018 days, p=1.53, α=0.98, D=1.2 km², q=2.71, and γ=1.17. The temporal and magnitude-related parameters (k, α, c, p) increased compared to the conventional temporal ETAS model. The trade-off between k and α is respected, as it has been proven that an increase in the $\alpha - value$ leads to a decrease in the $k - value$. We also observe an increase in the $p - value$, suggesting a faster decay for aftershocks.

Analyzing the spatial parameters (D, q, γ), we find that the effective triggering distance for direct aftershocks is associated with a small area, especially considering the high $q - value$ (2.71), which represents a faster decay in space for aftershocks (Figure 4.15). This implies that the triggering effect is confined to a limited region.

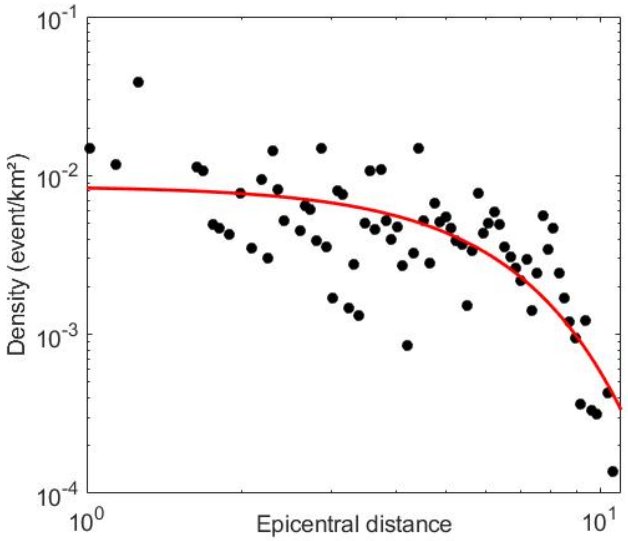

Figure 4.15: Spatial decay of aftershocks reltive to BI-MS1.

Moreover, the ETAS model assumes a constant background rate in time, and neglecting its temporal variation can introduce bias in parameter estimation (refer to chapter 2, section 2.5). Consequently, we employed a time-dependent background rate ETAS model, providing a better fit to the observations with an improved AIC (-1553.24) for a smoothing window equal to 12 (Figure 4.16).

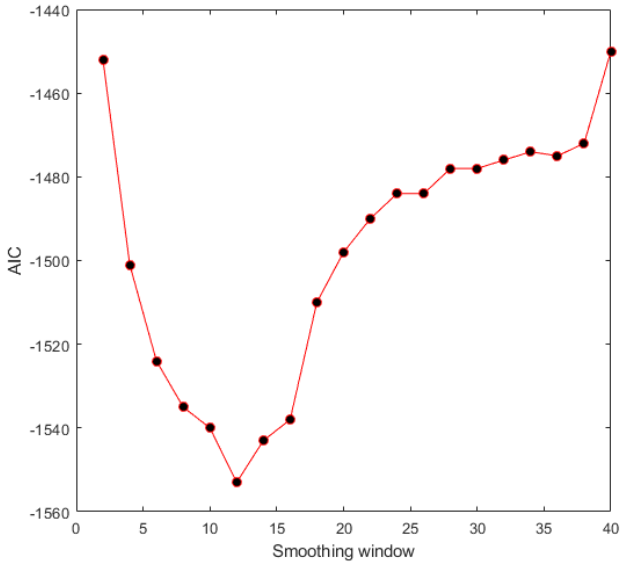

Figure 4.16: AIC for each smoothing window.

The higher $\alpha - value$ obtained, compared to the constant background rate ETAS model, is consistent with results found by Hainzl et al., 2013, suggesting that considering a constant background rate may underestimate the $\alpha - value$. The proportion of background events in the entire sequence is 52%, surpassing typical percentages observed in mainshock-aftershock sequences. Seismicity exhibits non-stationarity during the BI-MS1 and BI-MS-3 mainshocks, transitioning to a stationary trend after each event (Figure 4.17a). Notably, there is an increase in the background rate following the BI-MS1 mainshock and a sudden surge in the forcing rate after the BI-MS3 mainshock (Figure 4.17b). This pattern aligns with observations made in both the inter-event time analysis and the conventional temporal ETAS model, when employing a moving window.

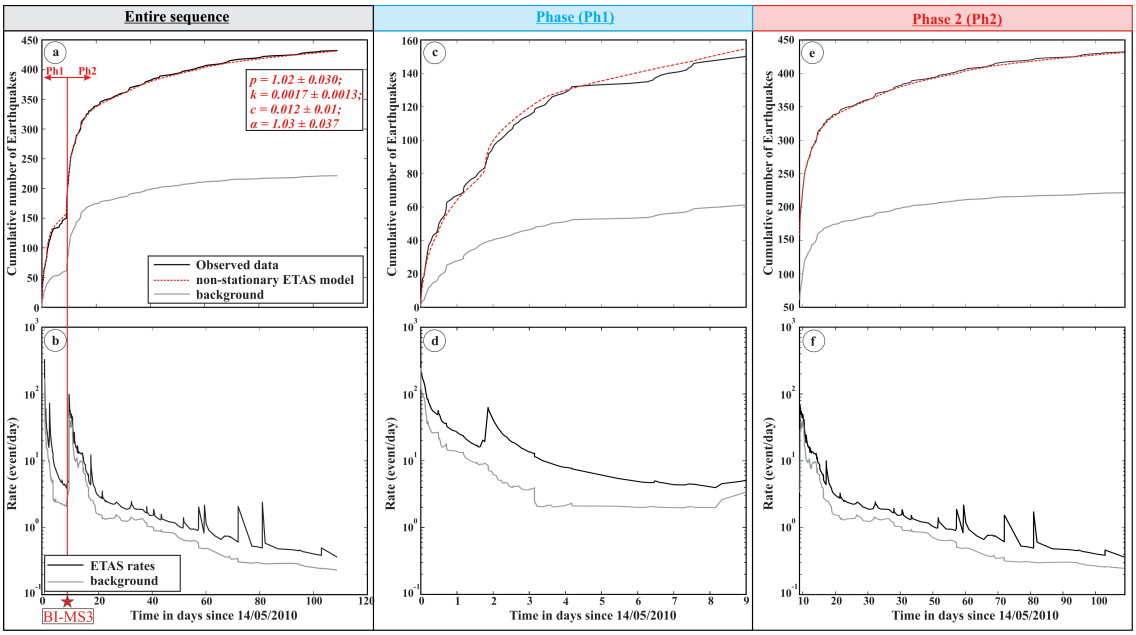

Figure 4.17: (a) Cumulative number of earthquakes observed and modeled with the non-stationary ETAS model of the entire sequence. The cumulative number of background events is also shown. (b) The event rate modeled and the background. (c) and (e) The cumulative number of events observed and modeled, along with the cumulative number of background events, for phase 1 and 2 respectively. (d) and (f) the event rate modeled and the background rate for phase 1 and 2, respectively

In the first phase, as revealed in the declustering analysis, background events constitute a small proportion of overall seismicity (43%) (Figure 4.17c). The seismicity rate initially increases in response to the rise in the background rate before reaching a more or less stationary state over time (Figure 4.17d). In the second phase, the contribution of background events to seismicity increases

to 53%. The abrupt increase in the number of events is reflected in the cumulative number of background events, corresponding to the BI-MS3 mainshock of 5.3 ML (Figure 4.17e). This rise is also mirrored in the event rate over time, aligning with the background contribution rate (Figure 4.17f). After approximately 40 days, the trend shifts, and the background seismicity no longer mirrors the rise in the cumulative number of events, indicating a stationary process (Figure 4.17e). The magnitude evolution with scaled colors based on background probability (Figure 4.18) reveals that events with the highest background probability are mainly located in the second phase, corresponding to the increase in background rate (Figure 4.17f). The spatial plot of background and aftershock seismicity (Figure 4.19a) also illustrates two distinct phases. In the first phase, most seismicity is concentrated in the E-W cluster and primarily comprises aftershocks (Figure 4.19a). Conversely, in the second phase, the majority of seismicity is observed in the NNE-SSW cluster and mainly consists of background events.

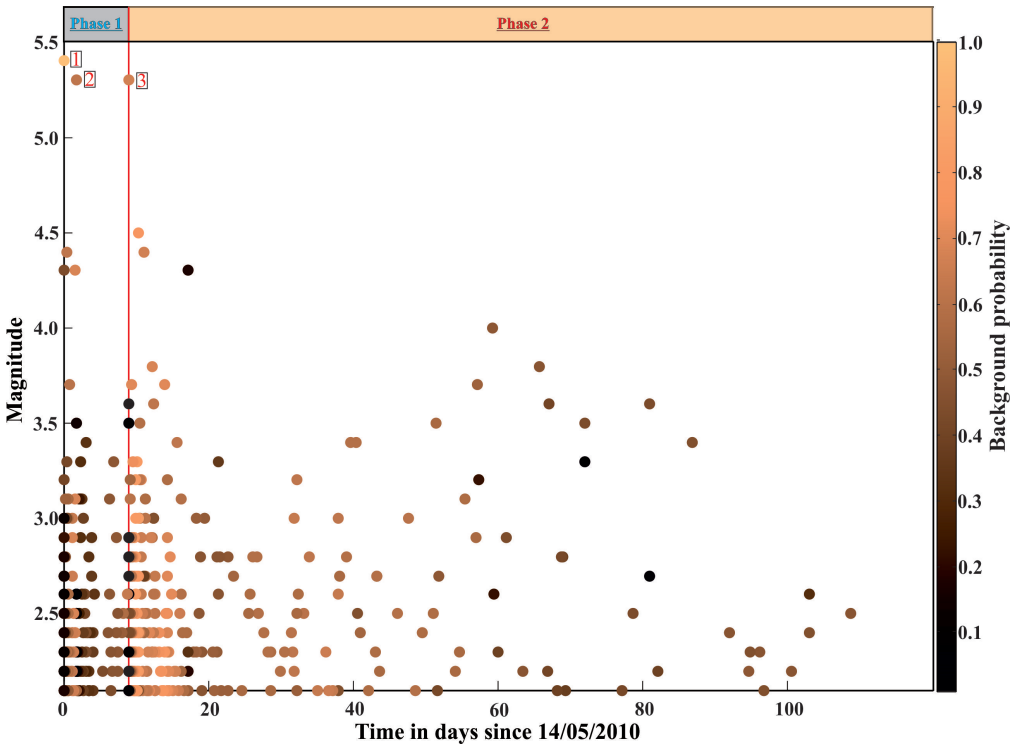

Figure 4.18: Magnitude against time with scaled colors based on background probability.

We have also determined the proportion of background events for each background probability exceeding 50% (Table 4.2).

data	>0.9(%)	>0.8(%)	>0.7(%)	>0.6(%)	>0.5(%)
Whole sequence	0.23	6.23	19.8	48	69
Phase 01	0.23	0.23	1.8	6	14
Phase 02	0	6	18	41	55

Table 4.2: Per cent of events for different background probabilities.

We observe that the second phase exhibits the highest number of events with a background probability exceeding 50%. In fact, over half of the sequences are indicative of external triggers. Additionally, this trend underscores the significance of external influences during this particular phase.

4.5 Discussion and interpretation of the results

The seismic sequence in Beni-Ilmane stands out as one of the most significant events in Algeria in terms of event count. Despite more than a decade passing, numerous mysteries surrounding this sequence remain incompletely understood. The occurrence of a moderate earthquake generating such a multitude of seismic events is noteworthy. Fortunately, the sequence comprised three mainshocks of the same magnitude, indicating that the energy release was divided among at least two primary faults, averting the potential for a catastrophic earthquake.

To gain deeper insights into the unprecedented 2010 Beni-Ilmane earthquake sequence, we conducted a comprehensive statistical investigation of seismicity. Our analysis reveals significant changes in earthquake generation pathways. Utilizing probabilistic estimations in two main phases, the declustering technique allows us to differentiate between background and aftershock contributions (see Figure 4.18).

The first phase spans from the initial mainshock (BI-MS1) on May 14, 2010, to the third mainshock (BI-MS3) on May 23, 2010. Mainshocks on May 14 and 16 (BI-MS2) played a crucial role in triggering aftershocks during this period. Approximately 57% of events in this phase are self-triggered. The $b-value$ of 0.82 suggests high stress, with the Omori-Utsu law's $p-value$ indicating a slow decay over time, possibly accompanied by slow stress relaxation.

The second phase begun just after BI-MS3 (May 23), featuring the highest number of events in the entire sequence, predominantly characterized by a high number of background events (53%). A sudden increase in forcing rate occurs post-BI-MS3, indicating that, in addition to stress changes triggering aftershocks, BI-MS3 induced aseismic transients. This induced additional earthquakes (background events) – potentially caused by phenomena like breaking a sealed source and fluid infiltration. Compared to the initial phase, a rise in the $p - value$ suggests a faster decay rate, possibly indicating fast stress relaxation, with a $b - value$ of 0.90, typical for natural fluid-driven seismicity (Lei et al., 2013).

Figure 4.19 illustrates a spatial plot of seismic events color-coded by background probability. During the first phase (Figure 4.19a), triggered aftershocks are more apparent in Cluster 1 along the E-W direction, with some occurring in Cluster 2. Following BI-MS3 in the second phase (Figure 4.19a), Cluster 2 experiences a significant increase in background events along the NNE-SSW direction. Thus, based on the spatio-temporal distribution of background probability (Figure 4.18 and 4.19), we conclude that the 2010 Beni-Ilmane earthquake sequence began with triggered aftershocks from BI-MS1 and BI-MS2, mainly along Cluster 1 in the E-W direction. Subsequently, background events emerged after BI-MS3 along Cluster 2 in the NNE-SSW direction.

Our findings align with a recent study by Abacha et al., 2023a, employing local earthquake tomography and 4-D Vp/Vs models, providing evidence that the processes triggering the 2010 Beni-Ilmane earthquake sequence were fluid-driven. Their study revealed a high-Vp/Vs anomaly in the central part post-BI-MS3, interpreted as fluid-saturated rocks and suggesting a hydrocarbon reservoir presence. Replicating their work for the two phases revealed by our study confirms a high-Vp/Vs anomaly appearing immediately post-BI-MS3 in the second phase.

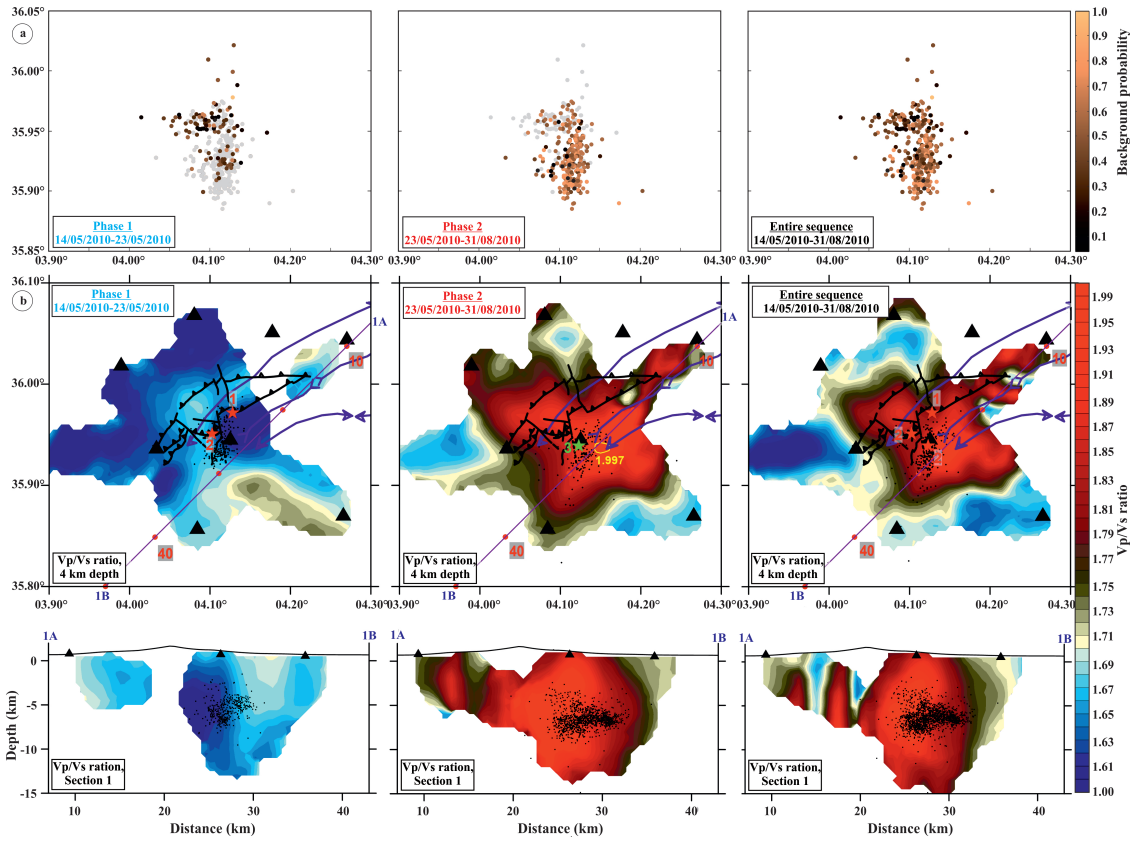

Figure 4.19: (a) Spatial plot of background and aftershock seismicity relocated for the two phases and the entire seismicity. Scaled colors are based on background probability and grey points are the whole seismicity. (b) Vp/Vs ratios in horizontal sections at depth of 4 km for the first, second phase and the entire sequence with their cross-sections.

Abacha et al., 2023a also investigated seismicity migration, modeling seismic events using the equation of Shapiro et al., 1997. They found a good fit on Cluster 2 with reduced diffusivity and a migration velocity, indicating a pore-pressure diffusion mechanism with a time-delayed response (Figure 4.3). Our results support their conclusions, emphasizing the significant role played by fluids in the production of Cluster 2. Additionally, upon plotting the spatial distribution of the background rate using the spatio-temporal ETAS model, there is a noticeable concentration of the highest values in the Cluster 2 (see Figure 4.20).

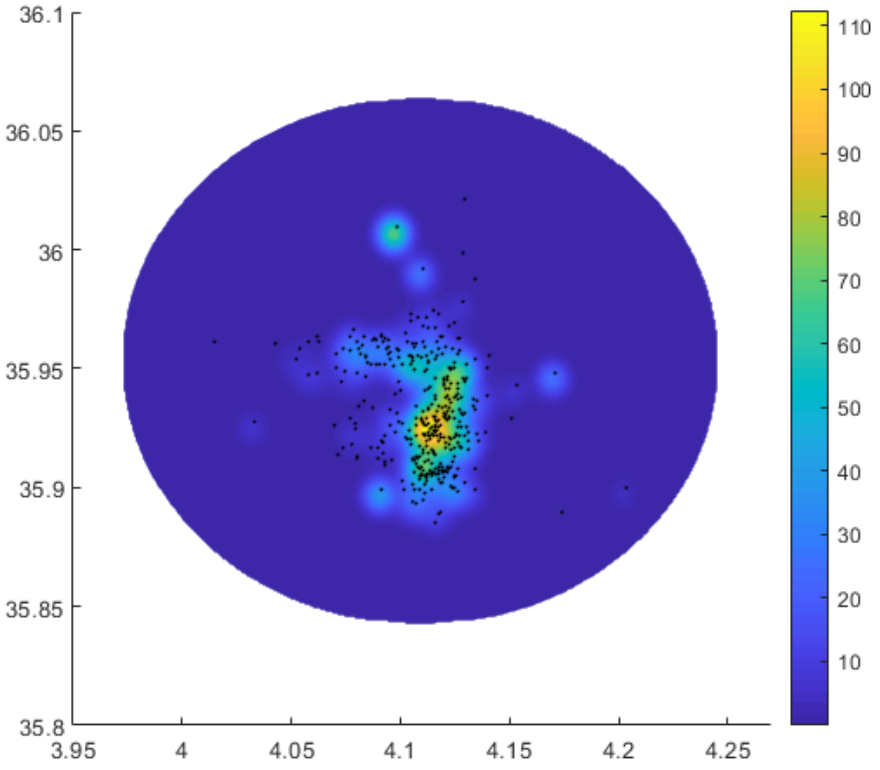

Figure 4.20: Background rate in space, accompanied by a plot of events.

In summary, our study of the Beni-Ilmane Earthquake sequence reveals a triggering process combining tectonic seismicity and aseismic forcing, occurring over a 4-month period from May 14 to August 31, 2010. The rupture of the NNE-SSW by BI-MS3 released high-pressure fluids that moved upward, triggering earthquakes by causing pore-pressure perturbations. Our findings align with examples of mixed seismic mechanisms in moderate to low seismic sequences worldwide, emphasizing the crucial role of fluids in such events.

Furthermore, the involvement of fluids in earthquake sequences is well-documented in Northeastern Algeria, including the 2012-2013 Bejaia-Babors seismic sequence, the 2015 Ain Azel sequence, and the 2020 Mila sequence. Future applications of the methodology used in this study aim to determine the seismic mechanisms behind these sequences through time-dependent and spatio-temporal statistical analysis.

4.6 Conclusion

In conclusion, this study provides a comprehensive investigation into the seismic activity in Algeria following the 2003 Boumerdes earthquake (Mw 6.9), with a specific focus on the intriguing 2010 Beni-Ilmane earthquake sequence. Unfolding over a four-month period starting from May 14, 2010, in the transition zone between the Bibans and Hodna mountains, this seismic event has been a subject of significant inquiry. The Beni-Ilmane sequence, marked by three mainshocks (BI-MS1, BI-MS2, and BI-MS3) with a magnitude of Mw$\geq$5.3, coupled with a notable clustering of events in two primary orientations (E-W and NNE-SSW), has presented a complex seismic puzzle. The seismic mechanism underlying this sequence has remained elusive, prompting our in-depth analysis.

The application of the Epidemic Type Aftershock Sequences (ETAS) model, coupled with a comparative examination using 4D Vp/Vs models, has allowed us to delineate two distinct phases in the sequence. During the initial phase (May 14-23), an intense earthquake sequence dominated seismicity, primarily propelled by aftershocks of BI-MS1 and BI-MS2. Stress changes induced by these mainshocks facilitated a subsequent aseismic process, significantly contributing to the observed seismic activity. In the second phase, following the occurrence of the third mainshock (BI-MS3), aseismic forcing (constituting 53% of the background contribution) manifested along the second cluster. The rupture of the fault by BI-MS3 led to the upward flow of high-pressure fluids through the damage zone, triggering earthquakes through pore-pressure perturbations. Supporting this conclusion is the observation of a high-Vp/Vs anomaly immediately after BI-MS3, suggestive of a hydrocarbon reservoir in the central part of the studied region.

The statistical analysis, incorporating temporal characteristics and the Gutenberg-Richter law, significantly advances our comprehension of the underlying mechanisms. This contribution is pivotal in refining seismic hazard models, underscoring the importance of extending similar studies to other sequences in the Northern part of Algeria. Furthermore, the broader implications of naturally fluid-driven seismicity, as highlighted by Atkinson, 1984, emphasize that regions with low-to-moderate seismic activity may face heightened seismic hazards. This study reinforces the notion that naturally fluid driven seismicity can substantially elevate earthquake rates, potentially

triggering events of considerable magnitude. Additionally, insights from Lei et al., 2013 regarding fluid-driven seismicity's potential to extend rupture lengths and generate larger earthquakes over time further accentuate the importance of understanding such phenomena.

It is noteworthy that the outcomes of this study have been disseminated through publication in Geophysical Journal International (GJI) Rahmani et al., 2023. Moreover, an ongoing study by Tikhamarine et al. (under review at GJI), where I am a co-author, further delves into the intricacies of the generation mechanism responsible for the seismicity. This forthcoming study includes a detailed analysis of repeating events and multiplets, complemented by a comprehensive spectral analysis.

General conclusion

This thesis endeavors to elucidate the spatio-temporal evolution of seismicity in the Northeastern part of Algeria through a comprehensive statistical analysis. Notably, this region has witnessed numerous earthquake sequences exhibiting consistent magnitudes, spatial distributions, and temporal patterns over the past decades. Since no study involving understanding the statistical parameters to describe the ongoing process has been done before, this thesis aims to fill this gap by categorizing seismic sequences according to their spatio-temporal pattern and uncovering the full complexity of one of the sequences, which is the Beni-Ilmane seismic sequence.

A thorough grasp of statistical models is indispensable, considering that each technique comes with its distinct set of advantages and drawbacks. Moreover, interpreting the results in alignment with the underlying physical processes proves to be challenging and intricate, primarily due to the unique tectonic characteristics exhibited by each region. Despite the passage of centuries and decades, the quest for a singular, all-encompassing model capable of effectively explaining every seismic sequence has remained elusive. This emphasizes the inherent complexity of seismic phenomena and underscores the imperative for nuanced, region-specific approaches in earthquake studies.

However, it is noteworthy that the ETAS model emerges as a cutting-edge tool for comprehending earthquake behavior. Recent developments in the model have demonstrated efficacy in modeling spatio-temporal patterns of earthquakes, with each parameter holding its distinct physical interpretation. Additionally, the G-R law, particularly with the $b-value$, retains its status as the sole model that provides a comprehensive understanding of magnitude distribution. It stands out as the only model requiring minimal information to understand the stress state of a specific region.

Recognizing the necessity to transition to physically-based statistical models is crucial, as these two domains are complementary. The combination of both can be exceptionally powerful in understanding the physical processes generating earthquakes, as recent developments in the field have illustrated. Finally, it is essential not to view statistical analysis as a simple 'add-on' in every study, but rather as potent complementary information that can even stand alone in certain cases. Understanding its role and potential in seismic research is key to harnessing its full capabilities for a comprehensive exploration of earthquake dynamics.

Although these models can be powerful, they are susceptible to bias if we do not carefully understand the earthquake catalog, which is the sole information needed for statistical studies. The parameters of these models can be significantly biased if we do not ensure that the processes of magnitude determination and location have been executed properly. One parameter, in particular, stands out as the most crucial, namely m_c. As elucidated in the thesis, opting for a small m_c can introduce bias into statistical analyses, while selecting a larger one may result in a loss of information. Striking the right balance to capture the appropriate m_c and, by extension, the right patterns is challenging but crucial. I encountered challenges in this aspect throughout the thesis and conducted a reevaluation of the detection, location, and magnitude determination process, especially to mitigate STAI. Even with the application of recent detection techniques, this incompleteness cannot be entirely eliminated due to its inherent connection to the nature of seismic events.

I find inspiration in a statement from a colleague at ETHZ, as expressed in one of her article title: "Embracing data incompleteness instead of avoiding it" by Mizrahi et al., 2021a. In my opinion, this is a powerful statement, and indeed, recent techniques such as the rate-dependent m_c from Hainzl, 2016a or the long-term m_c from Mizrahi et al., 2021a have proven effective in recovering the true statistical parameters without a loss of information. Another potentially controversial bias involves the impact of declustering on the estimation of the $b - value$. As explained in chapter 2, section 2.3, the $b - value$ is substantially underestimated when using the Gardner-Knopoff technique compared to stochastic declustering, as highlighted in various studies (Mizrahi et al., 2021b; Eroglu Azak et al., 2018). Choosing the right technique for declustering and understanding the regional catalog is crucial before attempting to decluster. It is also essential to emphasize that studying aftershocks is as important as studying mainshocks, given their potential for causing

damage. Additionally, acknowledging the capability of small earthquakes to generate larger ones is crucial.

Other issues related to the impact of aseismic transients were explored, as swarm activities are mostly generated by aseismic transients, and neglecting them may lead to biases in the productivity of the ETAS model (Hainzl et al., 2013). Furthermore, aseismic transients are significant, as every sequence may exhibit these phenomena (afterslip, fluid intrusion, etc.), confirming their importance in statistical analysis. Finally, the anisotropic distribution of aftershocks is one of the key elements in the spatial characterization of aftershocks.

These statistical models not only excel in characterizing earthquake sequences or general earthquake behavior, but they also prove to be powerful tools for detecting temporal and spatial anomalies known as swarms. As explained, the Northeastern part of Algeria has witnessed numerous sequences in recent decades, underscoring the importance of categorizing them into whether they are swarms or aftershock sequences. To achieve this, we employed two independent techniques for swarm detection, ensuring the reliability of our results.

We utilized the earthquake catalog from the Algerian Digital Network spanning from 2007 to 2020, comprising 9000 events. The region was divided into a grid of 0.2°x0.2°, and the spatial magnitude of completeness was calculated, with the highest value set at 2.8, resulting in 2634 events available for analysis. The first technique involved the spatio-temporal ETAS model, wherein parameters were calculated, and the '1σ criterion' introduced by Nishikawa and Ide, 2017 was applied. This identified 313 events as swarm events, constituting 13% of the overall seismicity.

The second technique utilized the determination of skewness and kurtosis of the temporal distribution of seismic moment release (Mesimeri et al., 2019). Aftershock sequences typically exhibit the highest moment release at the beginning, linked to the mainshock, while seismic swarms display the highest seismic moment release in the middle of the sequence or towards the end. Results from this technique identified 621 swarm events, representing 26% of the entire seismicity.

Despite the independence of both techniques, they revealed the same clusters, with variations in the number of events. This discrepancy is explained by the fact that the first technique considers events from clusters as having swarm behavior, whereas the second method determines if each

cluster exhibits swarm behavior. The swarms detected by both techniques were merged, resulting in a total of 676 events classified as swarm events. Each cluster was then assigned to a zone, and interpreting the generation mechanism of each swarm proved challenging. Some were interpreted as being generated by fluid intrusion, others by static and dynamic stress transfer, while some remain ambiguous in their interpretation. Future studies will delve into each cluster independently, employing additional statistical analyses. However, the current challenge lies in the low number of earthquakes in some clusters, making further investigation difficult at this stage.

One sequence, in particular, stands out among the detected swarms due to its unprecedented complexity and the number of earthquakes involved. This is the Beni-Ilmane seismic sequence, which displays spatio-temporal migration and includes three shocks with magnitudes above 5. Despite several conducted studies (Yelles-Chaouche et al., 2014;Beldjoudi et al., 2016;Hamdache et al., 2017;Abacha et al., 2019), this sequence has not yet unveiled all its secrets, making it an exceptionally intriguing natural laboratory in Algeria. The abundance of high-quality data adds to its attractiveness and stimulates curiosity.

Our reevaluation of this sequence unfolded in three steps. Firstly, a 4D tomography was performed, revealing the intrusion of fluid later in the sequence, interpreted as hydrocarbon by Abacha et al., 2014, particularly after the third-largest shock. This discovery points to a combination of stress transfer and aseismic transient forcing responsible for generating the sequence (Abacha et al., 2023a).

The second step involved a detailed statistical analysis to identify the periods when fluid intrusion occurred. Using the non-stationary ETAS model, we identified two phases. The first phase, spanning from the 14th of May to the 23rd, primarily encompassed aftershock sequences, revealing a stationary process for aseismic rate. On the other hand, the second phase indicated a transient aseismic forcing rate, leading to an increase in the number of independent events. This correlation with the tomography suggests a potential connection to fluid dynamics. The temporal evolution between the two phases of the $b - value$ of the Gutenberg-Richter law and the p-value from the Omori-Utsu law revealed similar processes. Additionally, the study included an examination of the temporal evolution of the inter-event time background rate and the stationary ETAS model parameters, highlighting the non-stationarity of the background rate (Rahmani et al., 2023).

The final step delved into the study of repeating events, grouping them together based on the similarity of their respective waveforms. This in-depth investigation aimed to understand how each group evolves in time and space and the physical interactions between them. The detailed study unveiled a combination of many processes responsible for the generation of the sequence. Excitingly, more studies are planned for the future, as the mystery surrounding this sequence remains intriguing and may require unconventional approaches for a comprehensive understanding (Tikhamarine et al., under review).

While this thesis represents a humble contribution to the Algerian research community and contributes to the field of statistical seismology, it is essential to acknowledge that we are still far from a complete understanding of the physical processes responsible for Algerian seismicity. The complexity of seismic phenomena in this region demands continuous exploration and investigation.

Looking ahead, I am hopeful and eager to persist in contributing to this field. Numerous ideas are currently circulating in my mind, including collaborative efforts with Sebastian Hainzl from GFZ to enhance the ETAS model. Collaborating with our research team in Algeria will further enable us to characterize earthquake sequences and delve deeper into comprehending the intricacies of seismic activity in the region.

Furthermore, I aspire for this thesis to serve as a valuable resource for upcoming researchers venturing into the realm of statistical seismology. My desire is that it not only provides knowledge but also sparks enthusiasm and attention, fostering a deeper appreciation for the complexities involved. As the journey in seismic research is ongoing, I remain committed to contributing and expanding our understanding of earthquake dynamics in Algeria and beyond.

Bibliography

Abacha, I. (2015). *Étude de la sismicité de la région nord-est de l'Algérie*. PhD thesis, Université Ferhat Abbas - Sétif 1.

Abacha, I., Bendjama, H., Boulahia, O., Yelles-Chaouche, A., Roubeche, K., Rahmani, S. T., Meliam, M. A., and Tikhamarine, E.-M. (2023a). Fluid-driven processes triggering the 2010 beni-ilmane earthquake sequence (algeria): evidence from local earthquake tomography and 4-d vp/vs models. *Journal of Seismology*, 27(4):77–94.

Abacha, I., Boulahia, O., Yelles-Chaouche, A., Bendjama, H., Fossen, H., Chabou, M., Khaled, R., Rahmani, S. T.-E., El-Mahdi, T., Mohammedi, Y., and Aidi, C. (2023b). The 24 january 2020 mw 5.0 el aouana earthquake, northeastern algeria: Insights into a new nw-se right-lateral bejaia-babors shear zone. *Pure and Applied Geophysics*, 180(3):1945–1971.

Abacha, I., Boulahia, O., Yelles-Chaouche, A., Semmane, F., Beldjoudi, H., and Bendjama, H. (2019). The 2010 beni-ilmane, algeria, earthquake sequence: statistical analysis, source parameters, and scaling relationships. *Journal of Seismology*, 23(3):181–193.

Abacha, I., Koulakov, I., Semmane, F., and Yelles-Chaouche, A. K. (2014). Seismic tomography of the area of the 2010 beni-ilmane earthquake sequence, north-central algeria. *SpringerPlus*, 3(2):650–667.

Abacha, I. and Yelles-Chaouche, A. (2019). *Overview of Recent Seismic Activity in Northeastern Algeria: Trends and Applications in Science and Engineering*, pages 203–206.

Abacha, I., Yelles-Chaouche, A., and Boulahia, O. (2022). *Statistical Study of Earthquake Swarms*

in Northeastern Algeria with Special Reference to the Ain Azel Swarm; Hodna Chain, 2015, pages 145–148.

Akaike, H. (1974). A new look at the statistical model identification. *IEEE Transactions on Automatic Control*, 19(6):716–723.

Aki, K. (1965). Maximum likelihood estimate of b in the formula logn=a-bm and its confidence limits. *Bulletin of Earthquake Research*, 43(2):237–239.

Amorese, D. (2007). Applying a Change-Point Detection Method on Frequency-Magnitude Distributions. *Bulletin of the Seismological Society of America*, 97(5):1742–1749.

Atkinson, B. K. (1984). Subcritical crack growth in geological materials. *Journal of Geophysical Research: Solid Earth*, 89(B6):4077–4114.

Atkinson, G. M. and Adams, J. (2013). Ground motion prediction equations for application to the 2015 canadian national seismic hazard maps. *Canadian Journal of Civil Engineering*, 40(10):988–998.

Beldjoudi, H. (2020). Fault interaction for the beni-ilmane (east of algeria) seismic sequence on may 2010. *Arabian Journal of Geosciences*, 13(5):959–975.

Beldjoudi, H., Delouis, B., Djellit, H., Yelles-Chaouche, A., Gharbi, S., and Abacha, I. (2016). The beni-ilmane (algeria) seismic sequence of may 2010: Seismic sources and stress tensor calculations. *Tectonophysics*, 670(3):101–114.

Beldjoudi, H., Guemache, M., Kherroubi, A., Semmane, F., Yelles-Chaouche, A., Djellit, H., Amrani, A., and Haned, A. (2009). The laalam (bejaa, north-east algeria) moderate earthquake (m-w=5.2) on march 20, 2006. *Pure and Applied Geophysics*, 166(2):623–640.

Bellalem, F., Talbi, A., Maouche, S., and Mobarki, M. (2023). Analysis of statistical features of the parametric earthquake catalog for algeria and adjacent regions (pecaar): case of the maximum magnitude estimation in northern algeria. *Mediterranean Geoscience Reviews*, 5(3):63–76.

Ben-Zion, Y. and Lyakhovsky, V. (2006). Analysis of aftershocks in a lithospheric model with seismogenic zone governed by damage rheology. *Geophysical Journal International*, 165(1):197–210.

Bendjama, H. (2022). *Caractérisation des séquences sismiques récentes dans la région tectonique de la faille décrochante de Mcid Aïcha-Debbagh, Nord-Est de l'Algérie*. PhD thesis, Université de Tlemcen - Abou Bekr Belkaid.

Bendjama, H., Yelles-Chaouche, A., Boulahia, O., Abacha, I., Mohammedi, Y., Beldjoudi, H., Rahmani, S. T.-E., and Belheouane, O. (2021). The march 2017 earthquake sequence along the e-w-trending mcid aïcha-debbagh fault, northeast algeria. *Geosciences Journal*, 25(5):697–713.

Benouar, D., Aoudia, A., Maouche, S., and Meghraoui, M. (1994). The 18 august 1994 mascara (algeria) earthquake—a quick-look report. *Terra Nova*, 6(6):634–638.

Bird, P. (2003). An updated digital model of plate boundaries. *Geochemistry, Geophysics, Geosystems*, 4(3):10–20.

Bohnenstiehl, D., Tolstoy, M., Dziak, R., Fox, C., and Smith, D. (2002). Aftershock sequences in the mid-ocean ridge environment: an analysis using hydroacoustic data. *Tectonophysics*, 354(1):49–70.

Bougrine, A. (2019). *Champ de vitesses crustal et déformation de l'Atlas a partir de mesures GNSS permanentes*. PhD thesis, Université de Tlemcen - Abou Bekr Belkaid.

Bougrine, A., Yelles-Chaouche, A. K., and Calais, E. (2019). Active deformation in Algeria from continuous GPS measurements. *Geophysical Journal International*, 217(1):572–588.

Boulahia, O. (2022). *Identification, caractérisation et interaction des sources sismiques : Implication sur des séquences d'évènements sismiques de la période 2010-2021 dans le Nord-Est Algérien*. PhD thesis, Université Ferhat Abbas - Sétif 1.

Boulahia, O., Abacha, I., Yelles-Chaouche, A., Bendjama, H., Kherroubi, A., Mohammedi, Y., Aidi, C., and Chami, A. (2021). Recent seismic activity in the bejaia–babors region (northeastern algeria): The case of the 2012–2013 bejaia earthquake sequences. *Pure and Applied Geophysics*, 178(6):1253 – 1279.

Bounif, A., Haessler, H., and Meghraoui, M. (1987). The constantine (northeast algeria) earthquake of october 27, 1985: surface ruptures and aftershock study. *Earth and Planetary Science Letters*, 85(4):451–460.

Bourouis, S. and Cornet, F. (2009). Microseismic activity and fluid fault interactions: some results from the corinth rift laboratory (crl), greece. *Geophysical Journal International*, 178(1):561–580.

Brodsky, E. E., Karakostas, V., and Kanamori, H. (2000). A new observation of dynamically triggered regional seismicity: Earthquakes in greece following the august 1999 izmit, turkey earthquake. *Geophysical Research Letters*, 27(17):2741–2744.

Calò, M., Dorbath, C., Cornet, F., and Cuenot, N. (2011). Large-scale aseismic motion identified through 4-D P-wave tomography. *Geophysical Journal International*, 186(3):1295–1314.

Cao, A. and Gao, S. S. (2002). Temporal variation of seismic b-values beneath northeastern japan island arc. *Geophysical Research Letters*, 29(9):48–1–48–3.

Chen, X. and Shearer, P. (2011). Comprehensive analysis of earthquake source spectra and swarms in the salton trough, california. *Journal of Geophysical Research: Solid Earth*, 116(B9):111–134.

Chinnery, M. A. (1963). The stress changes that accompany strike-slip faulting. *Bulletin of the Seismological Society of America*, 53(5):921–932.

Corral, A. (2003). Local distributions and rate fluctuations in a unified scaling law for earthquakes. *Phys. Rev. E*, 68(3):35–46.

Crespo-Martín, C., Martín-González, F., Yazdi, P., Hainzl, S., and Rincón, M. (2021). Time-dependent and spatiotemporal statistical analysis of intraplate anomalous seismicity: Sarria-Triacastela-Becerreá (NW Iberian Peninsula, Spain). *Geophysical Journal International*, 225(1):477–493.

Cristelli, M. (2014). *Universal Relation Between Skewness and Kurtosis in Complex Dynamics*, pages 141–150.

Dabouz, G., Beldjoudi, H., Delouis, B., Boulahia, O., Mohammedi, Y., and Yelles-Chaouche, A. (2021). The 2007 medea seismic sequence, north-central algeria: Source parameters, stress tensor, and static stress changes. *Pure and Applied Geophysics*, 178(2):3313–3337.

Dahm, T. and Hainzl, S. (2022). A coulomb stress response model for time-dependent earthquake forecasts. *Journal of Geophysical Research: Solid Earth*, 127(9):24–43.

Das, S. and Scholz, C. H. (1981). Theory of time-dependent rupture in the earth. *Journal of Geophysical Research: Solid Earth*, 86(B7):6039–6051.

Davis, S. D. and Frohlich, C. (1991). Single-link cluster analysis, synthetic earthquake catalogues, and aftershock identification. *Geophysical Journal International*, 104(2):289–306.

de Arcangelis, L., Godano, C., and Lippiello, E. (2018). The overlap of aftershock coda waves and short-term postseismic forecasting. *Journal of Geophysical Research: Solid Earth*, 123(7):5661–5674.

Demets, C., Gordon, R., Argus, D., and Stein, S. (1994). Effect of recent revisions to the geomagnetic reversal time-scale on estimates of current plate motions. *Geophysical Research Letters - GEOPHYS RES LETT*, 21(5):2191–2194.

Dieterich, J. (1994). A constitutive law for rate of earthquake production and its application to earthquake clustering. *Journal of Geophysical Research: Solid Earth*, 99(B2):2601–2618.

Eroglu Azak, T., Kalafat, D., Şeşetyan, K., and Demircioğlu, M. B. (2018). Effects of seismic declustering on seismic hazard assessment: a sensitivity study using the turkish earthquake catalogue. *Bulletin of Earthquake Engineering*, 16(8):3339–3366.

Evison, F. and Rhoades, D. (2000). The precursory earthquake swarm in greece. *Annali di Geofisica*, 43(2):54–79.

Gardner, J. K. and Knopoff, L. (1974). Is the sequence of earthquakes in Southern California, with aftershocks removed, Poissonian? *Bulletin of the Seismological Society of America*, 64(5):1363–1367.

Gomberg, J. (2001). The failure of earthquake failure models. *Journal of Geophysical Research: Solid Earth*, 106(B8):16253–16263.

Grimm, C., Käser, M., Hainzl, S., Pagani, M., and Küchenhoff, H. (2021). Improving Earthquake Doublet Frequency Predictions by Modified Spatial Trigger Kernels in the Epidemic-Type Aftershock Sequence (ETAS) Model. *Bulletin of the Seismological Society of America*, 112(1):474–493.

Gross, S. (1996). Aftershocks of nuclear explosions compared to natural aftershocks. *Bulletin of the Seismological Society of America*, 86(4):1054–1060.

Gulia, L. and Wiemer, S. (2010). The influence of tectonic regimes on the earthquake size distribution: A case study for italy. *Geophysical Research Letters*, 37(10):106–116.

Gutenberg, B. and Richter, C. F. (1956). Earthquake magnitude, intensity, energy, and acceleration: (Second paper). *Bulletin of the Seismological Society of America*, 46(2):105–145.

Hainzl, S. (2016a). Apparent triggering function of aftershocks resulting from rate-dependent incompleteness of earthquake catalogs. *Journal of Geophysical Research: Solid Earth*, 121(9):6499–6509.

Hainzl, S. (2016b). Rate-Dependent Incompleteness of Earthquake Catalogs. *Seismological Research Letters*, 87(2A):337–344.

Hainzl, S. and Marsan, D. (2008). Dependence of the omori-utsu law parameters on main shock magnitude: Observations and modeling. *Journal of Geophysical Research: Solid Earth*, 113(B10):325–344.

Hainzl, S. and Ogata, Y. (2005). Detecting fluid signals in seismicity data through statistical earthquake modeling. *Journal of Geophysical Research: Solid Earth*, 110(B5):261–286.

Hainzl, S., Scherbaum, F., and Beauval, C. (2006). Estimating Background Activity Based on Interevent-Time Distribution. *Bulletin of the Seismological Society of America*, 96(1):313–320.

Hainzl, S., Zakharova, O., and Marsan, D. (2013). Impact of Aseismic Transients on the Estimation of Aftershock Productivity Parameters. *Bulletin of the Seismological Society of America*, 103(3):1723–1732.

Hamdache, M., Henares, J., Peláez, J., and Damerdji, Y. (2019a). Fractal analysis of earthquake sequences in the ibero-maghrebian region. *Pure and Applied Geophysics*, 176(2):1397–1416.

Hamdache, M., Pelaez, J. A., Gospodinov, D., and Henares, J. (2017). Statistical features of the 2010 beni-ilmane, algeria, aftershock sequence. *Pure and Applied Geophysics*, 175(1):773–792.

Hamdache, M., Peláez, J. A., Yelles-Chaouche, A., Monteiro, R., Marques, M., Castro, M., Beldjoudi, H., and Kherroubi, A. A. (2019b). A preliminary seismic hazard modelling in northern algeria. In Sundararajan, N., Eshagh, M., Saibi, H., Meghraoui, M., Al-Garni, M., and Giroux, B., editors, *On Significant Applications of Geophysical Methods*, pages 231–235, Cham. Springer International Publishing.

Harbi, A. (2001). Analyse de la sismicité et mise en Évidence d'accidents actifs dans le nord-est algerien. Master's thesis, Université Des Sciences Et De La Technologie Houari-boumédièn - Alger.

Harbi, A., Maouche, S., and Ayadi, A. (1999). Neotectonics and associate seismicity in the eastern tellian atlas of algeria. *Journal of Seismology*, 3(1):95–104.

Helmstetter, A., Kagan, Y. Y., and Jackson, D. D. (2006). Comparison of Short-Term and Time-Independent Earthquake Forecast Models for Southern California. *Bulletin of the Seismological Society of America*, 96(1):90–106.

Helmstetter, A. and Sornette, D. (2002). Subcritical and supercritical regimes in epidemic models of earthquake aftershocks. *Journal of Geophysical Research: Solid Earth*, 107(B10):10–21.

Helmstetter, A. and Sornette, D. (2003). Foreshocks explained by cascades of triggered seismicity. *Journal of Geophysical Research: Solid Earth*, 108(B10):24–57.

Hill, D. and Prejean, S. (2015). 4.11 - dynamic triggering. In Schubert, G., editor, *Treatise on Geophysics (Second Edition)*, pages 273–304. Elsevier, Oxford, second edition edition.

Hill, D. P. (1977). A model for earthquake swarms. *Journal of Geophysical Research (1896-1977)*, 82(8):1347–1352.

Husen, S. and Hardebeck, J. (2010). Earthquake location accuracy.

Iervolino, I. (2019). Generalized Earthquake Counting Processes for Sequence-Based Hazard. *Bulletin of the Seismological Society of America*, 109(4):1435–1450.

Iervolino, I., Chioccarelli, E., and Giorgio, M. (2018). Aftershocks' Effect on Structural Design Actions in Italy. *Bulletin of the Seismological Society of America*, 108(4):2209–2220.

Iwata, T. (2008). Low detection capability of global earthquakes after the occurrence of large earthquakes: Investigation of the Harvard CMT catalogue. *Geophysical Journal International*, 174(3):849–856.

Jacobs, K. M., Smith, E. G. C., Savage, M. K., and Zhuang, J. (2013). Cumulative rate analysis (curate): A clustering algorithm for swarm dominated catalogs. *Journal of Geophysical Research: Solid Earth*, 118(2):553–569.

Kagan, Y. Y. (2002). Seismic moment distribution revisited: I. Statistical results. *Geophysical Journal International*, 148(3):520–541.

Kagan, Y. Y. (2004). Short-Term Properties of Earthquake Catalogs and Models of Earthquake Source. *Bulletin of the Seismological Society of America*, 94(4):1207–1228.

Kagan, Y. Y. and Houston, H. (2005). Relation between mainshock rupture process and Omori's law for aftershock moment release rate. *Geophysical Journal International*, 163(3):1039–1048.

Khelif, M. F., Yelles-Chaouche, A. Y.-C., Benaissa, Z., Semmane, F., Beldjoudi, H., Haned, A., Issaadi, A., Chami, A., Chimouni, R., Harbi, A., Maouche, S., Dabbouz, G., Aidi, C., and Kherroubi, A. (2018). The 2016 mihoub (north-central algeria) earthquake sequence: Seismological and tectonic aspects. *Tectonophysics*, 736(3):62–74.

King, G. C. P., Stein, R. S., and Lin, J. (1994). Static stress changes and the triggering of earthquakes. *Bulletin of the Seismological Society of America*, 84(3):935–953.

King Hubbert, M. and Rubey, W. W. (1959). Role of fluid pressure in mechanics of overthrust faulting: i. mechanics of fluid-filled porous solids and its application to overthrust faulting. *GSA Bulletin*, 70(2):115–166.

Kisslinger, C. and Jones, L. M. (1991). Properties of aftershock sequences in southern california. *Journal of Geophysical Research: Solid Earth*, 96(B7):11947–11958.

Kumazawa, T. and Ogata, Y. (2014). Nonstationary ETAS models for nonstandard earthquakes. *The Annals of Applied Statistics*, 8(3):1825 – 1852.

Lei, X., Ma, S., Chen, W., Pang, C., Zeng, J., and Jiang, B. (2013). A detailed view of the injection-induced seismicity in a natural gas reservoir in zigong, southwestern sichuan basin, china. *Journal of Geophysical Research: Solid Earth*, 118(8):4296–4311.

Lippiello, E., Cirillo, A., Godano, C., Papadimitriou, E., and Karakostas, V. (2016). Real-time forecast of aftershocks from a single seismic station signal. *Geophysical Research Letters*, 43(12):6252–6258.

Lohman, R. and McGuire, J. (2007). Earthquake swarms driven by aseismic creep in the salton trough, california. *Journal of Geophysical Research: Solid Earth*, 112(B4):195–218.

Lolli, B. and Gasperini, P. (2006). Comparing different models of aftershock rate decay: The role of catalog incompleteness in the first times after main shock. *Tectonophysics*, 423(1):43–59.

Marsan, D., Prono, E., and Helmstetter, A. (2013). Monitoring Aseismic Forcing in Fault Zones Using Earthquake Time Series. *Bulletin of the Seismological Society of America*, 103(1):169–179.

Marzocchi, W. and Sandri, L. (2009). A review and new insights on the estimation of the b-value and its uncertainty. *Annals of Geophysics*, 46(6):11–26.

Marzocchi, W., Spassiani, I., Stallone, A., and Taroni, M. (2019). How to be fooled searching for significant variations of the b-value. *Geophysical Journal International*, 220(3):1845–1856.

Marzocchi, W. and Taroni, M. (2014). Some Thoughts on Declustering in Probabilistic Seismic-Hazard Analysis. *Bulletin of the Seismological Society of America*, 104(4):1838–1845.

Merdasse, M., Hamdache, M., Peláez, J. A., Henares, J., and Medkour, T. (2023). Earthquake magnitude and frequency forecasting in northeastern algeria using time series analysis. *Applied Sciences*, 13(3):1566–1585.

Mesimeri, M., Karakostas, V., Papadimitriou, E., Schaff, D., and Tsaklidis, G. (2016). Spatio-temporal properties and evolution of the 2013 aigion earthquake swarm (corinth gulf, greece). *Journal of Seismology*, 20(3):595–614.

Mesimeri, M., Karakostas, V., Papadimitriou, E., and Tsaklidis, G. (2019). Characteristics of earthquake clusters: Application to western corinth gulf (greece). *Tectonophysics*, 767(1):228–246.

Mesimeri, M., Passarelli, L., Cesca, S., Maccaferri, F., and Lanza, F. (2023). Earthquake swarms and complex seismic sequences in tectonic and volcanic areas. *Frontiers in Earth Science*, 11(3):2296–6463.

Michael, A. J. and Toksöz, M. N. (1982). Earthquake swarms as a long-range precursor to large earthquakes in Turkey. *Geophysical Journal International*, 68(2):459–476.

Mignan, A. (2011). Retrospective on the accelerating seismic release (asr) hypothesis: Controversy and new horizons. *Tectonophysics*, 505(1):1–16.

Mizrahi, L., Nandan, S., and Wiemer, S. (2021a). Embracing data incompleteness for better earthquake forecasting. *Journal of Geophysical Research: Solid Earth*, 126(12):22–37.

Mizrahi, L., Nandan, S., and Wiemer, S. (2021b). The Effect of Declustering on the Size Distribution of Mainshocks. *Seismological Research Letters*, 92(4):2333–2342.

Mohammedi, Y., Djellit, H., Yelles-Chaouche, A., Hamidatou, M., and Nassim, H. (2019). *New Evidence of Active Faulting Along the Ain Smara Fault in the Constantine Province (North East Algeria): IEREK Interdisciplinary Series for Sustainable Development*, pages 271–273.

Nandan, S., Ouillon, G., Sornette, D., and Wiemer, S. (2019). Forecasting the rates of future aftershocks of all generations is essential to develop better earthquake forecast models. *Journal of Geophysical Research: Solid Earth*, 124(8):8404–8425.

Nishikawa, T. and Ide, S. (2017). Detection of earthquake swarms at subduction zones globally: Insights into tectonic controls on swarm activity. *Journal of Geophysical Research: Solid Earth*, 122(7):5325–5343.

Nocquet, J.-M. *Mesure de la déformation crustale en Europe occidentale par géodésie spatiale*. PhD thesis, Université de Nice.

Nocquet, J.-M., Willis, P., and Garcia, S. (2006). Plate kinematics of nubia–somalia using a combined doris and gps solution. *Journal of Geodesy*, 80(8):591–607.

Nur, A. and Booker, J. R. (1972). Aftershocks caused by pore fluid flow? *Science*, 175(4024):885–887.

Nyffenegger, P. and Frohlich, C. (2000). Aftershock occurrence rate decay properties for intermediate and deep earthquake sequences. *Geophysical Research Letters*, 27(8):1215–1218.

Ogata, Y. (1988). Statistical models for earthquake occurrences and residual analysis for point processes. *Journal of the American Statistical Association*, 83(3):9–27.

Ogata, Y. (1992). Detection of precursory relative quiescence before great earthquakes through a statistical model. *Journal of Geophysical Research: Solid Earth*, 97(B13):19845–19871.

Ogata, Y. (1998). Space-time point-process models for earthquake occurrences. *Annals of the Institute of Statistical Mathematics*, 50(2):379–402.

Ogata, Y. and Katsura, K. (1993). Analysis of temporal and spatial heterogeneity of magnitude frequency distribution inferred from earthquake catalogues. *Geophysical Journal International*, 113(3):727–738.

Omori, F. (1894). On after-shocks of earthquakes. *Journal of the College of Science*, 7(2):111–200.

Ouyed, M., Cisternas, A., Deschamps, A., Dorel, J., Frechet, J., Gaulon, R., Hatzfeld, D., and Philip, H. (1981). Seismotectonics of the el asnam earthquake. *Nature*, 292(2):26–31.

Pacchiani, F. and Lyon-Caen, H. (2010). Geometry and spatio-temporal evolution of the 2001 Agios Ioanis earthquake swarm (Corinth Rift, Greece). *Geophysical Journal International*, 180(1):59–72.

Passarelli, L., Heryandoko, N., Cesca, S., Rivalta, E., Rasmid, Rohadi, S., Dahm, T., and Milkereit, C. (2018). Magmatic or not magmatic? the 2015–2016 seismic swarm at the long-dormant jailolo volcano, west halmahera, indonesia. *Frontiers in Earth Science*, 6(2):6–24.

Pavlis, G. L. and Hamburger, M. W. (1991). Aftershock sequences of intermediate-depth earthquakes in the pamir-hindu kush seismic zone. *Journal of Geophysical Research: Solid Earth*, 96(B11):18107–18117.

Rahmani, S. T.-E., Abacha, I., Boulahia, O., Yelles-Chaouche, A., Crespo-Martín, C., and Roubeche, K. (2023). Time-dependent and spatio-temporal statistical analysis of seismicity: application on the complete data set of the 2010 Beni–Ilmane earthquake sequence. *Geophysical Journal International*, 236(3):1246–1261.

Reasenberg, P. (1985). Second-order moment of central california seismicity, 1969–1982. *Journal of Geophysical Research: Solid Earth*, 90(B7):5479–5495.

Reverso, T., Steacy, S., and Marsan, D. (2018). A hybrid etas-coulomb approach to forecast spatiotemporal aftershock rates. *Journal of Geophysical Research: Solid Earth*, 123(11):9750–9763.

Roland, E. and McGuire, J. J. (2009). Earthquake swarms on transform faults. *Geophysical Journal International*, 178(3):1677–1690.

Sattin, F., Agostini, M., Cavazzana, R., Serianni, G., Scarin, P., and Vianello, N. (2009). About the parabolic relation existing between the skewness and the kurtosis in time series of experimental data. *Physica Scripta*, 79(4):45–59.

Schorlemmer, D. and Wiemer, S. (2005). Microseismicity data forecast rupture area. *Nature*, 434(7037):1086–1086.

Semmane, F., Abacha, I., Yelles-Chaouche, A., Haned, A., Beldjoudi, H., and Amrani, A. (2012). The earthquake swarm of december 2007 in the mila region of northeastern algeria. *Natural Hazards*, 64(6):1855–1871.

Shanker, D., Singh, H., Paudyal, H., Kumar, A., Panthi, A., and Singh, V. (2010). Searching for an earthquake precursor—a case study of precursory swarm as a real seismic pattern before major shocks. *Pure and Applied Geophysics*, 167(3):655–666.

Shapiro, S. A., Huenges, E., and Borm, G. (1997). Estimating the crust permeability from fluid-injection-induced seismic emission at the KTB site. *Geophysical Journal International*, 131(2):15–18.

Shi, Y. and Bolt, B. A. (1982). The standard error of the magnitude-frequency b value. *Bulletin of the Seismological Society of America*, 72(5):1677–1687.

Sornette, D. and Werner, M. J. (2005). Apparent clustering and apparent background earthquakes biased by undetected seismicity. *Journal of Geophysical Research: Solid Earth*, 110(B9):110–134.

Utsu, T. (1961). A Statistical Study on the Occurrence of Aftershocks. *The Geophysical Magazine*, 30(3):521–605.

Utsu, T. (2002). 43 - statistical features of seismicity. In Lee, W. H., Kanamori, H., Jennings, P. C., and Kisslinger, C., editors, *International Handbook of Earthquake and Engineering Seismology, Part A*, volume 81 of *International Geophysics*, pages 719–732. Academic Press.

Utsu, T., Ogata, Y., S, R., and Matsu'ura (1995). The centenary of the omori formula for a decay law of aftershock activity. *Journal of Physics of the Earth*, 43(1):1–33.

van Stiphout, T., Schorlemmer, D., and Wiemer, S. (2011). The Effect of Uncertainties on Estimates of Background Seismicity Rate. *Bulletin of the Seismological Society of America*, 101(2):482–494.

Veen, A. and Schoenberg, F. P. (2008). Estimation of space–time branching process models in seismology using an em–type algorithm. *Journal of the American Statistical Association*, 103(482):614–624.

Vidale, J. E. and Shearer, P. M. (2006). A survey of 71 earthquake bursts across southern california: Exploring the role of pore fluid pressure fluctuations and aseismic slip as drivers. *Journal of Geophysical Research: Solid Earth*, 111(B5):120–148.

Werner, M. J. and Sornette, D. (2008). Magnitude uncertainties impact seismic rate estimates, forecasts, and predictability experiments. *Journal of Geophysical Research: Solid Earth*, 113(B8):302–316.

Wesnousky, S. G. (1994). The Gutenberg-Richter or characteristic earthquake distribution, which is it? *Bulletin of the Seismological Society of America*, 84(6):1940–1959.

Wiemer, S. and Wyss, M. (2000). Minimum magnitude of completeness in earthquake catalogs: Examples from alaska, the western united states, and japan. *Bulletin of the Seismological Society of America*, 90(2):859–869.

Wiens, D. A. and Gilbert, H. J. (1996). Effect of slab temperature on deep-earthquake aftershock productivity and magnitude–frequency relations. *Nature*, 384(6605):153–156.

Wiens, D. A. and McGuire, J. J. (2000). Aftershocks of the march 9, 1994, tonga earthquake: The strongest known deep aftershock sequence. *Journal of Geophysical Research: Solid Earth*, 105(B8):19067–19083.

Woessner, J. and Wiemer, S. (2005a). Assessing the quality of earthquake catalogs: Estimating the magnitude of completeness and its uncertainty. *Bulletin of the Seismological Society of America*, 95(2):684–698.

Woessner, J. and Wiemer, S. (2005b). Assessing the Quality of Earthquake Catalogues: Estimating the Magnitude of Completeness and Its Uncertainty. *Bulletin of the Seismological Society of America*, 95(2):684–698.

Wyss, M., Hasegawa, A., Wiemer, S., and Umino, N. (1999). Quantitative mapping of precursory seismic quiescence before the 1989, m 7.1off-sanriku earthquake, japan. *Annali di Geofisica*, 42(3):160–170.

Wyss, M., Sammis, C. G., Nadeau, R. M., and Wiemer, S. (2004). Fractal Dimension and b-Value on Creeping and Locked Patches of the San Andreas Fault near Parkfield, California. *Bulletin of the Seismological Society of America*, 94(2):410–421.

Yang, W. and Ben-Zion, Y. (2009). Observational analysis of correlations between aftershock productivities and regional conditions in the context of a damage rheology model. *Geophysical Journal International*, 177(2):481–490.

Yelles-Chaouche, A., Abacha, I., Boulahia, O., Aidi, C., Adel, C., Belheouane, O., Rahmani, S. T.-E., and Khaled, R. (2021). The 13 july 2019 mw 5.0 jijel earthquake, northern algeria: An indicator of active deformation along the eastern algerian margin. *Journal of African Earth Sciences*, 177(2):104–149.

Yelles-Chaouche, A., Abacha, I., Boulahia, O., Beldjoudi, H., Aidi, C., Bendjama, H., El-Mahdi, T., Mohammedi, Y., Chami, A., Chimouni, R., and Kherroubi, A. (2023). The 2021–2022 mw 6.0 bejaia bay, ne algeria, earthquake sequence: tectonic implications at the algerian margin between lesser and greater kabylian blocks. *Acta Geophysica*, 72(6):529–551.

Yelles-Chaouche, A., Aidi, C., Beldjoudi, H., Abacha, I., Chami, A., Boulahia, O., Mohammedi, Y., Chimouni, R., Kherroubi, A., Alili, A., and Bendjama, H. (2022). The recent seismicity of northern algeria: the 2006–2020 catalogue. *Mediterranean Geoscience Reviews*, 4(7):1–20.

Yelles-Chaouche, A., Boudiaf, A., Djellit, H., and Bracene, R. (2006). La tectonique active de la région nord-algérienne. *Comptes Rendus Geoscience*, 338(1):126–139.

Yelles Chaouche, A., Domzig, A., Déverchère, J., Bracène, R., de Lépinay, B., Strzerzynski, P., Bertrand, G., Boudiaf, A., Winter, T., Kherroubi, A., Roy, P., and Djellit, H. (2009). Plio-quaternary reactivation of the neogene margin off nw algiers, algeria: The khayr al din bank. *Tectonophysics*, 475(7):98–116.

Yelles-Chaouche, A., Khelif, M. F., Haned, A., Chami, A., Aidi, C., Beldjoudi, H., Kherroubi, A., and Benaissa, Z. (2019). The algiers (north-central algeria) earthquake of august 1st, 2014 mw 5.5 in the algiers bay tectonic context. *Journal of Seismology*, 23(2):287–302.

Yelles-Chaouche, A., Kherroubi, A., and Beldjoudi, H. (2017). The large algerian earthquakes (267 a.d.-2017).

Yelles-Chaouche, A. K., Abacha, I., Semmane, F., Beldjoudi, H., and Djellit, H. (2014). The beni-ilmane (north-central algeria) earthquake sequence of may 2010. *Pure and Applied Geophysics*, 171(7):1283–1298.

Yoshida, K. (2019). Temporal change in near-source attenuation probably due to the pore pressure diffusion in the source region of the intense earthquake swarm in the yamagata-fukushima border, ne japan.

Zaliapin, I. and Ben-Zion, Y. (2013). Earthquake clusters in southern california i: Identification and stability. *Journal of Geophysical Research: Solid Earth*, 118(6):2847–2864.

Zaliapin, I., Gabrielov, A., Keilis-Borok, V., and Wong, H. (2008). Clustering analysis of seismicity and aftershock identification. *Phys. Rev. Lett.*, 101(1):18–23.

Zhang, D., Zhao, N., Tong, M., and Du, C. (2016). Design of the rock coal shearer cutting mechanism and its vibration analysis. In *2016 IEEE International Conference on Mechatronics and Automation*, pages 720–725.

Zhuang, J., Ogata, Y., and Vere-Jones, D. (2002). Stochastic declustering of space-time earthquake occurrences. *Journal of the American Statistical Association*, 97(458):369–380.

Appendix A

Main scientific publications

Geophysical Journal International

Geophys. J. Int. (2024) **236,** 1246–1261
Advance Access publication 2023 December 20
GJI Seismology

https://doi.org/10.1093/gji/ggad483

Time-dependent and spatio-temporal statistical analysis of seismicity: application on the complete data set of the 2010 Beni–Ilmane earthquake sequence

Sofiane Taki-Eddine Rahmani,[1,2] Issam Abacha,[1] Oualid Boulahia,[1] Abdelkarim Yelles-Chaouche,[1] Cristina Crespo-Martín[3] and Khaled Roubeche[1]

[1]*Research Centre in Astronomy, Astrophysics, and Geophysics (CRAAG), Bouzareah,* 16340 *Algiers, Algeria. E-mail: s.rahmani@craag.dz*
[2]*Laboratory for Developing New Materials and their Characterizations, Department of Physics, Faculty of Science, University Ferhat Abbas Setif* 1, 19000 *Setif, Algeria*
[3]*Área de Geología - ESCET, TECVOLRISK Research Group, Universidad Rey Juan Carlos (URJC). C/Tulipan s/n,* 28933 *Mostoles, Madrid, Spain*

Accepted 2023 December 18. Received 2023 October 19; in original form 2023 March 7

SUMMARY

The Beni–Ilmane (BI) seismic sequence, situated in the north-central region of Algeria, began on 2010 May 14 with a main shock of M_L 5.4 followed by two other shocks on May 16 and 23 of M_L 5.3 for both. Using the complete data set from May 14 to August 31 and the Epidemic Type Aftershock Sequences (ETAS) model to separate background from aftershocks contribution gave a first insight around the uncertainty that surrounds the causes and mechanisms of the seismicity. According to our findings, two phases have been determined, the first one, beginning from May 14, shows low *b*- and *p*-values with most of the seismicity being self-triggered. In contrast, the second phase, beginning from May 23, demonstrates an increase of both the *b*- and *p*-values with a high number of background events. In the second phase, the background contribution involves 53 per cent of all seismic activity after May 23's peak which is high compared to typical main shock–aftershocks sequences. A possible explanation is that the main shocks began or assisted aseismic processes in addition to causing aftershocks. A sealed source at depth may have been broken by the third main shock, opening the way for the following incursion of highly pressurized fluids (hydrocarbures) confirmed by a high V_p/V_s ratios.

Key words: Africa; Spatial analysis; Earthquake hazards; Induced seismicity; Seismic tomography; Statistical seismology.

1 INTRODUCTION

The Tellian Atlas in northern Algeria has experienced numerous moderate to large earthquakes over the last two decades, beginning with the devastating earthquake in Boumerdes in 2003 May, which had a magnitude of M_w 6.8 (Yelles-Chaouche *et al.* 2004). These earthquakes are related to the oblique convergence between the African and Eurasian plates since the Late Cretaceous, with a rate of 4.5 ± 0.3 mm yr^{-1} along the N325 W ± 5° shortening direction (Nocquet 2012, Fig. 1a). Indeed, the present strain partitioning in northeastern Algeria is the result of convergence involving three major fault structures, as indicated by the study conducted by Bougrine *et al.* (2019). First, the Offshore Fault System exhibits a slip deficit rate of 1.5 mm yr^{-1}. Secondly, the Gharimadou–North–Constantine Fault accommodates dextral displacement and has a significant present-day slip deficit rate estimated at 2.4 mm yr^{-1}. Lastly, a deformation rate of 1.5 mm yr^{-1} is observed along the fault system extending from the well-known E-W Gafsa Fault in Tunisia to the South Atlas Fault System in Algeria, and further along the southwestern end of the NW-SE Aures Range until the Hodna Range near our study area (refer to Fig. 1b). Despite the relatively low deformation rate of 1.5 mm yr^{-1} and the main shock being considered a moderate event, the 2010 BI earthquake sequence generated a significant number of events during the first two weeks. Approximately 25 000 events were detected by a single nearby station, making it the most noteworthy seismic sequence in the northern part of Algeria.

One of the most significant features of this seismicity is the occurrence of seismic sequences with two or more main shocks and an important number of seismic events, which are mostly accompanied by spatial migration (Khelif *et al.* 2018; Yelles-Chaouche *et al.* 2018; Abacha & Yelles-Chaouche 2019; Bendjama *et al.* 2021; Boulahia *et al.* 2021; Abacha *et al.* 2022, 2023). The 2010 Bani-Ilmane (BI) earthquake sequence stands out as the most notable example due to the high number of seismic events. In Fig. 1(b), we present the recent main earthquake sequence that occurred in

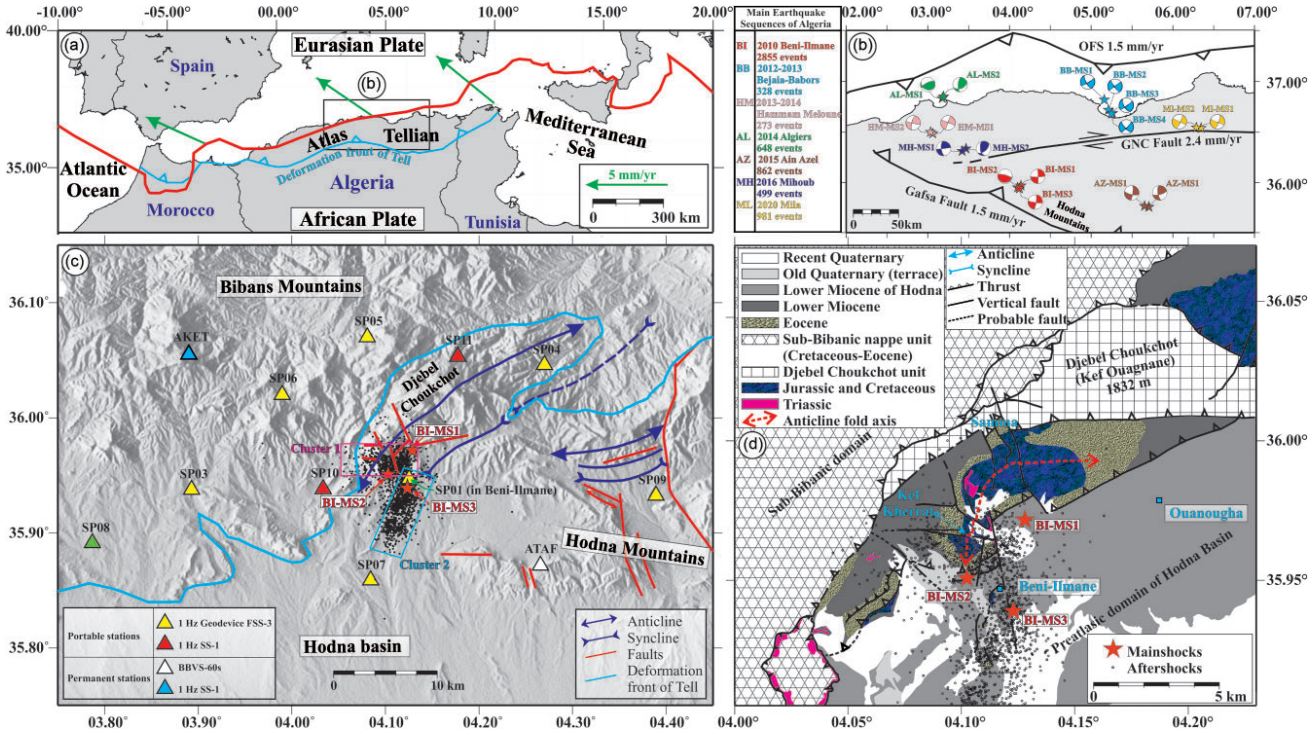

Figure 1. (a) Map of the southern part of the Western Mediterranean, delimiting the Tellian Atlas System Tell (one of the main geological units in Algeria). The line represents the Eurasia–Africa Plate boundary (simplified from Bird 2003), and the line with triangle represents the deformation front of Tell. Predicted velocities along the Eurasia–Africa Plate boundary (arrows) are simplified from Nocquet *et al.* (2006). (b) Spatial partitioning of strain in northeastern Algeria along the three major tectonic structures, which are schematized in lines according to the study of Bougrine *et al.* (2019). The main shocks and their focal mechanism of the main seismic sequences are also shown. (c) Tectonic map of the study area on a local scale, showing the seismic sources (dots) with the three main shocks (stars) and the seismic stations (triangles). (d) Geology of the epicentral area (modified from Beldjoudi *et al.* 2016; Abacha *et al.* 2023), showing the 2876 events that represent the complete number of located events.

northern Algeria, along with the corresponding number of located events for each one. It is evident that these sequences exhibit a significantly lower number of events in comparison to the BI sequence. Therefore, what physical mechanism underlies the initiation of this unusual sequence?

The 2010 BI earthquake sequence took place in the southern deformation front of the Atlas Tellian region, in a geologically complex area between the Hodna and Bibans Mountains ranges, specifically in the southern part of the NE-SW Djebel Choukchot massif (Fig. 1c). The massif is highly deformed, resulting in a network of faults and fractures of various types and orientations (Yelles-Chaouche *et al.* 2014; Beldjoudi *et al.* 2016; Abacha *et al.* 2023). Due to two tectonic phases, the geological formations in the area exhibit distinct characteristics. First, there are two main domains, namely the Sub-Bibanic allochthonous and Djebel Choukchot Parautochtonnous. These domains consist primarily of Jurassic, Upper Cretaceous, Eocene and Miocene sedimentary cover and have been thrust onto the Pre-Atlasic autochthonous domain of the Hodna basin, which is composed of Ouanougha Miocene sediments. Secondly, there is a strike-slip tectonic setting that cuts across these geological formations and the surrounding thrust faults (refer to Fig. 1d).

The earthquake sequence began on 2010 May 14, at 12:29 GMT, with the first main shock (BI-MS1) having a magnitude of M_L 5.4. Two other main shocks (BI-MS2 and BI-MS3) followed after two and nine days, respectively, with magnitudes of M_L 5.3 for both. The initial data set used in the first studies consisted of 1403 relocated events, while the total activity lasted for four months until 2010 August with 2876 relocated events. There were no instrumental seismological researches in the region before this sequence, except for the ones conducted by Hatzfeld (1978) and a macroseismic study carried out by Benouar (1994) on the 1960 Melouza earthquake (M 5.6), which is the first indication of active deformation in the region. A subsequent study by Abacha *et al.* (2019), using a scaling law determined from the 2010 BI sequence, obtained a seismic moment M_0 of 5×10^{17} N·m, a moment magnitude M_w of 5.8, a source radius r of 2.7 km and a stress drop $\Delta\sigma$ = of 10.5 MPa. While numerous studies have been carried out on general geology and some geophysical investigations were conducted by the Algerian oil company SONATRACH, unfortunately, these data are not accessible as it belongs to the country's economic sector.

Several studies have been performed on the 2010 BI earthquake sequence since its occurrence. These studies have led to the development of two seismotectonic models. The first model was proposed by Yelles-Chaouche *et al.* (2014) and suggests that the sequence was caused by two faults, a reverse E-W fault and a strike-slip NNE-SSW fault. The second model was proposed by Beldjoudi *et al.* (2016), who assigned each of the three main shocks to three different segments. Additionally, seismic tomography models have been used to understand the depth distribution of the seismic activity by Abacha *et al.* (2014, 2023). Hamdache *et al.* (2017) conducted a statistical analysis of the earthquake sequence using three different methods, including analysing the Gutenberg–Richter magnitude frequency relationship, the sequence with a stochastic point process model and the multifractal properties of the seismicity but without

taking into account changes in the network configuration. However, despite these studies, the mechanism behind the earthquake activity in the region is still not fully understood.

To further understand the seismic activity and the causes of earthquakes, scientists often use statistical methods. Two types of seismic events can occur: dependent and independent. Dependent events happen when stress changes occur due to main shocks, whereas independent events are a result of tectonic stress buildup or transient aseismic forces, including fluid migration or slow-slip events. The Epidemic Type Aftershock Sequence (ETAS) model, developed by Ogata (1988), is a statistical tool that separates earthquake-triggered and background seismic events. This model is useful for declustering earthquake catalogues and differentiating between dependent and independent events. The ETAS model usually assumes a constant background rate, but Hainzl & Ogata (2005), and later Marsan *et al.* (2013), modified it to account for time-dependent background rates. This modification can help identify the mechanisms behind the seismic activity and any significant changes that occur.

This study provides new insights into the analysis of seismic activity in the region. Compared to previous studies, our approach involves several novel aspects. First, we have calculated the magnitude of completeness and considered the bias that can be introduced by changes in the network configuration and incompleteness of the earthquake catalogue. This allowed us to apply the Omori–Utsu law, Gutenberg–Richter law and the ETAS model, and to analyse inter-event times. Secondly, we have used a time-dependent background rate ETAS model to identify the mechanisms responsible for the seismic activity in the region. Finally, we have reproduced the work of Abacha *et al.* (2023) by calculating the V_p/V_s ratio and comparing it with our results. Overall, these approaches provide a more comprehensive understanding of the seismic activity in the region and can help identify potential risks for seismic hazards.

2 DATA AND METHODOLOGY

2.1. Data description

The seismic data set used in this study was collected by Algeria's permanent network which has been operational since 2007, a mobile network was then installed gradually 1 d after the first main shock. Before conducting any statistical analysis, it was necessary to determine the magnitude of completeness M_c. To avoid any bias resulting from the installation of the mobile network over time, we only selected events recorded by the permanent network and calculated the magnitude of completeness using the maximum curvature method, the EMR (Entire Magnitude Range), the goodness of fit and the MBS (Magnitude Bin Shifting), with a bootstrap approach to quantify the uncertainties. The Algerian permanent seismic network recorded 815 events with magnitudes ranging from 0.4 to 5.4 M_L (Fig. 2a).

The chosen bin size for estimating the magnitude of completeness using each technique is set to 0.1. Studies have demonstrated that biases associated with this bin size are negligible when compared to larger bin sizes, especially when determining the *b*-value, as discussed later (Marzocchi *et al.* 2020). The maximum curvature method yields a magnitude of completeness of 2.1, with a standard deviation of 0.05. Similarly, the EMR method also yields a magnitude of completeness of 2.1, with a standard deviation of 0.04. The goodness-of-fit approach results in a magnitude of completeness of 2.0, with a standard deviation of 0.08. Finally, the MBS method produces a magnitude of completeness of 1.9, with a standard deviation of 0.11. After careful consideration, we have chosen to adopt the EMR magnitude of completeness, as it has been proven effective in recovering the true M_c (Mignan & Woessner 2012).

Another issue addressed in this study is the short-term incompleteness immediately following main shocks. It has been established that the completeness magnitude significantly increases after large earthquakes (Kagan 2004). In our study, we have excluded early aftershocks based on the empirical relationship between main shock magnitude and time (days), $M_c(M, t) = M - 4.5 - 0.75\log(t)$ (Helmstetter *et al.* 2006). According to this empirical law, the time windows of 38 min after the first main shock, 27 min after the second main shock and 28 min after the third main shock are considered incomplete (see Appendix B, Fig. B1). Therefore, the final catalogue contains 433 events sorted according to the obtained M_c (Fig. 2b).

The relocated hypocentres were distributed into two main clusters, Cluster 1 oriented E-W and Cluster 2 oriented NNE-SSW (Fig. 1c). The identification of these clusters was based on three criteria established in previous studies. First, the seismotectonic criterion by Yelles-Chaouche *et al.* (2014) used well-located aftershocks and focal mechanisms for earthquakes with a magnitude of ≥ 4, revealing two clusters with different orientations (E-W for Cluster 1 and NNE-SSW for Cluster 2), attributed to high-angle reverse and near-vertical left-lateral strike-slip faults, respectively (see Appendix A, Fig. A1). Secondly, Abacha *et al.* (2023) divided the data set into episodes, noting spatial separation between the clusters, particularly in Episodes A and B, where Cluster 2 displayed heightened activity along the strike-slip fault (see Appendix A, Fig. A2). Thirdly, the same study by Abacha *et al.* (2023) analysed seismicity migration, showing Cluster 1 with higher diffusivity and migration velocity compared to Cluster 2, which exhibited a slower, more extended migration process, possibly linked to a pore-pressure diffusion mechanism with a time-delayed response (see Appendix A, Fig. A3). The temporal evolution of the seismic activity reveals that both clusters began almost simultaneously, with the majority of events occurring in the first cluster, but after the May 23 main shock, almost all activity was concentrated in the second cluster (Yelles-Chaouche *et al.* 2014; Hamdache *et al.* 2017; Abacha *et al.* 2019; 2023). The sources of seismic activity were concentrated in a strip of approximately 10 km depth, corresponding to the seismogenic layer of all Algerian seismicity (Fig. 2c, Yelles-Chaouche *et al.* 2022).

2.2. The Gutenberg–Richter Law

The Gutenberg–Richter law describes the relationship between the frequency of earthquakes and their magnitudes (Gutenberg & Richter 1942)

$$\log(N_{>M}) = a - bM,$$

where 'N' is the number of events with a magnitude larger or equal to M, 'a' express the seismicity rate, and 'b' is the relative proportion of small and large earthquakes. The b-value is an important parameter interpreted as an inverse measure of the stress state in a region (Scholz 1968; Bufe 1970; Gibowicz 1973; Wyss 1973). This interpretation of the b-value is supported by the observation of its variability on different fault types (Petruccelli *et al.* 2019) where they found low b-values for thrust faulting events (high stress) and high values for normal faulting events (low stress).

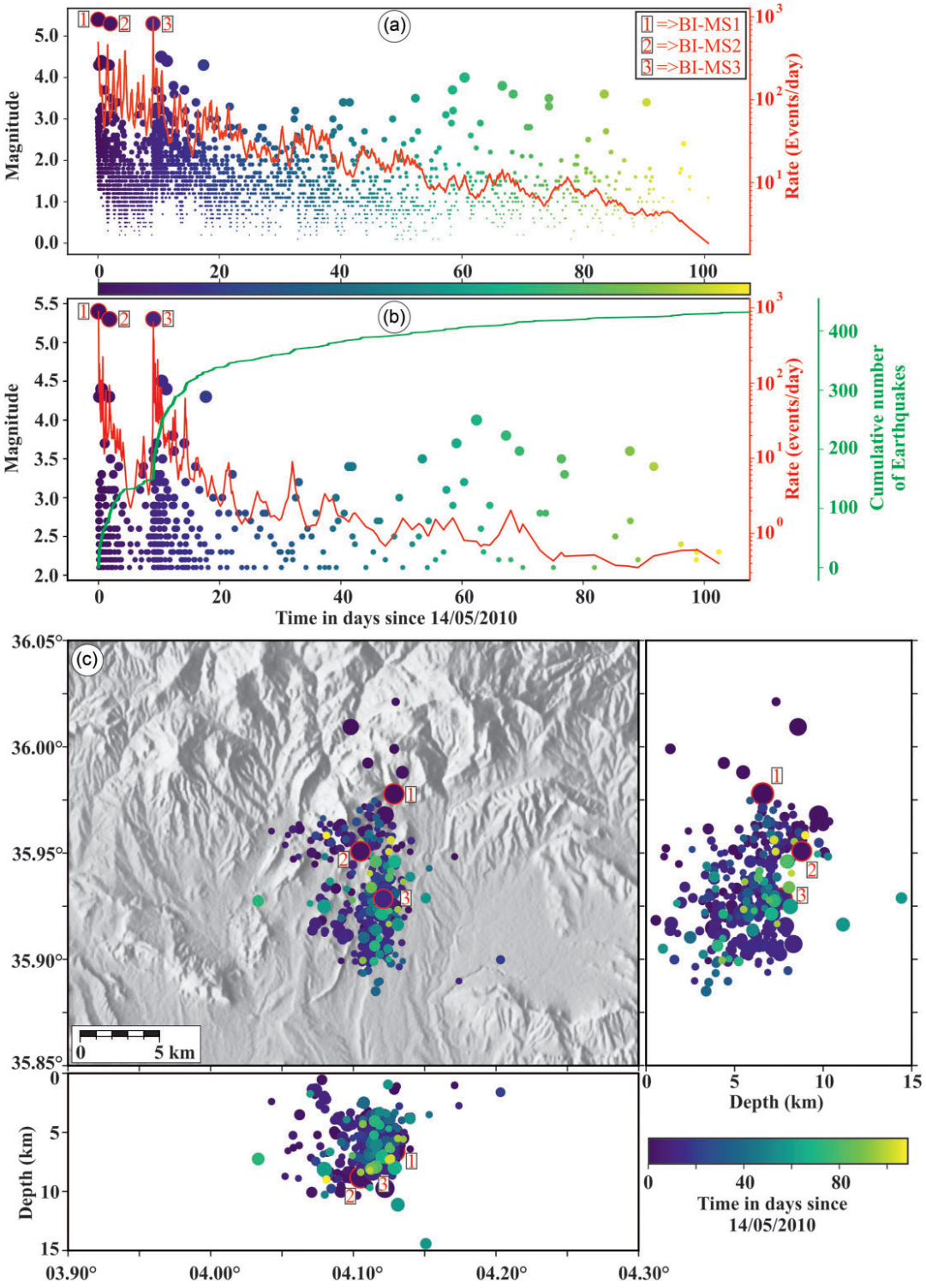

Figure 2. (a) Magnitude–time with the event rate of the events recorded by the permanent network. (b) Magnitude–time with the cumulative number of events plot and event rate of the BI seismic sequence above the magnitude completeness (c) the spatial distribution of the relocated earthquakes with two vertical sections oriented across and along the hypocentre trend, where symbol size is proportional to the magnitude. Events are colour coded according to their occurrence times.

The parameters of the Gutenberg–Richter law were determined by the maximum-likelihood estimate (Aki 1965; Utsu 1965),

$$b = \frac{1}{\ln 10.\ (\bar{m} - M_{\min})},$$

$$a = log_{10}(N(M \geq M_c)) + b.M_c,$$

where $\bar{m}$ is the mean value of the magnitudes and $M_{\min} = M_c - \Delta M/2$ represents a correction applied for magnitude binning and accounting for magnitude errors (Marzocchi & Sandri 2003), with

M_c being the magnitude of completeness and ΔM the magnitude binning.

2.3. Omori–Utsu law

The Omori–Utsu law describes the rate decay of aftershocks in time following the main shock. It is expressed as:

$$n(t) = k(t + c)^{-p},$$

where n is the number of events after the main shock, t is the time starting from the main shock, occured in $t = 0$, to the last event and k, c and p are constants. The k-value here expresses the productivity factor, the p-value varies significantly for the different tectonic regime and may reflects the proprieties of the fault system (Mogi 1967; Kisslinger 1996; Nanjo *et al.* 1998), and the c-value is a little controversial. Most studies suggest that high c-values are related to the incomplete part of the catalogue at the beginning of the sequence after a large event (Enescu *et al.* 2009), but others have found a physical correlation between the c parameter and the tectonic context (Narteau *et al*. 2009) where they found high c-values for normal faulting events and low c-values for thrust faulting events.

2.4. Inter-event time analysis

Previous studies have demonstrated that the probability density function of inter-event time between consecutive earthquakes can be approximated by a gamma function (Corral 2004)

$$p(\delta t) = C.e^{-\mu\delta t}.\delta t^{-n},$$

with δt the inter-event time between consecutive earthquakes, n a model parameter expressing the branching ratio (Helmstetter & Sornette 2003) which is the fraction of aftershocks among all the events, μ the forcing rate or background rate, and C a normalization constant. Hainzl *et al.* (2006) showed that the forcing rate and the branching ratio can be estimated according to

$$\mu = \frac{E(\delta t)}{var(\delta t)},$$
$$n = 1 - \mu E(\delta t),$$

where E(.) and var(.) are, respectively, the mean and variance of the inter-event time.

2.5. Time-dependent background ETAS model

The ETAS model proposed by Ogata (1988) is a point-process model which affirms that each earthquake triggers its own Omori-type aftershocks (Ogata 1988, 1993; Helmstetter & Sornette 2002). The model expresses that the overall rate is equal to the sum of the constant background rate (or forcing rate) and the aftershock rate (or earthquake-earthquake triggering):

$$\lambda(t) = \mu + \sum_{i:t_i<t} Ke^{\alpha(M_i - M_c)}(t - t_i + c)^{-p},$$

where M_c is the completeness magnitude of the catalogue, t_i and M_i represent the time occurrence and magnitude of the ith event, α denotes the efficiency in generating aftershock by an event of a specific magnitude, and K, c and p are the Omori–Utsu parameters.

We visually assess the goodness of fit of the estimated ETAS model by comparing the cumulative number of observed aftershocks with magnitudes (M) greater than or equal to the completeness magnitude (M_c) to the cumulative number calculated from the estimated ETAS model. To achieve this, we compute the theoretical cumulative function Λ(t) of the underlying aftershocks at time t and $\Lambda N(t)$ of the detected aftershocks. These functions are respectively calculated as follows. We define the transformed time $\tau \equiv \Lambda(t)$:

$$\Lambda(t) = \int_0^t \lambda(t)dt.$$

If the estimated model is correct, the observed sequence of aftershocks in the transformed time should exhibit characteristics of a stationary Poisson process. Consequently, the observed cumulative number in the transformed time will be represented by a nearly straight line when plotted. This crucial analysis serves as an indicator of the goodness of fit for the estimated model (Ogata 1988).

Marsan *et al.* (2013) developed a new approach for a variable forcing rate in time (Hainzl *et al.* 2016; Crespo-Martín *et al.* 2021). This method is based on the estimation of both the time-dependent background rate and ETAS parameters by using the maximum-likelihood estimation (MLE) with n-nearest-neighbour smoothing of the background rate. The overall steps to be followed are:

1. Estimate the ETAS parameters with a constant background rate in time $\mu(t) = \mu_0$ by maximizing the log-likelihood.
2. Calculate the probability that each event belongs to the background. This probability is defined as (Zhuang *et al.* 2002)

$$\omega_i = \frac{\mu(t_i)}{\mu(t_i) + \vartheta(t_i)}.$$

3. Smooth the background rate by using the n-nearest-neighbours (n_e). The best n_e will be chosen according to the Akaike criteria (Akaike 1974)

$$AIC(n_e) = -L + \frac{N}{n_e},$$

where L is the maximum-likelihood value of the model fit and N is the number of earthquakes.

The procedure will be repeated until the convergence to the best model. The application of this method in 2010 BI gives an insight into the characteristics of seismicity and generation mechanisms.

2.6. Declustering

This procedure enables the separation of independent events from dependent seismicity (background earthquakes and aftershocks). Separation is based on preceding shocks, the highest seismicity rate compared to the long-term average or the spatio-temporal proximity of earthquakes (van Stiphout *et al.* 2012). The approaches are either deterministic or stochastic. In the first case, the earthquakes are classified as main shock or aftershocks according to their space–time distance, while stochastic algorithms use the ETAS model to calculate probabilities (Zhuang *et al.* 2002; van Stiphout *et al.* 2012). In this study, we employ the probabilistic ETAS-approach based on Marsan *et al.* (2013) method, which is the most suitable approach for our study area where seismicity patterns change over time and since it takes into accounts a time-dependent background (Hainzl & Ogata 2005; Hainzl *et al.* 2013). As a result, each event is assigned

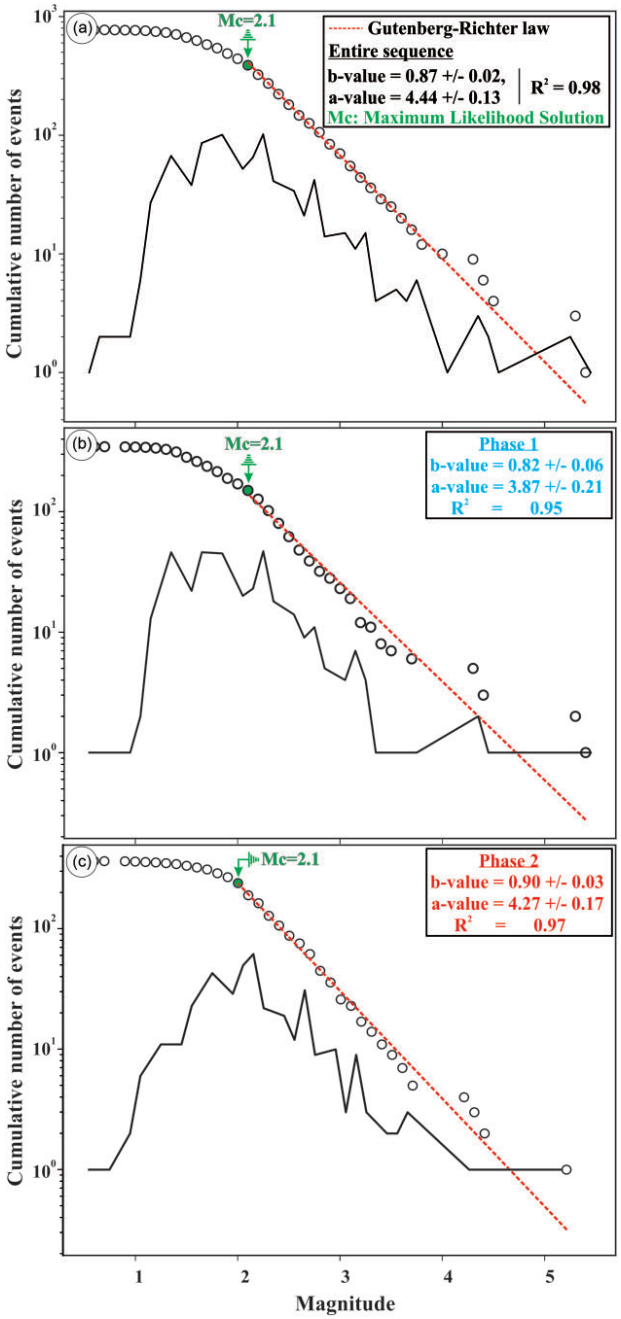

Figure 3. (a) Frequency–magnitude distribution of the entire sequence. The dashed line refers to a Gutenberg–Richter relation with $b = 0.87$. (b) Frequency–magnitude distribution of the first phase with a b-value of 0.82. (c) Frequency–magnitude distribution of the second phase with a b-value of 0.90

a probability of being either a background or an aftershock, ranging from 0 (aftershock) to 1 (background).

3 RESULTS

3.1. Frequency–magnitude distribution

The outcomes depict the frequency–magnitude distribution of the sequence with a b-value of 0.87 for $M_c > 2.1$ (Fig. 3a) which means that larger events are dominating the seismic sequence. The binning employed in this study is set to 0.1, as using larger bin sizes can introduce biases in the final results and lead to underestimation of the b-value (Marzocchi & Sandri 2003; Marzocchi *et al.* 2020). The plate or deviation observed for magnitudes < 2.1 events may be due to partial incompleteness. To observe the changes of the Gutenberg–Richter parameters, we divided the seismic sequence into two periods according to the changing observed in the cumulative number of events (Fig. 2b). The first period, starting from BI-MS1 to the event before BI-MS3, is characterized by a b-value equal to 0.82 and an a-value of 3.87 for a magnitude of completeness equal to 2.1 (Fig. 3b), then in the second period, after BI-MS3, we notice an increase of both the b- and a-values with each of them equal to 0.90 and 4.27, respectively, for a magnitude of completeness equal to 2.1(Fig. 3c). This changes are related to the relative increase of smaller earthquakes in the second period compared to the first one, but if we take into consideration the uncertainties, both the b- and a-values found for each phases are quite similar (Table 1).

Table 1. Parameters of the Gutenberg–Richter for the entire sequence and each phase,

Period	b-value	a-value
All data (staring from BI-MS1 14/05/2010 12:29:20)	0.87 ± 0.02	4.44 ± 0.13
1st period (starting from BI-MS1 14/05/2010 12:2920 to before BI-MS3 at 23/05/2010 08:42:02)	0.82 ± 0.06	3.87 ± 0.21
2nd period (starting from BI-MS3 23/05/2010 08:42:02)	0.90 ± 0.03	4.27 ± 0.17

3.2. Spatio-temporal characteristics

In order to investigate the temporal characteristics of the BI seismic sequence, we first fitted the Omori–Utsu to the entire sequence after the BI-MS1 of M_L 5.4. The parameters are obtained using the MLE: $p = 1.56$, c = 5.03 d and $k = 723.45$ (Fig. 4a). The p-value is high compared to the typical values found for different seismic sequences that range from 0.8 to 1.2 (Utsu *et al.* 1995; Hainzl & Marsan 2008) and the c-value here is also high (ranging usually from 0.5 to 20 hr; Utsu et al. 1995). These high values may be related to the secondary aftershock sequences triggered by aftershocks which can affect the temporal decay (Hainzl *et al.* 2016), which in our case must be related to three strong shocks occurring in less than 10 d. A notable increase in the events number per day immediately after the occurrence of BI-MS3 is noticed (Fig. 4a). To observe the changes of the Omori–Utsu parameters, we divided the seismic sequence into two periods as we did for the Gutenberg–Richter law. As observed, both periods seams to follow the Omori–Utsu law. For the first phase, we found a low p-value equal to 0.7 belonging to the interval mentioned above, which indicates a typical value found for different seismic sequences (Fig. 4b). The fit also shows a low c-value equal to 0.0045. However, the second phase shows high p- and c-values (Fig. 4c). The results found for the Omori–Utsu law are depicted in Table 2.

Analysis of the inter-event times, from the modified gamma function, revealed a background rate μ of 1.36, indicating that 146 events (34 per cent) were independent with a branching ratio n of 0.656 (Fig. 5a). The distributions correlate well with the gamma distribution, while it deviates notably from an exponential distribution, which would be anticipated for a Poissonian process, where activity is uncorrelated in time. To further investigate the evolution of

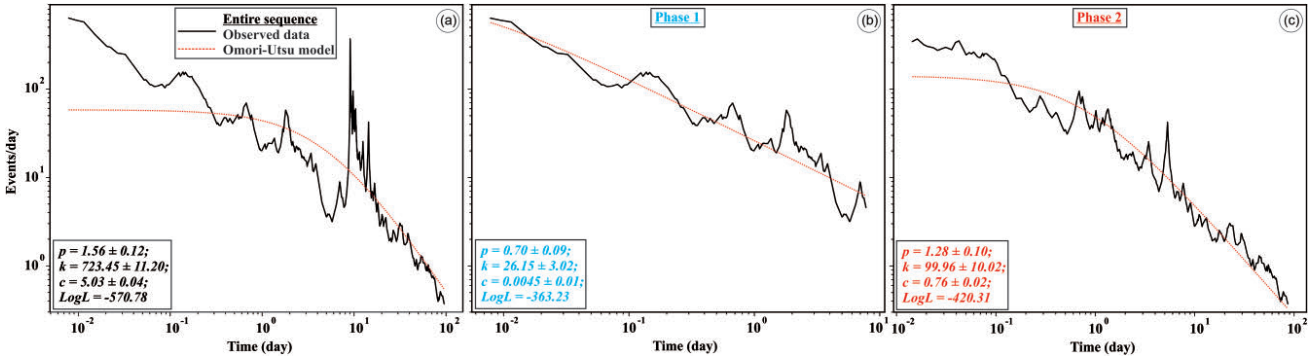

Figure 4. (a) Aftershock decay in comparison to the fit of the Omori–Utsu law of the entire sequence. (b) and (c) Aftershock decay in comparison to the fit of the Omori–Utsu law for phases one and two, respectively.

Table 2. Parameters of the Omori–Utsu for the entire sequence and each phase.

Period	*k*-value	*p*-value	*c*-value
All data (staring from BI-MS1 14/05/2010 12:29:20)	723.47 ± 11.20	1.56 ± 0.12	5.03 ± 0.04
1st period (starting from BI-MS1 14/05/2010 12:2920 to before BI-MS3 at 23/05/2010 08:42:02)	26.15 ± 3.02	0.70 ± 0.09	0.0045 ± 0.01
2nd period (starting from BI-MS3 23/05/2010 08:42:02)	99.96 ± 10.02	1.28 ± 0.10	0.76 ± 0.02

the background rate, we estimated it using a moving window of 100 events with a 10-event step (other window sizes were also explored, as shown in Appendix D, Fig. D1). The results show that the background rate increased after both BI-MS1 and BI-MS3, indicating that the background contribution is not stationary over time (Fig. 5b).

We then estimated the parameters of the ETAS model (Fig. 6a). The branching ratio was found to be less than 1 (0.48) with AIC $= -1455.3$, indicating that a stable optimal model can be assumed (Sornette & Werner 2005). Plotting the cumulative number of events against transformed time revealed negative and positive deviations (Fig. 6b), indicating that the ETAS model overestimates and underestimates earthquake occurrence, respectively. The μ-value equal to 0.17 indicates a low forcing rate which means that 4 per cent of the events are triggered externally. The low α-value is similar to the previous finding for swarm activities (0.35–0.85) compared to non-swarm activity, which is characterized by a high α-value (1.2–3.1). The deviations in seismic activity, where the downward and upward trends correspond to relative quiescence and activation in seismicity, respectively, are generally associated with changes in a specific parameter (Kumazawa & Ogata 2014). Additionally, the ETAS model assumes a constant background rate, and neglecting its variation in time can lead to some bias in parameter estimation (Hainzl *et al.* 2013). Therefore, we used a time-dependent background rate ETAS model, which may provide a better description for this seismic sequence.

The time-dependent background rate ETAS model provided a good fit to the observations, with a better AIC (-1553.24) for a smoothing window equal to 12 (Fig. 7a). The higher α-value obtained, compared to the constant background rate ETAS model, is coherent with the results found by Hainzl *et al.* (2013), who suggested that taking into account a constant background rate may underestimate the α-value. The number of background events in the entire sequence is 52 per cent, which is higher than what is typically seen in main shock–aftershock sequences. The seismicity is non-stationary during the BI-MS1 and BI-MS-3 main shocks, followed by a stationary trend after each event (Fig. 7a). Notably, there is an increase in background rate following the BI-MS1 main shock and a sudden increase in the forcing rate after the BI-MS3 main shock (Fig. 7b), which is consistent with the pattern observed in the inter-event time analysis. The first phase, as seen in the declustering analysis, shows a small proportion of background events in the overall seismicity (43 per cent, Fig. 7c). The seismicity rate also increases initially in response to the rise in background rate before becoming more or less stationary over time (Fig. 7d). In the second phase, the contribution of background events to seismicity increased to 53 per cent. The sudden increase in the number of events is also reflected in the cumulative number of background events, which corresponds to the BI-MS3 main shock of 5.3 M_L (Fig. 7e, also refer to Appendix C, Table C1). This increase is also reflected in the rate of events over time, which coincides with the background contribution rate (Fig. 7f). After around 40 d, the trend changes, and the background seismicity no longer follows the increase in the cumulative number of events, reflecting a stationary process (Fig. 7e). The magnitude evolution with scaled colours based on background probability (Fig. 8) shows that events with the highest background probability are mainly located in the second phase, corresponding to the increase in background rate (Fig. 7f). The spatial plot of background and aftershock seismicity (Fig. 9a) also shows two distinct phases. In the first phase, most of the seismicity is located in the E-W cluster and primarily consists of aftershocks (Fig. 9a). Instead, in the second phase, most of the seismicity is observed in the NNE-SSW cluster and mainly consists of background events.

4 DISCUSSION

The BI seismic sequence is one of the most notable occurrences in Algeria in terms of the number of events. Even after more than 10 yr, many of its mysteries have yet to be fully understood. It is remarkable that a moderate earthquake could generate so many seismic events. Fortunately, the sequence had three main shocks of the same magnitude, indicating that the energy released was split between at least two primary faults, thereby averting a catastrophic earthquake.

We performed a detailed statistical investigation of the seismicity to better understand the unprecedented 2010 BI earthquake sequence. Our investigation reveals important changes in the earthquake generation pathways. Using probabilistic estimations in two main phases, the declustering technique enables us to distinguish between the background and aftershock contributions, as shown in Fig. 8.

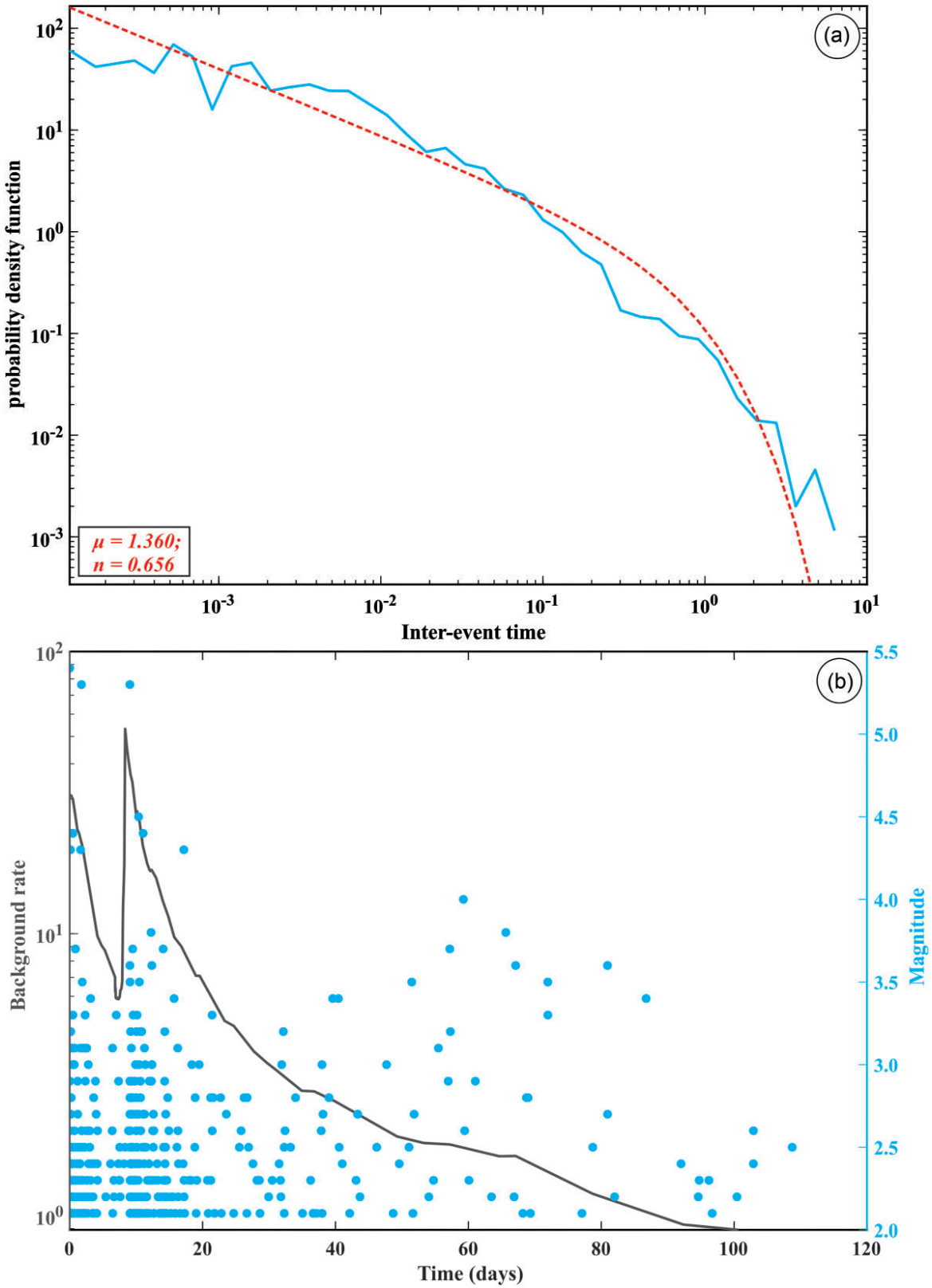

Figure 5. (a) Probability density function of inter-event time (solid line) with the gamma distribution fit (dashed line). (b) Background event rate modelling with a moving window of 100 events using the inter-event time declustering.

The first phase spacing from the first main shock (BI-MS1) on 2010 May 14 to the third one (BI-MS3) on 2010 May 23. The main shocks that occurred on May 14 and 16 (BI-MS2) played an important role in the triggering of aftershocks. We observed that this phase contains mainly self-triggered events (57 per cent). The *b*-value of 0.82, found for this period, indicates high stress with the

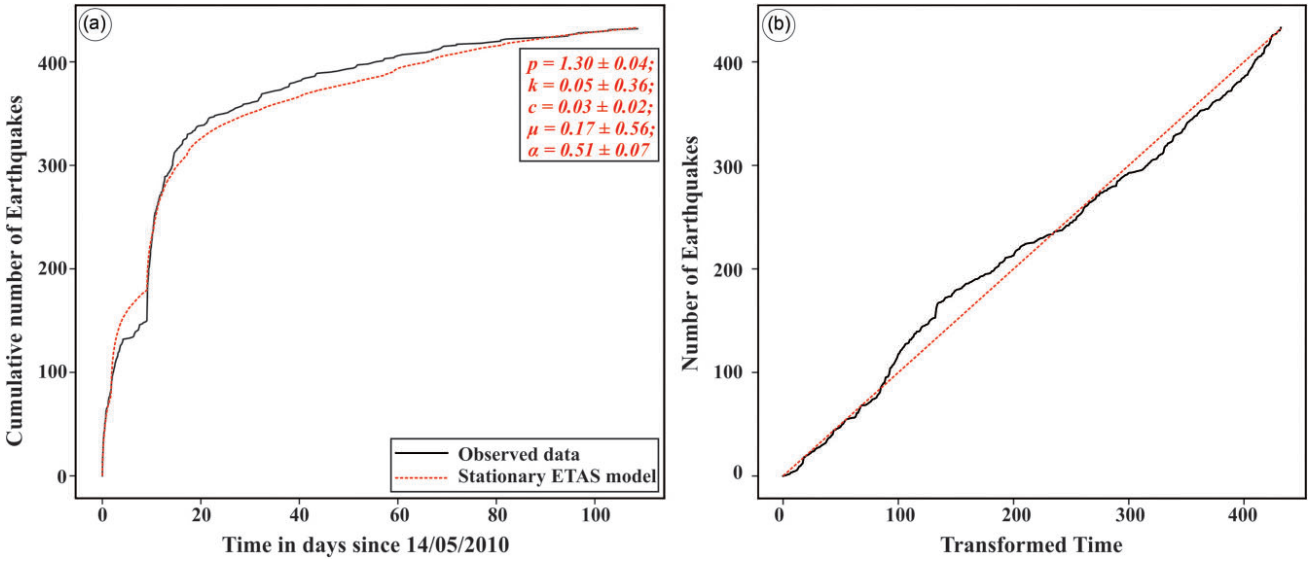

Figure 6. (a) Cumulative number of earthquakes observed and modelled. (b) Number of earthquakes versus transformed time according to the ETAS model.

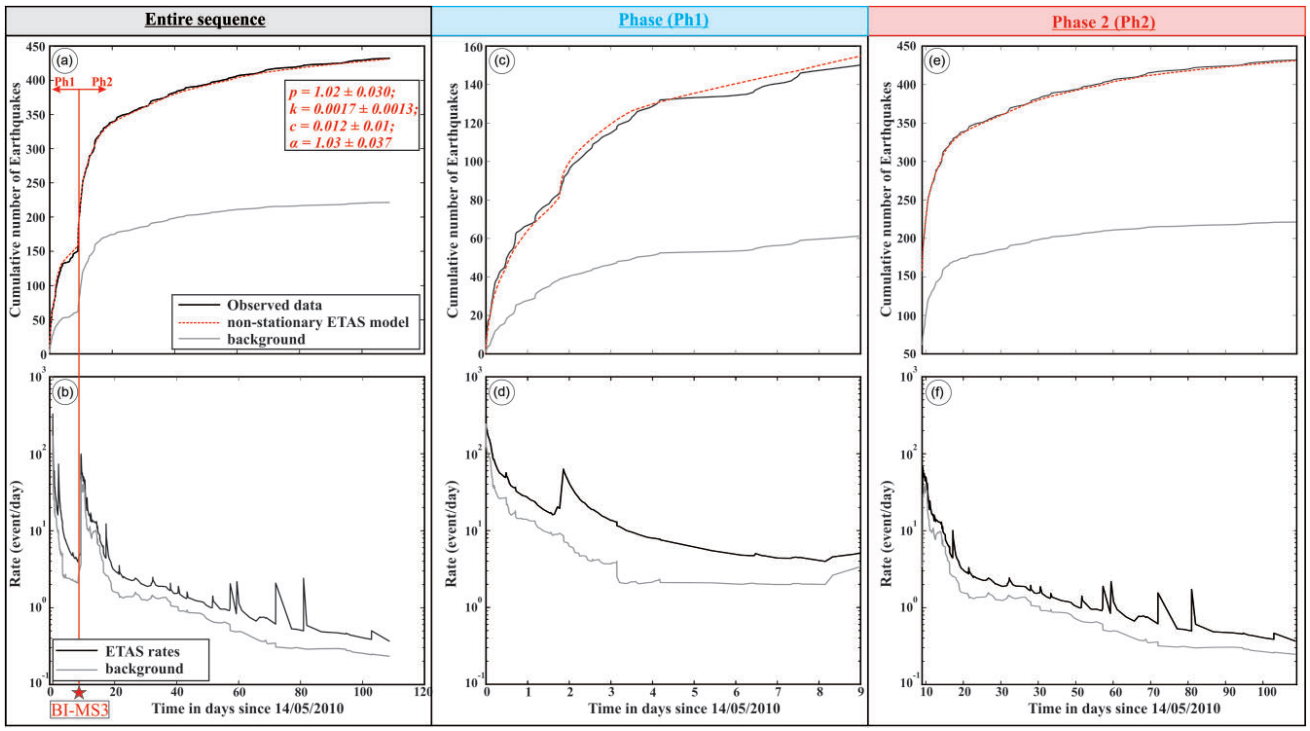

Figure 7. (a) Cumulative number of earthquakes observed and modelled with the non-stationary ETAS model of the entire sequence. The cumulative number of background events is also shown. (b) The event rate modelled and the background. (c) and (e) The cumulative number of events observed and modelled, along with the cumulative number of background events, for phases 1 and 2, respectively. (d) and (f) the event rate modelled and the background rate for phases 1 and 2, respectively

p-value of the Omori–Utsu law indicating a slow decay over time with maybe a slow stress relaxation.

The second phase started just after the occurrence of the BI-MS3 (May 23), which contains the largest number of events from all the sequence characterized by a high number of background events (53 per cent). A sudden increase in the forcing rate appears just after the occurrence of BI-MS3. These observations imply that in addition to the BI-MS3's stress changes, which in turn caused aftershocks, it also induced aseismic transients (e.g. by breaking a sealed source and allowing fluid infiltration from below), which in turn caused additional earthquakes (background events). In comparison to the initial phase, we also observed a modest rise of the *p*-value, indicating a faster decay rate with maybe a fast stress relaxation, and the *b*-value = 0.90. It is a typical value for a natural fluid driven seismicity, according to the study conducted by Karimi & Davidsen (2021). This study allowed to distinguish between natural swarms (*b*-value = 0.7–0.95) and induced seismicity (fluid induced by Man-made) (*b*-value = 1.50–2.44) in California (USA).

Fig. 9 shows a spatial plot of the seismic events colour coded by background probability. We can see through the first phase (Fig. 9a)

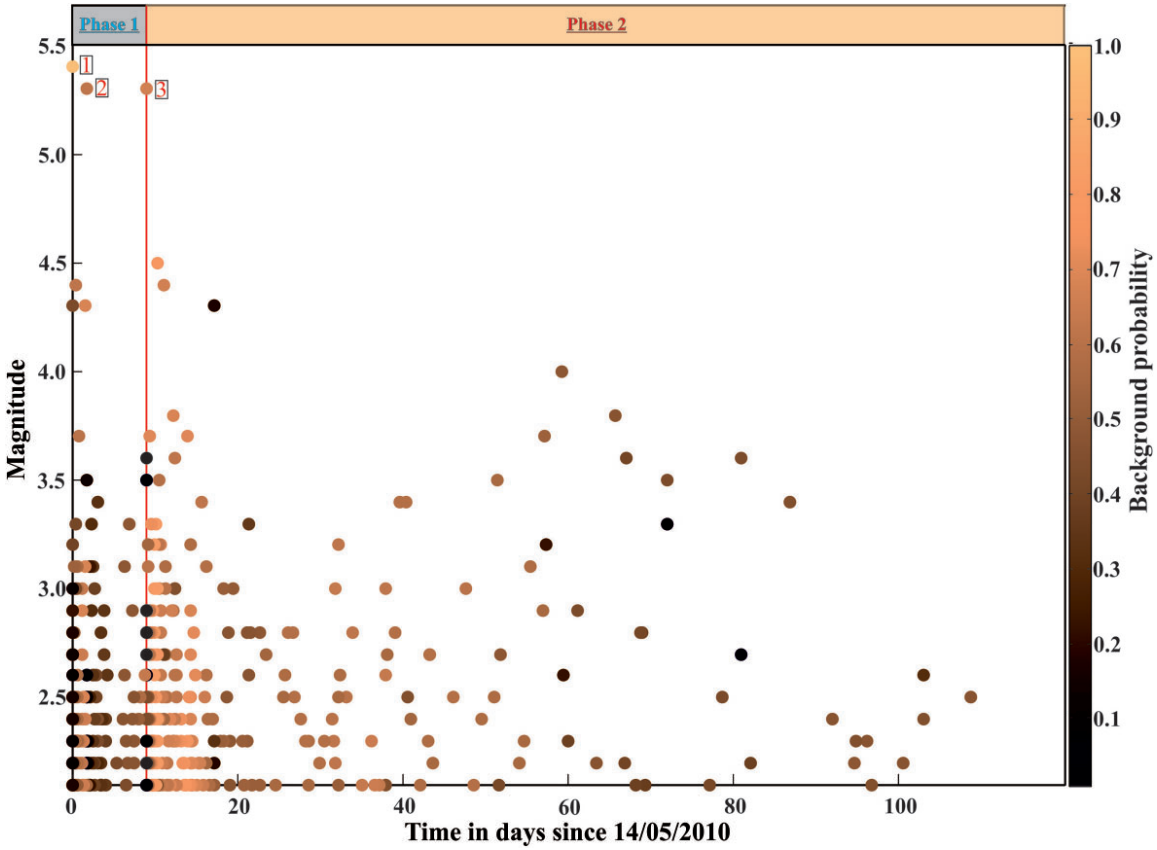

Figure 8. Magnitude against time with scaled colours based on background probability.

that the triggered aftershocks are manifested much more in Cluster 1 along the E-W direction with some being produced in Cluster 2. Then after the occurrence of the BI-MS3 in the second phase (Fig. 9a), Cluster 2 exploded by a significant number of the background events along the NNE-SSW direction. Therefore, from the spatio-temporal distribution of the background probability (Figs 8 and 9), we conclude that the 2010 BI earthquake sequence started with the triggered aftershocks of the BI-MS1 and BI-MS2 generally along the Cluster 1 on E-W direction, then the background events began to appear after the occurrence of the BI-MS3 along of Cluster 2 on NNE-SSW direction.

Our results are in agreement with the last study conducted by Abacha *et al.* (2023) where, from local earthquake tomography and 4-D V_p/V_s models, they show evidence that processes triggering the 2010 BI earthquake sequence were fluid-driven. They made four images of V_p/V_s models (an important parameter for determining fluid and crack migration within the crust) for four periods A, B, C and D chosen according to the events' cumulative number. The important result of this study is the apparition of the high-V_p/V_s anomaly in the central part after the occurrence of the BI-MS3 (period B), which is interpreted as fluid-saturated rocks. This fluid was considered by Abacha *et al.* (2014) as the presence of a hydrocarbon reservoir in the central part of the studied region. They also found an increase of the V_p/V_s ratio with depth, reaching its maximum value of 1.97 at 7-km depth not far from the third main shock. They suggest that it is more likely that a hydrocarbon reservoir is located near Cluster 2 at the 7-km depth, then the fluids migrated vertically and laterally, after being released by the third BI-MS3.

We reproduced this work with the same inversion parameters but for the two phases revealed by this study. The results are displayed in Fig. 9(b), which shows, as expected, a high-V_p/V_s anomaly appearing immediately after the BI-MS3 in the second phase with the maximal value of 1.97 recorded near this main shock. Therefore, the rupture of the NNE-SSW by BI-MS3 liberated the high-pressure fluids which moved upward through the damage area, triggering earthquakes by causing pore-pressure perturbations.

On the other hand, the study of Abacha *et al.* (2023) investigates, also, seismicity migration by modelling seismic events using the equation of Shapiro *et al.* (1997). Their results demonstrate a good fit on Cluster 2 with a reduced diffusivity and a migration velocity ($D = 2.4$ m^2 s^{-1} and 600 m d^{-1}, respectively), which points to a pore-pressure diffusion mechanism with a time-delayed response. However, the migration process underlying Cluster 1 is unclear due to the poor fit and the higher diffusivity than is normally expected for the upper crust. This supports our conclusion on the important role played by the fluids in the production of Cluster 2, as well as a large number of the produced events.

Thus, as a summary, our research of the BI Earthquake sequence reveals that the underlying triggering process is a combination of seismic mechanisms, beginning with tectonic seismicity and then moving on to an aseismic forcing, generated during a 4-month period from 2010 May 14 to August 31. A more probable explanation is that the (BI-MS3) broke a sealed source and helped the intrusion of fluid and therefore caused an increase of seismic events, which explains the high number of events recorded. Also, the migration of fluid may have expanded the rupturing fault. This mixing between two seismic mechanisms often appears in the case of moderate to

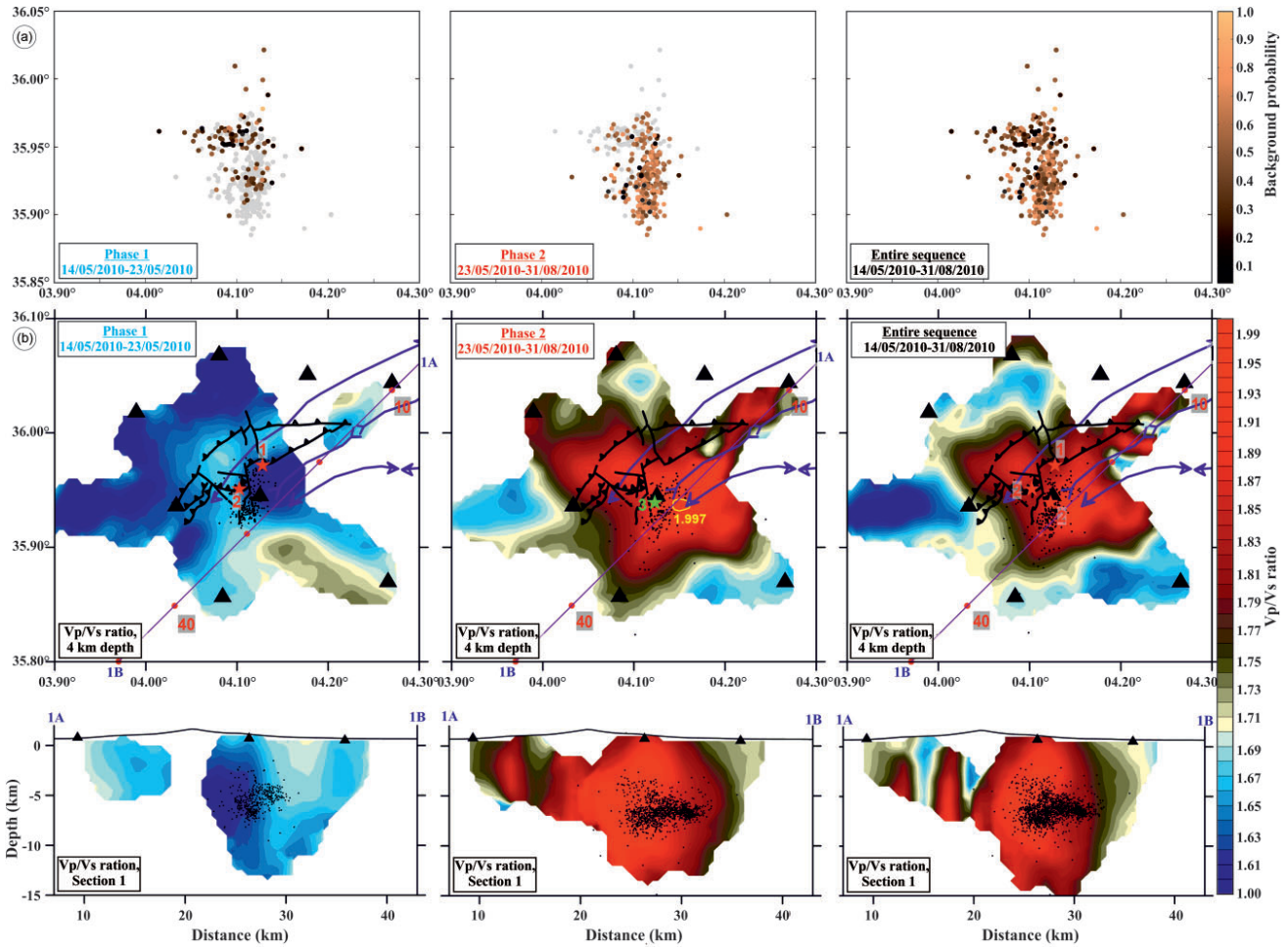

Figure 9. (a) Spatial plot of background and aftershock seismicity relocated for the two phases and the entire seismicity. Scaled colours are based on background probability and grey points are the whole seismicity. (b) V_p/V_s ratios in horizontal sections at depth of 4 km for the first and second phases, and the entire sequence with their cross-sections.

low seismic sequences. Some examples are the 2014 aftershock sequence that occurred in west Bohemia (Vogtland), which was triggered by fluid intrusion (Hainzl *et al.* 2016), and the intraplate anomalous seismicity that occurred in Sarria-Triacastela-Becerrea (NW Iberian Peninsula, Spain; Crespo-Martín *et al.* 2021).

Indeed the involvement of fluids in the triggering process of some earthquake sequences with several main shocks is well known in the northeastern part of Algeria. We can cite the 2012–2013 Bejaia-Babors seismic sequence (Boulahia *et al.* 2021), the 2015 Ain Azel sequence (Abacha *et al.* 2022) and the 2020 Mila sequence (Boulahia et al. in preparation). We intend to apply the same methodology applied in this study in order to determine the seismic mechanisms behind the occurrence of these earthquake sequences through time-dependent and spatio-temporal statistical analysis.

5 CONCLUSION

This study focused on the most representative seismic sequences in Algeria after the 2003 Boumerdes earthquake (M_w 6.9); this work investigates the 2010 BI earthquake sequence that hit the transition zone between the Bibans and Hodna mountains (one of the main southern geological massifs of the Atlas Tellian system), over 4 months since 2010 May 14. The BI sequence is marked by the occurrence of three main shocks (BI-MS1, BI-MS2 and BI-MS3) of $M_w \geq 5.3$ and by a great number of events distributed on the main clusters (first oriented E-W and the second oriented NNE-SSW), which left the inquiry about the seismic mechanism behind its occurrence.

Our study is based on a time-dependent and spatio-temporal statistical analysis of the BI sequence especially the isolation of background from the main shock–aftershock contribution by means of the application of the ETAS model and the comparison with the 4-D V_p/V_s models. Our results allow us to identify two phases.

In the first phase (May 14–23), intensive earthquake sequence dominated seismicity, particularly related to aftershocks of the BI-MS1 and BI-MS2. Due to the stress changes they caused, these main shocks also assisted a subsequent aseismic process that significantly aided in the triggering of the observed activity.

After the occurrence of the third main shock (BI-MS3) in the second phase the aseismic forcing (53 per cent background contribution) took place along the second cluster. After rupturing the fault by the BI-MS3, the high-pressure fluids flowed upward through the damage zone, triggering earthquakes by causing pore-pressure perturbations. This conclusion is supported by a high-V_p/V_s anomaly that appeared immediately after the occurrence BI-MS3. The fluid was interpreted as the presence of a hydrocarbon reservoir in the central part of the studied region.

The statistical analysis with the temporal characteristics and Gutenberg–Richter law allowed us to understand the underlying mechanism, which can improve our seismic hazard models. Hence, the need to make these studies on the other sequences of the northern part of Algeria. Indeed, a study conducted by Atkinson *et al.* (2015) demonstrated that the hazard from induced seismicity in a region with low-to-moderate seismic activity can exceed the hazard from natural background seismicity at most probabilities of engineering interest. In fact, induced seismicity can significantly increase the rate of earthquakes, and in some cases, it can trigger potentially damaging earthquakes as large as $M = 5.7$ (Keranen *et al.* 2013; Sumy *et al.* 2014). The latter study suggested that an induced earthquake can trigger an even larger event if a nearby fault is critically stressed.

On the other hand, a study conducted by Lei *et al.* (2013) demonstrated that the Zigong sequence, caused by fluid infiltration, showed an increase over time in the maximum magnitude with a decrease in the *b*-value. This suggests that fluid-driven seismicity can increase the rupture length and, in turn, generate larger earthquakes.

ACKNOWLEDGMENTS

We would like to express our gratitude to Dr Sidao Ni, the editor, and the two anonymous reviewers for their valuable comments that significantly contributed to the improvement of the manuscript. This study is part of the ES-04–2020 project conducted by the Seismological Studies Department of CRAAG.

CONFILICT OF INTEREST

The authors declare no competing interests.

DATA AVAILABILITY

The data are issued from the Algerian Seismological Network, which is made up of 80 stations. The data are primarily utilized by Algerian researchers, as CRAAG is not a Data Management Center like some well-known international centres such as IGN (Spain). Instead, CRAAG is a research centre that falls under the Algerian Interior Ministry, which manages the country's national security, including natural risks. The Ministry has its own policy for data exchange and allows CRAAG to exchange data with international agencies that have agreements and conventions with them, such as CESM, IGN and ISC. We have recently signed an agreement with INGV for future cooperation.

REFERENCES

Abacha, I. & Yelles-Chaouche, A., 2019. Overview of recent seismic activity in Northeastern Algeria. In: ,Sundararajan, N, ,Eshagh, M, ,Saibi, H, ,Meghraoui, M, ,Al-Garni, M& & ,Giroux, B(eds) *On Signifcant Applications of Geophysical methods. In: CAJG 2018. Advances in Science, Technology & Innovation*. Springer, Cham. https://doi.org/10.1007/978-3-030-01656-2_46

Abacha, I., Bendjama, H., Boulahia, O., Yelles-Chaouche, A.K., Roubeche, K., Rahmania, S.T., Meliam, M.A. & Tikhamarine, E.M., 2023. Fluid-driven processes triggering the 2010 Beni-Ilmane earthquake sequence (Algeria): evidence from local earthquake tomography and 4-D vp/vs models. *J. Seismol.,* **27,** 77–94.

Abacha, I., Boulahia, O., Yelles-Chaouche, A., Semmane, F., Beldjoudi, H. & Bendjama, H., 2019. The 2010 Beni-Ilmane, Algeria, Earthquake sequence: statistical analysis, source parameters, and scaling relationships. *J. Seismol.,* **23**(1), 181–193.

Abacha, I., Koulakov, I., Semmane, F. & Yelles-Chaouche, A.K., 2014. Seismic tomography of the area of the 2010 Beni-Ilmane Earthquake Sequence, North-Central Algeria. *Springerplus,* **3**(1), 1–10.

Abacha, I., Yelles-Chaouche, A. & Boulahia, O., 2022. Statistical study of earthquake swarms in northeastern Algeria with special reference to the Ain Azel swarm; Hodna Chain 2015. In: *Advances in Geophysics, Tectonics and Petroleum Geosciences. CAJG 2019. Advances in Science, Technology & Innovation*. Springer, Cham. https://doi.org/10.1007/978-3-030-73026-0_34.

Akaike, H., 1974. A new look at the statistical model identification. *IEEE Trans. Autom. Control,* **1,** 716–723, doi: 10.1109/TAC.1974.1100705.

Aki, K., 1965. Maximum likelihood estimate of b in the formula log N = a—bM and its confidence limits. *Bull. Earthq. Res. Inst. Univ. Tokyo,* **43,** 237–239

Atkinson, G.M., Ghofrani, H. & Assatourians, K., 2015. Impact of induced seismicity on the evaluation of seismic hazard: some preliminary considerations. *Seismol. Res. Lett.,* **86,** 1009–1021.

Beldjoudi, H., Delouis, B., Djellit, H., Yelles-Chaouche, A.K., Gharbi, S. & Abacha, I., 2016. The Beni-Ilmane (Algeria) seismic sequence of May 2010: seismic sources and stress tensor calculations. *Tectonophysics,* **670,** 101–114.

Bendjama, H., Yelles-Chaouche, A.K., Boulahai, O., Abacha, I., Mohammedi, Y., Beldjoudi, H., Rahmani, S.T. & Belheouane, O., 2021. The March 2017 earthquake sequence along the E–W-trending Mcid Aicha–Debbagh Fault, Northeast Algeria. *Geosci J.,* **25,** 697–713.

Benouar, D., 1994. The Melouza earthquake of 21 February 1960, seismicity of Algeria and adjacent region during the twentieth century. *Ann. Geofis.,* **37**(4), 427–435pp.

Bird, P., 2003. An updated digital model of plate boundaries. *Geochem. Geophys. Geosyst.,* **4,** doi: 10.1029/2001GC000252.

Bougrine, A., Yelles-Chaouche, A.K. & Calais, E., 2019. Active deformation in Algeria from continuous GPS measurements. *Geophys. J. Int.,* **217,** 572–588.

Boulahia, O., Abacha, I., Yelles-Chaouche, A., Bendjama, H., Kherroubi, A., Mohammedi, Y., Aidi, C. & Chami, A., 2021. Recent seismic activity in the Bejaia-Babors Region (Northeastern Algeria): the case of the 2012–2013 Bejaia Earthquake sequences. *Pure appl. Geophys.,* **178,** 1253–1279.

Bufe, C.G., 1970. Frequency-magnitude variations during the 1970 Danville earthquake swarm. *Earthq. Notes,* **41,** 3–7.

Corral, A., 2004. Long-term clustering, scaling, and universality in the temporal occurrence of earthquakes. *Phys. Rev. Lett.,* **92,** doi: 10.1103/physrevlett.92.108501.

Crespo-Martín, C., Martín-Gonzalez, F., Yazdi, Y., Hainzl, S. & Rincon, M., 2021. Time-dependent and spatiotemporal statistical analysis of intraplate anomalous seismicity: sarria-Triacastela-Becerrea (NW Iberian Peninsula, Spain). *Geophys. J. Int.,***225,** 477–493

Enescu, B., Mori, J., Masatoshi, M. & Kano, Y., 2009. Omori-Utsu law c-values associated with recent moderate earthquakes in Japan. *Bull. seism. Soc. Am.,* **99,** 884–891.

Gibowicz, S.J., 1973. Variation of the frequency-magnitude relation during earthquake sequences in New Zealand. *Bull. seism. Soc. Am.,* **63**(2), 517–528.

Gutenberg, B. & Richter, C.F., 1942. Earthquake magnitude, intensity, energy and acceleration. *Bull. seism. Soc. Am.,* **32,** 163–191.

Hainzl, S. & Marsan, D., 2008.Dependence of the Omori-Utsu law parameters on main shock magnitude: observations and modeling, *J. geophys. Res.,* **113,** doi: 10.1029/2007JB005492.

Hainzl, S. & Ogata, Y., 2005. Detecting fluid signals in seismicity data through statistical earthquake modeling. *J. geophys. Res.,* **110**(5), B05S07, doi: 10.1029/2004JB003247.

Hainzl, S., Fischer, T., Cermakova, H., Bachura, M. & Vlcek, J., 2016. Aftershocks triggered by fluid intrusion: evidence for the aftershock sequence

occurred 2014 in West Bohemia/Vogtland. *J. geophys. Res. Solid Earth,* **121,** 2575–2590,

Hainzl, S., Scherbaum, F. & Beauval, C., 2006. Estimating background activity based on interevent-time distribution. *Bull. seism. Soc. Am.,* **96,** 313–320

Hainzl, S., Zakharova, O. & Marsan, D., 2013. Impact of aseismic transients on the estimation of aftershock productivity parameters. *Bull. seism. Soc. Am.,* **103,** 1723–1732.

Hamdache, M., Pelaez, J.A., Gospodinov, D. & Henares, J., 2017. Statistical features of the 2010 Beni-Ilmane, Algeria, aftershock sequence. *Pure appl. Geophys.,* **175,** 773–792.

Hatzfeld, D., 1978. *Etude Sismotectonique De la Zone de Collision Ibéro-Maghrébine Thèse de Doctorat Ès-Sciences Physiques Laboratoire De Géodynamique Interne,* Université Scientifique et Médicale de Grenoble, p. 281.

Helmstetter, A. & Sornette, D., 2002. Subcritical and supercritical regimes in epidemic models of earthquake aftershocks. *J. geophys. Res.,* **107**(B10), doi: 10.1029/2001JB001580.

Helmstetter, A. & Sornette, D., 2003. Foreshocks explained by cascades of triggered seismicity. *J. geophys. Res.,* **108,** 2457, doi:10.1029/2003JB002409.

Helmstetter, A., Kagan, Y.Y. & Jackson, D.D., 2006. Comparison of short-term and time-independent earthquake forecast models for southern California. *Bull. seism. Soc. Am.,* **96**(1), 90–106.

Kagan, Y.Y., 2004. Short-term properties of earthquake catalogs and models of earthquake source. *Bull. seism. Soc. Am.,* **94**(4), 1207–1228.

Karimi, K. & Davidsen, J., 2021. Aftershock triggering and spatial Aftershock zones in fluid-driven settings: discriminating induced seismicity from natural swarms. *Geophys. Res. Lett.,* **48,** e2020GL092267, doi:10.1029/ 2020gl092267.

Keranen, K.M., Savage, H.M., Abers, G.A. & Cochran, E.S., 2013. Potentially induced earthquakes in Oklahoma, USA: links between wastewater injection and the 2011 Mw 5.7 earthquake sequence. *Geology,* **41,** 699–702.

Khelif, M.F. *et al.*, 2018. The 2016 Mihoub (north-central Algeria) earthquake sequence: seismological and tectonic aspects. *Tectonophysics,* **736**(2018), 62–74.

Kisslinger, C., 1996. Aftershocks and fault-zone properties. *Adv. Geophys.,* **38,** 1–36.

Kumazawa, T. & Ogata, Y., 2014. Nonstationary ETAS models for nonstandard earthquakes. *Ann. Appl. Stat.,* **8,** 1825–1852.

Lei, X., Ma, S., Chen, W., Pang, C., Zeng, J. & Jiang, B., 2013. A detailed view of the injection-induced seismicity in a natural gas reservoir in Zigong, southwestern Sichuan Basin, China. *J. geophys. Res.: Solid Earth,* **118,** 4296–4311.

Marsan, D., Prono, E. & Helmstetter, A., 2013. Monitoring aseismic forcing in fault zones using earthquake times series. *Bull. seism. Soc. Am.,* **103,** 169–179.

Marzocchi, W. & Sandri, L. 2003. A review and new insights on the estimation of the b-value and its uncertainty. *Annals of geophysics,* **46,** 1271–1282.

Marzocchi, W., Spassiani, I., Stallone, A. & Taroni, M., 2020. How to be fooled searching for significant variations of the b-value. *Geophys. J. Int.,* **220**(3), 1845–1856.

Mignan, A. & Woessner, J., 2012. Estimating the magnitude of completeness for earthquake catalogs, *Estimating the magnitude of completeness for earthquake catalogs,* doi: 10.5078/corssa00180805.

Mogi, K., 1967. Earthquake and fractures. *Tectonophysics,* **5,** 35–55.

Nanjo, K., Nagahama, H. & Satomura, M., 1998., Rates of aftershock decay and the fractal structure of active fault systems. *Tectonophysics,* **287,** 173–186.

Narteau, C., Byrdina, S., Shebalin, P. & Schorlemmer, D. 2009. dependence on stress for the two fundamental laws of statistical seismology. *Nature,* **462,** 642–645.

Nocquet, J.M., 2012. Present-day kinematics of the Mediterranean: A comprehensive overview of GPS results. *Tectonophysics,* **578,** 220–242, https://doi.org/10.1016/j.tecto.2012.03.037.

Nocquet, J.M., Willis, P. & Garcia, S., 2006. Plate kinematics of Nubia–Somalia using acombined DORIS and GPS solution. *Journal of Geodesy 80, 591–607,* http://dx.doi.org/10.1007/s00190-006-0078-0.

Ogata, Y. & Katsura, K., 1993. Analysis of temporal and spatial heterogeneity of magnitude frequency distribution inferred from earthquake catalogues. *Geophys. J. Int.,* **113,** 727–738

Ogata, Y., 1988. Statistical models for earthquake occurrence and residual analysis for point processes. *J. Am. Stat. Assoc.,* **83,** 9–27.

Petruccelli, A., Schorlemmer, D., Tormann, T., Rinaldi, A.P., Wiemer, S., Gasperini, P. & Vannucci, G., 2019. The influence of faulting style on the size-distribution of global earthquakes. *Earth planet. Sci. Lett.,* **527,** 10.1016/j.epsl.2019.115791.

Scholz, C.H., 1968. The frequency-magnitude relation of microfracturing in rock and its relation to earthquakes. *Bull. seism. Soc. Am.,* **58**(1), 399–415.

Shapiro, S.A., Huenges, E. & Borm, G., 1997. Estimating the permeability from fluid-injection-induced seismic emissions at the KTB site. *Geophys. J. Int.,* **131,** F15–F18.

Sornette, D. & Werner, M.J., 2005. Apparent clustering and apparent background earthquakes biased by undetected seismicity. *J. geophys. Res.,* **110,** B09303, doi:10.1029/2005JB003621.

Sumy, D.F., Cochran, E.S., Keranen, K.M., Wei, M. & Abers, G.A., 2014. Observations of static Coulomb stress triggering of the November 2011 M 5.7 Oklahoma earthquake sequence. *J. geophys. Res.,* **119,** 1904–1923.

Utsu, T., 1965. A method for determining the value of b in the formula log n = a—bm showing the magnitude-frequency relation for earthquakes. *Geophys. Bull. Hokkaido Univ.,* **13,** 99–103

Utsu, T., Y., Ogata, & R.S, Matsu'ura. 1995. The centenary of the Omori formula for a decay of aftershock activity. *J. Phys. Earth,* **43,** 1–33.

Van Stiphout, T., Zhuang, J. & Marsan, D., 2012. Seismicity declustering, community online resource for statistical Seismicity analysis, doi:10.5078/corssa-52382934. Available at http://www.corssa.org.

Wyss, M., 1973. Towards a physical understanding of the earthquake frequency distribution. *Geophys. J. R. astro. Soc.,* **31**(4), 341–359.

Yelles-Chaouche, A.K. *et al.*, 2022. The recent seismicity of northern Algeria: the 2006–2020 catalogue. *Mediterranean Geosci. Rev.,* **4,** 407–426.

Yelles-Chaouche, A.K., Abacha, I., Semmane, F., Beldjoudi, H. & Djellit, H., 2014. The Beni-Ilmane (north-central Algeria) earthquake sequence of May 2010. *Pure appl. Geophys.,* **171**(7), 1283–1298.

Yelles-Chaouche, K., Lammali, K., Mahsas, A., Calais, E. & Briole, P., 2004. Coseismic deformation of the May 21st, 2003, Mw = 6.8 Boumerdes earthquake, Algeria, from GPS measurements. *Geophys. Res. Lett.,* **31,** L13610, doi:10.1029/2004GL019884.

Yelles-Chaouche, K.A., Khelif, M.F., Haned, A., Chami, A., Aidi, C., Beldjoudi, H., Kherroubi, A. & Benaissa, Z., 2018. The Algiers (north central Algeria) earthquake of August 1st, 2014 Mw 5.5 in the Algiers Bay tectonic context. *J. Seismol.,* **23,** 287–302.

Zhuang, J., Ogata, Y. & Vere-Jones, D., 2002. Stochastic declustering of space-time earthquakes occurrences. *J. Am. Stat. Assoc.,* **97,** 369–380.

APPENDIX A. CLUSTERS IDENTIFICATION

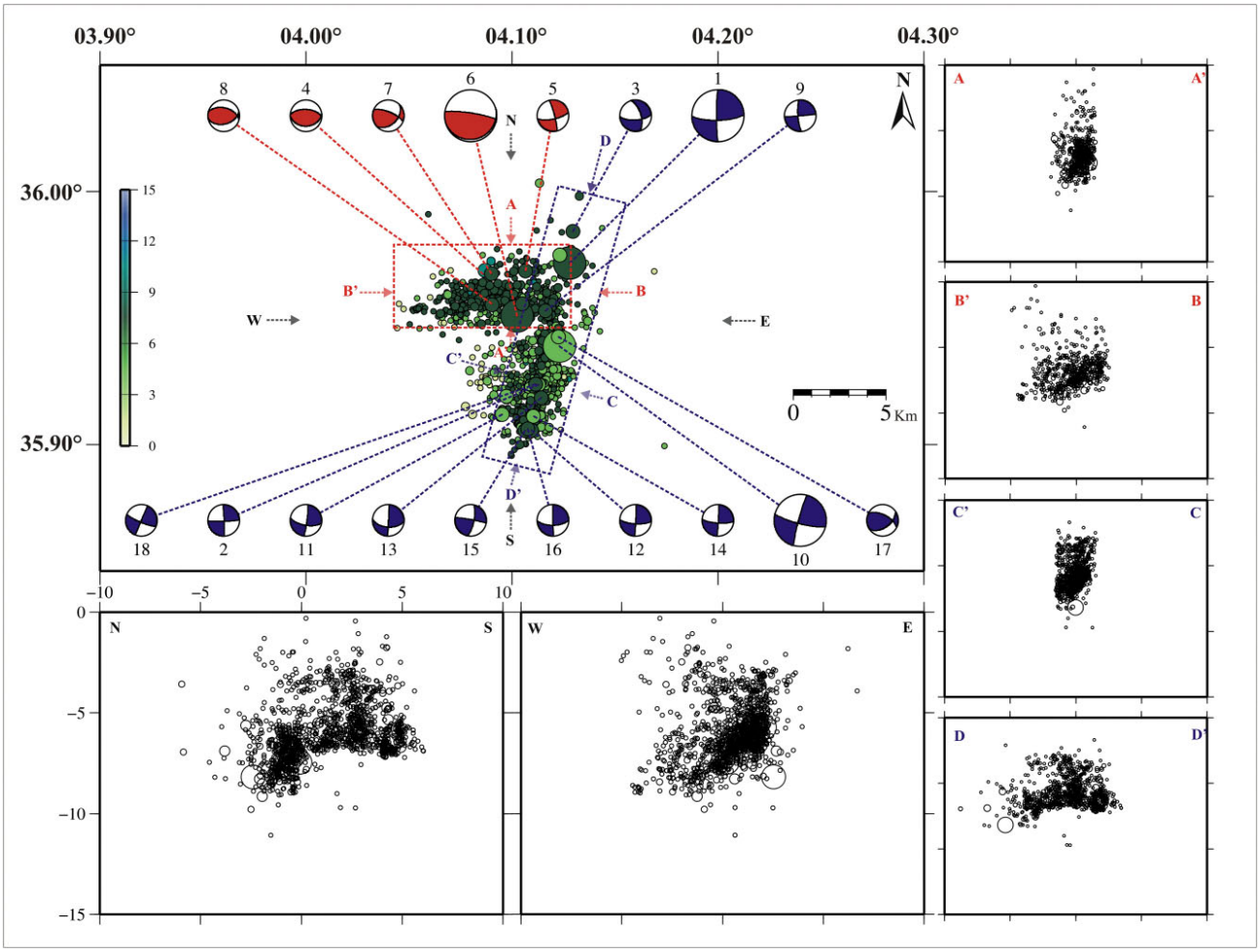

Figure A1. Horizontal and vertical distributions of the 1403 relocated events, showing focal mechanisms of events with $M \geq 4$. The E-W rectangle represents the first cluster and the NNE-SSW rectangle represents the second cluster (Yelles-Chaouche *et al.* 2014).

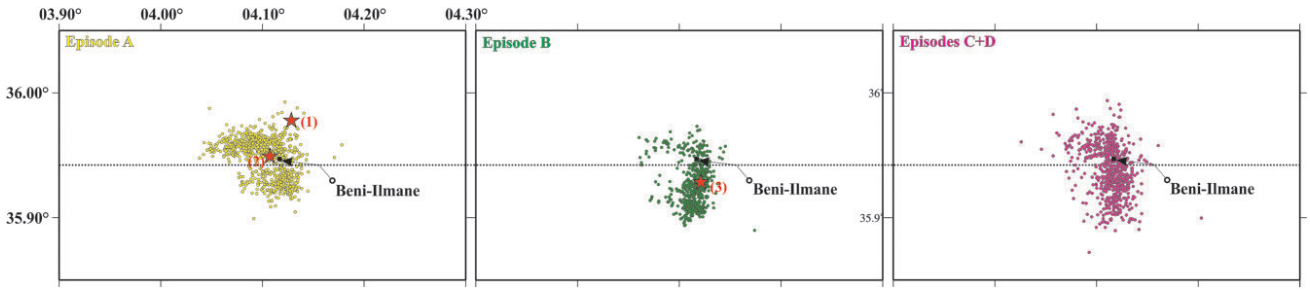

Figure A2. Horizontal distribution of the accurately located events for four episodes. Episode A (between the first and third main shocks), episode B (between the third main shock and 2010 May 31), and episodes C and D (from 2010 June 01 to the end of the data localized) according to the Abacha *et al.* (2023) study.

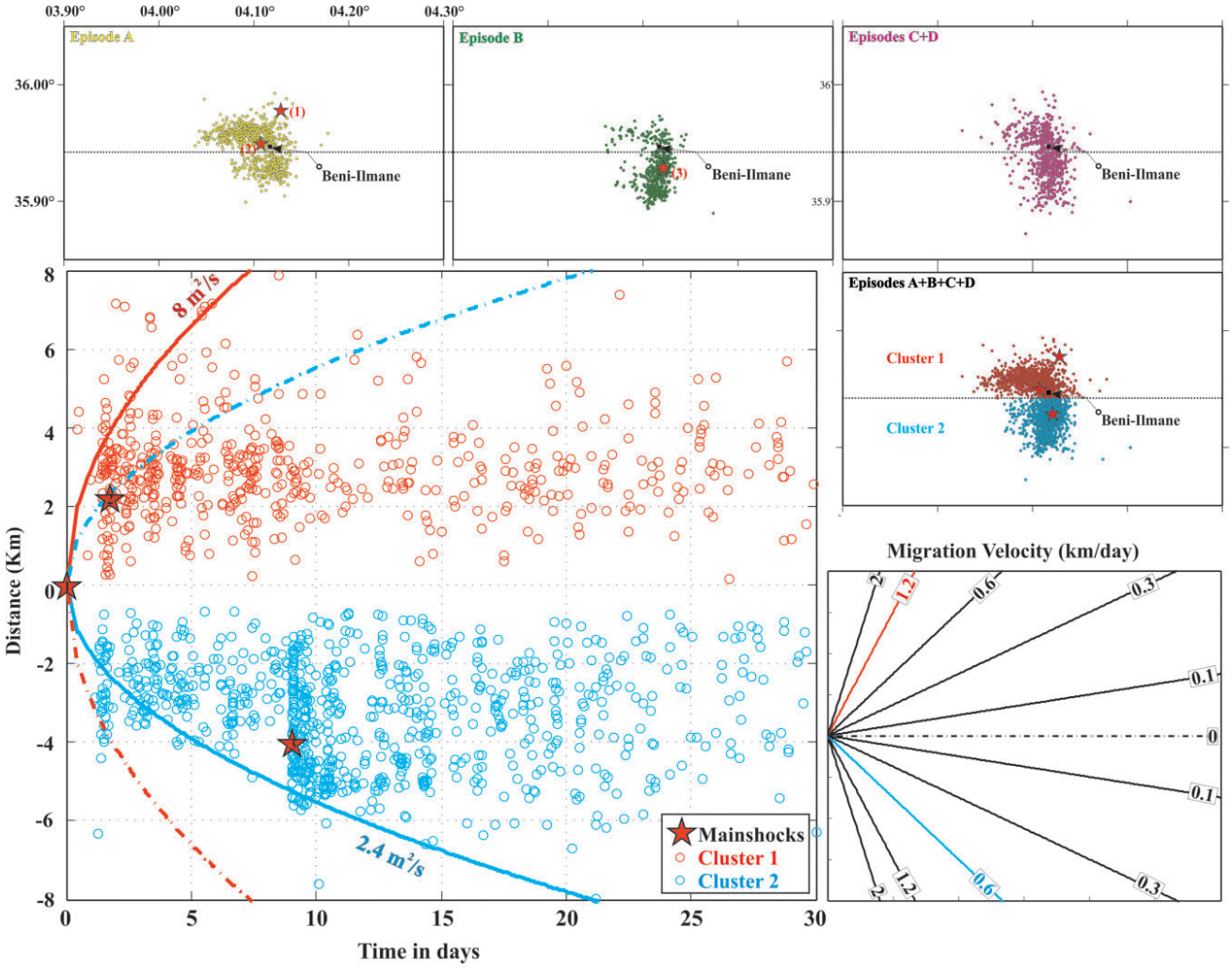

Figure A3. Spatio-temporal diagram for the evolution of the 2010 BI earthquake sequence over time since the first main shocks on 2010 May 14. Parabolic theoretical curves of the probable triggering fronts considering hydraulic diffusivity values $D = 8$ m^{2}s^{-1} for Cluster 1 (upper curve) and $D = 2.4$ m^2 s^{-1} for Cluster 2 (bottom curve). The migration velocity-indicating lines in the box in the bottom-right corner refer to horizontal migration (Abacha *et al.* 2023).

APPENDIX B. SHORT-TIME AFTERSHOCK INCOMPLETENESS

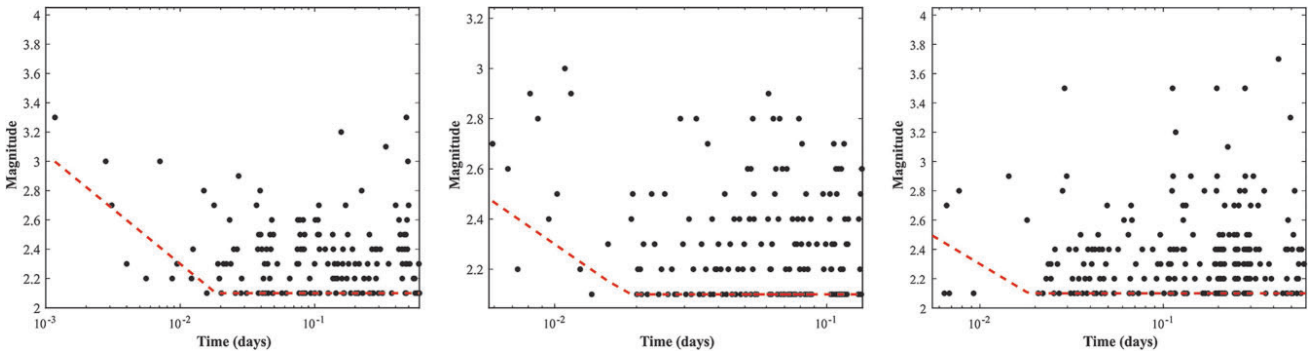

Figure B1. Magnitude versus time representing short-time incompleteness.

APPENDIX C. PER CENT OF EVENTS WITH BACKGROUND PROBABILITY GREATER OR EQUAL TO 50 PER CENT

Table C1. Per cent of events for different background probabilities.

Data	>0.9 (per cent)	>0.8 (per cent)	>0.7 (per cent)	>0.6 (per cent)	>0.5 (per cent)
Whole sequence	0.23	6.23	19.8	48	69
Phase 01	0.23	0.23	1.8	6	14
Phase 02	0	6	18	41	55

APPENDIX D. BACKGROUND RATE FOR DIFFERENT MOVING WINDOWS USING THE INTER-EVENT TIME

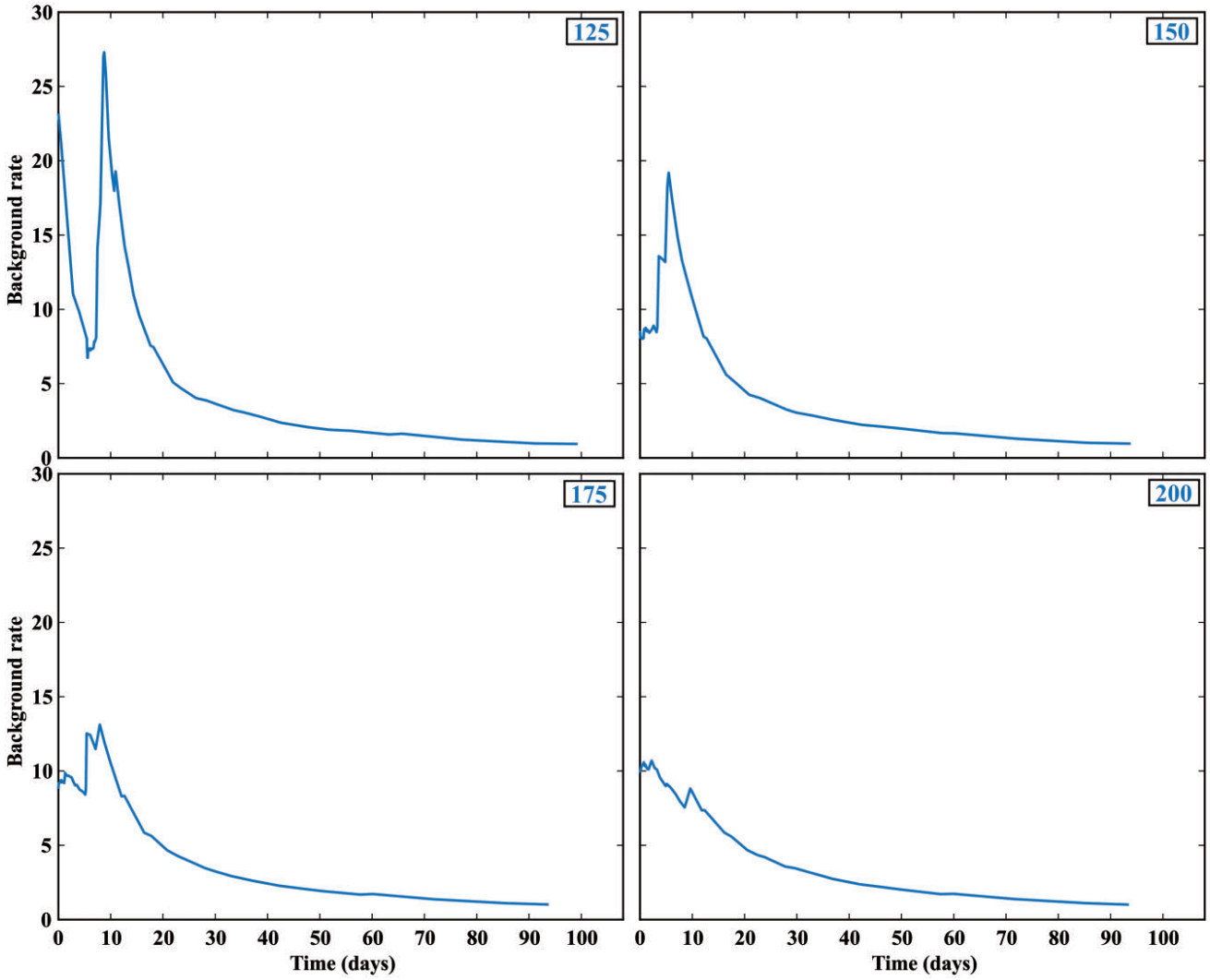

Figure D1. Background rate versus time for different windows ranging from 125 to 200 events.

Natural Hazards

Detecting and Interpreting Earthquake Swarms in Northeastern Algeria (2007-2020): Evidence from a Dual Approach.

--Manuscript Draft--

Manuscript Number:	NHAZ-D-24-00416
Full Title:	Detecting and Interpreting Earthquake Swarms in Northeastern Algeria (2007-2020): Evidence from a Dual Approach.
Article Type:	Manuscript
Keywords:	Northeastern Algeria, Earthquake swarms, ETAS, Fluid migration, Moment release
Corresponding Author:	Sofiane Taki-Eddine Rahmani CRAAG: Centre de Recherche en Astronomie Astrophysique et Geophysique Setif, Setif ALGERIA
Corresponding Author Secondary Information:	
Corresponding Author's Institution:	CRAAG: Centre de Recherche en Astronomie Astrophysique et Geophysique
Corresponding Author's Secondary Institution:	
First Author:	Sofiane Taki-Eddine Rahmani
First Author Secondary Information:	
Order of Authors:	Sofiane Taki-Eddine Rahmani
	Issam Abacha
	Oualid Boulahia
	El-Mahdi Tikhamarine
	Khaled Roubeche
Order of Authors Secondary Information:	
Funding Information:	
Abstract:	In northeastern Algeria, seismic activity is distinguished by the occurrence of swarms or classic sequences, showing intense temporal and spatial clustering, lasting from days to months and extending over distances of a few to tens of kilometers, sometimes displaying migration patterns over several weeks. Categorizing seismic swarms and comprehending their underlying mechanisms is essential for mitigating seismic risk in the region, especially as they are indicative of potential physical changes in the crust, such as slow slip or fluid flow, which makes them particularly noteworthy. To identify seismic swarms, two methodologies were applied, including the use of spatio-temporal ETAS models and moment release time series analysis, covering data from 2007 to 2020 in the region. Identifying 32 clusters, totaling 676 events and accounting for 29% of the catalog above the magnitude threshold of 2.8, revealed 32 swarm sequences marked by event counts exceeding five, with subsequent computation of the b-value across the entirety of the swarm catalog; these clusters were then classified into zones based on the geological and tectonic context of each area. Ultimately, we offer potential explanations for the mechanisms driving the formation of these swarms, alongside investigating their spatial migration and temporal evolution.
Suggested Reviewers:	David Marsan ISTerre david.marsan@univ-smb.fr He's one of the professional, who studied earthquake swarms trhough statistical analysis
	Tomoaki Nishikawa Kyoto university nishikawa@eps.s.u-tokyo.ac.jp

Appendix B

Scietific contributions

J Seismol (2023) 27:77–94
https://doi.org/10.1007/s10950-022-10130-8

ORIGINAL ARTICLE

Fluid-driven processes triggering the 2010 Beni-Ilmane earthquake sequence (Algeria): evidence from local earthquake tomography and 4D Vp/Vs models

Issam Abacha · Hichem Bendjama · Oualid Boulahia · AbdelKarim Yelles-Chaouche · Khaled Roubeche · Sofiane Taki-Eddine Rahmani · Mohamed Anis Melaim · El-Mahdi Tikhamarine

Received: 25 February 2022 / Accepted: 28 December 2022 / Published online: 25 January 2023

Abstract The 2010 Beni-Ilmane earthquake sequence, with 3 Mw ≥ 5.2 mainshocks, occurred in the southern Tellian Atlas approximately 200 km southeast of the Algiers. We offer updated 3D Vp and Vs models, and we outline the space and time variations in the Vp/Vs ratio of the Beni-Ilmane crust based on 2297 well-located aftershocks representing the complete aftershock sequence. Two main P-wave low-velocity patterns correspond to fault alignments determined from geological studies: the NE–SW thrust fault located at the foot of Djebel Chouk-chot and the NNW–SSE oriented Samma strike-slip corridor. The former crosscuts the two P-wave high-velocity anomalies of the Kef Ouagnane and Kef Kherrat summits of the Choukchot Mountains. The third high-velocity anomaly represents the Jebel Affroun Mountain in the sub-Bibanic domain. Two high-Vp/Vs ratio patterns were revealed in the central aftershock part and along the NE–SW Ouanougha syncline, which constitutes a fluid reservoir and a fluid-saturated fault zone filled after aftershock activity. The 4D Vp/Vs models monitored fluid migration, and the modeled pore-pressure diffusion revealed that earthquake rupture along an ~ N–S blind strike-slip fault fractured the closed reservoir and released high-pressure fluids, provoking a notable and long-lasting aftershock sequence. Our study underlines that local earthquake tomography (LET) can provide useful insights into the upward migration of fluids from a compartmentalized hydrocarbon reservoir.

Keywords Beni-Ilmane sequence · Seismotectonic · LET · Fluids · 4D Vp/Vs ratio, pore-pressure diffusion

Highlights
- This updated investigation used twice the number of events from a previous study.
- A high-Vp/Vs anomaly coincided with hydrocarbon reservoirs and fluid-saturated faults.
- The migration of high-pressure fluids released from a ruptured reservoir caused aftershock activity.

Supplementary Information The online version contains supplementary material available at https://doi.org/10.1007/s10950-022-10130-8.

I. Abacha (✉) · H. Bendjama · O. Boulahia · A. Yelles-Chaouche · K. Roubeche · S. T.-E. Rahmani
Center of Research in Astronomy, Astrophysics, and Geophysics, CRAAG, Route de L'Observatoire BP 63 Bouzaréah, Algiers, Algeria
e-mail: abacha.issam@yahoo.fr

M. A. Melaim · E.-M. Tikhamarine
University Ferhat Abbas of Setif, Setif, Algeria

1 Introduction

In May 2010, the Beni-Ilmane region (north-central Algeria, Fig. 1a) was struck by a never-before-seen seismic sequence, as this was the first time in Algeria that a sequence was observed with three mainshocks of a Mw ≥ 5.2 magnitude, recorded on May 14, 16,

Pure Appl. Geophys. 180 (2023), 1945–1971

https://doi.org/10.1007/s00024-023-03265-3

Pure and Applied Geophysics

The 24 January 2020 Mw 5.0 El Aouana Earthquake, Northeastern Algeria: Insights into a New NW–SE Right-Lateral Bejaia-Babors Shear Zone

Issam Abacha,[1] Oualid Boulahia,[1] Abdelkarim Yelles-Chaouche,[1] Hichem Bendjama,[1] Haakon Fossen,[2] Moulley Charaf Chabou,[3] Khaled Roubeche,[1] Sofiane Taki-Eddine Rahmani,[1] El-Mahdi Tikhamarine,[4] Yahia Mohammedi,[1] and Chafik Aidi[1]

Abstract—On January 24, 2020, a Mw 5.0 earthquake occurred in the El Aouana region, northeastern Algeria. This region is located at the western end of the Lesser Kabylian Block (LKB), a rigid body that was weakly deformed during the late Cenozoic tectonic phase, and it is characterized by a lower seismic activity than that in its bounding regions. The mainshock focal mechanism was estimated via both the P-wave first motion and waveform modeling methods. The earthquake was associated with the rupture of a NW–SE-oriented right-lateral strike-slip fault, as revealed by a 6 km long and 2 km wide aftershock cluster. The seismic moment estimated through waveform modeling was 3.6×10^{16} Nm, while spectral analysis yielded a value of 3.9×10^{16} Nm corresponding to a magnitude of Mw 5.0, a source radius of 1.6 km, and a stress drop of 4 MPa. The spatiotemporal evolution of the aftershock sequence, as modeled using a restricted epidemic-type aftershock sequence (RETAS) stochastic model, yielded a slope p = 1, indicating that the earthquake was generated by tectonic forces and that the aftershock sequence included many subsequences. The calculated stress tensor suggested N–S compression, rotated clockwise relative to NW–SE Eurasia–Africa convergence. Finally, the recent seismic activity (2012–2021) and geological observations in the area led to the suggestion of a new NW–SE right-lateral shear zone, namely, the Bejaia-Babors shear zone, which was incorporated into a seismotectonic growth model involving slip along inherited E–W structures. The pattern of stepover structures throughout this wide shear zone was enhanced during the recent seismic evolution.

Keywords: El Aouana, RETAS, source parameters, stress tensor, shear zone, stepovers.

1. Introduction

Northeastern Algeria is subjected to substantial, moderate, and shallow seismic activity due to its location along the African–Eurasian plate boundary (blue line in Fig. 1a). One of the main statistical characteristics of Algerian seismicity is its concentration in the country's eastern part, where nearly two-thirds of the recorded seismic events have occurred (Abacha, 2015; Yelles-Chaouche et al., 2006). In this territory, numerous seismic sequences took place over the past decade (2012–2021), particularly around the Lesser Kabylian Block (LKB) (Fig. 1b). These include the 2017 seismic sequences along the Mcid Aïcha-Debbagh Fault (MADF) in the south (Bendjama et al., 2021), the 2014 Ziama and 2019 Jijel earthquakes in the north (Yelles-Chaouche et al., 2021), and the 2012–2013 Bejaia-Babors sequences in the west (Boulahia et al., 2021).

On January 24, 2020, at 07 h 24 m 20 s, the region of Jijel was shaken once more by a shallow earthquake of magnitude Mw 5.0, namely, the El Aouana earthquake at the western boundary of the LKB, 20 km southwest of Jijel (Fig. 1c). The western transverse fault system of Bejaia-Babors constitutes a NW–SE-trending structure associated with right-lateral strike-slip earthquake focal mechanisms. Recent advances in understanding the fault geometry mechanism in this region have been obtained by Boulahia et al. (2021), who identified the majority of the currently known en echelon fault segments that define the western boundary of the transverse fault system. The El Aouana 2020 earthquake exhibits a focal mechanism with one of the planes subparallel to the eastern boundary of the transverse fault system.

Supplementary Information The online version contains supplementary material available at https://doi.org/10.1007/s00024-023-03265-3.

[1] Center of Research in Astronomy, Astrophysics, and Geophysics, CRAAG, Route de l'Observatoire BP 63 Bouzaréah, Algiers, Algeria. E-mail: abacha.issam@yahoo.fr

[2] Museum of Natural History, University of Bergen, Allégaten 41, 5007 Bergen, Norway.

[3] Emerging Materials Research Unit, Department of Earth Sciences, Institute of Architecture and Earth Sciences, Ferhat Abbas University Setif 1, Setif, Algeria.

[4] Departement of Physics, Ferhat Abbas University Setif 1, Setif, Algeria.

Article

https://doi.org/10.1007/s12303-020-0059-y
pISSN 1226-4806 eISSN 1598-7477

Geosciences Journal GJ

The March 2017 earthquake sequence along the E-W-trending Mcid Aïcha-Debbagh Fault, northeast Algeria

Hichem Bendjama*, Abelkarim Yelles-Chaouche, Oualid Boulahia, Issam Abacha, Yahia Mohammedi, Hamoud Beldjoudi, Sofiane Taki-Eddine Rahmani, and Othmane Belheouane

Center of Research in Astronomy, Astrophysics, and Geophysics, Algiers 16340, Algeria

ABSTRACT: In Northeast Algeria, a sequence of 143 small earthquakes ($M_d \leq 4.7$) occurred near the Mcid Aïcha-Debbagh (MAD) Fault between 4 and 16 March, 2017. During this sequence, 74% of the seismic activity occurred in the first two days. Although the earthquakes were not large, they yielded important new information and have improved our understanding of seismic activity in three distinct regions along the fault. In the Sidi Dris region (western MAD Fault), 106 events ($1 \leq M_d \leq 3.2$) were located in an aftershock cluster trending NNE-SSW, highlighting a transverse fault with ~6 km of strike-slip displacement that locally cuts the MAD Fault. In the El Kantour region (central MAD Fault), 31 events were recorded along a 3 km long fault segment, including the M_w 4.7 mainshock. The mainshock had a focal mechanism consistent with predominantly strike-slip motion on a N110°E-striking fault plane, in agreement with the WNW-ESE orientation of the central MAD Fault segment. Finally, six diffuse events occurred in the Hammam Debbagh region (eastern MAD Fault). A significant event (M_d 3.0) in this region had a focal mechanism consistent with strike-slip movement and a normal component trending NW-SE. This is consistent with the fault plane orientations of key events in the time period 2003–2014, likely related to the NW-SE-striking Hammam Debbagh Fault. The present-day stress tensor is characterized by a strike-slip tectonic regime and a σ_1 orientation (N342°E) that closely matches the maximum regional compressive stress orientation (NNW-SSE).

Key words: Mcid Aïcha-Debbagh Fault, strike-slip, focal mechanism, source parameter, waveform modeling

Manuscript received September 11, 2019; Manuscript accepted November 1, 2020

1. INTRODUCTION

Using earthquake data to delineate seismically active geologic structures is one of the primary goals of seismic monitoring. Although large earthquakes provide the most direct information regarding seismically active structures, they are relatively rare in areas with low to moderate strain rates. Fortunately, sequences of small to moderate earthquakes can sometimes be used to highlight active geologic structures that have the potential to generate larger events.

Small to moderate earthquakes have been used to identify and map many faults in the Tellian Atlas, Northeast Algeria. Examples include the 2000 M_d 5.3 Beni-Ouartilane Earthquake (Bouhadad et al., 2003); the 2006 M_d 5.2 Lalam Earthquake (Beldjoudi et al., 2009); the 2010 Beni-Ilmane earthquake sequence that contained three M_d ~5 mainshocks (Yelles-Chaouche et al., 2014); the 2012–2013 Bejaia earthquake sequences, including an M_d 5.2 mainshock (Abacha and Yelles-Chaouche, 2019); and the 2015 M_d 4.8 Ain Azel Earthquake (Abacha and Yelles-Chaouche, 2019). Some of the seismic activity in the Eastern Tellian Atlas occurs along the E-W-trending Mcid Aïcha-Debbagh (MAD) Fault, also referred to as the North Constantine Fault (Raoult, 1974), an > 80 km long strike-slip fault that has been described previously as a late Quaternary active transpressive structure (Meghraoui, 1988; Meghraoui et al., 1996). The MAD Fault has received little attention from the geophysical community despite kinematic models of the Tellian Atlas showing a significant present-day slip-rate deficit of ~2.4 mm yr^{-1} (Bougrine et al., 2019). The relationship between minor seismic events and local geologic structures along the MAD Fault is unclear, mainly because of the paucity of seismic records and a lack of detailed geological investigations.

At 01:46 UTC on 5 March, 2017, the small village of Ain

***Corresponding author:**
Hichem Bendjama
Center of Research in Astronomy, Astrophysics, and Geophysics, Route de l'Observatoire B.P. 63 Bouzaréah 16340, Algiers, Algeria
Tel: +213-6-98-15-18-70, Fax: +213-31-97-32-25,
E-mail: bendjama_2006@yahoo.fr

Journal of African Earth Sciences 177 (2021) 104149

Contents lists available at ScienceDirect

Journal of African Earth Sciences

journal homepage: www.elsevier.com/locate/jafrearsci

The 13 July 2019 Mw 5.0 Jijel Earthquake, northern Algeria: An indicator of active deformation along the eastern Algerian margin

AbdelKarim Yelles-Chaouche, Issam Abacha *, Oualid Boulahia, Chafik Aidi, Adel Chami, Athmane Belheouane, Sofiane Taki-Eddine Rahmani, Khaled Roubeche

Centre de Recherche en Astronomie Astrophysique et Géophysique, CRAAG, Route de L'Observatoire BP 63 Bouzaréah, Algiers, Algeria

ARTICLE INFO

Keywords:
The 2019 jijel earthquake
Thrust fault
Waveform modeling
Source parameters
Stress tensor
Coulomb stress
Deformation process

ABSTRACT

On July 13, 2019, a moderate earthquake shook the Jijel region of Algeria, ~300 km east of Algiers (Capital of Algeria). In the past, the Jijel region experienced a destructive earthquake (I_0: X) on 21–22 August 1856, triggering a moderate tsunami in the western Mediterranean region. The 2019 event is the second important event to have occurred along this part of the Algerian margin, which has been undergoing an inversion process since the Pliocene Epoch. The event occurred 40 km to the north of Jijel City, at 10 km depth. No property damage or injuries were associated with this event. The seismic moment release estimated from waveform modeling was $M_0 = 3 \times 10^{16}$ Nm, corresponding to a Mw 5.0 event. The mainshock focal mechanism is associated with the rupture of an E–W thrust fault that is clarified by a 4-km-long × 10-km-wide aftershock cluster along the continental slope of the Jijel margin. In the same area, ~30 km to the west and offshore of the coastal village of Ziama–Mansouriah (west of Jijel) a Mw 4.1 earthquake occurred in 2014. This event is also associated with the rupture of a western contiguous E–W thrust fault. Stress tensor inversion produces a main (σ_1) maximum stress axis oriented N356E, which is in agreement with previous stress studies of the Lesser Kabylia–Babors block. The present-day stress field is characterized by a compressional tectonic regime ($R' = 2.96 \pm 0.21$). Coulomb stress analysis of the 2014 Ziama and 2019 Jijel earthquakes indicates that the two earthquakes appear to be individually triggered events with no stress transfer between them. The 2019 Jijel earthquake is associated with one of the three active *en echelon* faults that have already been identified in the central part of the Algerian margin via recent marine surveys. It belongs to the serie of many moderate seismic events that have recently affected the Algerian margin (Boumerdes, Algiers, Bejaia), and is representative of the active deformation process along the Algerian margin that is marked by the initiation of an incipient subduction zone with a progressive plate boundary migration since the late Miocene.

1. Introduction

The Algerian margin seismicity has been poorly constrained for decades due to the lack of a high-performance seismic network and marine investigations. Few studies have investigated the deformation process that affects this region crosscutting by the African–Eurasian plate boundary of the western Mediterranean (Fig. 1a).

The offshore region of northern Algeria was the site of a number of historic marine seismic events, such as the 1365 Algiers Earthquake (Mokrane et al., 1994) and 1790 Oran Earthquake (Benhallou, 1985; Chimouni et al., 2018). However, archives and historical reports have provided only sparse descriptions of these events. The 1856 Jijel earthquake sequence on 21–22 August remains one of the best known historical offshore events (Benhallou, 1985; Yelles-Chaouche et al., 2009b; Harbi et al., 2003). A moderate tsunami was generated from one of the mainshocks of this sequence, and impacted the Mediterranean coast. The recent 1989 offshore Ms 6.0 Tipaza Earthquake (Bounif et al., 2003) and 2003 Mw 6.8 Boumerdes Earthquake (Yelles-Chaouche et al., 2004) occurrence demonstrated the crucial importance for more marine investigations along the Algerian margin (Fig. 1b) to better understand the deformation pattern along the African–Eurasian plate boundary in the western Mediterranean region.

To address the urgent need to improve our knowledge of Algerian margin geodynamics, several marine projects have recently

* Corresponding author. CRAAG, Route de l'Observatoire B.P. 63 Bouzaréah, 16340, Algiers, Algeria.
E-mail addresses: a.yelles@craag.dz (A. Yelles-Chaouche), abacha.issam@yahoo.fr (I. Abacha), o.boulahia@craag.dz (O. Boulahia), c.aidi@craag.dz (C. Aidi), a.chami@craag.dz (A. Chami), a.belheouane@craag.dz (A. Belheouane), sofianerah1@outlook.fr (S.T.-E. Rahmani), roubechk1@outlook.fr (K. Roubeche).

https://doi.org/10.1016/j.jafrearsci.2021.104149
Received 14 April 2020; Received in revised form 4 January 2021; Accepted 11 February 2021
Available online 16 February 2021
1464-343X/

Geophysical Journal International

Unveiling Complex Fault Geometry and Driving Mechanisms: Insights from a Refined Data Processing and multiplet analysis of the 2010 Beni-Ilmane Seismic Sequence (NE Algeria)

Journal:	*Geophysical Journal International*
Manuscript ID	GJI-S-23-0683.R1
Manuscript Type:	Research Paper
Date Submitted by the Author:	11-Jan-2024
Complete List of Authors:	Tikhamarine, El-Mahdi; Université Ferhat Abbas Sétif 1 Faculté des Sciences, Department of Physics Abacha, Issam; CRAAG Boulahia, Oualid; CRAAG Bendjama, Hichem; CRAAG, Seismology Roubeche, Khaled; CRAAG; Université Ferhat Abbas Sétif 1 Faculté des Sciences Rahmani, Sofiane; CRAAG, Geophysics; Université Ferhat Abbas Sétif 1 Faculté des Sciences,
Keywords:	Earthquake dynamics < SEISMOLOGY, Induced seismicity < SEISMOLOGY, Dynamics and mechanics of faulting < TECTONOPHYSICS, Fracture and flow < COMPOSITION and PHYSICAL PROPERTIES

Tectonophysics

Local Magnitude Scale (ML) for Northern Algeria

--Manuscript Draft--

Manuscript Number:	TECTO16847
Article Type:	Research Paper
Keywords:	Local Magnitude Scale; Station Correction; Trilinear Regression; Algerian Digital Seismic Network; Northern Algeria
Corresponding Author:	Khaled Roubeche, Engineer Centre for Research in Astronomy Astrophysics and Geophysics Bouzareah, Alger ALGERIA
First Author:	Khaled Roubeche, Engineer
Order of Authors:	Khaled Roubeche, Engineer
	Fethi Semmane
	Issam Abacha
	Oualid Boulhaia
	Sofiane Taki-Eddine Rahmani
	El-Mahdi TIKHAMARINE
Abstract:	This study presents a local magnitude scale (ML) based on the original Richter definition and designed for use within the Algerian Digital Seismic Network (ADSN). The magnitude scale is derived from the analysis of 17377 zero-peak maximum amplitude traces extracted from the vertical component, simulated as Wood-Anderson seismograms. These traces are taken from a complete seismic dataset of 1901 high-quality earthquakes recorded between January 1, 2010, and June 1, 2022, at a minimum of five stations in the ADSN network. To better account for the attenuation of direct and refracted waves over different distances in northern Algeria, amplitude decay analysis reveals the presence of two transition distances at 90 and 190 km, resulting in three segments. Therefore, a distance correction term, -log10(A0), is introduced and described by the following trilinear function: $$-\log(A0) = \begin{cases} 0.6747\log_{10}(R) - 0.0002R + 1.6306 & R<90 \\ 1.7736\log_{10}(R) - 0.0002R - 0.5169 & 90\leq R<190 \\ 2.4580\log_{10}(R) - 0.0002R - 2.0765 & R>190 \end{cases}$$ R represents the hypocentral distance in kilometers. The derived distance correction formula provides a well-constrained ML relationship for northern Algeria that is valid over a distance range of 5 to 600 kilometers. Compared to other local magnitude relationships, the correlation proposed in this study consistently gives ML values slightly higher than those calculated by the Southern California relationship over all distances, with an average difference of 0.2 units. We computed corrections for 72 stations by minimizing the ML residuals. These corrections range from -0.50 to 0.54, highlighting the influence of local site effects on the amplitude of the seismic signal. The magnitude residuals using our magnitude relationship and incorporating the station corrections, show that the standard deviation has improved significantly, from 0.34 to 0.24. An ML relationship specific to the northern Algerian region provides a valuable tool for seismic monitoring, hazard assessment, and earthquake research in the region.
Suggested Reviewers:	Dino Bindi bindi@gfz-potsdam.de He is one of the professionals that work mainly on the magnitude scale
	Massimo Di Bona massimo.dibona@ingv.it He has already published a detailed article on the estimation of the local magnitude scale

Physics of the Earth and Planetary Interiors

Exploring the Structural Components of the Bejaia-Babors Shear Zone (BBSZ) in NE Algeria: Evidence from Local Earthquake Tomography using Recent Seismic Events (2012-2022).

--Manuscript Draft--

Manuscript Number:	
Article Type:	Research Paper
Keywords:	Northeastern Algeria; BBSZ; LET; LOTOS; Brittle-Ductile Shear
Corresponding Author:	Issam ABACHA, Ph.D Centre for Research in Astronomy Astrophysics and Geophysics Bouzaréah, Algiers ALGERIA
First Author:	Issam ABACHA, Ph.D
Order of Authors:	Issam ABACHA, Ph.D
	Khaled Roubeche, PhD student
	Hichem Bendjama, Dr
	El-Mahdi Tikhamarine, PhD student
	Oualid Boulahia, Dr
	Radia Kherchouche, Dr
	Sofiane Taki-Eddine Rahmani, PhD student
	Hamoud Beldjoudi, Prof
Abstract:	In recent years, the Algerian region of Bejaia-Babors (BB) has experienced significant seismic activity, including the Bejaia-Babors seismic sequence in 2012-2013, the Jijel earthquake in 2019, the El Aouana earthquake in 2020, and Bejaia subsequent earthquakes in 2021 and 2022. These seismic events have not only brought to light the existence of the Bejaia-Babors Shear Zone (BBSZ) but have also emphasized the importance of discerning its structural components, depth, and extent. Our study focuses on the analysis of seismological data from 2012 to 2022, with a particular emphasis on elucidating the intricacies of this geological structure. Using the LOTOS (local tomography software) algorithm, we conducted three iterations of tomographic inversion, successfully obtaining horizontal and vertical sections that facilitated the identification and characterization of subsurface anomalies. The resulting 3D velocity models unveiled key tectonic structures within the BBSZ, including the Offshore Faults System of Jijel (OFSJ), South Greater Kabylia Fault (SGKF), Transversal Fault 1 (TF1), and the collision between the Lesser Kabylia Block (LKB) and the Babors (THF-1). Futhermore, brittle-ductile shears were identified along the Aftis Fault (AF) in the east and brittle shears along the Babors Transverse Fault (BTF) in the west. P-wave velocity analysis indicated the presence of rigid blocks. The observed high Vp/Vs ratio near segment 3 of the BTF fault suggests the presence of a fluid reservoir, likely involved in the Bejaia-Babors seismic sequence (2012-2013), as previously documented. These findings provide valuable insights into the tectonic framework of the BBSZ, highlighting major fault systems and the interaction between different tectonic blocks. The presence of brittle-ductile shears along the AF suggests complex deformation processes in this region. Overall, by identifying key fault systems, characterizing subsurface anomalies, and unveiling the presence of fluid reservoirs, our research not only contributes significantly to geodynamic knowledge but also holds immense significance for seismic hazard assessment, resource exploration, and future research in this field.
Suggested Reviewers:	Haakon Fossen, Prof haakon.fossen@uib.no Hakon Fossen is a prominent structural geologist who has conducted extensive research on shear zones
	Ivan Koulakov, Prof